

**DEVELOPMENT OF AN ACTIVE MORPHING WING
WITH NOVEL ADAPTIVE SKIN FOR AIRCRAFT
CONTROL AND PERFORMANCE**

A thesis submitted for the degree of Doctor of
Philosophy

by
Erdogan Kaygan

College of Engineering, Design and Physical Sciences
Brunel University
May 2016

ABSTRACT

An investigation into an adaptable morphing concept for enhancing aircraft control and performance is described in this thesis. The impetus for the work was multi-legend. Initially, the work involved identifying and optimizing winglets on a swept wing baseline configuration to enhance the controllability and aerodynamic efficiency of unmanned aerial vehicles. Moreover, the other objective was to develop a realistic skin for a morphing aircraft concept that would allow subtle, more efficient shape changes to improve aircraft efficiency.

In this regard, preliminary computations were performed with Athena Vortex Lattice modelling in which varying degrees of twist, swept and dihedral angle were considered. The results from this work indicated that if adaptable winglets were employed on small scale UAVs improvements in both aircraft control and performance could be achieved. Subsequent to this computational study, novel morphing wing and/or winglet mechanisms were developed to provide efficient shape changing as well as to develop a novel alternative method for a morphing skin. This new technique was numerically optimized in ANSYS Mechanical, experimentally investigated in a wind tunnel, and also compared with a baseline aileron configuration. Afterwards, flight testing was performed with an Extra 300 78 inch remote controller aircraft with the results being compared against existing fixed wing configurations.

After evaluating numerical results, from various winglet configurations investigated in AVL, selected cases were found to provide good evidence that adaptable winglets, through morphing, could provide benefits for small scale aircraft control and performance as well as offering an acceptable alternative aircraft control methodology to the current discrete, 3-axis control philosophies. Using ANSYS Mechanical for structural analysis, rib configurations were also optimised in terms of weight, stress, and displacement, as well as required twist deformation magnitudes ($\pm 6^\circ$ of twist achieved). Furthermore, the skin was found to be rigid with a low rate of surface wrinkling promoting a low drag surface.

Ultimately, the viability of this novel concept mechanism was validated through flight testing with similar roll authority achieved compared to traditional aileron

configuration. Finally, a morphing concept also provided potential shape changing performance with smooth aerodynamic surface finish. Leading to the possibility of the concept is being a viable skin for morphing application.

TABLE OF CONTENTS

ABSTRACT	ii
TABLE OF CONTENTS	iv
NOMENCLATURE	viii
ABBREVIATIONS	x
LIST OF FIGURES	xi
LIST OF TABLES	xxii
LIST OF APPENDICES	xxiv
LIST OF PUBLICATIONS	xxvi
ACKNOWLEDGEMENT	xxvii
AUTHOR’S DECLARATION	xxviii
CHAPTER 1 Introduction	1
1.1 Background	1
1.2 Aim of the Thesis	2
1.3 Organisation of the Thesis.....	2
CHAPTER 2 Literature Review	4
2.1 Introduction	4
2.2 History of Morphing Aircraft	4
2.3 Dedicated Morphing Research Programs	13
2.3.1 Mission Adaptive Wing (MAW) Program	13
2.3.2 Active Aero-elastic Wing (AAW) Program	14
2.3.3 Smart Wing Program	15
2.3.4 NASA’s Morphing Aircraft Program 1998-2030.....	15
2.3.5 DARPA’s Morphing Aircraft Structure Program 2002.....	16
2.4 Challenges of Adaptive Aircraft Configurations.....	18
2.5 Adaptable Wing Mechanism Technology	22
2.5.1 Planform altering concepts	22

2.5.2	Wing twist concepts.....	27
2.6	Winglets and Wingtip Devices: Their Adaptability	35
2.7	Morphing Winglets.....	42
2.8	Morphing Skin.....	48
2.9	The Morphing Concept	57
2.10	Summary	59
CHAPTER 3 Computational Setups and Methodologies.....		60
3.1	Introduction	60
3.2	Athena Vortex Lattice (AVL)	60
3.2.1	Limitation of the AVL Software.....	64
3.2.2	Wing and Winglet Geometry	65
3.2.3	Panel Size and Grid Refinement Analysis	67
3.2.4	Uncertainty of AVL Computations.....	68
3.3	Finite Element Modelling (FEM).....	69
3.3.1	ANSYS Structural Mechanics	69
3.3.2	Wing and Winglet Parameter.....	70
3.3.3	Aerodynamic Load Prediction	70
3.3.4	CATIA V5 and ANSYS Static Structure Modelling	73
3.3.5	Meshing Size and Approaches.....	76
3.3.6	Solver Setup.....	77
3.4	Computational Analysis of Prototype Model for Flight Testing.....	78
3.4.1	Wing Geometry.....	78
3.4.2	Aerodynamic Analysis of the RC Configuration.....	79
3.4.3	Computer Aided Design (CAD) of RC Wing Prototype	80
3.4.4	Finite Element Modelling	81
3.5	Summary	84
CHAPTER 4 Experimental Setups and Methodologies		85

4.1	Introduction	85
4.2	Wind Tunnel Model Design and Manufacturing.....	85
4.2.1	Computer Aided Design (CAD) and Analysis	85
4.2.2	Wind Tunnel Test Model and Twist Mechanism	87
4.2.3	Aileron Design and Comparison.....	97
4.3	Wind Tunnel Setup and Apparatus	100
4.3.1	The Hotwire System	100
4.3.2	Wake Surveys and Wind Tunnel Flow Quality Assessment	103
4.3.3	Force Balance Setup	107
4.3.4	Servo Driver System and Angle of Attack Adjustment.....	110
4.3.5	Model Installation and Testing Process	110
4.3.6	Force Balance Calibration	114
4.3.7	Moment Data Reduction.....	115
4.3.8	Experimental Procedures and Data Processing	115
4.3.9	Experimental Uncertainty (Experimental Error)	116
4.4	Design and Manufacturing of Prototype Wing for Flight Testing .	119
4.4.1	RC Plane Wing Manufacture and Implementation.....	120
4.4.2	Instrumentation	128
4.4.3	Flight Environment and Testing procedures.....	130
4.5	Summary	132
CHAPTER 5 Results and Discussion		133
5.1	Introduction	133
5.2	Initial Computational Results for Swept Wing/Winglet Configurations.....	133
5.2.1	Effects of Changing Winglet Dihedral Angle on the Static Force and Moment Coefficients	134
5.2.2	Effects of Changing Winglet Twist Angle on Aircraft Control and Performance	147

5.2.3	Effects of Changing Winglet Swept Angle on Control and Performance	149
5.2.4	Optimized Winglet Sweep Angle and Twist Analysis	151
5.2.4.1	Effects of Changing Dihedral Angle on Twisted Winglet Performance	152
5.2.4.1	Effects of winglet twist on Aerodynamic Performance and Control Moments.....	159
5.3	Prototype Wind Tunnel Model FEA and Experiments results.....	162
5.3.1	Finite Element Analysis and Rib Shape Optimisation	162
5.3.2	Experimental and Numerical Analysis of Wind Tunnel Model .	173
5.3.3	Static Forces and Moments.....	174
5.3.4	Influence of Reynold Number on Aerodynamic Response of Wing Twist	180
5.3.5	Comparison between Standard Aileron and Morphing Concept	185
5.4	Flight Testing	192
5.4.1	FEA of the Concept for Flight Testing	192
5.4.2	Structural Comparison between FEA and Prototype Morphing Wing	195
5.4.3	Rolling Rate comparison between the traditional wing structure and prototype morphing wing concept.....	197
5.5	Summary	202
	CHAPTER 6 Conclusion and Future Work.....	204
	REFERENCES	208
	APPENDIX-A.....	221

NOMENCLATURE

A	non-linear function of a matrix	[-]
AR	Wing Aspect Ratio	[-]
c	Mean Aerodynamic Chord	[m]
C_D	Drag Coefficient	[-]
C_L	Lift Coefficient	[-]
C_Y	Side Force Coefficient	[-]
C_l	Rolling Moment Coefficient	[-]
C_m	Pitching Moment Coefficient	[-]
C_n	Yawing Moment Coefficient	[-]
C_p	Pressure Coefficient	[-]
D	Drag Force	[N]
E	Young Modulus	[Pa]
E_p	Percentage error in energy norm	[-]
e	Total energy error for the entire model	[mJ]
I_i	Total vortex strength	[-]
L	Lift Force	[N]
M	Pitching Moment	[Nm]
m	Mach Number	[-]
N	Yawing Moment	[Nm]
n	Load Factor	[-]
P	Pressure	[Pa]
q	Dynamic Pressure	[Pa]
R	Roll Moment	[Nm]
R_0	Specific Gas Constant	$[\frac{J}{kg \times ^\circ K}]$
Re	Reynolds Number	[-]

S	Wing Area	[m]
t	Rib edge thickness	[mm]
T	Temperature	[°K or °C]
U_ε	Strain energy over the model	[Pa]
u	Velocity components aligned with X axis	[m/s]
v	Velocity components aligned with Y axis	[m/s]
V	Flow Velocity	[m/s]
V'	Root mean square of velocity	[m/s]
w	Velocity components aligned with Z axis	[m/s]
x	Model length	[m]
x_l	Characteristic Length	[m]
Y	Side Force	[N]
Z	Transverse co-ordinate	[m]
Z_w	Distance between model and side wall	[m]

Greek Symbols

γ	Aileron Angle	[deg]
ρ	Air Density	[kg/m ³]
α	Angle of Attack	[deg]
ω	Average Value	[-]
Γ	Dihedral Angle	[deg]
μ	Dynamic viscosity	[kg/ms]
ν'	Effective Poisson's Ratio	[-]
ε_e	Equivalent Strain	[Pa]
Ψ	Incidence Angle	[deg]
ν	Kinematic viscosity	[m ² /s]
σ	Magnitude of Stress	[Pa]

σ_e	Von-Mises Stress	[Pa]
σ_0	Principal Stress	[Pa]
ε_0	Principal Strain	[Pa]
δ	Magnitude of Deflection	[mm]
\ddot{r}	Wing Rotation Angle	[deg]
π	Ratio of a circle's perimeter to its diameter	[-]
σ_o	Standard deviation	[-]
Λ	Sweep Angle	[deg]
ϕ	Twist Angle	[deg]

ABBREVIATIONS

AAW	Active Aero-elastic Wing
AFLR	Air Force Research Laboratory
AVL	Athena Vortex Lattice Method
CFD	Computational Fluid Dynamics
DARPA	Defence Advanced Research Projects Agency
DOF	Degree of Freedom
FEM	Finite Element Modelling
FMCs	Flexible Matrix Composites
MAC	Mean aerodynamic Chord
MAV	Mission Adaptive Wing
MDO	Multi Design Optimisation
NGC	Northrop Grumman Corporation
NW	Normal Winglet
RC	Radio Controller
SB	Sweep Back
SF	Sweep Forward
SMA	Shape Memory Alloys
TI	Turbulence Intensity
UAV	Unmanned Aerial Vehicle

LIST OF FIGURES

Figure 2.1 Picture of the Wright Flyer Plane.	4
Figure 2.2 Effects of changing wing parameters on the flight performance [3].	5
Figure 2.3 Classification of morphing aircraft technology [3].....	6
Figure 2.4 Parker’s smooth camber change design [9]	7
Figure 2.5 Variable camber and swept wing aircraft models :(a) Burnelli’s variable cambered design aircraft (GX-3) [10], (b) Hill’s variable swept tailless aircraft (Pterodactyl IV) [11] and (c) Ivan Makhonine’s variable area aircraft model (MAK-10)[12].....	8
Figure 2.6 Bakashev’s prototype models: (a) RK (1937), (b) RK-1 (Modified model) [14].	9
Figure 2.7 The variable incidence wing aircrafts: (a) Republic XF-91 "Thunderceptor" (1949) [15] and (b) Vought F8U Crusader (1955) [3].	10
Figure 2.8 The first ‘swing’ wing aircraft: (a) Messerschmitt P-1101 (1944) [3] and (b) Bell X-5 (1952) [16].	10
Figure 2.9 Variable sweep wing aircraft: (a) XF10F-1 Jaguar (1952) [17] and (b) F-111 Aardvark (1964) [18]	11
Figure 2.10 F-14 Tomcat: sweep back position (Left) and un-swept configuration (Right) [19].	12
Figure 2.11 Russian variable dihedral wing aircraft MiG 105-11 [20].....	12
Figure 2.12 The Mission Adaptive Wing Program: Modified F-111 [24].....	13
Figure 2.13 NASA Dryden Flight Research Center F/A-18 with flexible wing [21].	14
Figure 2.14 Shape memory alloyed wires to achieve wing twist movements [28]...	15
Figure 2.15 Modelling of NASA’s futuristic morphing aircraft [29].	16
Figure 2.16 Lockheed Martin foldable morphing wing ideas [30].	16
Figure 2.17 NextGen Aeronautics sliding morphing wing aircraft [17].	17
Figure 2.18 Technical challenges of Morphing Aircraft [3]	19
Figure 2.19 Mission segments for AAF aircraft configuration [43].	20
Figure 2.20 Spider plot comparing predicted performance of the baseline Firebee, a morphing airfoil, Firebee and a morphing planform Firebee [35].	21
Figure 2.21 Configuration of planform changing concepts	22

Figure 2.22 Blondeau’s wing span mechanism: pneumatic actuators and root rib [52].	23
Figure 2.23 Neal et al. [50] wing span altering mechanism: (a) Pneumatic actuator for wing span change and (b) wind tunnel model with an extended wing span.	24
Figure 2.24 Morphing Span extending mechanisms: (a) Morphing core design for non-extended state and extended state and (b) Ajaj’s wing box span extending mechanism [55] [56].	24
Figure 2.25 Reed [57] interpenetrating rib concepts: Compressed state (left) and extended state (right).	25
Figure 2.26 Swept wing aircraft and its mechanism: (a) Marmier[59] wind tunnel model and (b) Neal[60] lead-screw mechanism.	26
Figure 2.27 Mattioni[61] interconnected truss rib structures: (a) Straight configuration and (b) Sweep configuration.	26
Figure 2.28 Scissors mechanism: (a) test setup and (b) schematic of scissors mechanism [62].	27
Figure 2.29 Schematic view of Adaptive Shell-positioning Flexspar [66].	28
Figure 2.30 Neal[60] twisting mechanism: (a) Internal design of twisting mechanism (b) External design of twisting mechanism.	29
Figure 2.31 Review of Garcia[68] design: micro air vehicle (left) and (b) torque rod assembled membrane wing (right).	29
Figure 2.32 Cooper[78] Wing Twist Mechanisms: (a) rotating spar mechanism and (b) translating spar mechanism [78].	30
Figure 2.33 Vos[72] Twist mechanism: (a) Internal wing structure consisting of four ribs that rotate independently about the circular main spar and (b) Final design of a wing with covered CFRP (carbon fiber reinforced polymer).	31
Figure 2.34 The Adaptive Torsion Wingbox: (a) Maximum and (b) Minimum torsional stiffness web positions [81].	32
Figure 2.35 Shape morphing aero control surface in two configurations: (a) both actuator ribs at minimal curvature, (b) both actuators at maximal curvature [73].	33
Figure 2.36 Fish Bone Active Camber Wing.	34
Figure 2.37 Different Wingtip Devices: (a) Most common winglet devices, and (b) Kroo’s wingtip configuration [91].	35
Figure 2.38 The wing model including winglet shapes [95].	37
Figure 2.39 Hossain[100] elliptical winglet configuration with 60° cant angle.	38

Figure 2.40 Various raked wingtip test models : Raked angle of 15°, 20°, 25°, 30°, and 0° from Left to right [102].....	38
Figure 2.41 Heller[103] wind tunnel test models: (a)various winglet shapes and (b) wind tunnel model with an fitted winglet configuration.....	39
Figure 2.42 Manufactured wing and winglet models [104].....	39
Figure 2.43 Installed Sharklets on Airbus A-320 family [108].....	40
Figure 2.44 Differences between Boeing 787 Dreamliner aircraft’s winglet (left side raked winglets) [107] and Airbus A-350XW’s winglet configuration (Right side blended winglets) [109].....	41
Figure 2.45 Multi Winglet Models: (a) Smith[112] five aluminium multiple flat winglets and (b) Srikanth[113] tufts flow visualization for multi winglet model at $\alpha=5^\circ$	42
Figure 2.46 Experimental wind tunnel models: (a) two active winglets [114] and (b) split wingtip configuration [116].	43
Figure 2.47 Schematic view of narrow body fixed wing and morphing parts [120].	44
Figure 2.48 Morphing Winglet application: (a) the corrugated skin for the MORPHLET and (b) the mechanical demonstrator [121].....	44
Figure 2.49 Numerical Investigation of the corrugated skin showing buckling pattern of the non-supported skin (left three models) and the effect of reinforcement (right three models) [121].	45
Figure 2.50 Bistable Winglet Modelling: (a) Unsnapped winglet and (b) Snapped winglet configurations [122].....	45
Figure 2.51 Multi active winglet applications: (a) Dragon Eye UAV with multiple winglets [128] and (b) Three cant angled split winglet configuration [129].	47
Figure 2.52 Experimental setup for active wing-tip flying wing [131].	47
Figure 2.53 Smith’s C-Winglet configuration [133].....	48
Figure 2.54 Structural deformation of the FE airfoil section after final step iteration [138].....	49
Figure 2.55 Honeycomb structures: (a) Skin made of a cellular core and face-sheets [139] and (b) Prototype of hybrid cellular honeycomb with attached polymeric face sheet [140].....	50
Figure 2.56 Morphing 1D skin application: (a) proposed morphing skin prototype including PAM actuation system [143] and (b) Murray’s FMC test apparatus [4]. ..	51

Figure 2.57 Composite Corrugated Skin: (a) the corrugated-form composites that are flexible in the corrugation direction and stiff in the transverse direction to the corrugation and (b) corrugated composites with one-sided filling of rubber (upside) and rod stiffened corrugated with one-sided filling of rubber (downside) [136].....	53
Figure 2.58 Tamai’s Dragonfly corrugated airfoil: (a) Corrugated cross section of a dragonfly wing, (b) Instantaneous velocity fields for streamlined traditional airfoil, (c) Instantaneous velocity fields for flat plane, and (d) Instantaneous velocity fields for corrugated dragonfly airfoil [147].....	54
Figure 2.59 Profile shape of the unmodified NACA 0012 (top), modified with 2 sinusoidal waves and amplitude of 1% chord (middle), modified with 10 sinusoidal waves and amplitude of 0.6% chord (bottom) [150].....	55
Figure 2.60 Thill’s corrugated structures: (a) picture of rectangular corrugated sandwich structure and (b) pictures of out of wind tunnel tests [144].	56
Figure 2.61 CAD design of an adaptable wing/winglet model.	58
Figure 3.1 Location of the Bounded Vortex	61
Figure 3.2 Selected panel in three component vortex lines for Vortex Filament Strength	62
Figure 3.3 The range of validity for AVL calculation [153].....	65
Figure 3.4 Schematic View of Variable Winglet Structures: (a) Normal positioned winglet (NW), (b) swept back winglet (SB), (c) swept forward winglet (SF), (d) winglet dihedral angle (Γ), (e) winglet positive twist angle ($+\phi$), and (f) winglet negative twist angle ($-\phi$).....	66
Figure 3.5 Lift Coefficient versus Number of Panels.	67
Figure 3.6 Drag Coefficient versus Number of Panels.	67
Figure 3.7 Flowchart for ANSYS Mechanical solution steps.	69
Figure 3.8 Wing and Winglet Parameters: (a)Positive twist(Washin) and (b) Negative twist(Washout).....	70
Figure 3.9 Schematic view of wing setup in AVL.....	71
Figure 3.10 Divided strips to obtain the force results for each rib components.	71
Figure 3.11 Maximum force distribution on wing structure at $+10^\circ$ of twist.	72
Figure 3.12 Maximum force distribution on winglet structure at $+10^\circ$ of twist.	72
Figure 3.13 The geometric design of a fixed end section.	73
Figure 3.14 CATIA boundary conditions for morphing element.....	74
Figure 3.15 Boundary condition applied to a morphing structure.	75

Figure 3.16 Applied appropriate meshing size to morphing elements.....	76
Figure 3.17 Mesh independent results for maximum stress occurred on morphing structure.....	77
Figure 3.18 Mesh independent results for maximum deformation magnitudes occurred on morphing structure.	77
Figure 3.19 RC plane analysis: (a) Airfoil shape and (b) Schematic View of Wing Structures in AVL.	79
Figure 3.20 Aero load on wing structure.....	80
Figure 3.21 CAD for Extra300 Wing Twist Section.....	81
Figure 3.22 Load Applied the wing structure.	82
Figure 3.23 Mesh Refinement Test for RC Plane Wing: (a) Von-Mises Stress and (b) Deformation Magnitude with different number of elements.	83
Figure 3.24 Final Mesh for Wing Structure.	84
Figure 4.1 Wind Tunnel Model.....	86
Figure 4.2 Structure Analysis of a wing: (a) Von-Mises Stress analysis of a wing under aerodynamic load and (b) Displacement vector of a wing under aerodynamic load.....	87
Figure 4.3 Design of a Morphing Twist Mechanism.	88
Figure 4.4 Manufacture of Raku-Tool WB-1700 Wing: (a) Wing manufacturing process, (b) Fixed baseline model for comparison, (c) Half wing profile, and (d) Removed bottom section of the wing and installed parts.	89
Figure 4.5 Wing and glued carbon fibre tube.....	90
Figure 4.6 Morphing Twist Mechanism.....	91
Figure 4.7 End-section and its mechanism.....	92
Figure 4.8 End-section structure stress analysis: (a) CAD modelling and (b) Stress result.....	93
Figure 4.9 Laser Cutting Machine.....	93
Figure 4.10 Morphing element construction: (a) assembly process for rib structures and (b) completed wing structure and aluminium cover for mechanism.....	94
Figure 4.11 Internal mechanism of an active wing.	95
Figure 4.12 Complete active wing structure: (a) without lacquered skin and (b) lacquered skin.....	96
Figure 4.13 Effects of changing surface smoothness on drag coefficient (<i>CD</i>) results.	97

Figure 4.14 Structural Analysis for Aileron.....	98
Figure 4.15 Aileron Configurations :(a) CAD design for full wing with an aileron, (b) CAD design for Aileron, (c) Manufactured wing profile and (d) Manufactured wing and ailerons.	99
Figure 4.16 Brunel University Wind Tunnel Environment.....	100
Figure 4.17 Router and slots for probe position.....	101
Figure 4.18 Hotwire probe setup: (a) Installed Probe and probe support bar and (b) Probe position slots and traverse.....	101
Figure 4.19 Hot Wire Probe Calibration Setup: (a) Velocity Calibration and (b) Angular Calibration.....	102
Figure 4.20 Hotwire anemometry calibration graphs: (a) sensor E1 versus velocity (U), (b) sensor E1 error rate, (c) sensor E2 versus velocity (U), and sensor E2 error rate.....	102
Figure 4.21 Hotwire probe position and the boundary layer plate.....	104
Figure 4.22 Velocity maps front side of the plate (x=150mm): (a) without plate and (b) with plate.	105
Figure 4.23 Turbulent intensity maps front side of the plate (x=150mm): (a) without plate and (b) with plate.....	105
Figure 4.24 Velocity maps middle side of the plate (x=0mm): (a) without plate and (b) with plate.	105
Figure 4.25 Turbulent intensity maps middle side of the plate (x=0mm): (a) without plate and (b) with plate.....	106
Figure 4.26 Velocity maps rear side of the plate (x=-300mm): (a) without plate and (b) with plate.	106
Figure 4.27 Turbulent intensity maps rear side of the plate (x=-300mm): (a) without plate and (b) with plate.....	106
Figure 4.28 Wind tunnel balance.	108
Figure 4.29 Instrumentation to obtain results: (a) AMTI MC3A-500 Load Cell and (b) DigiAmp six channel strain gage amplifier.....	108
Figure 4.30 Force and Moment Balance Mechanism Setup.	109
Figure 4.31 Installed boundary layer plate and the airfoil shaped fairing.....	109
Figure 4.32 Manual Angle of Attack Mechanism.....	110
Figure 4.33 Boundary Layer Plate.	111
Figure 4.34 Experimental setup for Adaptive Wing Configuration.....	111

Figure 4.35 Experimental Setup for Full Wing Configuration.	112
Figure 4.36 Wind Tunnel Setup for Aileron (-30°).....	112
Figure 4.37 Twist cases for wind tunnel model.	113
Figure 4.38 Schematic of the Extra 300-78inch aerobatic plane and prototype wing concept.	119
Figure 4.39 Full Wing was cut to implement novel design concept.	120
Figure 4.40 Structural analysis for full wing profile: (a) Von-Mises stress and (b) total deformation.	121
Figure 4.41 Full wing profiles: (a) normal wing structure and (b) Modified wing structure (bottom side).	122
Figure 4.42 Morphing element design: (a) Rib assembly process and (b) completed morphing configurations.	123
Figure 4.43 Wing manufacturing: (a) Clamped the additional support ribs and (b) Glued active wing internal carbon tube to inside the wing model.	124
Figure 4.44 Internal structure of the morphing elements: (a) the point where the wing attached and (b) tip of the wing structure.....	125
Figure 4.45 Stress Analysis of end-bit due to rotation.....	126
Figure 4.46 Final structure of a wing model.	126
Figure 4.47 Preparing wing for covering.	127
Figure 4.48 Wing Structures: Fixed wing with an aileron (top side) and wing with twist section (bottom side).	127
Figure 4.49 Scale Measurements: (a) Fixed (baseline) wing and (b) morphing wing.	128
Figure 4.50 Futaba radio systems: (a) Transmitter and (b) Receiver.....	129
Figure 4.51 Aircraft Instrumentations.....	129
Figure 4.52 The flying site: Little Harlington Playing Fields.....	130
Figure 4.53 Flight Testing: (a) Wing with ailerons and (b) Wing with morphing concept.	131
Figure 5.1 Effects of changing winglet dihedral and twist angle in normal winglet (NW) configuration at $CL_0 \cong 0.6$ (a) CL and (b) ΔCL	134
Figure 5.2 Effects of changing winglet dihedral, sweep, and twist angle in sweep back winglet (SB) configuration at $CL_0 \cong 0.6$ (a) CL and (b) ΔCL	135
Figure 5.3 Effects of changing winglet dihedral, sweep, and twist angle in sweep forward winglet (SF) configuration at $CL_0 \cong 0.6$ (a) CL and (b) ΔCL	136

Figure 5.4 Effects of changing winglet dihedral and twist angle in normal winglet (NW) configuration at $CL0 \cong 0.6$ (a) CD and (b) ΔCD	137
Figure 5.5 Effects of changing winglet dihedral, sweep, and twist angle in sweep back winglet (SB) configuration at $CL0 \cong 0.6$ (a) CD and (b) ΔCD	138
Figure 5.6 Effects of changing winglet dihedral, sweep, and twist angle in sweep forward winglet (SF) configuration at $CL0 \cong 0.6$ (a) CD and (b) ΔCD	139
Figure 5.7 Effects of changing winglet dihedral and twist angle in normal winglet (NW) configuration at $CL0 \cong 0.6$ (a) CL/CD and (b) $\Delta CL/CD$	140
Figure 5.8 Effects of changing winglet dihedral, sweep, and twist angle in sweep back winglet (SB) configuration at $CL0 \cong 0.6$ (a) CL/CD and (b) $\Delta CL/CD$	141
Figure 5.9 Effects of changing winglet dihedral, sweep, and twist angle in sweep forward winglet (SF) configuration at $CL0 \cong 0.6$ (a) CL/CD and (b) $\Delta CL/CD$	142
Figure 5.10 Effects of changing winglet dihedral and twist angle in normal winglet (NW) configuration at $CL0 \cong 0.6$ (a) Cm and (b) ΔCm	143
Figure 5.11 Effects of changing winglet dihedral, sweep, and twist angle in sweep back winglet (SB) configuration $CL0 \cong 0.6$ (a) Cm and (b) ΔCm	144
Figure 5.12 Effects of changing winglet dihedral, sweep, and twist angle in sweep forward winglet (SF) configuration $CL0 \cong 0.6$ (a) Cm and (b) ΔCm	145
Figure 5.13 Effects of changing winglet dihedral and twist angle in normal winglet (NW) configuration $CL0 \cong 0.6$ (a) Cl and (b) ΔCl	146
Figure 5.14 Effects of changing winglet dihedral, sweep, and twist angle in sweep back winglet (SB) configuration $CL0 \cong 0.6$ (a) Cl and (b) ΔCl	147
Figure 5.15 Effects of changing winglet dihedral, sweep, and twist angle in sweep forward winglet (SF) configuration $CL0 \cong 0.6$ (a) Cl and (b) ΔCl	148
Figure 5.16 Effects of changing winglet dihedral and twist angle in normal winglet (NW) configuration $CL0 \cong 0.6$ (a) Cn and (b) ΔCn	149
Figure 5.17 Effects of changing winglet dihedral, sweep, and twist angle in sweep back winglet (SB) configuration $CL0 \cong 0.6$ (a) Cn and (b) ΔCn	150
Figure 5.18 Effects of changing winglet dihedral, sweep, and twist angle in sweep forward winglet (SF) configuration $CL0 \cong 0.6$ (a) Cn and (b) ΔCn	151
Figure 5.19 Effects of Changing Winglet Dihedral and Twist angle on Performance (ΔCL) at $CL0 \cong 0.6$: a) Wash-in (Positive Twist) and b) Wash-out (Negative Twist).	153

Figure 5.20 Effects of Changing Winglet Dihedral and Twist angle on Performance (ΔCD) at $CL0 \cong 0.6$: a) Wash-in (Positive Twist) and b) Wash-out (Negative Twist).	154
Figure 5.21 Effects of Changing Winglet Dihedral and Twist angle on Performance ($\Delta CL/CD$) at $CL0 \cong 0.6$: a) Wash-in (Positive Twist) and b) Wash-out (Negative Twist).	155
Figure 5.22 Effects of Changing Winglet Dihedral and Twist angle on Performance (ΔCl) at $CL0 \cong 0.6$: a) Wash-in (Positive Twist) and b) Wash-out (Negative Twist).	157
Figure 5.23 Effects of Changing Winglet Dihedral and Twist angle on Aircraft Performance (ΔCm) at $CL0 \cong 0.6$: a) Wash-in (Positive Twist) and b) Wash-out (Negative Twist).	158
Figure 5.24 Effects of Changing Winglet Dihedral and Twist angle on Performance (ΔCn) at $CL0 \cong 0.6$: a) Wash-in (Positive Twist) and b) Wash-out (Negative Twist).	160
Figure 5.25. Trailing edge deformation for three different rib designs near the wing tip under twist deformation: (a) rib thickness is 1mm and the maximum gap between two ribs is 0.635mm, (b) rib thickness is 0.8mm and the maximum gap between two ribs is 0.496mm, and rib thickness is 0.6 mm and the maximum gap between two ribs is 0.212mm.	163
Figure 5.26 Optimised rib structure with parameters ($r1=2mm$, $r2=2mm$, $R = 10mm$, and $t=2mm$).	164
Figure 5.27 Von-Mises Stress for $t=2mm$: (a) Von-Mises stress analysis and (b) Detail surface analysis of morphing concept.	166
Figure 5.28 Total twist deformation on morphing concept (Wash-out): (a) $t=3mm$, (b) $t=2.5mm$, (c) $t=2mm$, (d) $t=1.5mm$, and (e) $t=1mm$	167
Figure 5.29 Total twist deformation on morphing concept (Wash-in): (a) $t=3mm$, (b) $t=2.5mm$, (c) $t=2mm$, (d) $t=1.5mm$, and (e) $t=1mm$	168
Figure 5.30 Rib deformation under aerodynamic load (wash-out): (a) $t=1mm$, (b) $t=1.5mm$, (c) $t=2mm$, (d) $t=2.5mm$, and (e) $t=3mm$	170
Figure 5.31 Rib deformation under aerodynamic load (wash-in): (a) $t=1mm$, (b) $t=1.5mm$, (c) $t=2mm$, (d) $t=2.5mm$, and (e) $t=3mm$	171

Figure 5.32. Maximum negative twist (wash-out) of the morphing concept without any flow interaction: (a) Experimental model twist and (b) Numerical modelling twist movement.	173
Figure 5.33 Maximum positive twist (wash-in) of the morphing concept without any flow interaction: (a) Experimental model twist movement and (b) Numerical modelling twist movement.	174
Figure 5.34 . Effects of changing twist angle on the longitudinal static forces and moments, $Re_n = 3.85 \times 10^5$	175
Figure 5.35 Effects of changing twist angle on the lateral static forces and moments, $Re_n = 3.85 \times 10^5$	179
Figure 5.36 Effects of changing twist angle on the longitudinal static forces and moments, $Re_n = 5.14 \times 10^5$	183
Figure 5.37 Effects of changing twist angle on the lateral static forces and moments, $Re_n = 5.14 \times 10^5$	184
Figure 5.38 Comparison between plain aileron and twist configuration: (a) CL , (b) CD , (c) CY , (d) Cl , (e) Cm , and (f) Cn	188
Figure 5.39 Lift to drag ratio for wing twist and aileron configurations.	189
Figure 5.40 Rolling moment Coefficient versus drag coefficient.	191
Figure 5.41 The wingtip structure for flight testing: (a) Von-Misses Stress of structure and (b) Detail analysis of surface Von-Misses stress.	193
Figure 5.42 Displacement magnitudes of morphing concept: (a) Washin case (positive twist) and (b) Washout case (negative twist).	194
Figure 5.43 Skin (rib) displacement under aerodynamic load: (a) wash-in case (positive twist) 0.40mm and (b) washout case (negative twist) 0.36mm.	195
Figure 5.44 Maximum twist of the morphing concept without any flow interaction: (a) Experimental model twist movement (wash-out) and (b) Numerical modelling twist movement (wash-out).	196
Figure 5.45 Maximum twist of the morphing concept without any flow interaction: (a) Experimental model twist movement (wash-in) and (b) Numerical modelling twist movement (wash-in).	196
Figure 5.46 Altitude and Approximate Flight Path.	197
Figure 5.47 Flight Data for baseline (aileron) and morphing (twist) configuration: (a) Roll angle for rotation 1 and 2 and (b) Load factor for rotation 1 and 2.	198

Figure 5.48 Flight Data for baseline (aileron) and morphing (twist) configuration: (a) Roll angle for rotation 3 and 4 and (b) Load factor for rotation 3 and 4.	199
Figure 5.49 Velocity profile for baseline (aileron) and morphing (twist) configurations.....	200
Figure 5.50 Morphing concept during flight: (a) and (b) washout, and (c) and (d) washin cases.	201
Figure 5.51 Morphing concept after flight testing.	202

LIST OF TABLES

Table 1 Uncertainty Analysis of AVL.....	68
Table 2 Summary of Material Properties	75
Table 3 ANSYS Solver Options [161]	78
Table 4 Summary of Material Properties	81
Table 5 Technical Specification of AMTI MC3A-500 M [173].....	107
Table 6 AMTI Calibration Equations for Force and Moment.....	114
Table 7 Streamline Calibration Equations for Force and Moment.....	115
Table 8 Uncertainty values of devices.....	118
Table 9 Uncertainty values of calculated parameters.....	118
Table 10 Uncertainty values of measured force and moments	118
Table 11 Deformation and Stress on Carbon rods for Various Rod Sizes	164
Table 12 Summary of Stress on carbon rods for various rib designs.....	169
Table 13 Stress and Deformation of a morphing structure	193

LIST OF EQUATIONS

(3-1).....	62
(3-2).....	62
(3-3).....	62
(3-4).....	62
(3-5).....	62
(3-6).....	63
(3-7).....	63
(3-8).....	63
(3-9).....	63
(3-10).....	63
(3-11).....	63
(3-12).....	63
(3-13).....	64
(4-1).....	103
(4-2).....	103
(4-3).....	111
(4-4).....	111
(4-5).....	115
(4-6).....	115
(4-7).....	116
(4-8).....	116
(4-9).....	117
(4-10).....	117
(4-11).....	117

LIST OF APPENDICES

Figure A- 1 Airfoil data analysis CL/CD	221
Figure A- 2 Airfoil data analysis: CL versus alpha (Up-Left), CD versus alpha (Up-Right), Cm versus alpha (Down-Left), and CL/CD versus alpha (Down-Right).	221
Figure A- 3 Sanded Wing and Morphing Structure.	222
Figure A- 4 Enamel Spray paint & Clear Lacquer for Wing.	222
Figure A- 5 CATIA Structural Analysis Setup for Aileron	223
Figure A- 6 Directional Calibration Graphs: (a) Probe Velocity versus Angle and (b) Velocity error versus angle.	223
Figure A- 7 Wind Tunnel Setup for Aileron (-10°).	224
Figure A- 8 Wind Tunnel Setup for Aileron ($+10^\circ$).	224
Figure A- 9 Wind Tunnel Setup for Aileron ($+20^\circ$).	225
Figure A- 10 Wind Tunnel Setup for Aileron (-20°).	225
Figure A- 11 Wind Tunnel Setup for Aileron ($+30^\circ$).	226
Figure A- 12 Wind Tunnel Setup for Aileron (-30°).	226
Figure A- 13 Effect of deflected tips on pitch: when one or both tips of the trimmed, longitudinally stable, planar configuration are folded up or down at fixed angle of attack, a nose-up pitching moment is created (aerodynamic center jumps forward while CG is fixed) reduced static margin, Cm is less negative). If the angle of attack is allowed to be adjusted, one can then trim at a larger CL [114].	227
Figure A- 14 Equivalent stress results for $r = 1$ mm (Wash-in)	227
Figure A- 15 Equivalent stress results for $r = 1.5$ mm (Wash-in).	228
Figure A- 16 Equivalent stress results for $r = 2.5$ mm (Wash-in).	228
Figure A- 17 Equivalent stress results for $r = 1$ mm (Wash-out).	228
Figure A- 18 Equivalent stress results for $r = 1.5$ mm (Wash-out).	229
Figure A- 19 Equivalent stress results for $r = 2.5$ mm (Wash-out).	229
Figure A- 20 Deformation Results for $r = 1$ mm (Wash-in).	230
Figure A- 21 Deformation Results for $r = 1.5$ mm (Wash-in).	230
Figure A- 22 Deformation Results for $r = 2.5$ mm (Wash-in).	230
Figure A- 23 Deformation Results for $r = 1$ mm (Wash-out).	231
Figure A- 24 Deformation Results for $r = 1.5$ mm (Wash-out).	231
Figure A- 25 Deformation Results for $r = 2.5$ mm (Wash-out)	231
Figure A- 26 Equivalent stress results for $t = 1$ mm (Wash-out).	232

Figure A- 27 Equivalent stress results for $t = 1\text{mm}$ (Wash-in).....	232
Figure A- 28 Equivalent stress results for $t = 1.5\text{mm}$ (Wash-out).....	232
Figure A- 29 Equivalent stress results for $t = 1.5\text{mm}$ (Wash-in).....	233
Figure A- 30 Equivalent stress results for $t = 2\text{mm}$ (Wash-in).....	233
Figure A- 31 Equivalent stress results for $t = 2.5\text{mm}$ (Wash-out).....	233
Figure A- 32 Equivalent stress results for $t = 2.5\text{mm}$ (Wash-in).....	234
Figure A- 33 Equivalent stress results for $t = 3\text{mm}$ (Wash-out).....	234
Figure A- 34 Equivalent stress results for $t = 3\text{mm}$ (Wash-in).....	234
Figure A- 35 Von-Mises stress for 20 rods twist system.	235
Figure A- 36 Von-Mises stress for 17 rods twist system.	235
Figure A- 37 Von-Mises stress for 16 rods twist system.	235
Figure A- 38 Von-Mises stress for 15 rods twist system.	236
Figure A- 39 Von-Mises stress for 14 rods twist system.	236
Figure A- 40 Von-Mises stress for 12 rods twist system.	236
Figure A- 41 Von-Mises stress for 11 rods twist system (washin).	237
Figure A- 42 Total Deformation for 20 rods twists system.	237
Figure A- 43 Total Deformation for 17 rods twists system.	237
Figure A- 44 Total Deformation for 16 rods twists system.	237
Figure A- 45 Total Deformation for 15 rods twists system.	238
Figure A- 46 Total Deformation for 14 rods twist system.....	238
Figure A- 47 Total Deformation for 12 rods twists system.	238
Figure A- 48 Total Deformation for 11 rods twists system (washout).	238
Figure A- 49 Total Deformation for 11 rods twists system (washin).	238

LIST OF PUBLICATIONS

Conferences:

- Kaygan, E., Gatto, A. (2014), 'Investigation of Adaptable Winglets for Improved UAV Control and Performance', World Academy of Science, Engineering and Technology, INTERNATIONAL CONFERENCE ON AEROSPACE, MECHANICAL, AUTOMOTIVE AND MATERIALS ENGINEERING (ICAMAME 2014), Istanbul, Turkey.
- Kaygan, E., Gatto, A. (2015), "Computational Analysis of Adaptable Winglets for Improved Morphing Aircraft Performance ', World Academy of Science, Engineering and Technology, INTERNATIONAL CONFERENCE ON AEROSPACE, MECHANICAL, AUTOMOTIVE AND MATERIALS ENGINEERING (ICAMAME 2015), Oslo, Norway.

Journals:

- Kaygan, E., Gatto, A. (2014), 'Investigation of Adaptable Winglets for Improved UAV Control and Performance', World Academy of Science, Engineering and Technology, International Science Index 91, International Journal of Mechanical, Aerospace, Industrial and Mechatronics Engineering, 8(7), 1289 - 1294.
- Kaygan, E., Gatto, A. (2015), 'Computational Analysis of Adaptable Winglets for Improved Morphing Aircraft Performance', World Academy of Science, Engineering and Technology, International Science Index 103, International Journal of Mechanical, Aerospace, Industrial, Mechatronic and Manufacturing Engineering, 9(7), 1069 - 1075.
- (Ready to Submit) Kaygan, E., Gatto, A. (2016), 'Novel Design Concepts of Morphing Skin to Enhance Aircraft Control and Performance, Journal of Intelligent Material System and Structures.

ACKNOWLEDGEMENT

I would like to express my great gratitude to Dr Alvin Gatto, my supervisor, for his patience, encouragement throughout this research and excellent suggestions for the project work. During the project, he has taught me, both consciously and unconsciously, how good experimental and computational design is done. I really appreciate all his contributions of time, ideas, and help to make my Ph.D. experience productive and stimulating.

I would like to grateful my parents for funding my studies and for their belief and for their encouragements which always gave me the much motivation throughout my PhD.

I would also like to thankful my dear friends Dr Ali Shefik and Fuat Uyguroglu, for their never-ending support to always keep me enthusiastic.

Finally, I would like to thank the staff at the Brunel University for their support as well as for providing me a friendly and quiet environment during the project work.

AUTHOR'S DECLARATION

This research was conducted at Brunel University London, under the supervision of Dr Alvin Gatto. The research presented in this thesis, unless otherwise stated or referenced, is the work of the author.

The work has not been submitted for another degree or award to any other institution.

Erdogan Kaygan

Date: 09/05/2016

CHAPTER 1 INTRODUCTION

1.1 Background

Aircraft control through the use of traditional discrete control surfaces has achieved widespread success over many years [1]. These traditional methods, widely accepted on the vast majority of aircraft, however can be detrimental to an aircraft aerodynamic performance as they rely on hinged control surfaces which can generate significant flow separation when actuated fully. To meet the ever increasing demands for more efficient, robust, and cost effective designs, there is an argument that conventional control surface methodologies need to be re-examined, in favour of more “morphing” technologies and techniques.

Morphing technologies typically revolve around adaptive geometry structures and mechanisms and are very attractive to aircraft designers as they can provide substantial benefits to aircraft performance. The concept or ‘morphing’ however is not new. Wing warping techniques were employed by the Wright Brothers to control the first powered, heavier than air, aircraft through wing twist via subtended cables [2]. However, even with the substantial research efforts over the last few decades morphing concepts still suffer significant challenges. These include added weight, a compliant skin, and/or overall complexity. Jha and Kudva [3] summarised some of the technical challenges and classifications of morphing aircraft, with the most significant challenges tending to be in the structural design of the concepts and mechanisms employed.

A critical component of a compliant morphing structure is the morphing skin, which has to be flexible for actuation, but also rigid to allow favourable aerodynamic performance to be obtained. Some prior literature on morphing skins, involve flexible skins such as FMC [4], [5], elastomeric skin[6], and corrugated skin [7], [8], however none have yet to achieve widespread use. This problem is particularly difficult as there are conflicting requirements. The skin needs be capable of transferring aerodynamic loads and be flexible in order to move and/or change shape. These requirements are particularly challenging as the surface should also remain smooth and possess a low rate wrinkle at the location of moveable

mechanism. In the view of these challenges this thesis presents concept for active wing twist with an adaptive skin for morphing aircraft control and performance.

1.2 Aim of the Thesis

The motivation for this study was to explore novel concepts of adaptable wing and/or winglet concepts for morphing aircraft control and performance. The primary variable investigated involved changing the angle of twist of the configurations with one goal to assess the concept using both experimental and numerical approaches. Another principle aim was to assess and demonstrate the developed concept within both the wind tunnel and flight test environment. This investigation also aimed to develop an alternative approach for a morphing skin. Overall, the objectives of the research project can be summarised as follows:

- To initially investigate adaptable wing and/or winglet concepts numerically to illustrate the benefits compared to the fixed wing/winglet configuration.
- To design and develop novel twistable wing and/or winglet technology.
- To develop a realistic skin for a morphing aircraft concept that will allow subtle, more efficient shape changes to improve aircraft efficiency.
- To understand the durability of the system, through structural evaluation using ANSYS Mechanical structure.
- To demonstrate the viability of the concept with integration onto a small scale aircraft via flight testing.

1.3 Organisation of the Thesis

Following this introduction, the research proceeds with a literature review in **CHAPTER 2** in which topics related to morphing aircraft concepts are presented. With regard to morphing aircraft, the technical benefits and the challenges of identifying the recent mechanism and morphing skin development concepts are also presented.

In **CHAPTER 3**, the computational design and analysis of the adaptable wing/winglet concept are described. All of the computations were performed with Athena Vortex Lattice modelling and varying degrees of twist, swept and dihedral angle were considered. Moreover, to investigate in detail the concepts of an

adaptable wing or winglet mechanism, the ANSYS Mechanical tool was used. The computational setup is also described in this chapter.

CHAPTER 4 outlines the experimental design and methodology employed. This chapter includes a comprehensive description of the experiments conducted with the main intention to provide information and knowledge of the wind tunnel test programme preparation and data processing. Furthermore, flight testing and instrumentations used for concept validation is also presented.

In **CHAPTER 5**, the results of the computational analysis and experiments are presented and discussed. This chapter includes the effects of the twist, sweep and dihedral angle. The focus here was specifically on winglet configurations as the concept developed is considered adaptable to both. ANSYS structure testing is also described in this chapter as is flight testing results conducted at the end of the development process.

Finally, conclusions and recommendations for future work are summarised in **CHAPTER 6**.

CHAPTER 2 LITERATURE REVIEW

2.1 Introduction

Current interest in morphing vehicles is accelerating with the development of advanced materials, sensors and actuators. Although this area is fairly new, the applications were developed many years ago. This chapter seeks to succinctly map out the morphing applications by highlighting the latest research as well as presenting the historical connections of adaptive aerial vehicles. In this framework, **Section 2.2** and **2.3** introduce the concept of morphing vehicles and the research programme. The latest research related to morphing applications and skin research is presented in **Section 2.4 - 2.8** respectively. A brief summary concludes the chapter in **Section 2.10**.

2.2 History of Morphing Aircraft

A morphing aircraft is a multi-role flight vehicle that changes the configuration of its geometry during flight to adapt to different flight conditions. Morphing technologies typically revolve around adaptive geometry structures and mechanisms and are very attractive to aircraft designers as they can provide substantial benefits to aircraft performance. The concept or ‘morphing’ however is not new. Wing warping techniques were employed in 1903 by the first aeronautical engineers, ‘The Wright Brothers’, to control the first powered, heavier than air, aircraft through a wing twist



Figure 2.1 Picture of the Wright Flyer Plane.

via subtended cables, as shown in **Figure 2.1** [2]. The Wright Brothers paid attention to aerodynamics, control systems, airframe structures, and propulsion systems in order to achieve this revolutionary concept. However this technique is no longer in widespread use. Nowadays ailerons, rudders, and elevators provide primary stability and control for air vehicles. This current traditional methodology, widely accepted on the vast majority today's operational of aircraft, can however, be detrimental to an aircraft's aerodynamic performance principally as they rely on hinged control surfaces that can generate significant flow separation when actuated fully. To meet the ever increasing demand for more efficient, robust and cost effective designs, there is an argument that conventional control surface methodologies need to be re-examined, in favour of more "morphing" technologies and techniques. Jha et al. [3] summarized how using morphing can affect an aircraft's flight performance. As shown in **Figure 2.2**, to achieve efficiency in high-speed flight, the aspect ratio of the wing should be low and the swept angle should be high. In contrast to high-speed flight, low speed flight requires a low sweep angle as well as high aspect ratio wings. In order to have the same aircraft fly diversified missions the aircraft requires large configuration changes representing significant challenges to aircraft through morphing aircraft technology.

Parameter	Effects of Variability – all other parameters unchanged
Wing Plan Area	↑ Increased lift, load factor capability ↓ Decreased parasitic drag
Wing Aspect Ratio	↑ Increased L/D, loiter time, cruise distance, turn rates ↓ Decreased: engine requirements Increased maximum speed; Decreased parasitic drag
Wing Dihedral	↑ Increased Rolling moment capability, lateral stability ↓ Increased maximum speed
Wing Sweep	↑ Increased critical Mach no., dihedral effect ↓ Decreased high-speed drag Increased C_{Lmax}
Wing Taper Ratio	Wing efficiency (spanwise lift distribution); Induced drag
Wing Twist Distribution	Prevents tip stall behavior; Spanwise lift distribution
Airfoil Camber	Zero-lift angle of attack, airfoil efficiency, separation behavior
Airfoil Thickness/Chord Ratio	↑ Improved low-speed airfoil performance ↓ Improved high-speed airfoil performance
Leading Edge Radius	↑ Improved low-speed airfoil performance ↓ Improved high-speed airfoil performance
Airfoil Thickness Distribution	Airfoil characteristics, laminar/turbulent transition

Figure 2.2 Effects of changing wing parameters on the flight performance [3].

Over the years, various shape changing ideas have been used by several researchers. The numerous concepts have been categorized by Jha et al. [3] as shown in **Figure 2.3**. It can clearly be seen that the most achievable techniques are applied

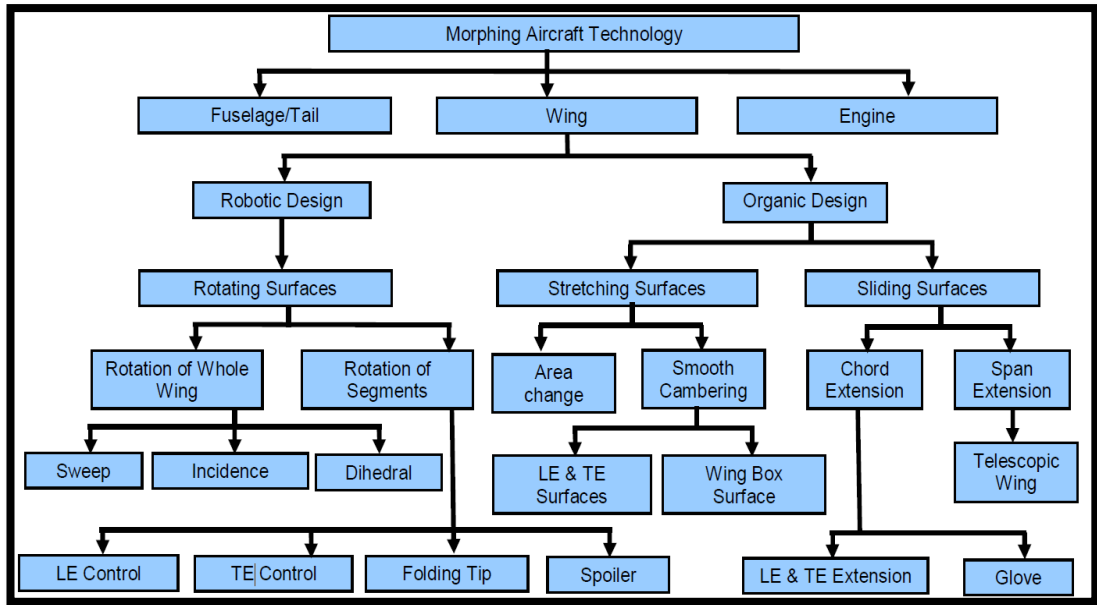


Figure 2.3 Classification of morphing aircraft technology [3].

to aircraft wings, principally because wings are one of most effective benefit-producing parts of the aircraft; there is a large influence on aircraft performance. As can be seen, holistically, the design of the variable wing parts is principally done in two ways: Through robotic or organic design. In robotic design, designers consider rotating the wings and some parts of the wings rather than changing the whole wing. For instance, they change the sweep and incidence angle of the wing, use folding wing tips, spoiler mechanisms, and leading and trailing edge control surfaces. In organic design, wings are organized to change their shape (internal and external) and can be classified into two groups: stretching surfaces and the sliding surfaces. In the stretching surface group, flexible wings aim to stretch the surface to increase the wing area as needed. In the sliding wing group, the wings can be moved over other surfaces. The most extensive example of sliding surfaces is telescopic wings. Whole wings are split into two wings in a span-wise direction with one wing sliding inside the other. A glove wing is another common example with an increase or decrease of the chord length of an airplane. In the following sections, examples of early morphing aircrafts will be presented.

Variable camber wing, telescopic wing and variable incidence wings are other common examples of morphing concepts. These configurations were first proposed in the United States in 1916. The first and most significant project was done by H. F. Parker in 1920 [9]. Variable camber wing concepts were used by Parker for bi-planes

and tri-planes. The goal of the project was to obtain additional lift force in order to provide easy landing and taking off. In Parker's design, spars were located at the leading edge and trailing edge positioned $\frac{2}{3}$ the chord rearward. The front of the aerofoil unit was flexible and the rear was rigid with the ribs allowed to slide over the rear spar. The change in camber of the wing was produced automatically by the load bending the flexible section of the airfoil and produces more lift force. During take-off or under high speed conditions, the airfoil was configured in such a way that it was aligned with the airstream, with essentially no camber as shown in **Figure 2.4**. The wind tunnel and even the real flight-testing stages were completed successfully, but this design was not taken to the fabrication stage, due to added risk of increased bending at a high angle of attack.

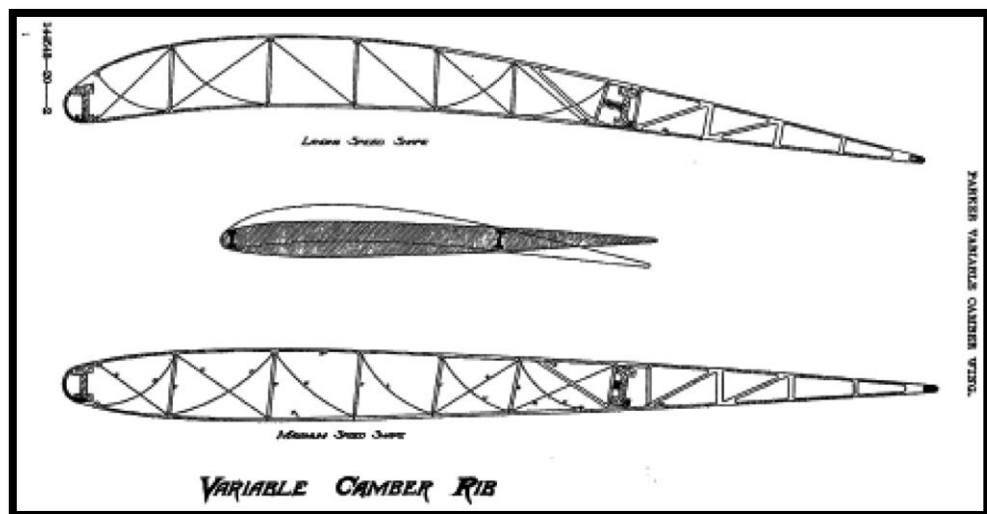
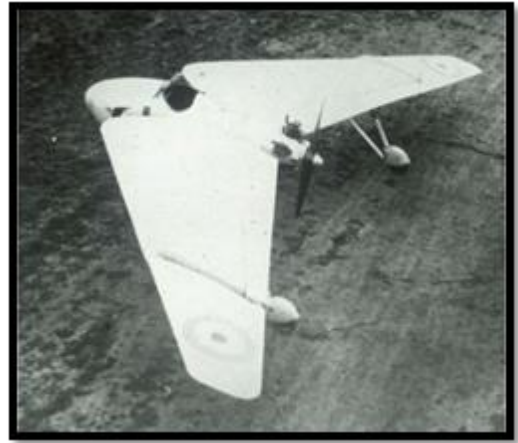


Figure 2.4 Parker's smooth camber change design [9]

Another wing altering concept was reported by V. J. Burnelli [10] of the Upper Burnelli Aircraft Corporation. As illustrated in **Figure 2.5 (a)**, they designed the Burnelli GX-3 aircraft with a variable camber wing in 1929 [10]. In this design, the wings were mounted on the fuselage midway between the spars. Both edges were able to move outwards and downwards in order to alter the camber of the wing. This configuration was capable of taking off at a maximum speed of 200 km/h within very short distances. The advantage of this design was that it reduced the movement of the centre of pressure. In order to minimize the movement of the centre of pressure, the mechanism was designed in such a way that it provided higher movement in the leading edge than in the trailing edge [3].



(a)



(b)



(c)

Figure 2.5 Variable camber and swept wing aircraft models : (a) Burnelli's variable cambered design aircraft (GX-3) [10], (b) Hill's variable swept tailless aircraft (Pterodactyl IV) [11] and (c) Ivan Makhonine's variable area aircraft model (MAK-10)[12].

Another successful design was developed by Hill [11]. He designed the Pterodactyl IV tailless monoplane in 1931 shown in **Figure 2.5 (b)**. In this design, variable sweep was applied to the wings through an angular range of 4.75° . During the same period, Ivan Makhonine designed the MAK-10 aircraft (**Figure 2.5 (c)**) [12]. The purpose of this research was to investigate the possibility of reducing the surface area of a wing in flight by deploying telescopic wings. Another aim was to improve the cruise performance by reducing the induced drag. This was principally accomplished by reducing the span loading, (ratio of the aircraft's weight to wing span) [13]. The Mak-10 successfully passed flight tests in 1931 with wing area and wing span changes in from 31 to 33 square metres and 13 to 21 metres demonstrated.

With the telescopic wing retracted, the maximum speed was 186 mph with 155 mph achieved when the wings were fully extended. This started the myriad of telescopic wings to design thereafter.

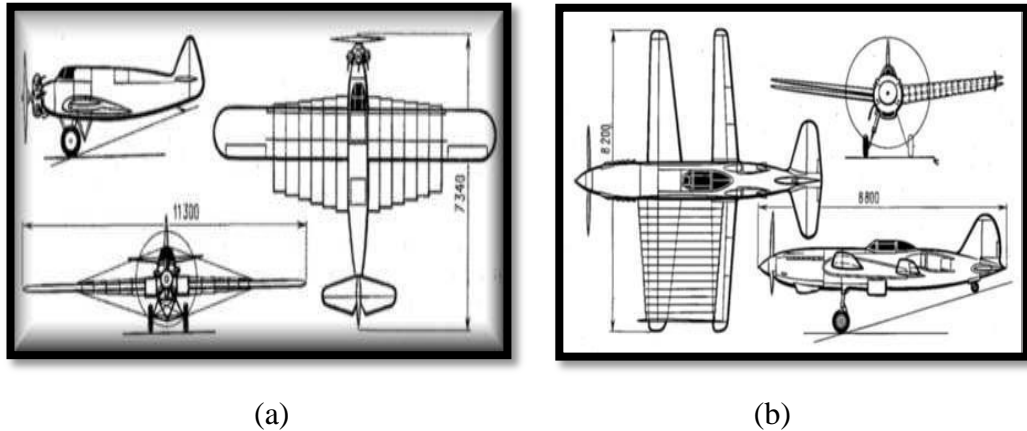


Figure 2.6 Bakashev's prototype models: (a) RK (1937), (b) RK-1 (Modified model) [14].

In 1937, the new and intriguing design was reported by G. I. Bakashaev [14] . This telescopic wing named the RK and shown in **Figure 2.6 (a)** used a mechanism consisting of six chord wings that was able to spread out to two thirds of the wing length on each side. To extend or retract the telescopic wings, steel wires were used [14]. Four years later, Bakashaev improved his design by modifying the steel wires (new design was named RK-1 and shown in **Figure 2.6 (b)**). For this design, a telescopic glove was used to alter the wings and the wings were extended from the fuselage to the full wingspan. The wing area of the RK-1 could change by 135%, whereas Bakashaev's first design (RK) could only change by 44%.

In 1949, the XF-91-Thunderceptor aircraft was developed by the Republic Aircraft Corporation. This was the first aircraft to use variable incidence wings, as shown in **Figure 2.7 (a)** [15]. These incidence wings' could be varied from $\Psi = -2^\circ - 5.65^\circ$ with a maximum speed of 984 mph, the endurance of the aircraft was very short (25 minutes) and together with control and flight mechanism challenges did not reach the production stage. In 1955, the incident wing configuration was improved by Chance Vought; the new design was named the F-8 Crusader, as shown in **Figure 2.7 (b)** [3]. The F-8 Crusader could rotate its wings from $\dot{\tau} = -2^\circ$ to 7° . Together with this capability, the F-8 Crusader could also lower its ailerons to improve slow speed



(a)



(b)

Figure 2.7 The variable incidence wing aircrafts: (a) Republic XF-91 "Thunderceptor" (1949) [15] and (b) Vought F8U Crusader (1955) [3].

performance to enable a safe landing.

There is little doubt that the most impressive morphing application or the best planform changing design is the variable sweep wing. The first aircraft was made by German Messerschmitt [3]. He developed the P-1101 aircraft in 1944, as shown in **Figure 2.8** (a). Sweep angles could change from $\Lambda = 35^\circ$ to 45° to adapt to different flight conditions.



(a)



(b)

Figure 2.8 The first 'swing' wing aircraft: (a) Messerschmitt P-1101 (1944) [3] and (b) Bell X-5 (1952) [16].

In 1952, the Bell Aircraft Company designed another variable sweep wing aircraft, the Bell X-5 (shown in **Figure 2.8** (b)) [16]. It was the first aircraft that was capable of large scale changes in sweep angle, from 20° to 60° . From tests, the X-5 was found to decrease drag by sweeping the wings backwards for high speed flight and with low speed performance through improved for take-off and landing with the wings fully extended. These designs faced challenges both the aircraft needed

additional mechanisms to alter the planform, which were costly heavy. Furthermore, fuel consumption was high because of the additional weight. In addition to these issues, another significant problem was that while the aircraft was extending its sweep wings, the location of the centre of gravity changed, making it difficult to control the aircraft. The solution to the aerodynamic centre problem was solved by NACA Engineering. Their idea was to develop a new mechanism that helped to move the pivot points of the wings outside the fuselage to minimise aerodynamic centre travel by redistributing the longitudinal lift distribution.

In 1952, Grumman developed a new aircraft with sweep wings, named the XF10F Jaguar (**Figure 2.9 (a)**) [17], his design achieved short landing and taking off distances with the wing pivot placed near the wing root to reduce the wave drag. It worked effectively, but when the aircraft flew into the supersonic, its stability and control became difficult. For this reason, a limited number of XF10F Jaguars were built and the programme was eventually stopped. However, improvements in the swing wing technology continued and in 1964 the most impressive morphing design was created by General Dynamics. They created the F-111 Aardvark for Air the US Force purposes (**Figure 2.9 (b)**) [18]. The F-111 Aardvark could sweep its wings from $\Lambda = 16^\circ$ to 72.5° whereas other designs, such as that shown in **Figure 2.9 (a)** could only manage a maximum of $\Lambda = 20^\circ$ to 60° [17]. Landing and take-off performances were improved by changing sweep angle. It could land or take-off within 609.6 metres when the wings were fully expanded. Although the F-111 one of the most successful morphing aircraft, not many were built due to structural problems, engine surge, weight, and the lack of stability and control. For example,



Figure 2.9 Variable sweep wing aircraft: (a) XF10F-1 Jaguar (1952) [17] and (b) F-111 Aardvark (1964) [18].

when the F-111 was in high speed mode, because of the inboard pivot points, the trim drag was quite high. Later on, in 1970, this problem was solved by moving the pivot points outboard on the Grumman F-14 Tomcat aircraft (as shown in **Figure 2.10**) [19].



Figure 2.10 F-14 Tomcat: sweep back position (Left) and un-swept configuration (Right) [19].

Another planform change related to morphing aircraft is dihedral angle. In 1979, aircraft designers built a space plane named the Russian MiG 105-11 [20]. This plane could change the dihedral angle of its wing while cruising. A rotation mechanism was applied above the horizontal stabilizer and it could be set to $\Gamma = 25^\circ$ (**Figure 2.11**). A total of eight flights were performed, resulting in a hard landing and the write-off of the aircraft. Although sufficient aerodynamic data gathered at subsonic flight, it was decided to stop all development of the design.

Up to the late 70's, several additional of planform changing aircraft were developed. However, most of them were not widely produced due to added weight, compliance skin, and/or overall complexity.



Figure 2.11 Russian variable dihedral wing aircraft MiG 105-11 [20]

2.3 Dedicated Morphing Research Programs

From the early 80's, designers worked to produce airplanes capable of withstanding higher speeds and greater aerodynamic loads. This resulted in configurations with semi-monocoque structures in which the loads were carried partly by the frame and stringers, and partly by the skin. While flying these aircraft, pilots soon discovered a wide variety of aeroelastic problems including, among others, wing flutter, divergence, buffeting, and control reversal. The designers responded by increasing the wing stiffness, but this also increased the structural weight. They then often opted to reduce the wingspan, increase the airfoil thickness, and accept reduced aerodynamic performance in exchange for increased speed [21]. With the advent of smart materials in the early 80's, several research programmes were proposed with some beginning to further understand the potential for adaptive aircraft technologies. The following sub-sections consider these research programmes.

2.3.1 Mission Adaptive Wing (MAW) Program

The Mission Adaptive Wing Program was a morphing research programme that began in 1980 [18], [22], [23] [24]. With conventional control surfaces creating discontinuous curvatures, which increase drag and the aim of the programme was to reduce drag by developing a smooth camber changing mechanism for aircraft wings. During the period of the MAW programme, a variable wing was installed on an F-111 aircraft operated by the United States Air Force Research Laboratory (**Figure 2.12**) [24].

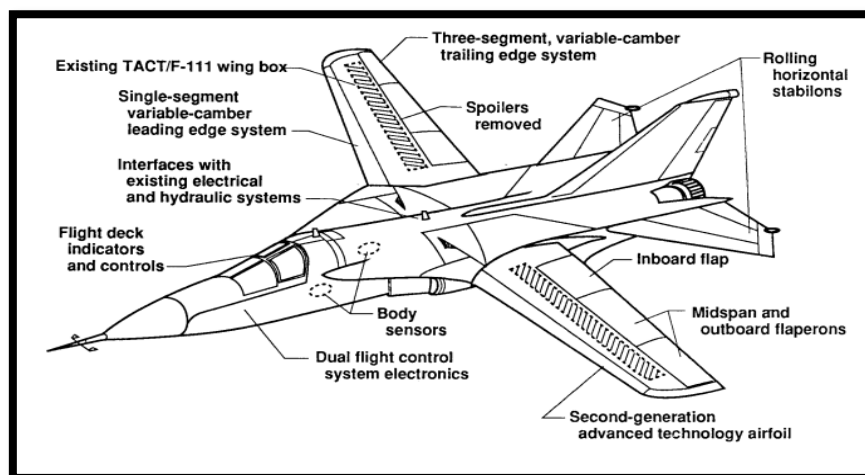


Figure 2.12 The Mission Adaptive Wing Program: Modified F-111 [24].

The wings consisted of internal mechanisms and hydraulic actuators, which allowed for varying the wing camber, and covered by flexible fibre-glass materials. To control the camber change, eight wing segments were used (three segments for the trailing edges and a single segment for the leading edge). A digital flight control system was also used to perform automatic wing shape changes according to flight circumstances. The experimental and real flight tests were carried out by the National Aeronautics and Space Administration (NASA), Dryden Flight Research Center. The modified F-111 underwent several flight tests and results were reported between 1985 and 1988. Due to the smoothness of the resulting wing surface, the drag was found to decrease by approximately 7% in sweep back condition with a revolution in around 20% cruise. Although the variable camber wing provided advantages for the F-111 aircraft model, the programme was terminated in 1988, due to actuator size requirements.

2.3.2 Active Aero-elastic Wing (AAW) Program

The Active Aero-elastic Program was established in 1996 by the US Air Force Research Laboratory Wright Patterson Air Force Base, NASA Dryden Flight Research Center and Boeing Phantom Works [21], [25], [26]. The aim of the programme was to show the benefits of an aero-elastic wing through the use of multiple leading and trailing-edge control surfaces activated by a digital flight control system on F/A-18 aircraft. The new panels were designed and constructed of a thinner composite skin with a honeycomb structure in contrast to previous F/A-18's. The flaps were also modified and they could change from 10° to 34° (**Figure 2.13**). To achieve this level of deflection angle, a hydraulic drive system was used. Deflection of the inboard and outboard flaps was found to increase the roll control and aerodynamic performance of an aircraft as well as reduce the drag force.



Figure 2.13 NASA Dryden Flight Research Center F/A-18 with flexible wing [21].

2.3.3 Smart Wing Program

Earlier programmes were terminated due to additional components being needed for structural stiffness as well as to actuate the wings, which resulted in increasing overall weight. After advances in aerospace materials made shape changing concepts more realistic the Smart Wing Program was initiated in 1995 by the Defence Advanced Research Projects Agency (DARPA), NASA, Air Force Research Laboratory (AFRL), Langley Research Center, and Northrop Grumman Corporation (NGC). The goal of the programme was to design and analyse newly integrated smart wing materials in order to improve the aerodynamic and aero-elastic performance of a military aircraft [27], [28]. The programme was divided into two phases. Phase 1 aimed to develop a mechanism to replace the traditional control surfaces using SMA wires and in Phase 2, SMA-actuated, hingeless, smoothly contoured, flexible leading and trailing edge control surfaces were integrated into a tailless aircraft model. Nickel Titanium shape memory alloys were used to actuate trailing edge control surfaces and to provide smooth contoured shape control (**Figure 2.14**). From the wind tunnel test results, sufficient roll moments (17% at 15 degree of deflection), as well as significant improvements in lift force generation were observed (8- 12%) compared to the untwisted conventional wing.

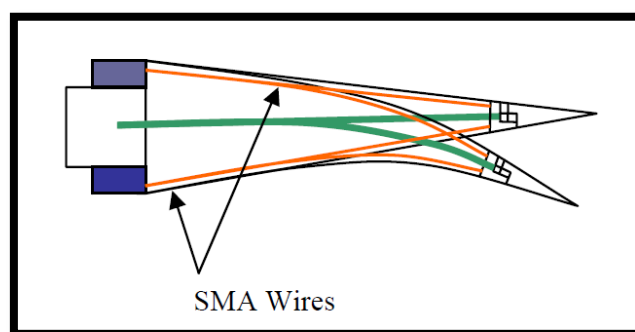


Figure 2.14 Shape memory alloyed wires to achieve wing twist movements [28].

2.3.4 NASA's Morphing Aircraft Program 1998-2030

In 1998, NASA's Morphing Aircraft Program aimed to investigate new shape changing morphing aircraft using adaptive materials, micro control devices, and also biologically inspired material technologies to enhance the manoeuvrability and aerodynamic performance of the aircraft. The research programme will continue to develop new aircraft structures using updated materials until 2030. As can be seen from **Figure 2.15**, NASA's morphing aircraft concept will be able to sweep back its wings to provide a supersonic speed capability as well as reduce drag force. The

wing area could also be increased to get more lift for take-off and landing. Feather like control surfaces such as adaptable winglets would also provide more manoeuvrability with additional control force and greater safety during flight.



Figure 2.15 Modelling of NASA’s futuristic morphing aircraft [29].

2.3.5 DARPA’s Morphing Aircraft Structure Program 2002

Similar to NASA’s Morphing Aircraft Program, DARPA’s Morphing Aircraft Structure Program is currently engaged in large-scale coordinated efforts to develop morphing flight vehicles capable of drastic shape change in flight. This programme, which is sponsored by NextGen Aeronautics, Lockheed Martin and Raytheon Missile System, started in 2002 [30].

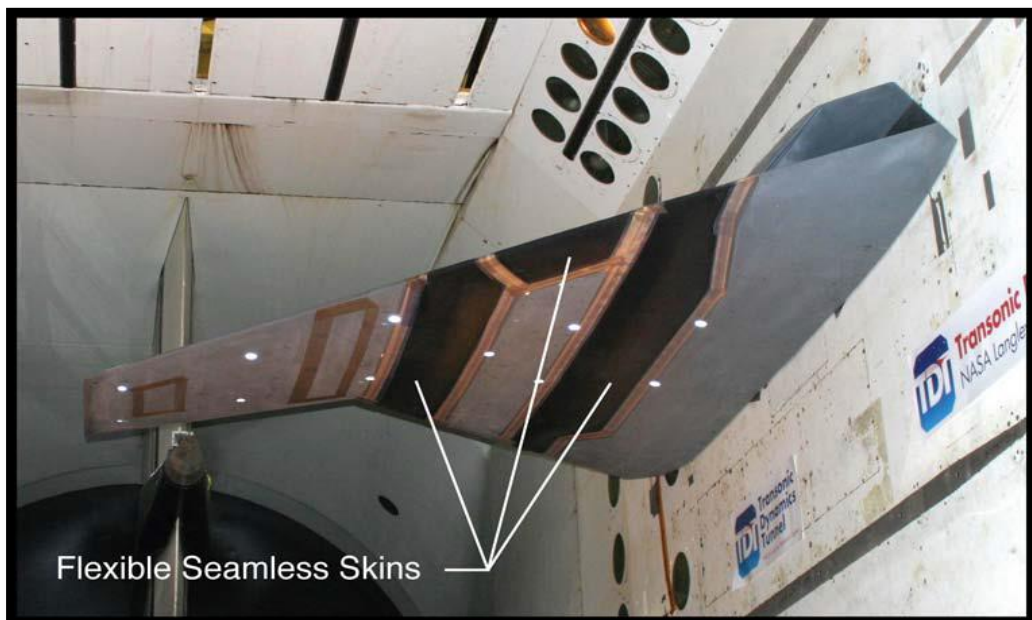


Figure 2.16 Lockheed Martin foldable morphing wing ideas [30].

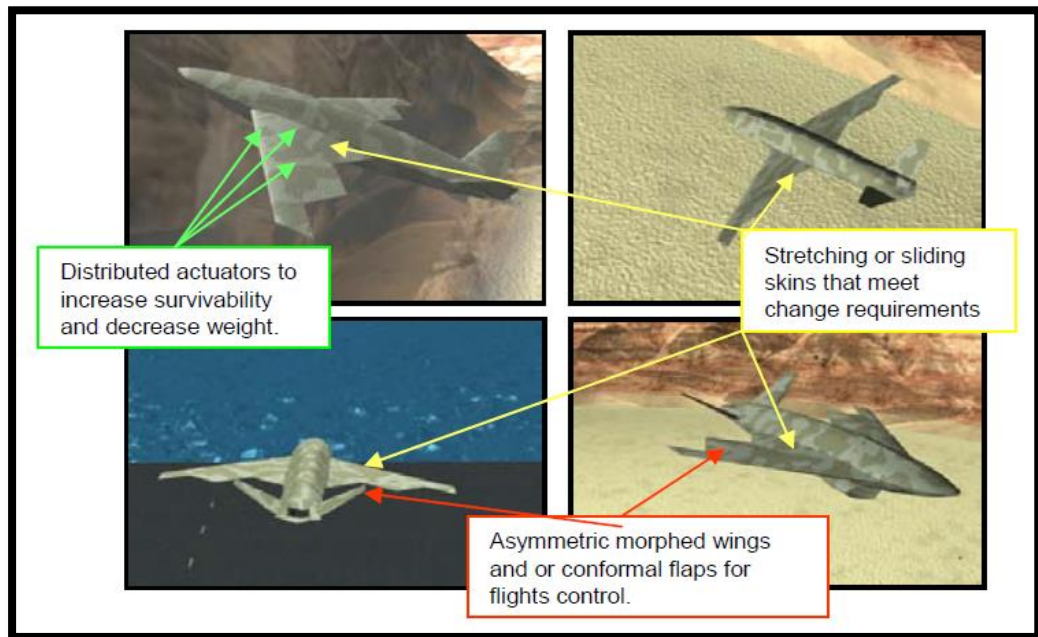


Figure 2.17 NextGen Aeronautics sliding morphing wing aircraft [17].

One of the most interesting morphing ideas was developed by the Lockheed Martin Company. Their ideas relate to folding wing concepts, (**Figure 2.16**). The initial design was completed using seamless skin and shape memory polymers. However, due to an electrical resistive heating problem, silicon based reinforced materials were used for the skin. To fold the wing structure, electric actuators were placed inside the wing model with a vacuum pump connected to the fold region to ensure that the elastomer material on the top surfaces did not bunch as the wing folded [31].

NextGen Aeronautics Corporation also developed the morphing wing concept named ‘bat-wing’, (**Figure 2.17**). The scope of this design was to achieve specific planform geometries based on the instantaneous mission requirements to move between five different wing planforms and create wing planform changes in area, span, chord and sweep that vary by 51%, 36%, 110%, and 30°, respectively [32] [33]. To achieve these variable wing platforms, a stretchable flexible cover skin was used with hydraulic actuators to change the wing platform. A wind tunnel testing programme was successfully completed and it showed that the morphing wing could move smoothly from one position to another [31]. Finally, although the MAS programme was completed successfully, the requirement to adapt those mechanisms to a real flight environment were difficult to fulfil, due to the weight restrictions,

installation cost, complexity, higher torque requirements as well as the wrinkling formed on the skin.

2.4 Challenges of Adaptive Aircraft Configurations

It can be seen from the previous sections that most morphing aircraft designs as well as research programmes have attempted to create actually adaptive configured aircraft. However, even with the substantial research efforts over the last few decades, morphing concepts still face significant challenges. These include added weight, costs, skin, and/or complexity. Jha and Sofla et al. [3], [34] summarized some of the technical challenges of morphing aircraft. The most significant challenges tend to be in the structural design of the concepts, morphing the skin, and the mechanisms employed. These challenges are depicted in **Figure 2.18** with the main challenges discussed thereafter.

As far as past research is concerned, morphing aircraft involves various flight conditions unlike traditional fixed wing aircraft. The benefits of different flight configurations were proved by Joshi et al. [35]. In this regard, the design strategy is the first challenging step in the creation of adaptive shape changing aircraft. At this stage, in order to adapt to different flight regimes, designers need to optimize the geometry to get the full benefits in flight; reversible changes are also necessary. Martin and Roth et al. [36][37] have applied demonstrated such optimization techniques on morphing aircraft geometry. In order to obtain the best possible conditions for morphing aircraft, several shapes must be considered, which results in a large running time and memory allocation. Due to the large number of geometric variables, [38] used a genetic algorithm and, similar to that, aero-elastic analysing tools were presented by Breuker et al.[39]. They developed numerical codes to analyse the aeroelasticity of a morphing aircraft. The validation of the codes was tested on a sweep wing configuration with results showing that the sweep wing configuration improved the aerodynamic performance of the aircraft (~3% at 55 degree of sweep). Aerodynamic centre and centre of gravity movements due to the varying aircraft geometry remain challenges for these configurations.

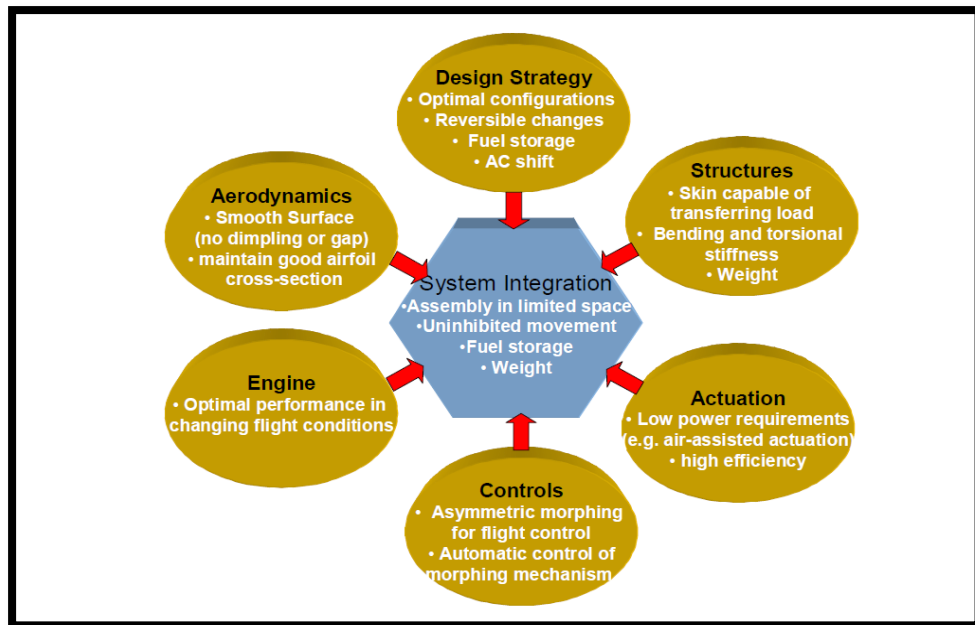


Figure 2.18 Technical challenges of Morphing Aircraft [3]

Another challenge facing morphing aircraft design is the skin (for a detailed survey of morphing skin applications see **Section 2.8**). Aircraft skin plays a significant role in aerodynamic performance; therefore morphing aircraft skin should be capable of transferring loads, and should also be flexible in order to retract/extend, or adapt. Furthermore, the surface should remain smooth surface with low wrinkle rate at all locations. Thill et al. [40] offers potential solutions for flexible morphing skins. According to his article, the flexibility and stiffness problems in morphing air vehicles can be solved by using novel materials such as composite corrugated structures.

Actuation also seems to be a unique challenge in the morphing area. In contrast to conventional aircraft, supplementary high power actuation is required to maintain the shape change. Besides that, the actuator must be efficient and light. Therefore, large durable actuators are needed for the design, but space allocation and overall weight problem must be considered by designers. Many studies have aimed to reduce this weight, increase actuation efficiency, and reduce the size of the actuations [3] [41].

Flight Control is another hurdle for morphing configurations. Internal control systems are needed to organize the shape altering process, which involves coordinating sensors, braking systems, and actuators [17]. To do so, novel algorithms and programmable devices are required to ensure that the structure

altering system sends the right signal to the actuators. Likewise, the control systems should ideally work with a changing frequency range (low or high frequency operations) in respect to planform altering configurations [42].

Despite the drawbacks of morphing applications, enormous advantages can be gained by using variable shape changing concepts. The best examples of the benefits of morphing shape changing aircraft have been indicated by Butt [43]. In this research, supersonic air to air fighter (AAF) aircraft modelling was utilized with the aim of showing the fuel consumption and required actuator energy for morphing aircraft in contrast with fixed wing aircraft. **Figure 2.19** illustrates the mission segments for AAF aircraft. Morphing wing concepts were considered and the aircraft wings were allowed to vary their aspect ratio, wing sweep, and tip and root length geometry. The results show that no improvements can be gained in order to decrease fuel consumption when morphing aircraft are seven times heavier than fixed wing aircraft. Also 100% of the power is needed to run the actuators. However, if the morphing aircraft is twice as heavy as a fixed wing aircraft and 10% more actuator power is needed, then 22% less fuel is used.

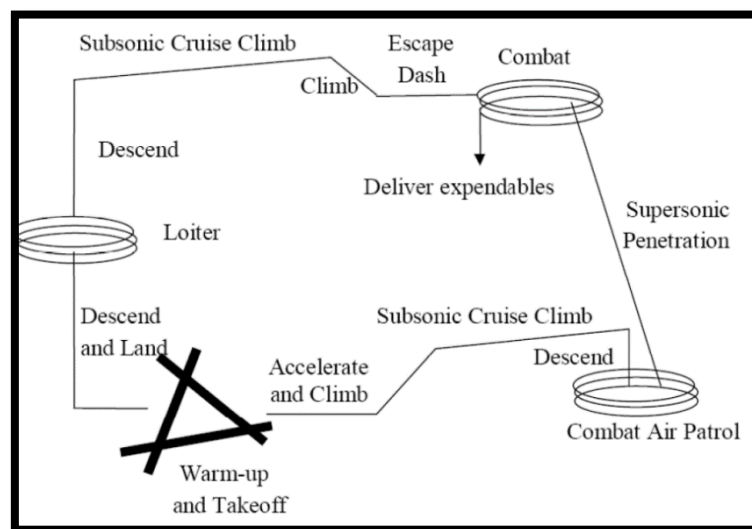


Figure 2.19 Mission segments for AAF aircraft configuration [43].

Joshi et al. [35] carried out a study to illustrate another advantage of dissimilar flight configurations. The wing area, wing span and sweep back changing concepts were used to visualize the viability of morphing concepts compared to fixed wing aircraft.

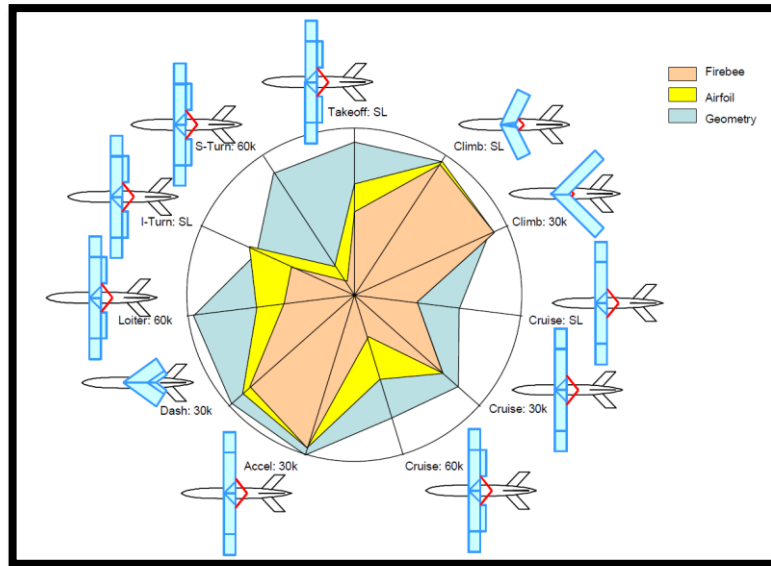


Figure 2.20 Spider plot comparing predicted performance of the baseline Firebee, a morphing airfoil, Firebee and a morphing planform Firebee [35].

Figure 2.20 illustrates 11 different flight condition measurements for unmanned aircraft considering morphing geometry, and morphing airfoil (alone). The outer radius of the plot shows the best possible performance in flight. It can clearly be seen that the morphing shape altering aircraft achieved excellent performance compared to the others. According to the results, during take-off no sweep configuration was needed; only a large wing area and span were required to provide high lift forces. However, during the climb, a swept back configuration was required to maintain climb performance as well as high-speed flight.

Another aspect to consider with regard to adaptive shape changing concepts and the aerodynamic and aeroelastic benefits of morphing aircraft was investigated by Sanders et al. [44]. In contrast to conventional surfaces, conformal control surfaces were used to achieve high lift performance. The results were obtained through simulation software (Vortex Lattice Method for aerodynamic calculation, ASTROS simulation for aeroelastic performance of morphing wings). According to the simulation results, high lift (approximately 40%) and a greater roll rate (25-30%) with low dynamic pressure could be obtained by the conformal control surfaces. Aerodynamic performance can also be improved via a variable wing span, as noted by Bae et al. [45]. This work aimed to reduce the induced drag to improve the range and endurance of a cruise missile. Simulation results showed a high lift distribution (37.5% improvement in lift by extending 50% wing span) and a noticeable decrease in induce drag (51%) as a result of the extending wingspan. Numerical and

experimental results on the wingspan altering structure also showed a large influence on increasing aerodynamic efficiency and roll control.

Another morphing aircraft wing concepts was demonstrated by Wittmann et al. [46]. According to his research, the lift coefficient of a morphing aircraft improved by 74% by increasing the wing area and camber with aerodynamic efficiency can be improved by 24% (Lift to Drag Ratio) through changing chord length.

2.5 Adaptable Wing Mechanism Technology

In the last few decades, several investigations have been done on interesting and usable mechanisms for adaptable wing mechanism. Various publications present an overview of the possible morphing concepts [34], [47],[48][49]. Typically these concepts are divided into three major types: planform changing, wing aerodynamic behaviour altering, and airfoil adjustments.

2.5.1 Planform altering concepts

Planform altering concepts consist of several shape changing configurations, as indicated in **Figure 2.21**.

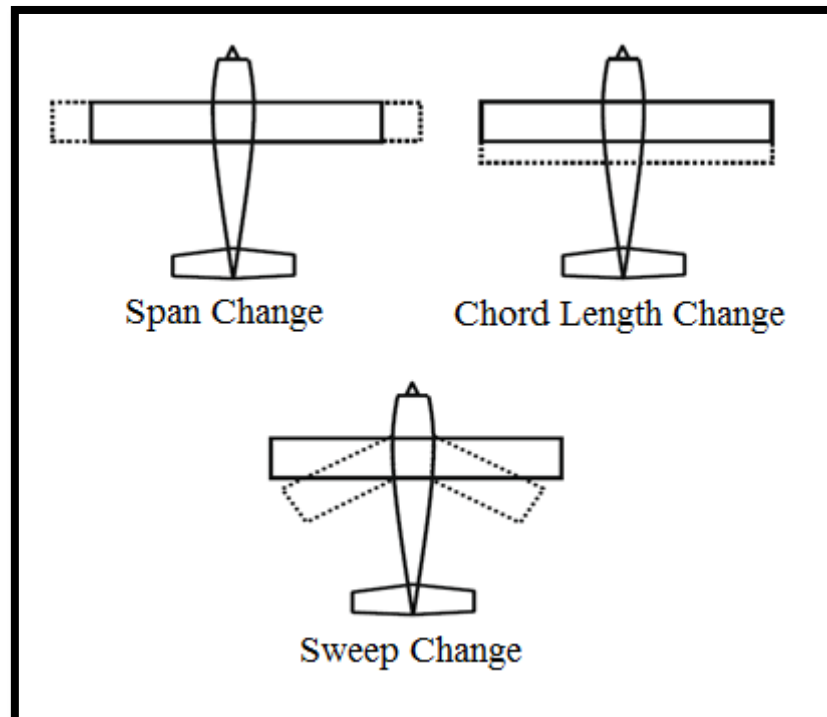


Figure 2.21 Configuration of planform changing concepts

Span changing concepts have been researched more since the 1970s with various techniques and mechanisms used to achieve wingspan extension using pneumatic

actuators [50] [51], a wing box, DC motors [56], and linear actuators [55]. Effective span changing concepts were investigated by Blondeau et al. [52][53]. To achieve wingspan changing, a pneumatic piston system was developed as shown in **Figure 2.22** with hollow shells to create a telescopic wing skin. The ribs were attached to a piston system which could react and extend the wing spar. The wind tunnel experiments showed that the skin and actuator mechanism worked well under the aerodynamic load and an improvement of 25% was seen in lift/drag ratio when the wing span was varied from 40% to 100%.

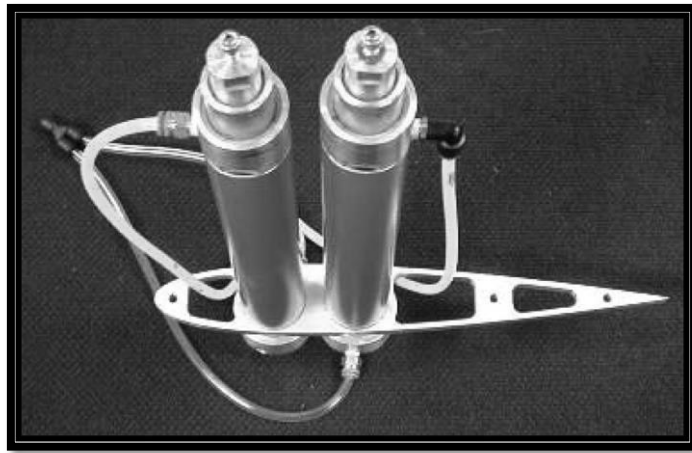
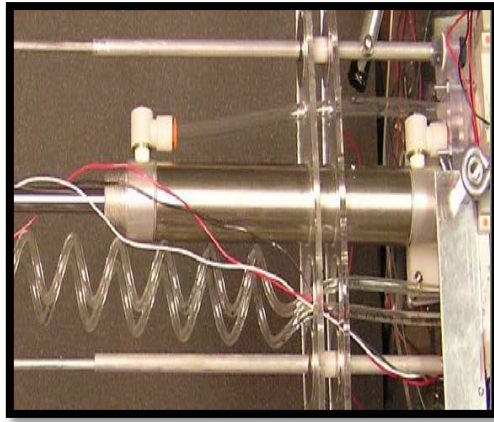


Figure 2.22 Blondeau’s wing span mechanism: pneumatic actuators and root rib [52].

Similar to Blondeau[53], Neal et al. [50] designed and demonstrated a variable planform aircraft capable of wing span change. In order to achieve the span extension, a telescopic pneumatic actuator, as shown in **Figure 2.23** (a), was used with the wing achieving up to a 38% span change. Wind tunnel testing showed this variable span wing was able to reduce the drag (up to 17%) in contrast to fixed wings. After successfully completing the first UAV, Neal et al. [50] modified the variable wing and tail sweep as well as adding wing twists changing mechanisms. According to his research, the flight envelope could be improved by increasing the wingspan (2%). When the wings were twisted with aerodynamic efficiency improvements (2.2%) obtained. In addition, sweeping the winglets helped reduce the induced drag, and hence total drag (15%) and fuel consumption.

Recently, Vocke et al. [54] developed a span extending morphing wing mechanism using smart materials (morphing core and fibre skin) as illustrated in **Figure 2.24** (a). The core section consists of NACA63-618 airfoil-shaped acrylic-based photopolymer materials, which bend easily with a carbon elastomeric skin is



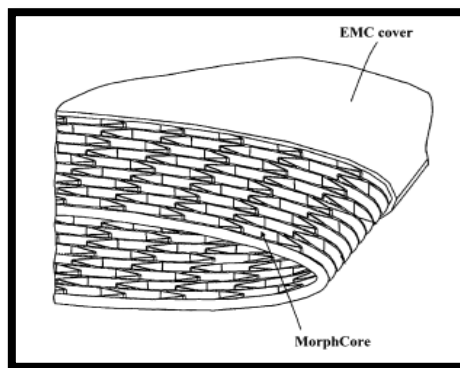
(a)



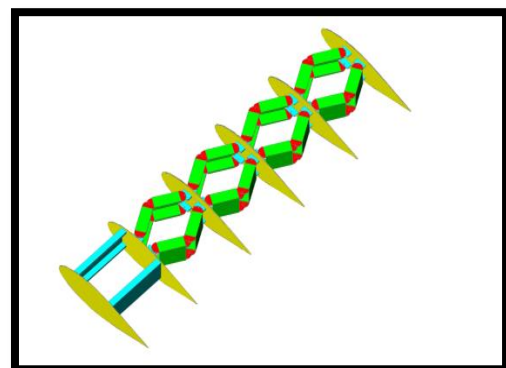
(b)

Figure 2.23 Neal et al. [50] wing span altering mechanism: (a) Pneumatic actuator for wing span change and (b) wind tunnel model with an extended wing span.

applied to the external design. According to Vocke[54], the design can provide 100% span extension with less than 2.54mm out-of-plane deflection under aerodynamic loading. Similar research has been carried out by Ajaj et al. [55] [56] using a novel zigzag wing box (**Figure 2.24**). The wing box consists of two parts: a rigid part and a morphing part. The non-morphing part, which is located on the wing chord, has two spars, and the morphing part has a rib with hinged beams and morphing elements. The hinged beams are able to provide the movement in respect to the Z-axis. According to their investigation, the wingspan can undergo a 44% change (22% retract and 22% extend), and although heavy, shows 5.5% greater efficiency in endurance to a conventional semi-monocoque constructed wing box.



(a)



(b)

Figure 2.24 Morphing Span extending mechanisms: (a) Morphing core design for non-extended state and extended state and (b) Ajaj's wing box span extending mechanism [55] [56].

Traditionally, the chord length of the wing on a conventional aircraft is changed by means of leading trailing edge flaps and slats, which are moved by a lead or screw actuation system. Unfortunately, very few researchers have such concepts with the possible exception being Reed et al. [57]. They used an interpenetrating rib mechanism, which allows the partially designed ribs to slide through the chord to change the position of the leading and trailing edges (**Figure 2.25**). The ribs were designed to carry high aerodynamic loads. To increase or decrease the chord length size, a miniature DC motor lead screw arrangement was used. Although, the chord

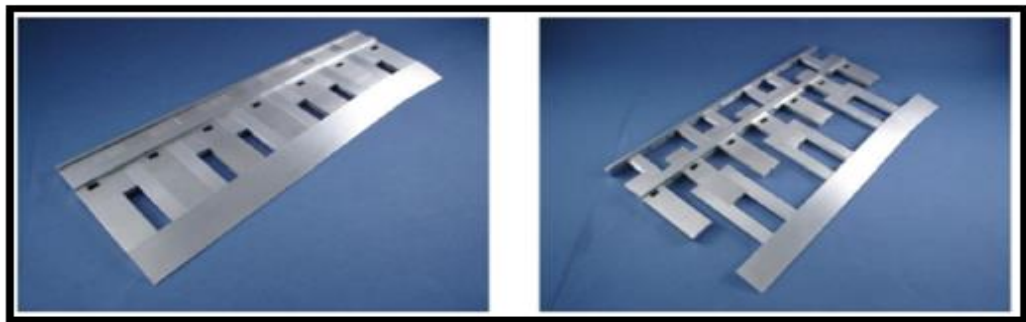


Figure 2.25 Reed [57] interpenetrating rib concepts: Compressed state (left) and extended state (right).

length change could provide aerodynamic benefits for aircraft performance, this design was limited due to added weight and complexity of the design. Also, when the ribs are fully extended, there is a large gap between each of the rib elements, which causes wrinkling of the morphing skin, so additional support was required for the skin.

A much more commonly accepted planform changing concept is to actively vary the swept angle of an aircraft's wings during flight. Highly Swept wings reduce drag significantly at high speed [58]. The main aim is to combine high speed and low speed flight using differing swept angle configurations. Challenges for sweep wing mechanisms are in normally high weight actuator requirements. There is normally also significant movement of the aerodynamic centre as well and centre of gravity to further complicate lateral and longitudinal stability [47]. Marmier et al. [59] designed a morphing variable sweep wing UAV using a pair of antagonistic inflatable bellow actuators embedded in a UAV fuselage. The wind tunnel model is shown in **Figure 2.26** (a). The inflatable bellow actuators were controlled by a solenoid valve and from the test results achieved wing sweep from $\Lambda = 0^\circ - 45^\circ$. Neal

et al. [60] also built a high-powered new sweeping mechanism for morphing UAVs. Instead of using pneumatic actuators, two electromechanical lead screw actuators were used to provide the sweep movements. This design led wing sweep of up to 40° (**Figure 2.26 (b)**).

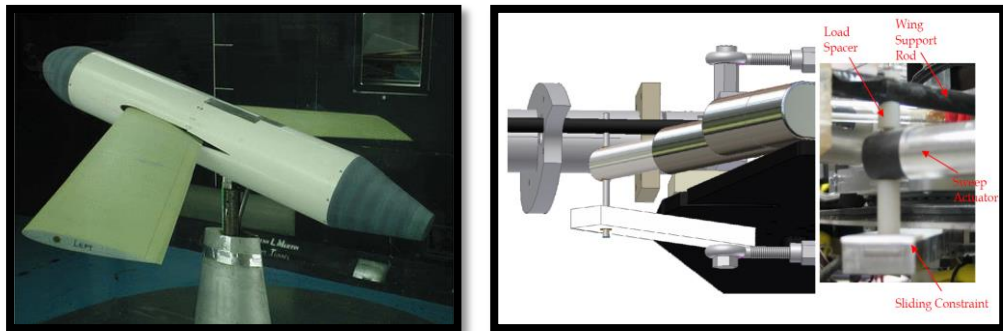
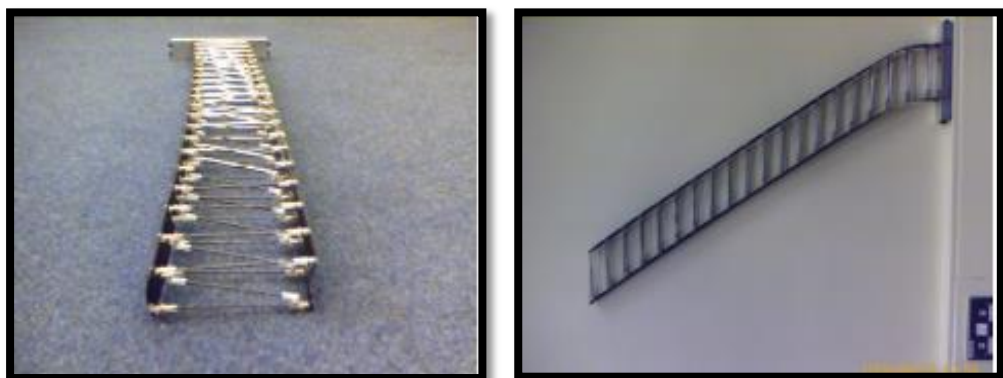


Figure 2.26 Swept wing aircraft and its mechanism: (a) Marmier[59] wind tunnel model and (b) Neal[60] lead-screw mechanism.

Mattioni et al. [61] studied a wing sweep altering concept using interconnected truss ribs placed on two bi-stable composite spars (**Figure 2.27**). The aim was to eliminate mechanisms and to reduce stress when the straight wings were rotated to sweep back and forward. No skin was included. During high loading conditions, each spar was found to provide excellent bending stiffness because of the substantial transverse curvature [61].



(a)

(b)

Figure 2.27 Mattioni[61] interconnected truss rib structures: (a) Straight configuration and (b) Sweep configuration.

Additionally, Joo et al. [62] proposed a novel method for altering sweep angle of morphing aircraft using a scissors mechanism (**Figure 2.28**). Pneumatic actuators were used and these were located between two neighbouring links to both extend and retract. The comparison between the numerical data and experimental data showed good agreement with the mechanism shown to be suitable for morphing wing sweep applications [62].

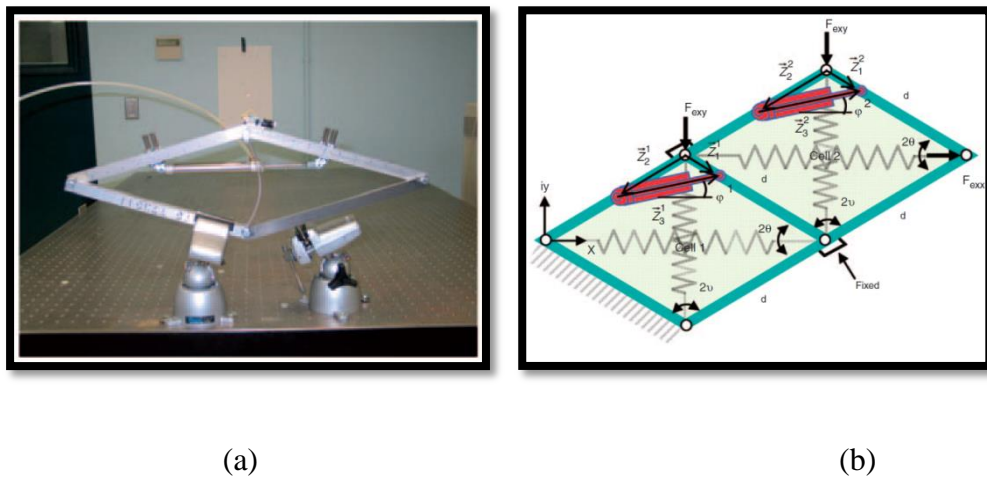


Figure 2.28 Scissors mechanism: (a) test setup and (b) schematic of scissors mechanism [62].

2.5.2 Wing twist concepts

Prandtl's Lifting Line Theory was the first mathematical method to estimate the performance of a wing's lift capabilities for an aircraft [63]; being thereafter modified by Philips [64] [65] to estimate the influences of wing twist on lift distribution. Following this seminal work, more studies have considered morphing wing and/or winglet twist configuration both theoretically and experimentally, to investigate influences on the aerodynamic performance of an aircraft. Recent work have detailed of wing twist systems using piezoelectric and pneumatic actuators [66], [67], [60], torque rods [68][69][70], adaptive stiffness structures[71], threaded rods [72], and shape memory alloys[73][74][75]. Barrett et al. [66] used Piezoelectric actuators were used to provide the twist movements. **Figure 2.29** shows the Flexspar design used is based on a single bimorph actuator that drives an aerodynamic shell in pitch. The structurally stiff main spar and bimorph piezoelectric bender elements are bonded rigidly at the root of the fixed base and the bender element is melded to the trailing edge of the shell (the shell is free to rotate around the spar). Using a piezoelectric actuator, the bender element can move upwards, which causes the

model to rotate the shell resulting in wing twist. According to the wind tunnel testing, $\pm 1.5^\circ$ of twist was achieved, which equates to $\pm 8.4^\circ$ aileron deflection [66].

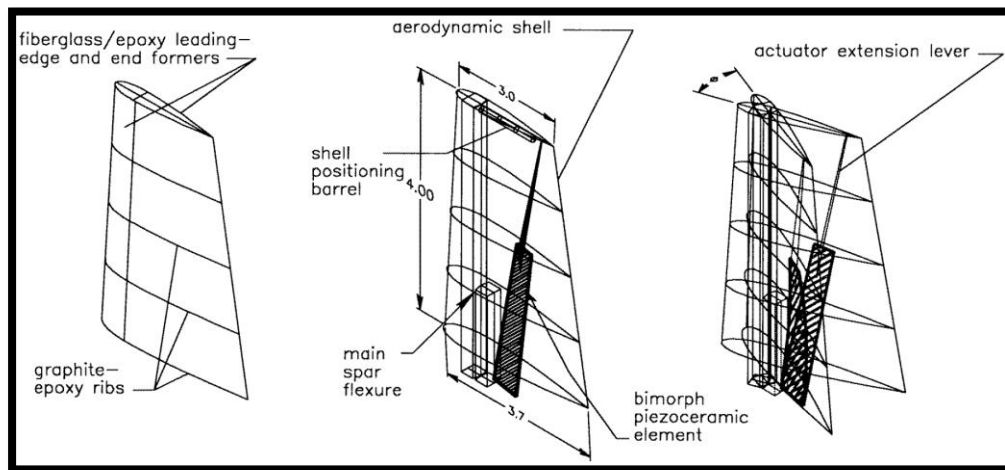
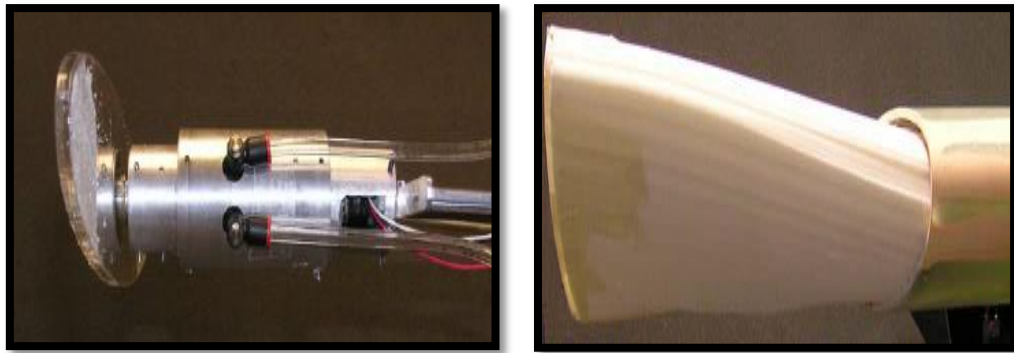


Figure 2.29 Schematic view of Adaptive Shell-positioning Flexspar [66].

The use of high authority anisotropic piezoelectric actuators to induce wing warping was also investigated by Sahoo et al. [67]. The aim of the research was to achieve roll controllability in place of traditional, discrete control surfaces. A numerical framework was tested for relatively simple models, with a Boeing X-45A based UCAV model used to assess the authority requirement on the piezocomposite actuators to achieve representative roll rate. The results showed the current state-of-the-art technology for anisotropic piezocomposite actuators (e.g. active fiber composites) does not have the authority needed for wing warping control. A three to four-fold increase in actuation authority is needed to adequately enable this control approach for this type of aircraft.

Neal et al. [60] also proposed the new twisting mechanism shown in **Figure 2.30**. This mechanism used pneumatic actuators to drive airfoil-shaped acrylic materials to produce wing twist. The acrylic airfoil was bonded to a flexible, closed-cell polyethylene wing section with a fixed boundary condition at the root. This caused a linear twist distribution when the internal twist mechanism rotates. This system is able to twist wings from -20° to $+20^\circ$ and although the skin had some wrinkles (shown in **Figure 2.30(b)**), observations from the wind tunnel showed that the twisting could be beneficial for aircraft aerodynamic performance by 2.2%.



(a)

(b)

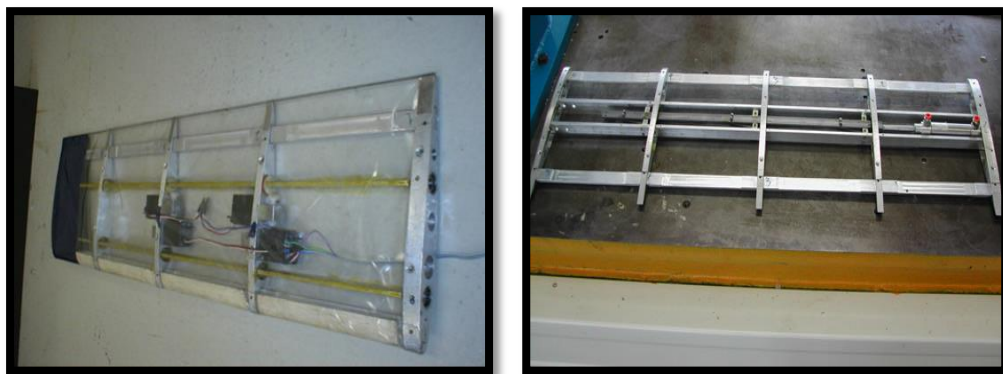
Figure 2.30 Neal[60] twisting mechanism: (a) Internal design of twisting mechanism (b) External design of twisting mechanism.

In an alternative approach, a torque rod twist mechanism for membrane wings was investigated by Garcia and Abdulrahim et al. [68][76][70]. In their design, Mylar membrane wings were used with a torque-rod fixed to the wing at the 66% span position (**Figure 2.31**). A servomotor was used to actuate this rod to achieve twist distribution. According to their flight tests, roll rates comparable to a traditional aileron were achieved via these twisting wings. Similar to Garcia et al. [68], Stanford et al. [69] also controlled the roll of a mini UAV using a torque rod mechanism. This micro air vehicle, constructed using a thin membrane wing and skeleton, was made from carbon-fibre, with the torque rod rotating the span-wise length of each wing. To achieve rotation, servomotors were used and connected to the torque rod. Numerical analysis was done using Athena Vortex Lattice software and then validated by wind tunnel testing data. The data indicated roll control (45°) can be achieved by varying the twist angle (up to -15°) of an UAV, but only with a considerable drag penalty.



Figure 2.31 Review of Garcia[68] design: micro air vehicle (left) and (b) torque rod assembled membrane wing (right).

Majji et al. [77] also studied wing twisting and with comparison to wind tunnel tests. The model consisted of an elastic wing-box structure covered with an elastomeric skin. The box structure was also rigidly coupled to the four main tubes that were placed along the wingspan with front and rear supports to retain the airfoil shape. To actuate the wing structure, a servomotor was placed outside the wing root section. With wind tunnel testing showing stall at a later stage than the other two sections. Skin deformation however was observed under aerodynamic loading, which tended to increase drag. Similar to Majji[77], Cooper [78] investigated adaptive stiffness structures such as rotating and translating spar concepts. These design approaches (**Figure 2.32**) were constructed from aluminium and comprised five ribs with an additional two fixed spars positioned horizontally near the leading and trailing edges. For the rotating spar concept, two moveable spars were used and actuated by four motors positioned at either end of the spars (**Figure 2.32 (a)**). For the translating spar concept (similar to the rotating spar model) these moveable spars could translate in the chord-wise direction along tracks in the ribs (**Figure 2.32 (b)**). To provide an aerodynamic surface finish, thin polyethylene skin was used. Both investigations showed good agreement with the wind tunnel experiments and sufficient wing twist and/or control moments were demonstrated. Although this system found to work well in the wind tunnel environment, application to real flight conditions suffered from excess weight and power problems.



(a)

(b)

Figure 2.32 Cooper[78] Wing Twist Mechanisms: (a) rotating spar mechanism and (b) translating spar mechanism [78].

Further studies on twisted wings were carried out using a threaded torque rod mechanism. Vos et al. [72] investigated wing twist using threaded torque rod with a carbon fibre reinforced polymer skin. In this design, 4 different rib structures were

spaced equally along the round aluminium bar as shown in **Figure 2.33** (a). A threaded rod with in sliding mounts is free to move along the span of the wing near the trailing edge of the wing. The wing skin was covered by a carbon fibre reinforced polymer (see **Figure 2.33** (b)) and glued to each rib flange to ensure a smooth aerodynamic surface. When the threaded rod is actuated, it provided guides for the wing skin to twist. Wind tunnel testing at 15 m/s showed that this mechanism works well under aerodynamic load. A small reduction was observed in the lift-induced drag with augmentation of lift (25% at trailing edge displacement of 4mm). It should also be noted that this system is heavier and was more complex than other morphing actuation systems.

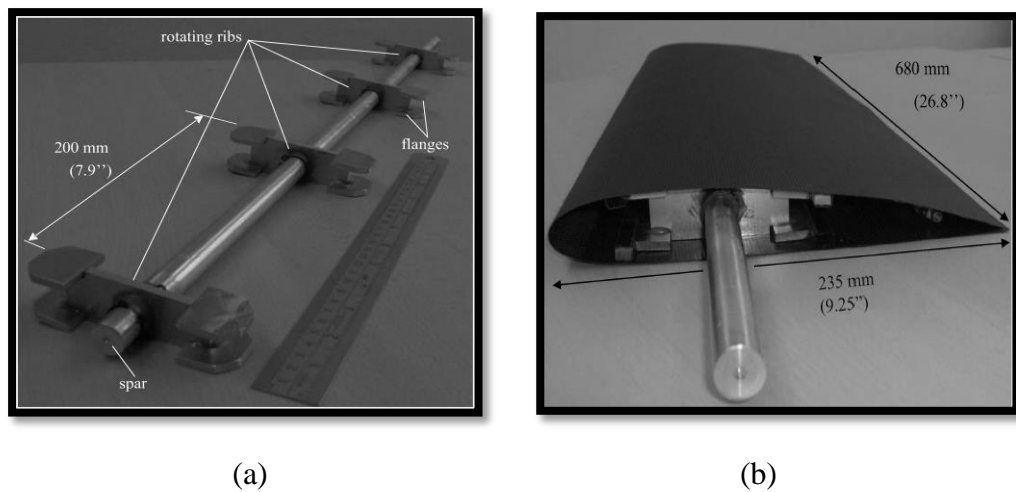


Figure 2.33 Vos[72] Twist mechanism: (a) Internal wing structure consisting of four ribs that rotate independently about the circular main spar and (b) Final design of a wing with covered CFRP (carbon fiber reinforced polymer).

Adaptive aeroelastic methods have also been studied by several researchers using a variable stiffness spar. A smart stiffness spar for improved roll control was investigated by Griffin et al.[79]. The aim was to increase the roll rate and aircraft performance at high dynamic pressures. Smart spar concepts have been utilized to increase the aeroelastic behaviour of a wing by altering the spars from the location of a reference point (the leading edge of a wing) to the wingtip. Another approach to adaptive torsion wing spar concepts has been investigated by Chen [80]. Adaptive spars were used instead of the existing spars to provide more rolling and lift force. An F/A18 aircraft model was chosen for this study. Variable stiffness spars were bonded with articulated joints and then the articulated joints were connected to the wing ribs. To achieve spar rotation, an electronic actuator was used. The numerical

results obtained proved that by using adaptive spars, the aircraft's manoeuvrability could be enhanced by 30%.

Another innovative way of variable stiffness spars has been developed by Ajaj et al. [81][82][83][84] with the aim to optimize the performance and control of unmanned aerial vehicles. Vortex Lattice Methods were used to predict the aerodynamic efficiency of a model and a genetic algorithm was used for the optimization process. As depicted in **Figure 2.34**, an aluminium wing box and two variable torsional stiffness spars were used to alter the chordwise position of the front and rear spar webs. Initial testing was done, only to change the location of the spars (no twist geometry). Unfortunately, there were no significant improvements in aerodynamic efficiency of the UAV, because the span wise lift distribution moved outboard of the wing, hence increasing the induced drag. In contrast to the initial case, 2.5% greater aerodynamic efficiency as well as good rolling moments was obtained by twisting the wings from 2° to 4° .

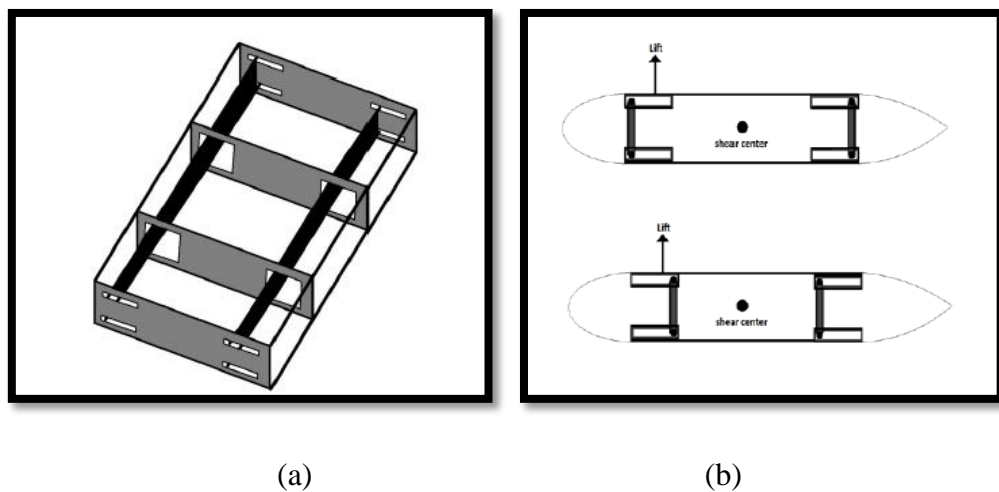
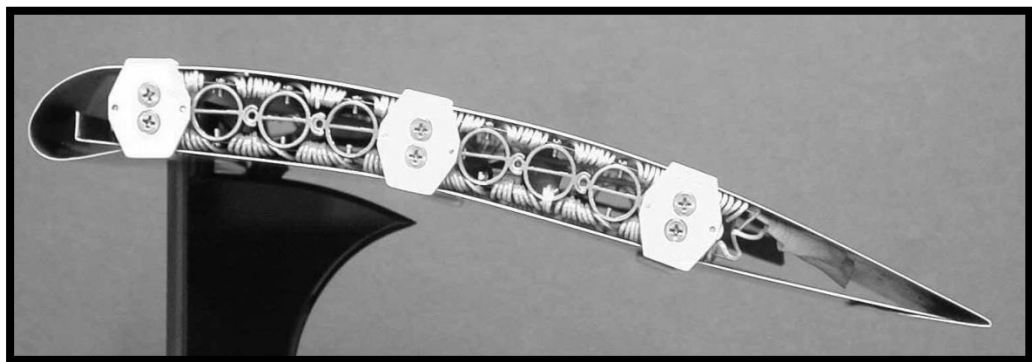


Figure 2.34 The Adaptive Torsion Wingbox: (a) Maximum and (b) Minimum torsional stiffness web positions [81].

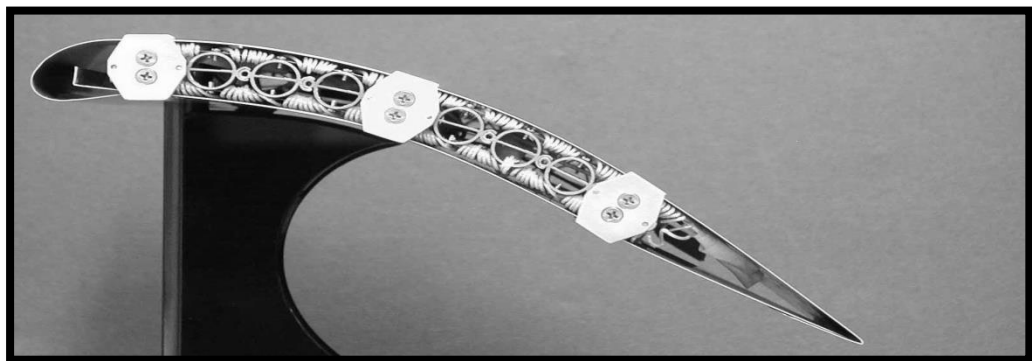
Using Shape Memory Alloys (SMA) to actuate wing twist is another approach that has attracted researchers in recent years. A detailed review on shape memory alloys with applications to morphing aircraft was carried out by Barbarino et al.[85] and sub-reviews have been done by several researchers [13] [34], [47], [86]. In the literature, a full morphing wing using SMA in DARPA's Smart Wing Project [27] is discussed in **Section 2.3.3**. These wings were actuated using SMA wires to create wing twist movements. Nam et al.[87] used SMA spars to replace the mechanically actuated variable stiffness spar used by Chen et al. [80]. A numerical analysis was

conducted for a wing model based on an F-16 wing structure. According to the results, the SMA spar could increase the aeroelastic forces and significantly increase the roll performance (59%). Also, by moving the spars towards the trailing edge, the roll rate were amplified further resulting in a 61% improvement was obtained in roll performance.

A bio-inspired cellular metal vertebrate structure that relies on shape memory alloys (SMA) to achieve fully reversible shape change concepts has investigated by Elzey et al.[73]. The idea behind this design was the fabrication of an internal structure that is strong and lightweight when idle and flexible when actuated. It can be seen from **Figure 2.35** that the internal wing comprises a cellular flexible core, which is able to rotate relative to one another with this system sandwiched between SMA face sheets. Heating either SMA element causes contraction of that face and results in a corresponding curvature.



(a)



(b)

Figure 2.35 Shape morphing aero control surface in two configurations: (a) both actuator ribs at minimal curvature, (b) both actuators at maximal curvature [73].

Sofla et al. [74] investigated antagonistic flexural cells (AFC) to create antagonistic shape actuation based on the one-way shape memory effect. Two of the positions provided by the AFC require no external energy to be maintained, making

the AFC suitable for devices requiring two different end shapes to be fixed for long periods. Jacob et al. [88] also investigate ways of using twisting wings via using shape memory alloys were highlighted. SMA wires used to rotate the trailing edge of the wing. The SMA wires were located at the bottom of the wing with wires attached to the wing tip. The wires could rotate the wing tips by 3° while the position of the leading edge remained the same. In order to reverse the deflection; a servomotor was used.

Lastly, the fish bone active camber wing concepts was introduced by Woods and Friswell et al. [89]. The core of the Fish Bone Active Camber (FishBAC) concept is a compliant skeletal structure inspired by the anatomy of fish (**Figure 2.36**). There is a central bending beam “spine” with a series of stringers (similar to fish ribs) branching off to support the skin. Baseline wing (front side) structure was manufactured with 3D printing and the rest of structure was covered with carbon reinforced EMC skin. Spooling pulley mechanism with high torque servo motor provides the required camber twist and maximum 36 mm camber twist displacement was achieved. Also flapped airfoil geometry was manufactured ($0^\circ - 30^\circ$ of flap angle) to make comparison between the twist and flap configurations.



Figure 2.36 Fish Bone Active Camber Wing.

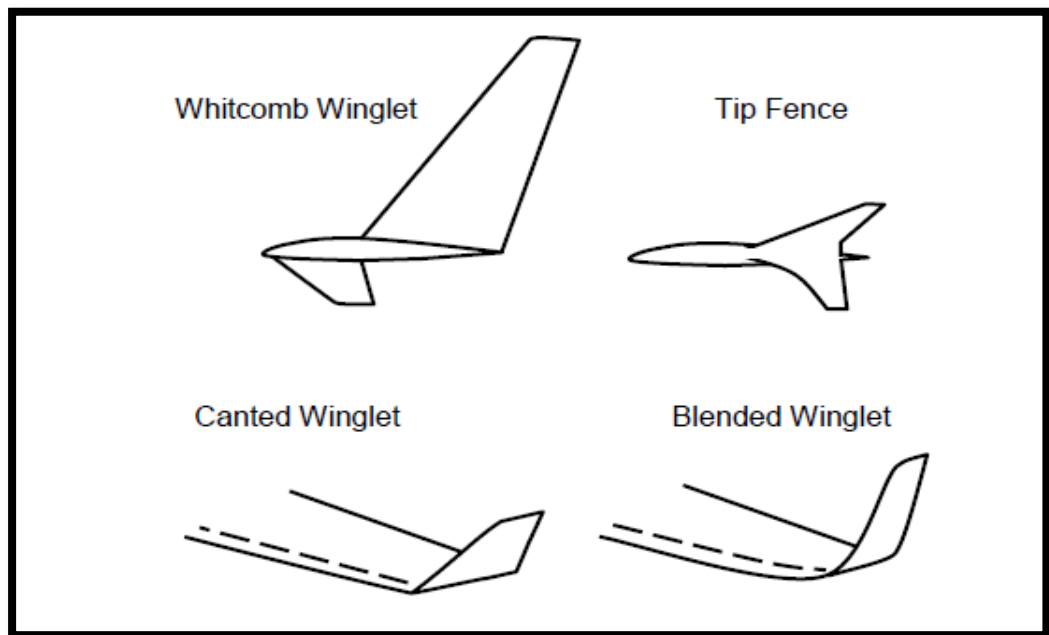
Wind tunnel testing showed that using the FishBAC morphing structure remarkable increase in lift-to-drag ratio of 20%– 25% was achieved compared to the flapped airfoil over the range of angles of attack.

Overall, these concepts have shown through theoretical and wind tunnel analysis large benefits in terms of aerodynamics and roll control. The requirements to adapt

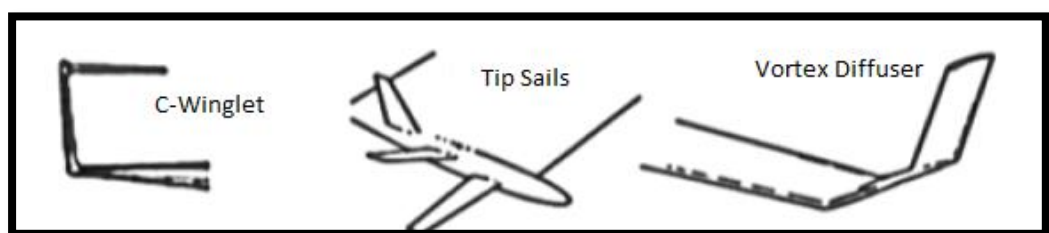
those mechanisms to a real flight environment remain however, difficult to fulfil due to the heavy twist mechanisms, their installation cost, their complexity, and higher torque requirements. The development of a practical skin is also a major challenge.

2.6 Winglets and Wingtip Devices: Their Adaptability

The past surveys and investigations have shown that winglets and/or wingtip devices offer possible solutions to both reducing induced drag as well as improve the range and aerodynamic performance of an aircraft [90]. Although all winglets have different functionalities, they are all intended improve aerodynamic performance and for that matter wingtip devices. Within the recent past, more work has involved adding morphing capabilities to these elements. Looking back initially, the first



(a)



(b)

Figure 2.37 Different Wingtip Devices: (a) Most common winglet devices, and (b) Kroo's wingtip configuration [91].

major breakthrough was introduced by Whitcomb [91]. As illustrated in **Figure 2.37 (a)**, Whitcomb's winglet design consisted of two parts, a combination of a long upper section and a shorter lower section.

Whitcomb's [91] initial analysis showed that dihedral angles of 72° for the upper and -54° for the lower winglet dihedral angles was ideal. Whitcomb mentioned that the purpose of adding the lower structure was to reduce the aerodynamic loading on the upper winglet [91]. A wind-tunnel investigation at high subsonic speeds showed a 9% improvement in the overall aerodynamic performance through a 20% drag reduction. Likewise, NASA provided good evidence for the efficiency of winglet devices between 1974 and 1976 [92]. They assessed different drag reducing devices and wingtip devices with results showing winglets can improve aircraft efficiency by 10-15 % during cruise.

Similar concepts were also explored by Kuhlman et al. [93]. Their investigation was an initial step to better determine the potential for winglets to reduce drag of low-aspect-ratio fighter-type wing configurations at high subsonic Mach number. Overall, a 12% aerodynamic benefit was obtained using winglets on low aspect ratio wings. Over subsequent years, various other winglet shapes have been investigated by several researchers to find the best possible configurations. The aerodynamic design and experimental investigation of the sailplane wingtip device was investigated by Anderle et al. [94]. The concept investigated consisted of a larger extension winglet, a highly swept back winglet, and a small upward swept winglet. The impetus for the work was to identify the flow field behind the wing tip models. A hot wire system was used to obtain the data and according to the results, a greater vorticity profile was found to exist for non-winglet configurations. Also, the velocity distribution was seen to be substantially higher for this condition. Similar to Anderle [94], the effects of various winglet shapes was also explored by Soltani et al. [95] and Nazarinia et al. [96]. It can be seen from **Figure 2.38** that five different winglets were used with measurements including total wake surveys at various angles of attack, and flow visualization over the wing surface using tufts. Experimental results showed the total pressure data in the wake to exhibit substantial changes for each winglet shape and blended winglets. Examples of these are shown in **Figure 2.38**. The more traditional configuration (shown attached to the wing in **Figure 2.38**) was found to perform the best with the vortices slightly weaker than other types of winglets.



Figure 2.38 The wing model including winglet shapes [95].

Later, non-planar concepts in a broader taxonomy were discussed by Kroo [97]. A variety of winglet designs and their merits were reported. According to Kroo's research, winglets decrease vortex drag and reduce the fuel consumption particularly from using the vortex diffuser wing tip devices, shown in Figure 2.37 (b). In addition, Kroo mentioned a further study for 'C' and 'tip sails' winglet configurations to reduce drag coefficients (applied to large aircraft and tailless designs [98] from **Figure 2.37(b)** first left configuration).

A study using triangular, rectangular and circular winglets was also presented by Inam [99]. The tests were carried out in a closed loop system wind tunnel with several Reynolds numbers. The results indicate that sharp or swept edge winglets (triangular) are capable of decreasing the induced drag by up to 31%. Various winglet concepts were also studied by Hossain et al. [100]. Elliptical and circular winglets were tested and a 60° Cant angle winglet and achieved a reduction in the drag coefficient of approximately 25-30% together with an improvement in lift coefficient of approximately 10-20% (**Figure 2.39**). A preliminary CFD study was also conducted by Babigian et al. [101] to compare the wingtip vortices and induced drag generated by three different wing and wingtip models. These geometries consisted of a wing with winglets, a clean wing (without winglets), and a wing with a raked wingtip. According to the numerical results, the clean wing configuration produced the highest vortex magnitudes when compared to wing configurations that

employed either winglets or raked wingtip designs. Similarly, aerodynamic optimization and evaluation of the KC-135R winglets, raked wingtips and a wingspan extension were investigated by Halpert et al. [102]. Various winglet sizes with different winglet raked angles were investigated. It was shown that swept back winglets with approximately a 25° swept back angle or 25° raked winglets gave the highest aerodynamic performance compared to the other cases presented (**Figure 2.40**). Winglet cant and toe angle were also investigated with results showing winglets with a 15° cant and -4° toe angle were optimal to achieve the best aerodynamic performance.



Figure 2.39 Hossain[100] elliptical winglet configuration with 60° cant angle.



Figure 2.40 Various raked wingtip test models : Raked angle of 15° , 20° , 25° , 30° , and 0° from Left to right [102].

Similar to Halpert et al. [102], the development and integration of new high performance wingtip devices for transport aircraft concept was investigated by Heller et al [103]. As shown in **Figure 2.41**, various winglet configurations were

fitted to a transport aircraft model to investigate the aerodynamic effects. According to the wind tunnel testing, the winglet configuration as shown in **Figure 2.41 (a)** (rightmost) achieved a 5% drag reduction target at cruise.

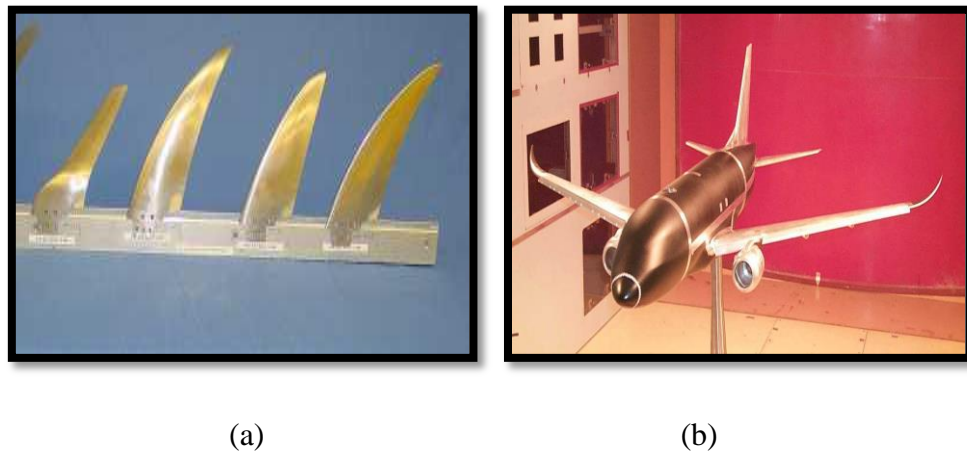


Figure 2.41 Heller[103] wind tunnel test models: (a) various winglet shapes and (b) wind tunnel model with an fitted winglet configuration.

More related specifically to morphing applications, aerodynamic analysis of cant angle winglets has been investigated by Beechook et al. [104]. Four different cant-angled winglet models (0° , 30° , 45° , and 60°) were utilized to understand the effects of cant angle on aircraft performance. The winglets are shown in **Figure 2.42**, was used together with tests. Lift force for a 45° cant angle winglet was found to produce best results with low vortex generation at low angle of attack (low induced drag). Similar to Beechook[104], Yen et al. [105], and Gerontakos et al. [106] investigated the effects of winglet dihedral on the flow behaviour and aerodynamic performance of wing profiles. According to their investigation, vortices magnitude reduced by adding winglets and in some of the cases, (17% at $\Gamma = 90^\circ$ [105] and 6% at $\Gamma = 67.5^\circ$ [106]) enhanced performance benefits compared to other winglet dihedral angles was achieved.

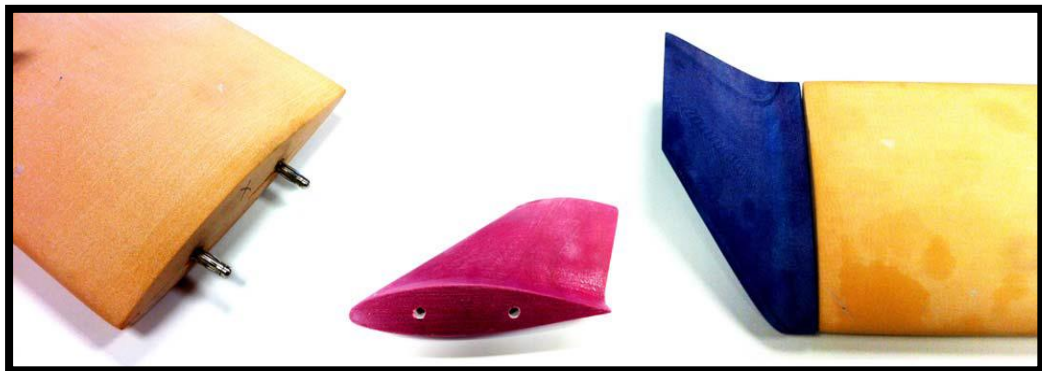


Figure 2.42 Manufactured wing and winglet models [104].

In recent years, blended winglets has been introduced to reduce induced drag, maximize lift distribution, and minimize flow separation [107]. From wind tunnel, and real flight test results, blended winglets decrease total drag by approximately 2% by reducing the discontinuity between the winglets and wing tips [107]. When applied to a Boeing 737-400 Business jet plane and a 7% drag reduction was observed.

The sharklet, as shown in **Figure 2.43** has also been introduced to reduce induced drag and boost the aerodynamic performance. Results taken from real flight testing, show fuel consumption decreases of 15% compared to a non-winglet configuration with 4-5% further benefits compared to other winglet models [108].



Figure 2.43 Installed Sharklets on Airbus A-320 family [108].

The latest winglet technology uses a highly degree of sweep, helping to improve the aerodynamic efficiency of an aircraft by reducing the induced drag. An example can be on the Boeing 787 Dreamliner (**Figure 2.44** left-side picture) and Airbus A-350 XWB (**Figure 2.44** right side of the picture). Boeing uses approximately 40° sweep for its winglets and according to real flight tests, obtains 3.5%-4.5% drag reduction compared to other conventional winglets [107]. Developments in blended winglets with a high sweep technology have recently been proposed by the Airbus Company[109]. Instead of using a mounted winglet, they manufacture the wing and winglet components together with higher degrees of sweep. Flight tests have shown 25% reduced fuel burn compared to other aircraft [109].

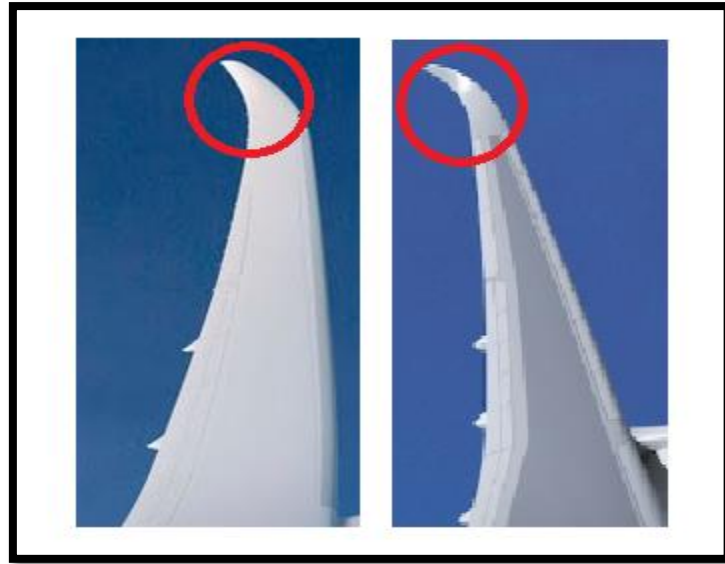


Figure 2.44 Differences between Boeing 787 Dreamliner aircraft's winglet (left side raked winglets) [107] and Airbus A-350XW's winglet configuration (Right side blended winglets) [109].

A split-tip design has also been proposed by Klug [110]. For this design, leading auxiliary winglets are located upstream of the elastic wing axis, and possess both forward sweep and sweepback. The combination of these features permits a simultaneous reduction in the induced drag and in the stress caused by wind gusts, increasing the effectiveness of the wing's ailerons [110]. Prior to this multiple winglet design, biologists also carried out extensive research and concluded that multiple winglets were highly effective in terms of the improving aerodynamic performance of soaring birds; they could reduce drag by 6% [111]. Other multi winglet projects have been completed by Smith et al. [112]. **Figure 2.45** (a) illustrates Smith's five aluminium multiple flat winglets. The winglets are mounted at the tip of an NACA 0012 airfoil shaped wing. The numerical simulations were done using Cobalt flow simulation software in three stages. The first stages involved only the base wing without winglets, and the second stage consisted of five flat winglets without any dihedral angle (all of the winglets were tilted at a 0° dihedral angle) with the last stage having, each winglet at a different dihedral angle, (through $\pm 20^\circ$ in 10° steps). Experimental results showed multiple winglets could increase the lift curve slope (15-20%) through deflecting the winglets (five multiple winglet deflection with 20° , 10° , 0° , -10° , -20° respectively) with good improvement shown for the lift to drag ratio($\sim 9\%$) [112].



(a)

(b)

Figure 2.45 Multi Winglet Models: (a) Smith[112] five aluminium multiple flat winglets and (b) Srikanth[113] tufts flow visualization for multi winglet model at $\alpha=5^\circ$.

An extensive experimental study has also been conducted to investigate the potential of multi-winglets to reduce the induced drag and increase the lift coefficient without increase in wing span [113]. These concepts consisted of multiple and single winglet configurations as well as a wing without winglet model. The concept, shown in **Figure 2.45** (b), showed a 15% reduction in induced drag when multi winglets were used. At high angles of attack, maximum lift coefficient was 26.5% better than the other configurations tested.

2.7 Morphing Winglets

It is clear winglets have a beneficial impact on the aerodynamic efficiency of an aircraft during cruise. Unfortunately, fixed position winglets do not provide the optimum solution for aircraft performance in all flight regimes as the lift requirements for aircraft change due to fuel burn. Recent studies have started to investigate possible ways of alleviating this fixed condition through incorporating methods to actively optimize the winglet position under different flight conditions. A novel method of controlling aircraft via adaptable cant-angled winglet concepts was investigated by Bourdin et al. [114] [115]. The concept consists of a pair of winglets with adaptive cant angle, independent actuation mounted at the tips of a flying wing. The objective of the research was to explore a novel method for primary aircraft control by changing the dihedral angle of the winglets. Experimental testing used a swept wing configuration made of expanded polypropylene foam and a Zagi 12% airfoil profile (**Figure 2.46** (a)). The winglet was also made of foam material and connected via a hinge system; with rotation capability of $\pm 90^\circ$. To achieve the

winglet rotation four high torque robot servos were used. Initial numerical calculation was carried out with wind tunnel test validation. The results showed greater possible manoeuvrability characteristics and a better lift/drag ratio at the $+30^\circ$ cant angle position.

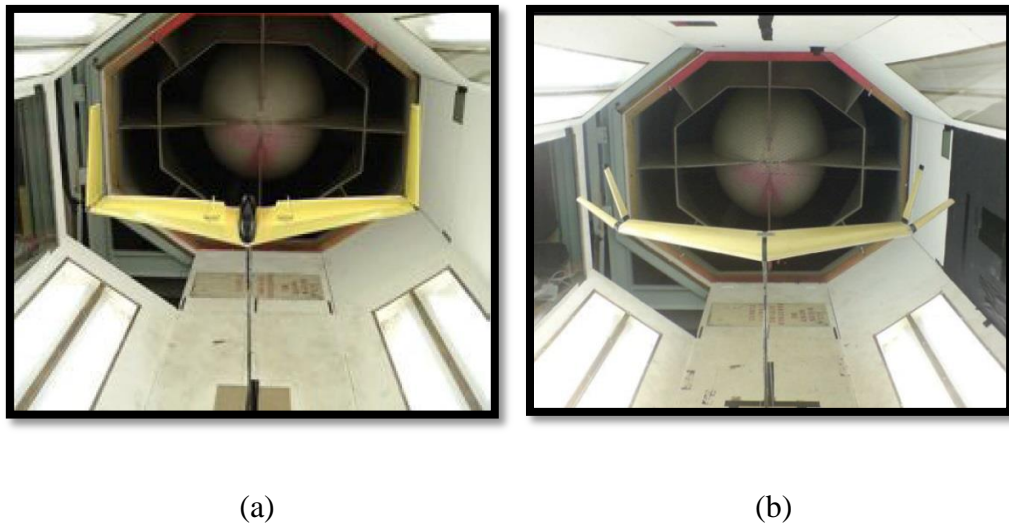


Figure 2.46 Experimental wind tunnel models: (a) two active winglets [114] and (b) split wingtip configuration [116].

Although the concept was effective, a single pair of folding wing-tips was not able to substitute for all conventional control surfaces, so another concept was developed. To achieve a full control envelope, Bourdin et al. [116] [117] adapted a second pair of winglets (**Figure 2.46** (b)) using similar design method. Four active winglets were tested and produced more efficient control moments than the single winglets. Also they led to a redundancy for the possible flight control system. Similar flying wing geometries were also investigated by Ameri et al. [118] [119]. This work focused on the dynamic and shape changing response as well as aeroelastic effects of active morphing winglets. A dynamic simulation model of the flying wing was built using the SimMechanics Simulink tool and the aerodynamic loads were provided by Athena Vortex Lattice software package. The results of this work show a strong and non-negligible dependency of the aerodynamic transient behaviour on shape variation[119].

Ursache et al. [120] has also studied morphing winglet (MORPHLET) concepts to increase the flight performance of an aircraft. A narrow body jet wing was used as a simulation model (**Figure 2.47**).

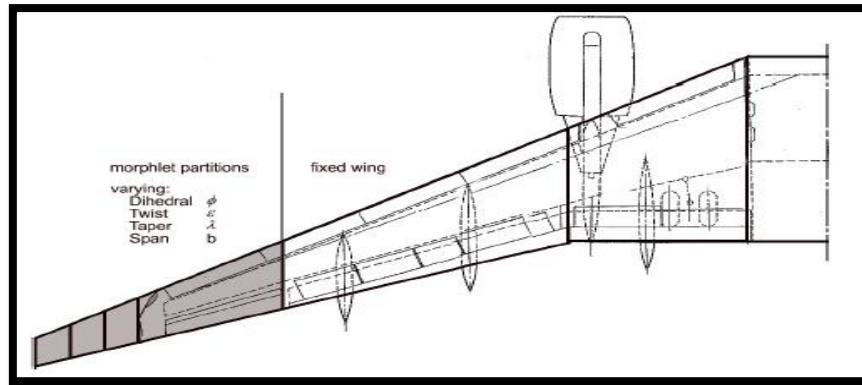


Figure 2.47 Schematic view of narrow body fixed wing and morphing parts [120].

Three different flight regimes (initial cruise, final cruise, and end of descent) were considered to investigate the best possible configuration of the MORPHLET configurations. A Matlab integrated Vortex Lattice method was used for the aerodynamic modelling and a genetic algorithm was used for the Multi-disciplinary optimization. The preliminary optimization results show that in order to achieve high aerodynamic performance significant shape changing is needed. To get the full benefit during the initial cruise and descent, the winglet span needs to be increased, and a 33° cant angled MORPHLET structure configured for cruise. Using these geometric properties in three different flight regimes, the range could be improved by 5.17% with induced drag could be reduced by 18.5%. Subsequent work developed MORPHLET mechanical prototypes for tested. These winglets were allowed to alter cant and twist angle using a servo actuation system; the prototype is shown in **Figure 2.48** (b). Corrugated skins were used to achieve desired flexibility (**Figure 2.48** (a)).



(a)

(b)

Figure 2.48 Morphing Winglet application: (a) the corrugated skin for the MORPHLET and (b) the mechanical demonstrator [121].

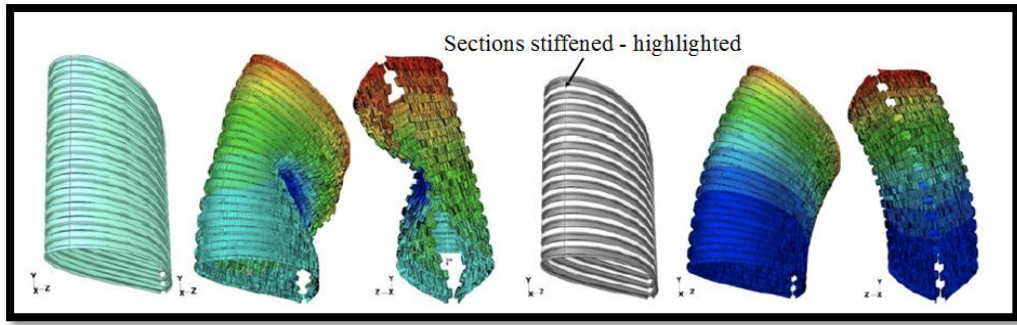
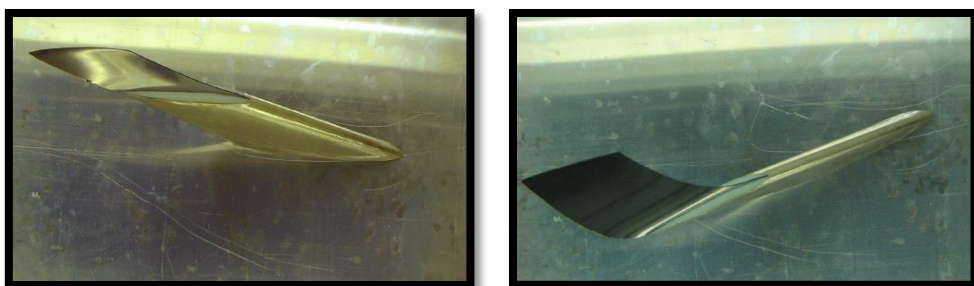


Figure 2.49 Numerical Investigation of the corrugated skin showing buckling pattern of the non-supported skin (left three models) and the effect of reinforcement (right three models) [121].

Although the numerical and experimental data show good agreement, it was difficult to design a morphing skin. As illustrated in **Figure 2.49**, the principle problem lies with on unsupported skin causing it to buckle. In this case, careful support design is needed with corrugation space and depth chosen with sufficient stiffness placed between the corrugations (**Figure 2.49** (right three models)).

To enhance wing lift capability, bistable winglets were introduced by Gatto et al. [122]. A swept wing configuration was used as the base model for this study with the wings made from blue foam and a lacquered skin to provide a smooth aerodynamic surface finish. For the winglets, bistable composite materials were used together with a customised transition (between wing and winglet), insert aid bistable winglet deployment. As shown in **Figure 2.50**, two separate winglet configurations, “snapped” and “unsnapped”, were tested. Results obtained showed enhanced performance for to lift with the unsnapped configuration (take-off) during cruise, for the snapped configuration.



(a)

(b)

Figure 2.50 Bistable Winglet Modelling: (a) Unsnapped winglet and (b) Snapped winglet configurations [122].

Multidisciplinary design optimization of a morphing wingtip has been studied by Falcao et al. [123] [124]. The aim of the project was to illustrate the potential benefits of variable wing-tip devices via a Multidisciplinary optimization technique. The investigated concepts consist of variable winglets that are able to rotate about two different axes: the aircraft's longitudinal axis (winglet cant angle from 0° to 180°) and the vertical axis (toe angle from 0° to 8°). Computations carried out in CFX showed distinct advantage over the fixed winglet configuration, giving estimated 25% additional aerodynamic efficiency with winglets positioned at the desired angle (42.49° of cant and 1.22° of toe angle) according to the flight conditions. Further investigation into aero-structural design optimization for morphing winglet concepts was also carried out (Falcao et al. [125]). Servo actuation and a hinged mechanism were proposed as an alternative mechanism to alter winglet shape. Similarly, Smith et al. [126] [127] also studied multidisciplinary design optimization(MDO) concentrating on active nonplanar polymorphing wing concepts. MDO was applied to the problem of maximizing the performance benefit through the retrofit of a morphing nonplanar outer wing system to a commercial narrow body aircraft. Through optimizing the outer partition span for the maximum range sizing case and re-optimizing the partition twist and cant angles for different flight conditions, it was determined that the morphing system not only provides a substantial 6% specific air range improvement over the datum aircraft but is also able to maintain a 4.5 to 5.5% SAR enhancement for all of the analysed flight phases. With fixed sizing geometry the improvements fall to approximately 3.5%. These results also indicate substantial improvements for the lift to drag ratio in climb, take-off, and for reducing landing field length [127].

After active multiple winglet concept was investigated by Shelton et al. [128]. The goal of the research was to determine the potential benefits of active multiple winglets to augment both cruise and manoeuvring performance. Five winglets were applied to a Dragon Eye Unmanned Air Vehicle as shown in **Figure 2.51(a)**. Multiple winglets for low speed aircraft were also studied by Cosin [129] and Catalano et al. [130]. Six different cant angled winglet models as shown in **Figure 2.51 (b)** were tested with results showing performance increase through the induced drag enhancement. Cant angles of 15° , 0° and, -30° showed a 7% improvement in the lift/drag ratio over other configurations.

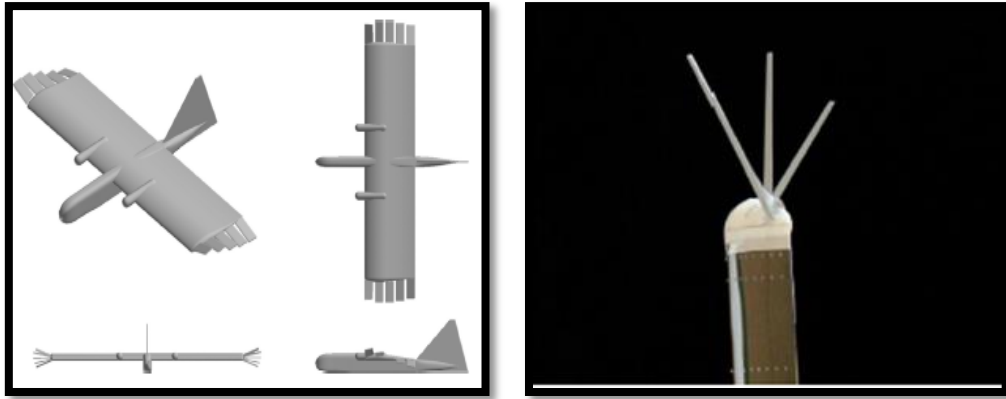


Figure 2.51 Multi active winglet applications: (a) Dragon Eye UAV with multiple winglets [128] and (b) Three cant angled split winglet configuration [129].

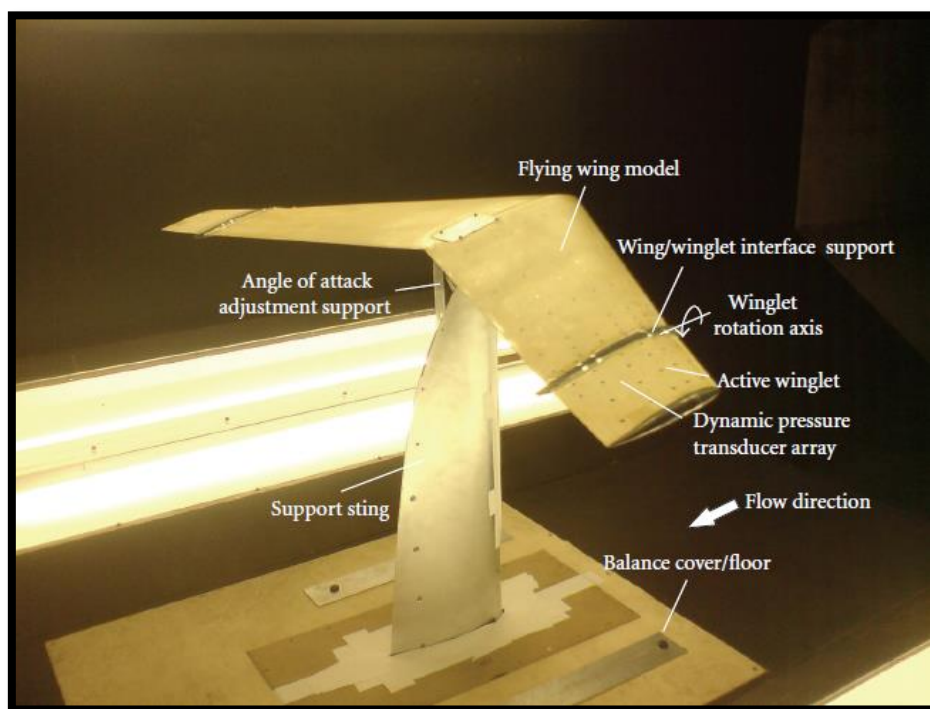


Figure 2.52 Experimental setup for active wing-tip flying wing [131].

The effect of articulated winglets on wing surface pressure aerodynamics has also been investigated by Gatto et al. [132] [131]. This study aimed to further extend and understand the concept of variable winglets for roll control. In this study, a swept wing model made of blue foam was used with winglet rotation capability set a 0° to $\pm 75^\circ$ (**Figure 2.52**). Dynamic pressure sensors were also placed inside the wing and winglet model. With results sharing changes in pressure coefficient with

dihedral angle changes. This investigation provided insight into the roll control aerodynamic mechanism as well as insight into real time changes in lift distribution.

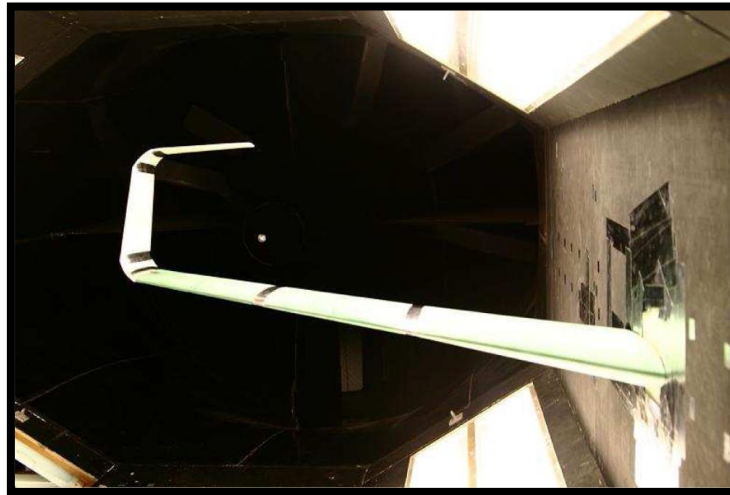


Figure 2.53 Smith's C-Winglet configuration [133].

Studies using novel design concepts of twisted and cant angled C wingtip configurations were also presented in [134] [133]. This concept consisted of 4 different degrees of twist and 5 different degrees of cant angle. To decide the wing geometry, TAU CFD codes were used to define optimal conditions. **Figure 2.53** shows the wind tunnel model, angled up to 90° (cant angle). In total, 20 different outboard parts were manufactured and tested with results indicating that in most of the dihedral cases concerned, lift production reduced as the dihedral angle increased. Drag was also found to be considerably lower than expected. For the twist cases, high twist angles tended to increase the lift coefficient with winglet twist angles of up to $\phi = -3^\circ$ providing good aerodynamic efficiency.

2.8 Morphing Skin

The development of suitable morphing skins is very challenging. The desire to have a suitable aerodynamic fairing to cover the underlying morphing structure is fundamental, but signifies a major problem for morphing technologies. Instead, very few of the concepts for morphing skin deal with the conflicting problems are requiring a smooth and continuous surface that contains adequate structural compliancy while adequately carrying the aerodynamic loads. In widely cited article by Thill et al. [40], potential solutions for flexible morphing skins is presented. In this article, flexibility and stiffness problems in morphing air vehicles are thought to

be solved by using novel materials like elastomeric skins, flexible matrix composites, and composite corrugated structures. Many papers mention that elastomers are promising solutions for morphing skins [27] [40][135][136] with one of the most commonly cited being DARPA's high strain-failure silicon skin [27]. The important feature of this skin is that it has low density cross-links, which provides the ability to undergo large deformation as well as the ability to return to the original shape. However, they were generally unsuitable for carrying an aerodynamic load, which questions their suitability. Furthermore, if elastomers work against the strain material, larger actuation power to both hold and actuate the deformed shape is typical. These Elastomer skins for morphing wing skins has also been studied by Kikuta [137]. Different thermoplastic polymers, co-polyesters, and woven materials were investigated experimentally. From test results, Tecoflex 80A was found to be the best polymer material as it more easily strain and return to its original shape, however this material was found to lack the ability to carry the aerodynamic load.

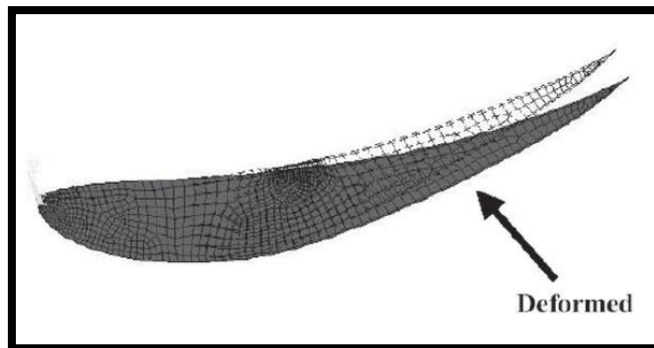


Figure 2.54 Structural deformation of the FE airfoil section after final step iteration [138].

Auxetic materials are another approach in for stretchable structural concepts for morphing aircraft applications. These materials are able to become narrow when compressed and expand when elongated due to their negative Poisson's ratio. These materials can be foams, ceramics, composites, or polymers. Morphing airfoil concepts using such materials hexagonal and chiral honeycomb structures have been studied by Bornengo et al.[138]. A set of numerical (finite element, FE) simulations was carried out into shear and elastic deformations of elements when subjected to uniaxial loading. An acrylonitrile-butadiene-styrene (ABS) plastic honeycomb structure was used within a truss-like internal structure for an adaptive wing box.

The box allowed conforming deformations with external flow, giving a variation in the camber-line and trailing-edge displacement of 5mm (**Figure 2.54**).

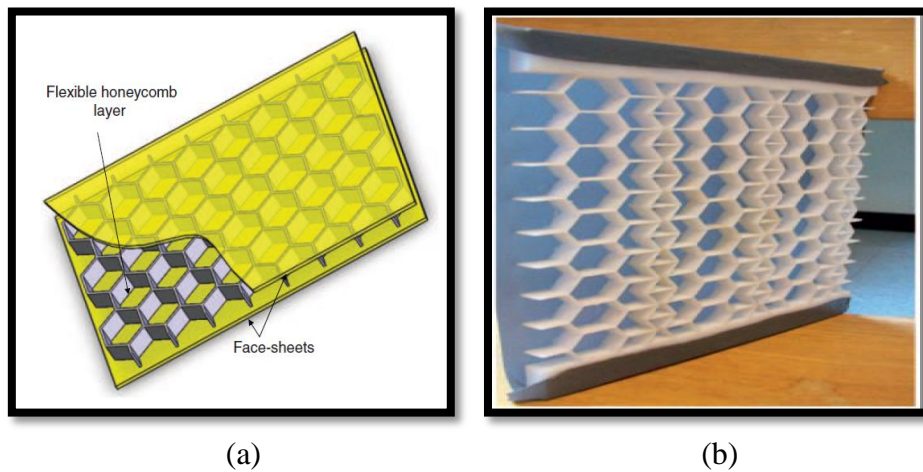


Figure 2.55 Honeycomb structures: (a) Skin made of a cellular core and face-sheets [139] and (b) Prototype of hybrid cellular honeycomb with attached polymeric face sheet [140].

Olympio[141] was the first to suggest the idea of flexible skins comprising a cellular substructure (Honeycomb) and pretension face sheet for morphing applications (**Figure 2.55 (a)**). Olympia and Gandhi et al. [140] [139] [142] extended these concepts by designing the zero Poisson's ratio honeycomb structures for 1D morphing skin applications. This can be seen from **Figure 2.55 (b)**. Comparing the properties shows that the hybrid and accordion honeycombs proposed generally have similar in-plane axial stiffness and strain capabilities as conventional honeycombs when the latter is unrestrained in the non-morphing direction. However, with the zero Poisson's ratio of the hybrid and accordion honeycombs, it is observed that the axial stiffness in the morphing direction will not increase when the skins are restrained in the non-morphing direction. The zero Poisson's ratio of the accordion and hybrid cellular honeycombs is not helpful from an out-of-plane load carrying ability standpoint. However, the out-of-plane load carrying ability of the accordion honeycombs can be superior to those of conventional honeycombs if the 'continuous fibers' are sufficiently thick, leading to a very large modulus in the non-morphing direction. The effective out-of-plane stiffness of hybrid cellular honeycombs, on the other hand, is poorer than conventional cellular honeycombs [140]. Similarly, studies on the design of a flexible skin for a shear morphing wing concept have also investigated a flexible skin and honeycomb structure [5]. According to the research, a honeycomb cellular

structure was found to be effective a way to reduce the peak strain, which results in reducing the actuation energy, but wrinkling was found at the face-sheet, which disrupted the aerodynamic smooth surface finish [5]. Similar to Olympio et al [141], elastomeric matrix composites for a passive 1D morphing aircraft skin were investigated by Bubert et al. [143]. This research focused on the development of a passive anisotropic elastomer composite skin with the potential for use in a 1D span-morphing UAV wingtip. The proposed morphing skin prototype including the PAM actuation system is shown in **Figure 2.56**. It can be seen that a flexible honeycomb structure was used to support the out-of-plane loads with the structure covered by a very thin elastomeric fiber composite surface layer. To provide stiffness and correctly align substructures, 4 carbon rods were used. Also, to achieve the span changing, a PAM system was used to extend the honeycomb structures as well as the skin. Design goals of 100% global strain and 100% area change were demonstrated on a laboratory prototype using the combined skin and actuation mechanism. Also, the morphing skin strained smoothly and exhibited a very low in-plane Poisson's ratio [143].

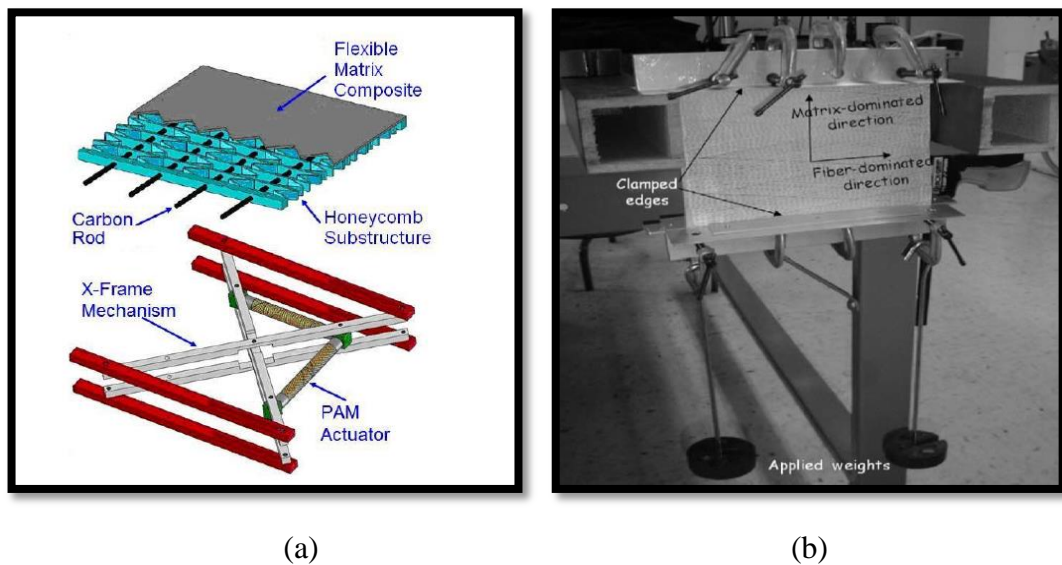


Figure 2.56 Morphing 1D skin application: (a) proposed morphing skin prototype including PAM actuation system [143] and (b) Murray's FMC test apparatus [4].

Other efforts at 1D morphing skins have been made by Murray et al. [4]. The purpose of this investigation was to analyse the in-plane properties and out of plane deflection of FMC skins. This analysis was then compared with experimental results to validate the concept. The model for the skin comprises a flexible matrix and was

constructed using glass fiber and Dragon Skin Shore 10A elastomer matrix. The test setup is shown in **Figure 2.56** (b). As can be seen, the top and the bottom surfaces were clamped, and while the top clamp was secured, weights were suspended from the bottom to extend the FMC skin in the matrix dominated direction. This was done to measure the strain. Other tests were conducted to measure the out of plane midpoint deflection of the membrane when it was clamped along its edges and subjected to out of plane loads. According to the results, aligning the fiber dominated direction to the normal morphing direction does not only impede the in-plane stiffness, but also increases its capacity to carry out of plane loads (it does not deform the skin). However, if the skin uses only the matrix dominated direction, due to low modulus properties, the pretension needed to keep out of plane displacement is limited, leading to rupture [4].

As an alternative, the use of corrugated skins has been investigated by several researchers [136][144][145][146][7][8]. The benefits of these materials allow the wing structure to be stiff to withstand the bending due to aerodynamic forces, but also flexible (chord-wise direction) to adapt to different flight conditions. A fundamental drawback of corrugated laminates however, is their low out of plane stiffness, which is likely to be unable to resist aerodynamic loading at the typical speeds required actual for flight. Yokozeki et al. [136] demonstrated the use of such corrugated composite sheets for flexible wing structures (**Figure 2.57(a)**). The corrugated samples underwent four different tests to assess their mechanical properties with predominantly. Tensile and flexural tests conducted in the longitudinal and transverse directions. A simple analytical model, based on a sinusoidal cross-section of the corrugation, was used to calculate the longitudinal and transverse Young's modulus as well as the longitudinal and transverse flexural modulus of the corrugated structure. The composite corrugated structures were found to be sufficiently rigid against aerodynamic forces. Moreover, as a further improvement, a stiff rod and flexible rubber were used to provide stiffness to the morphing skin in the longitudinal direction. Yokozeki et al. [136] installed stiff carbon fiber rods and one-sided filling (e.g. flexible rubber) as shown in **Figure 2.57** (b). It was found that the flexible rubber decreased the specific stiffness with suggestions that a thin film should be used instead of rubber. Furthermore stiff rods were found to be an effective method of increasing stiffness in the longitudinal direction without loss of flexibility in the transverse direction. Overall these hence

the modified composite corrugated skins were found to be very stiff as well as lightweight [136].

Although Yokozeki et al. [136] tried to come up with a smooth aerodynamic surface, a non-smooth surface at low Reynolds numbers could be beneficial Tamai et al. [147]. An experimental study was conducted to investigate the flow behaviour around a corrugated dragonfly airfoil (**Figure 2.58** (a)) compared with a traditional airfoil, and flat plate. The measurement results clearly show that the corrugated dragonfly airfoil performs much better over the traditional airfoil and flat plate in preventing flow separation; the airfoil stalls at a lower Reynolds number (**Figure 2.58** (d)). Also, the detailed PIV measurements near the leading edge of the airfoil provide details of the underlying physics as to why the corrugated dragonfly airfoil can suppress flow separation and stall at low Reynolds numbers. Instead of having laminar separation, the protruding corners of the corrugated dragonfly airfoil were found to be acting as “turbulators”, generating unsteady vortices to rapidly promote the transition of the boundary layer from laminar to turbulent [147].

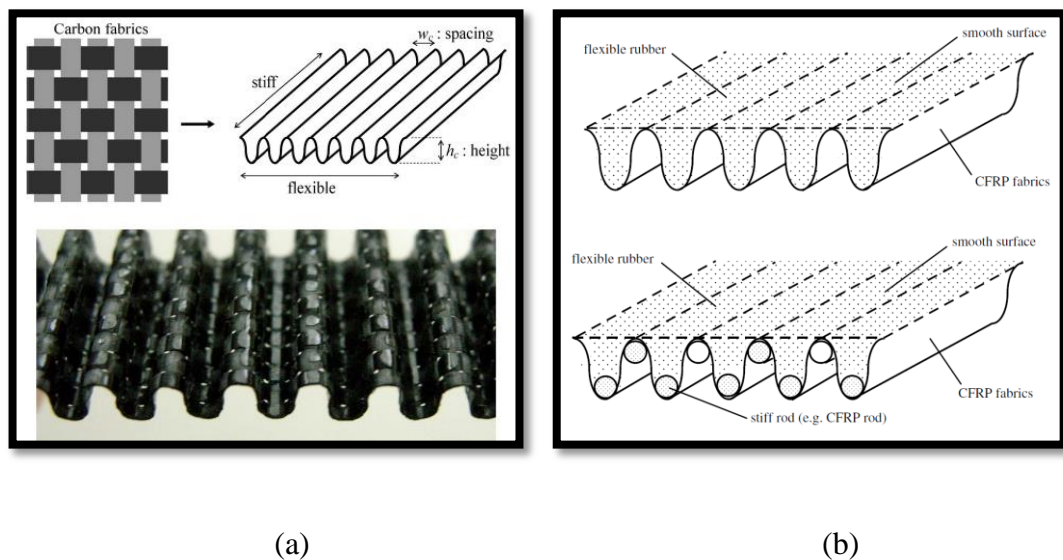
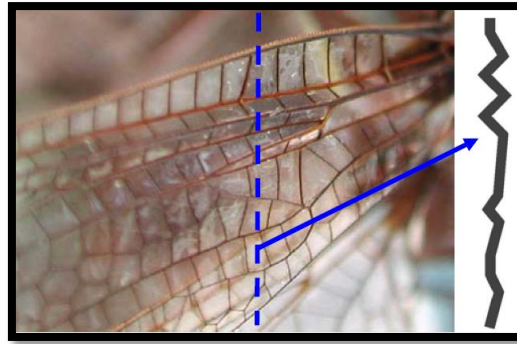
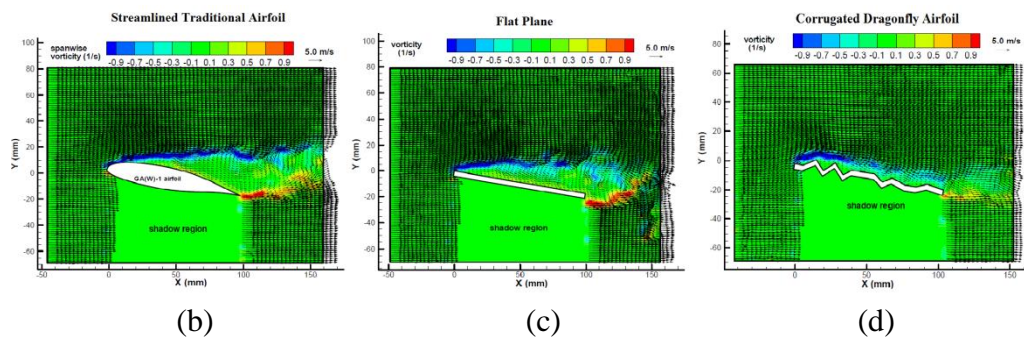


Figure 2.57 Composite Corrugated Skin: (a) the corrugated-form composites that are flexible in the corrugation direction and stiff in the transverse direction to the corrugation and (b) corrugated composites with one-sided filling of rubber (upside) and rod stiffened corrugated with one-sided filling of rubber (downside) [136].



(a)



(b)

(c)

(d)

Figure 2.58 Tamai’s Dragonfly corrugated airfoil: (a) Corrugated cross section of a dragonfly wing, (b) Instantaneous velocity fields for strealined traditional airfoil, (c) Instantaneous velocity fields for flat plane, and (d) Instantaneous velocity fields for corrugated dragonfly airfoil [147].

As stated previously, corrugated laminates have very low out of plane stiffness, which prevents them from resisting aerodynamic loading at the speeds required for conventional flight. However, a corrugated sandwich structure (suggested by Thill et al. [148] [149]), has attempted to overcome the out of plane stiffness problem. Experimental analysis of the corrugated sandwich structures is presented in [148]. Various geometries (rectangular, triangular, re-entrant, round, sinusoidal, and trapezoidal) were attempted to analyse the effect of the geometry on the structural elastic strain and equivalent elastic tensile modulus traverse to the corrugation direction. The results show that the rectangular geometry achieved 50% structural strain if stiffness is of no primary concern. Also, corrugated laminates with a traverse equivalent elastic modulus of about 4GPa can be designed. Furthermore, the re-entrant configuration gave the highest strain value while the triangular corrugations had the highest modulus. The results indicate that by using corrugated laminates structures, the requirements for morphing aircraft skin would be met [148]. Although corrugated structures offer potential solutions for morphing skin, they have some

detrimental effects on aerodynamic performance due to their non-smooth surfaces. In this regard, Thill et al. [150] investigated the effect of corrugated trailing edged airfoil both experimentally and numerically. Various corrugated models with different corrugations (sinusoidal, triangular, and trapezoidal) were used (**Figure 2.59**). The results highlighted the fact that the aerodynamic performance is highly dependent on the corrugation wavelengths and amplitudes as well as the Reynolds number with the best performance achieved with low amplitude and low wavelength profile. Changing the sinusoidal to triangular and trapezoidal had very effects. Some penalties associated with corrugated skin were also observed. Due to the non-smooth surface, the rear section had a detrimental effect on the aerodynamic performance but these effects were minimised by adequately designing the corrugation shapes. Additionally, to reduce the drag penalty, a segmented skin on top of the corrugated profile was suggested for the suction surface [150].

Details of the structural and aerodynamic behaviour of composite corrugated sandwich structures were investigated by Thill et al. [144]. **Figure 2.60(a)** shows the rectangular corrugated sandwich structure with additional foam supports that were used and applied to the NACA 0024 airfoil profile as a test model. The tested parameters involved changing the chord length (maximum 4%) and deflecting the trailing edge of the structure (maximum 12°). According to the results, as would be

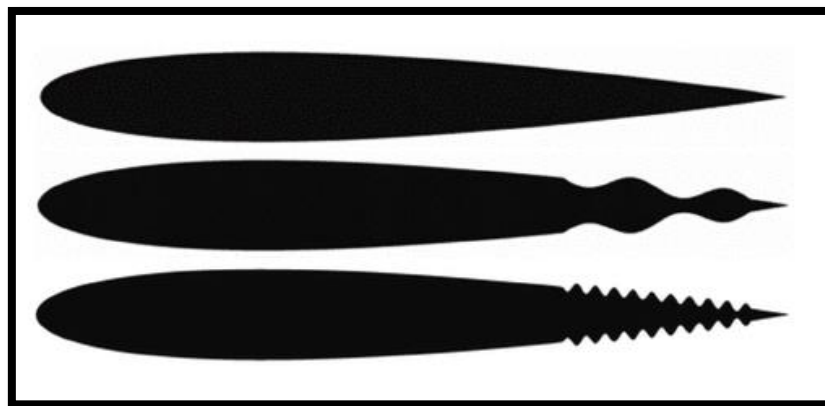


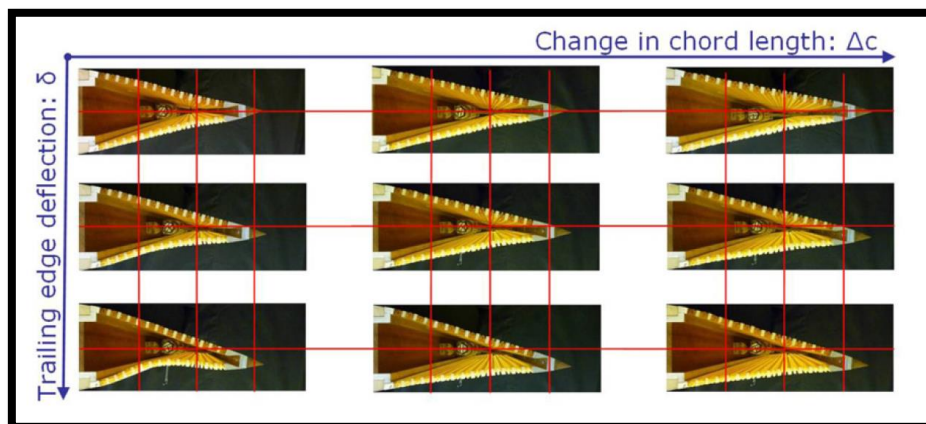
Figure 2.59 Profile shape of the unmodified NACA 0012 (top), modified with 2 sinusoidal waves and amplitude of 1% chord (middle), modified with 10 sinusoidal waves and amplitude of 0.6% chord (bottom) [150].

expected, increasing the chord length and deflecting the trailing edge downwards tended to increase the lift slope and in general, results showed that the structure generates a low drag profile. Additional support however is needed to stiffen the

morphing skin as well as maintain smooth surfaces, because, as can also be seen in **Figure 2.60** (b), the lower surface bulges inwards when it is not under tension (the wind tunnel demonstration showed the concepts work well under aerodynamic load at only low speeds). The author also noted that as a piece of future work, additional ribs could be developed to prevent the skin bulges [144].



(a)



(b)

Figure 2.60 Thill's corrugated structures: (a) picture of rectangular corrugated sandwich structure and (b) pictures of out of wind tunnel tests [144].

Studies comparing experimental and numerical models for the mechanical behaviour of coated corrugated panels made of glass fiber have been carried out by Dayyani et al. [7]. The results obtained from this study show good agreement between the numerical and experimental testing. Also, Dayyani et al. [7] proposed ideas to deal with the smooth surface problem. According to these ideas, a composite corrugated covered with a pre-stretched coating and a triangular corrugated core with an elastomer coating could be a solution for morphing skin, with the main drawback

being corrugated skin requires frequent elastomer covering to provide smooth surfaces. Shaw et al [8] also investigated optimization of a composite corrugated skin for buckling in morphing aircraft. This work analysed the performance of corrugated panels under buckling loads, and optimized the corrugation patterns to improve weight, buckling performance, and actuation compliance.

2.9 The Morphing Concept

Previous sections emphasize the morphing skin and mechanism challenges. These include added weight, a compliant skin, and/or overall complexity. These are important reasons for creating novel design concepts to allow the aircraft skin to vary with an aerodynamic smooth surface as well as to provide high stiffness to withstand aerodynamic loads.

A study of early designs and approximation techniques made the assumption that changing the twist in the outboard sections of the wings can improve the desired control forces needed for manoeuvring flight. Wing warping techniques were employed by the Wright Brothers to control the first powered, heavier than air, aircraft through wing twist via subtended cables [2]. Similar to wing twist concepts, winglet twist can also provide performance increases. The use of winglets to increase the aerodynamic efficiency of an aircraft through the production of forward thrust has been around for many years [91]. Unfortunately, fixed positioned winglets do not provide the optimum solution for aircraft performance in all flight regimes as the lift requirements for aircraft can change within a typical flight due to fuel burn. Therefore, ultimately, this proposed concept was aimed to provide a novel alternative mechanism for morphing winglets to enhance the performance and controllability of the aircraft.

Prior to the variable twist concept, a novel design concept was proposed as shown in **Figure 2.61**, which consists of multiple ribs with each rib assembled with multiple carbon rods. As is known for morphing concepts challenges such as surface deformation and the strength under aerodynamic load are the main issues. Therefore, these carbon rods are used at the origin of the wing chord to provide stiffness for the structure and to offer an aerodynamically smooth surface finish while allowing the wing twist. The main Carbon tube is also placed at the quarter chord of the model to

provide actuator torque. This also provides durability to the wing structure and alignment together with the other morphing elements.

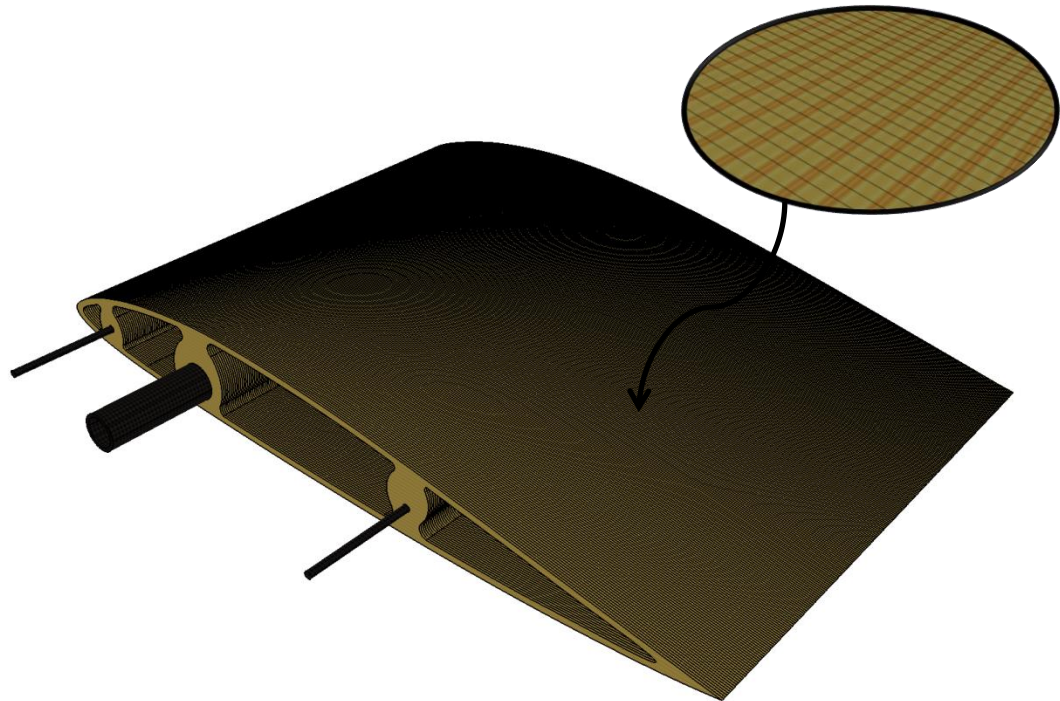


Figure 2.61 CAD design of an adaptable wing/winglet model.

The morphing elements are made of thin wood materials. The thickness size decision was made from initial structural analysis, with the surface smoothness the main consideration to decide the right size for the morphing elements. Following that, the weight of the morphing elements was also reduced to increase twist angle and to reduce friction effects, hence low actuation energy is required to achieve twist. In Assembly, significant attentions needed for the interface between the ribs and rods, consequently they were tightly fitted to reduce any wrinkling and separation on the surface. This helps to achieve the similar drag profile relative the baseline fixed wing configurations. In addition, due to wood's rough surface, morphing elements need to be sanded and lacquered to receive the full benefits of the morphing twist system. A servo actuator is used with a servo-driven mechanism to actuate the twist. To enact twist deformation on the structure, moment (3.43 Nm) was applied to the main carbon tube. This moment was estimated through the torsion equation with desired twist change (minimum $\pm 6^\circ$). Although, the friction effects are negligible in this model due to small surface area between each rib and the interface between the ribs and rods, additional torque was also estimated and the servo

actuator was chosen based on high torque requirements. To allow the actuator tube to rotate the entire model, an end section was designed and placed at the tip of the structure with rods a fixed. When servo torque is applied to the carbon tube, the end-support would enact twist by rotating all morphing elements correspondingly. This co-ordination was controlled by the carbon rods and the end-section.

One of the important benefits of this concept is the ability to maintain a skin with a low drag (smooth surface finish) while twist deformation in an action. Moreover, the structure is lightweight and strong to carry aerodynamic loads. Comparing with other mechanisms in literature, this mechanism largely meets all requirements addressed for morphing wing challenges. Therefore, it is considered suitable for morphing wing applications and is the principal founds of this research work.

2.10 Summary

In this chapter, a detailed description of past and current morphing aircraft concepts is provided. Various investigations have been carried out into morphing aircraft concepts and the benefits have been outlined and compared to conventional hinged control surface air vehicles. Although huge possible advantages of morphing concepts have been discussed, the majority of concepts have been limited due to problems such as excess weight, cost, structural integrity, skin configuration, and smooth surface design. An efficient widely accepted mechanism with a corresponding realistic skin still eludes development and widespread application. Smart materials aim to meet these needs; however the skin problem remains unsolved. The Morphing skin remains one of the significant challenges in this area.

CHAPTER 3 COMPUTATIONAL SETUPS AND METHODOLOGIES

3.1 Introduction

This chapter describes the computational setup and methodologies used to investigate the different phases of computational analysis. **Section 3.2** considers a computational setup for the wing and/or winglet geometry where concepts computational methods (Athena Vortex Lattice) were used to investigate the performance enhancements possible from varying degrees of twist, sweep, and dihedral angle to quantify and better understand the overall benefits available as well as set an initial data point for subsequent design stages. In this framework, **Section 3.3** presents the twist system, adaptive skin technology development and their computational analysis setups as well as the Finite Element Modelling. As a first step of the adaptive skin development and to ease the manufacturing difficulty, the straight wing was initially considered and created in AVL to provide aerodynamic data for ANSYS FEA tests. Obtained FEA data was used to compare with a wind tunnel model. Following that the analysis tool for the flight testing model mechanism and structural analysis setups are also described in **Section 3.4**. Both adaptive skin and twist system were analysed in ANSYS and data used for comparison. A brief summary thereafter concludes this chapter (**Section 3.5**).

3.2 Athena Vortex Lattice (AVL)

The aerodynamic modelling and numerical calculations were carried out using the Athena Vortex Lattice (AVL) software, which was originally coded by Harold Younger in 1988 and further developed by Mark Drela [151]. Athena Vortex Lattice is a numerical simulation package that determines solutions to a linear aerodynamic flow model. It includes the following major features: Aerodynamic modelling, basic force and moment calculation, flight performance calculation, and stability and control analysis. All of the features are calculated as a function of the angle of attack. Moreover, to achieve a morphing wing and/or winglet structure, AVL provides an opportunity to easily alter the angle and size of the wing and/or winglets in terms of span, sweep, dihedral, and twist. The fundamental philosophy behind AVL is as

follows: the shapes are modelled as a set of wing lift panels along the wing span and chord axes. Each surface panel was assigned as a single horse-shoe vortex. In order to compensate for the boundary conditions, “1/4-3/4” rules were applied [152]. With this rule, the bounded vortex is positioned at a quarter of the chord length with one

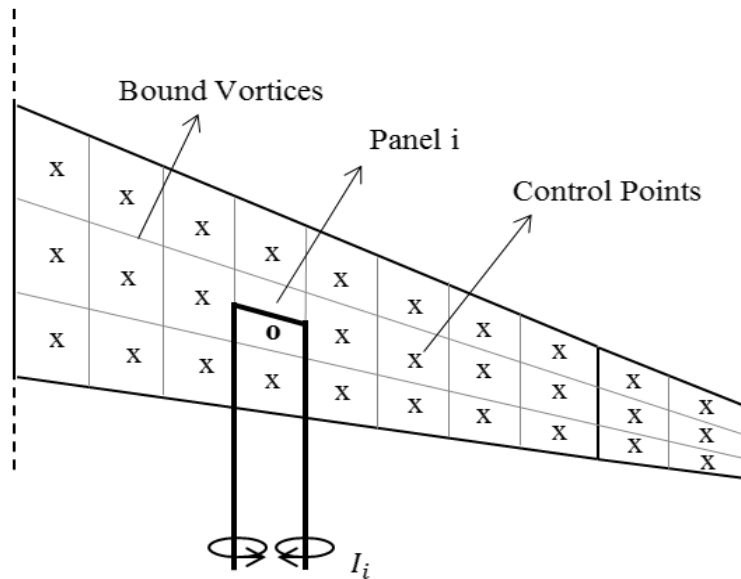


Figure 3.1 Location of the Bounded Vortex

vertical finite and two horizontal infinite vortex lines, as illustrated in **Figure 3.1**. The variation in lift can be modelled as a step change from one panel to other. The control points are placed at 3/4 chord for each panel at the midpoint position in the span wise direction to achieve the required vortex strength by applying the flow tangency condition. Then, the Biot-Savart law was applied to solve the linear equations for the selected panel in three component vortex lines. One of the selected panel models is shown in **Figure 3.2**. For each panel, the same processes are followed to obtain the total vortex strength I_i .

The velocity at the control point of the panel is calculated by solving the formulas shown in **Equation (3-1)**. R_1 and R_2 are the magnitude vectors of \mathbf{r}_1 and \mathbf{r}_2 respectively (**Equation (3-2)**). The influenced matrix is created to solve the required vortex filament strength by multiplying the vortex strength vector and the free stream velocities as illustrated in **Equation (3-3)** (Where A is a non-linear function of a matrix depending on the wing shape, b is a vector that can be changed by varying the angle of attack and U_∞ is the given freestream velocity).

The lift force is obtained thereafter by integrating the panel lift distribution. The lift coefficient for a wing can then be calculated using **Equation (3-6)**.

$$C_L = \frac{L}{\frac{1}{2} \rho V^2 S} \quad (3-6)$$

Once the wing loading of the structure had been calculated, the variation between the flow angle and freestream velocity for each panel can be obtained. To determine drag force, each panel's lift vector is rotated backwards relative to the freestream direction and integrated as follows:

$$dF = \rho U_\infty \times I dl \sin(\alpha) \quad (3-7)$$

with the drag coefficient being calculated as;

$$C_D = \frac{D}{\frac{1}{2} \rho V^2 S} \quad (3-8)$$

Similar to the lift and drag coefficient, Side force coefficient also obtained by rotating each panel's lift vector in the z-direction with side force coefficient obtained through **(Equation (3-9))**.

$$C_Y = \frac{Y}{\frac{1}{2} \rho V^2 S} \quad (3-9)$$

For moment coefficient, calculated panel lift distributions were multiplied by the moment arm, (which extends in the x direction from the leading edge of the wing) relevant to the bound vortex for the panel. The fundamental moment equations are as follows:

$$C_l = \frac{R}{\frac{1}{2} \rho V^2 S b} \quad (3-10)$$

$$C_m = \frac{M}{\frac{1}{2} \rho V^2 S c} \quad (3-11)$$

$$C_n = \frac{N}{\frac{1}{2} \rho V^2 S b} \quad (3-12)$$

3.2.1 Limitation of the AVL Software

Like any aerodynamic simulation software, AVL also has some restrictions. AVL is best-suited for aerodynamic configurations that involve primarily thin lifting surfaces at small angles of attack and sideslip. These surfaces and their trailing wakes are represented as single-layer vortex sheets, discretised into horseshoe vortex filaments, with trailing legs assumed to be parallel to the x-axis, as described in detail in **Section 3.2** [154]. Due to AVL assuming a quasi-steady flow where unsteady vortices are adequately slow, the given angle of attack needs to be low. Similar to the angle of attack, the angular velocity should also be low. It should be limited to 0.1 in roll (multiplied by the span), 0.03 in pitch (multiplied by the MAC) and 0.25 in yaw (span), for the vortex lattice method to work properly [154].

AVL also offers the capability to design fuselages of a model. The resulting force and moment estimates are reliable with a slender-body concept, but the widespread experience for this purpose limited, citing that the modelling of bodies should be done carefully. If a model's fuselage is expected to have little impact on the aerodynamic loads, it is advised to avoid it from the AVL model [151].

As stated in **Section 3.2**, the force and moments were obtained using the Kutta-Joukowski Law. Before applying this theorem to each vortex, a basic incompressible method is applied to the model. Due to the assumed thin surfaces, linearisation assumes small perturbations and only works well at a Mach numbers up to 0.6. With a Mach greater than $m=0.6$, the AVL predictions become unreliable. These limits are increased if swept wings are used. The range of validity for the AVL calculation is shown in **Figure 3.3** where $1/B$ is a transformation factor and is calculated as follows:

$$\frac{1}{B} = \frac{1}{\sqrt{(1 - m^2)}} \quad (3-13)$$

M	1/B	
0.0	1.000	
0.1	1.005	
0.2	1.021	
0.3	1.048	- PG expected valid
0.4	1.091	
0.5	1.155	
0.6	1.250	
0.7	1.400	PG suspect (transonic flow likely)
0.8	1.667	PG unreliable (transonic flow certain)
0.9	2.294	PG hopeless

Figure 3.3 The range of validity for AVL calculation [153]

Although there are some limitations of the AVL software, it has many advantages. Compared to other CFD software packages, AVL has good agreement between experimental results, as noted by Pereira [154]. In his investigation, four varieties of CFD software packages (AVL, TORNADO, PANAIR, and Preliminary Method) were tested on Boeing 777-300, Boeing 747-100, and Aero Commander 680 Super aircraft types. According to the results, AVL and Tornado provided the most accurate results and almost similar results in most of the cases tested. AVL obtains accurate results for lift coefficient (relative to Tornado), but is limited for drag coefficient. Compared to other CFD software packages, AVL is a fastest analysis tool as well. Considering all these points together AVL was chosen as a CFD simulation tool for this investigation.

3.2.2 Wing and Winglet Geometry

The initial model chosen for this study was a flying wing (**Figure 3.4**). The flying wing is one of the most efficient aerodynamic configurations with low parasitic drag, and up to 30% less total drag. This configuration was also selected in order to make a direct comparison with previous research [114], [131] where swept-back, tailless planes use variable winglets.

To investigate the potential benefits of the morphing concept considered in this thesis. An initial exploratory investigation was conducted on a baseline configuration. This baseline wing configuration (without winglet) comprised a 12% thick, Zagi airfoil section, and 30° leading edge sweep angle, a 1.2m wing span, a 0.33m root

chord, and a 0.185m tip chord, with aspect and tip ratios of 6.19 and 0.47 respectively with an addition of a winglet (0.15m winglet tip chord, and a span of 0.15m) the overall span increased to 1.5m. For this initial investigation, the winglet performance for different winglet configurations (winglet sweep ($-40 < \Lambda < 40$), twist ($-10 < \phi < 10$) and dihedral angle ($-90 < \Gamma < 90$)) was investigated.

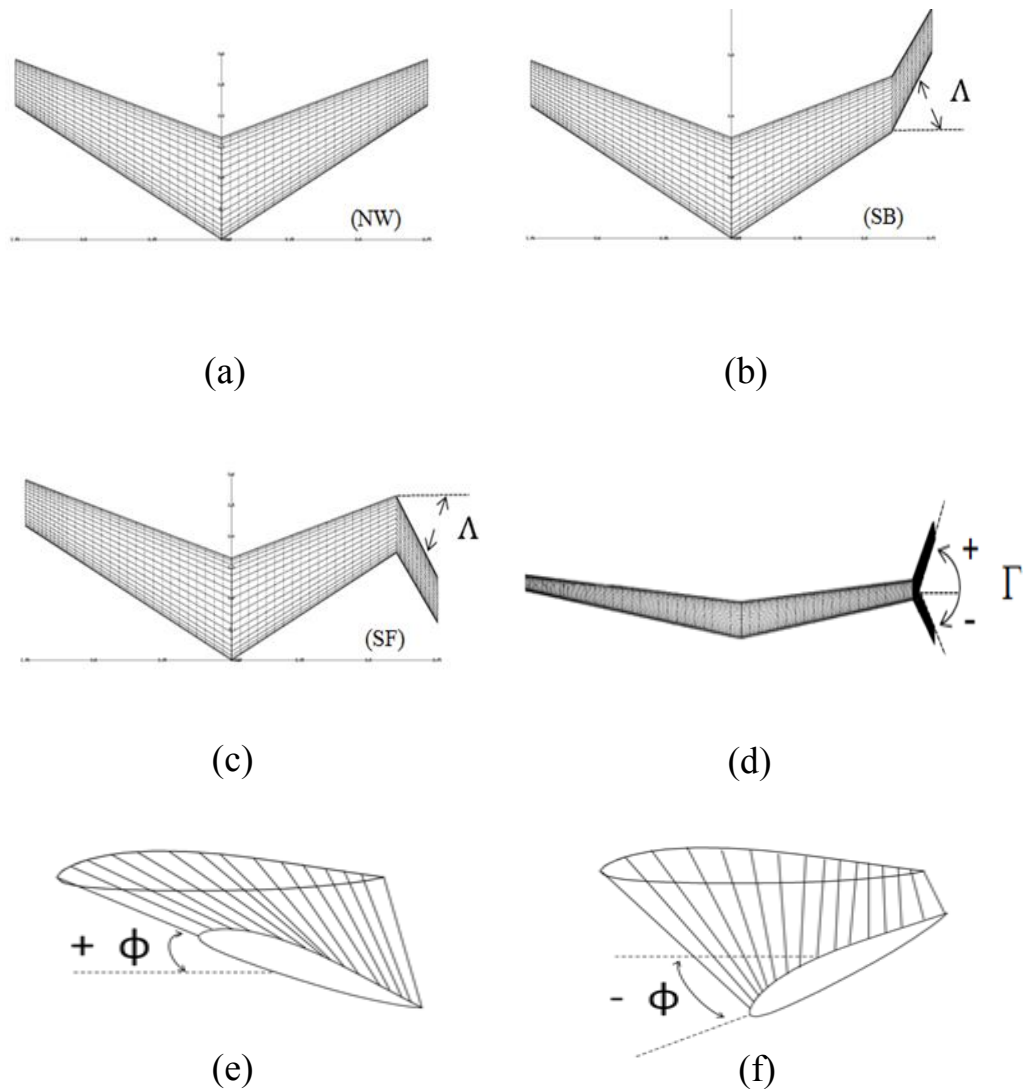


Figure 3.4 Schematic View of Variable Winglet Structures: (a) Normal positioned winglet (NW), (b) swept back winglet (SB), (c) swept forward winglet (SF), (d) winglet dihedral angle (Γ), (e) winglet positive twist angle ($+\phi$), and (f) winglet negative twist angle ($-\phi$).

It should also be noted that for these configurations, a 12% thick Zagi airfoil profile was used (which has a reflexed trailing edge) which provides corrective pitching moments and is designed specifically for tailless aircraft models [155]. Another reason for selecting this model was that comparisons to previous numerical and experimental investigations could be performed.

3.2.3 Panel Size and Grid Refinement Analysis

In order to be computationally efficient, a grid refinement study was performed on the baseline configuration prior to widespread use of the developed model. Grid refinement analysis is a method of defining the best panel size in order to reduce the complexity increase speed of analysis. The findings from the grid refinement study were also used as a guide to define the best structural models of the configuration. Overall, this involved monitoring the coefficient values for several different panel densities. The lift coefficient graph, shown in **Figure 3.5** was found to remain constant after 990 panels.

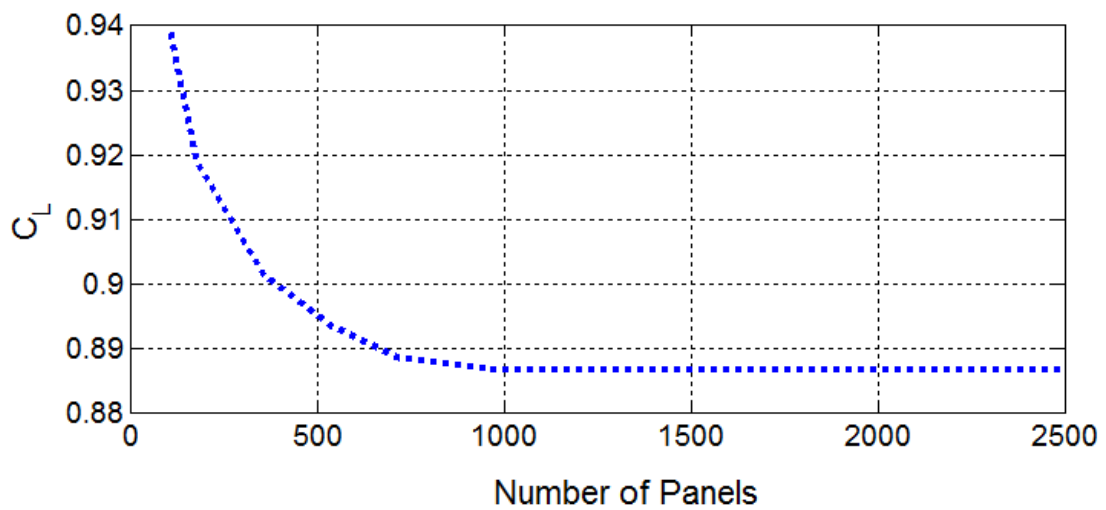


Figure 3.5 Lift Coefficient versus Number of Panels.

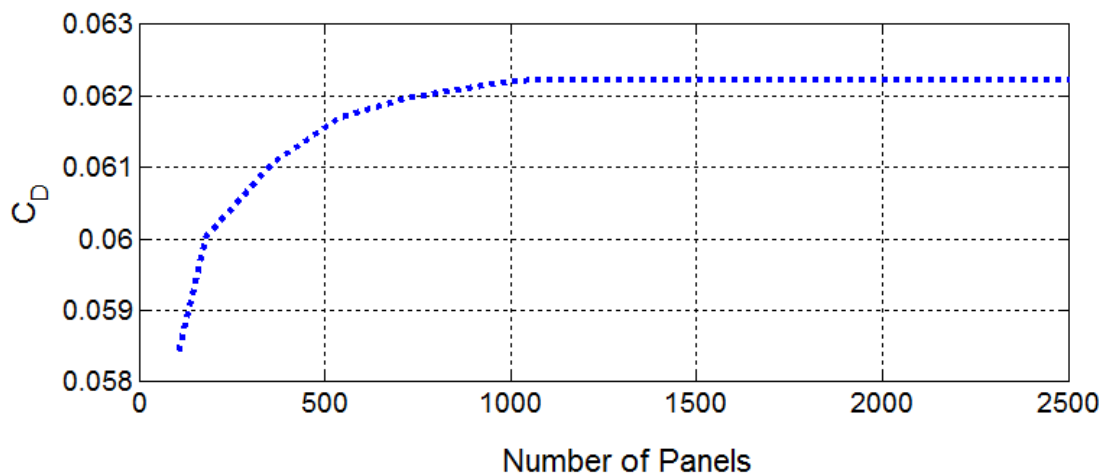


Figure 3.6 Drag Coefficient versus Number of Panels.

In order to check this proposed selection and to obtain the best panel size, drag coefficient results were also simulated (**Figure 3.6**). According to this study, it was found that the drag values became stable after 1044 panels. The maximum value chosen therefore for this study was 1044 panels. Based on these results, all

subsequent computations were based on 18 horseshoe vortices along the wing and winglet chord, and 58 along the semi-span of the baseline wing and winglet (totally 1044 panels).

3.2.4 Uncertainty of AVL Computations

Quantifying uncertainty is important for all simulation environments to gauge the ultimate accuracy of the results. As is well known, concepts of uncertainty can be categorised into three groups. Round-off errors, iterative errors, and discretisation errors. The round-off error arises from the finite precision of the computers, the iterative error is due to the non-linearity of the mathematical equations, and the discretisation error is a consequence of the grid converges. To reduce the error rate, meshing studies are usually performed by the user and involve changing the mesh density as well as the mesh structure. Depending on the fluctuation in the results, uncertainty can be defined as noted in [156], [157]. However, AVL has only one panel structure and therefore here a mesh size study could be completed very quickly. For the investigated wing /winglet cases, tests were performed as indicated in **Section 3.2.3**. It can be seen that little change was found after the 1044 panel size selected, uncertainty can also be estimated. Due to the AVL input file being code-based, inevitably some coordinate numbers are fractional with AVL rounding those coordinates leading to truncation problem. The existing rounding rate is $\pm 0.0005m$ maximum. **Table 1** illustrates the geometry parameter change error rates. It can be seen that each coefficient value has a different uncertainty.

Table 1 Uncertainty Analysis of AVL

Force and Moments	Error Rate for Parameter +0.0005m	Error Rate for Parameter -0.0005m
C_L	-1E-05	0.00034
C_D	-1E-05	1E-05
C_Y	-2E-05	2E-05
C_l	-2E-05	1E-05
C_m	-0.00071	0.0026
C_n	1E-05	-3E-05

3.3 Finite Element Modelling (FEM)

Finite Element Modelling (FEM) was carried out using ANSYS Mechanical and CATIA V5 software packages. The wing structure was modelled in CATIA V5 design software and then imported to the ANSYS software package to evaluate the design structurally and, together with AVL results, investigate further the aerodynamic and structural relationship. The FEM structural model of the wing was also used to assess magnitude of the wing-twist deformation magnitudes for the concept. In order to achieve this, external AVL of aerodynamic loads were applied to this morphing concept. The following sections detail the methodology used for these computations.

3.3.1 ANSYS Structural Mechanics

ANSYS Mechanical is a widespread Finite Element Analysis (FEA) module in the ANSYS software, which provides advanced FEA analysis for complex structural models with dynamic, linear and non-linear studies [158]. It provides accurate results due to the robustness of the solution algorithms. Additionally, it enables users to import files from different CAD environments as well as supporting different file format. This makes ANSYS useful in a range of application areas. ANSYS also has some fundamental solution steps that need to be followed by the user. The basic solution flowcharts are shown in **Figure 3.7**. It can be seen from the flowchart that

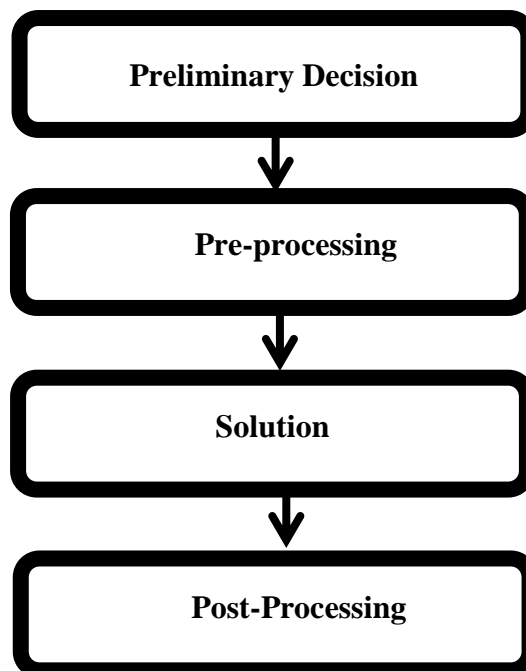


Figure 3.7 Flowchart for ANSYS Mechanical solution steps.

the first step is to decide the simulation environment that is suitable for the model, such as the static structural, rigid body dynamics etc. After deciding on the simulation tool, in the pre-processing stage, the user needs to choose the material properties and the model geometry needs to be attached to a simulation. At this stage, boundary conditions need to be applied such as aero-loads, supports, and contacts. A mesh refinement study also needs to be completed by the user to obtain assess the accuracy of the results. Once all of these required steps have been completed, the third step is to run it and obtain the results.

3.3.2 Wing and Winglet Parameter

The model chosen for this twist demonstration study is shown in **Figure 3.8**. As can be seen that rectangular wing has been initially investigated due to ease implementation compared to a swept wing and winglet geometry. The baseline wing configuration (without winglet) comprised a 12% thick, Zagi airfoil section, no leading edge sweep angle, a 0.330m half wing span, a 0.2m root chord, a 0.2m tip chord, with aspect and tip ratios of 1.65 and 1 respectively. The winglet had a 0.2m winglet tip chord, and a span of 0.15m.

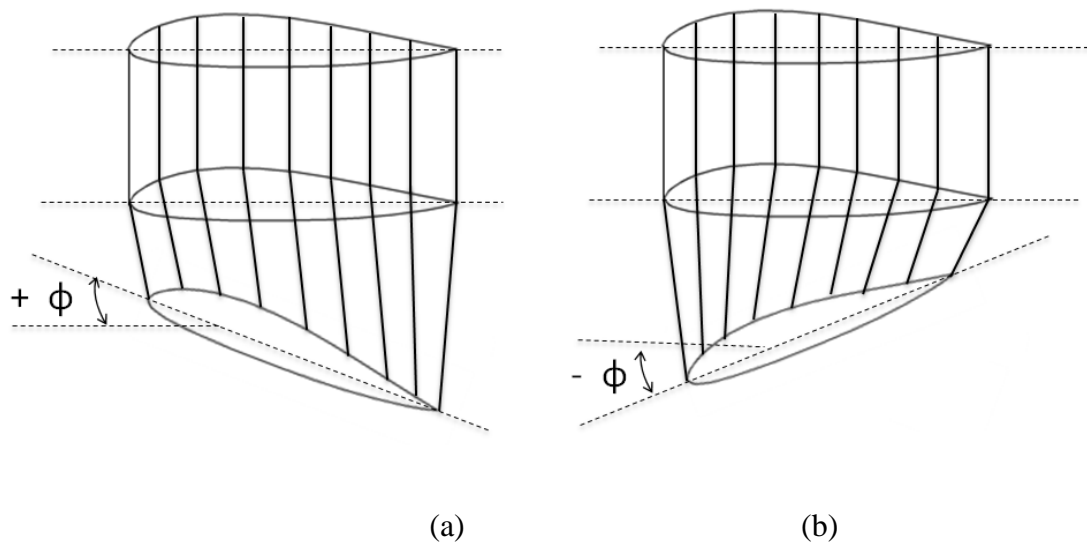


Figure 3.8 Wing and Winglet Parameters: (a)Positive twist(Washin) and (b) Negative twist(Washout)

3.3.3 Aerodynamic Load Prediction

Each surface panel was assigned a single horse-shoe vortex with velocities induced by each vortex evaluated at certain control points using the “Biot-Savart

law”. The forces and moments were obtained from the solved load distribution by applying the “Kutta-Joukowski Theorem” as indicated in **Section 3.2**. For all of the simulations, the free-stream velocity was set to 30 m/s and all of the results were calculated without the influence of compressibility. In order to be computationally efficient, a grid refinement study was performed on the baseline configuration prior to widespread use of the developed model. Subsequent to this activity all computations were thereafter based on 13 horseshoe vortices along the wing and winglet chord, and 58 along the semi-span of the baseline wing and winglet.

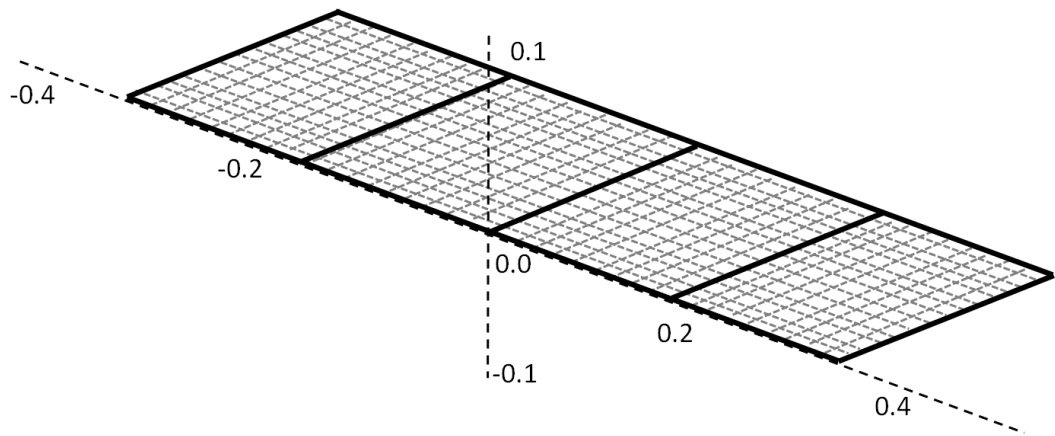


Figure 3.9 Schematic view of wing setup in AVL.

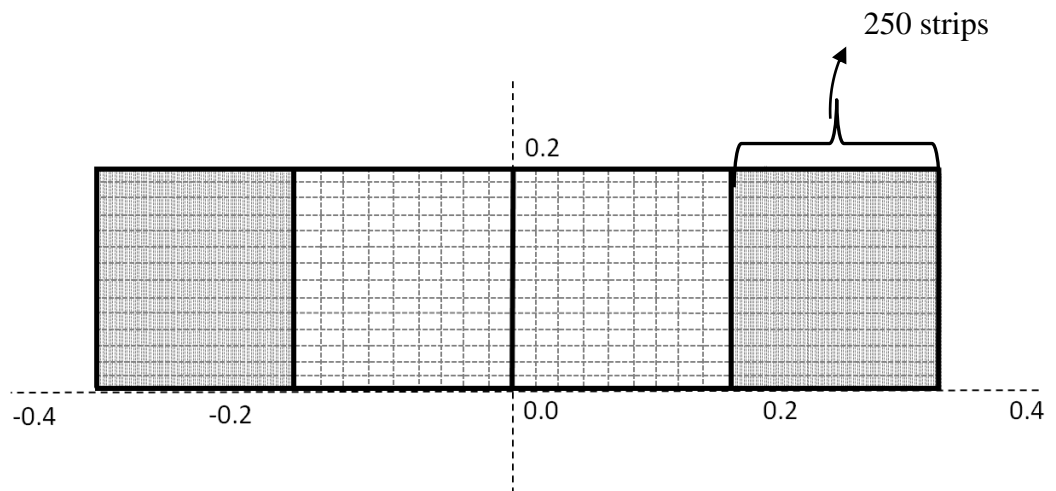


Figure 3.10 Divided strips to obtain the force results for each rib components.

As described in detail in **Section 2.9**, to achieve twist movements, the winglet structure needs to be divided into several ribs. In order to conduct an appropriate analysis of a winglet twist mechanism, the forces acting over each rib need to be examined. To do so, after completion of the grid refinement study, the winglet grids

were divided into 250 strips as shown in **Figure 3.10** and then each strip force was computed using AVL.

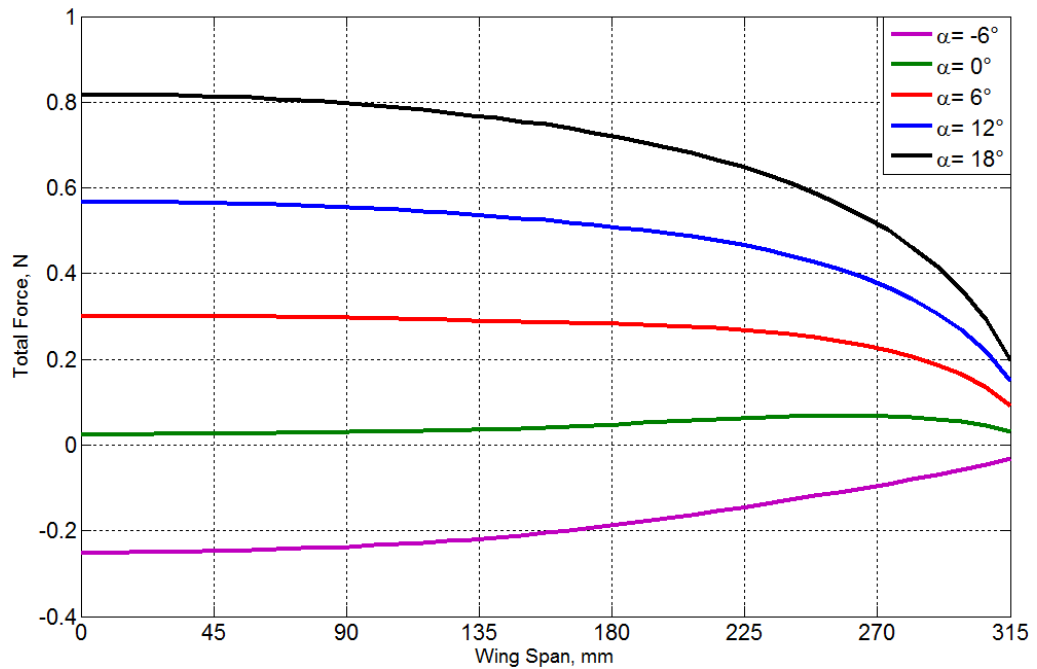


Figure 3.11 Maximum force distribution on wing structure at +10° of twist.

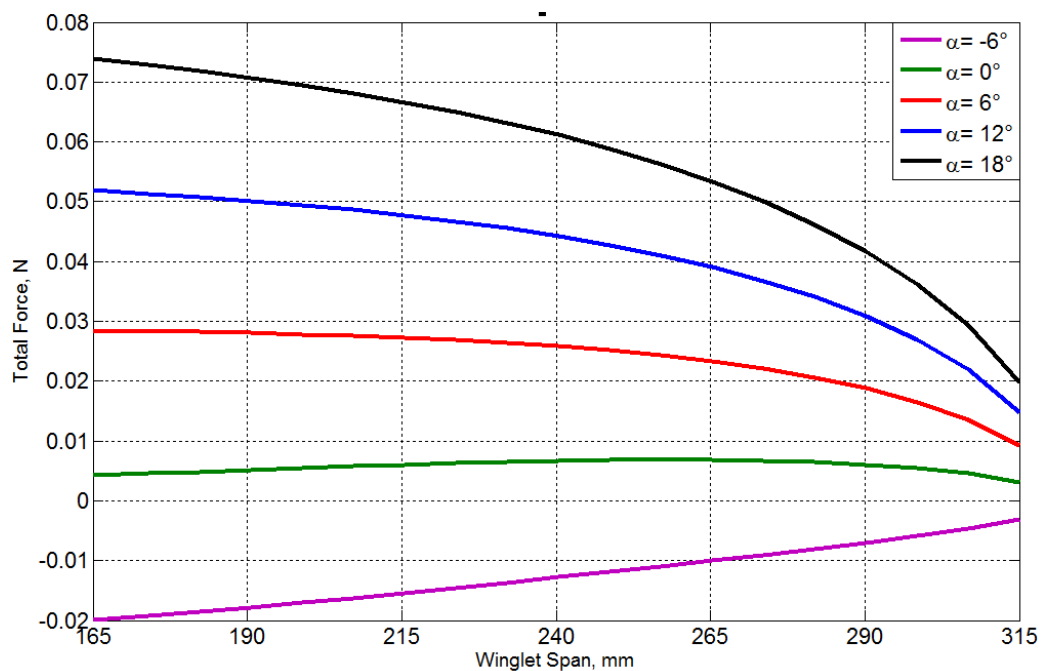


Figure 3.12 Maximum force distribution on winglet structure at +10° of twist.

The overall aerodynamic loads taken from AVL simulation are shown in **Figure 3.11** and **Figure 3.12**. It can be seen that there was a greater tendency for an elliptical load distribution at $\alpha=18^\circ$. This was expected due to the increment in the

angle of attack on the twisted winglets also adding more angles at the tip of the winglet, which tends to be a stall, and the lift distribution over the wing/winglet structures reduces when away from the chord. At the maximum angle of attack, a 165N total force was obtained.

3.3.4 CATIA V5 and ANSYS Static Structure Modelling

The geometric design of the morphing element was performed using CATIA V5. It can be seen from **Figure 2.61** that the morphing structure was split into 250 ribs with each rib assembled with 2 small (2mm diameter) and 1 main carbon (10mm diameter) tube. In order to choose the best carbon rod size, structure testing was performed in ANSYS. A 2mm rod size was found to be the best option for this model (detail analysis shown in **Section 5.3**). To provide the rotation, a fixed end section was also added to the tip of the winglet structure (**Figure 3.13**).

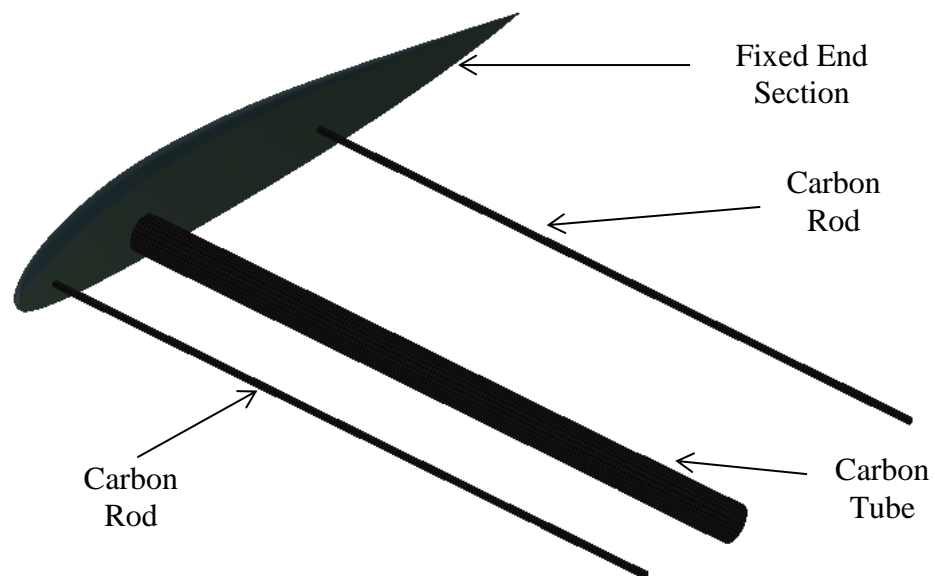


Figure 3.13 The geometric design of a fixed end section.

The boundary conditions for the CATIA simulation were (as shown in **Figure 3.14**) set up after the assembly design. Each rib was started constrained within each other with sliding contacts. Also each rod were assembled to the each rib with sliding contact constrains and to achieve twist movement, fixed contact properties were used between the end section and the carbon rods. Load distribution data obtained from AVL was then applied to each rib. The wing was a clamped at the root

through the two small carbon rods and the first rib. To enact twist deformation on the structure, a pure moment (3.43 Nm) was applied to the main carbon rod.

Initial structure design as well as the initial feasibility of the design was performed in CATIA. As a well-known concept of morphing applications, skin plays a significant role in obtaining a good aerodynamic performance. Therefore, for our concepts it was considered critical that rib thickness is chosen to comply with the boundary layer thickness displacement rule. This initial simulation in CATIA was conducted to choose the best possible rib thickness (detailed expression can be found in **Section 5.3**). Due to the inefficient computational power requirements in CATIA as well as the need to investigate the concepts of adaptable twist winglet movements to greater fidelity, the selected models were further investigated in ANSYS.

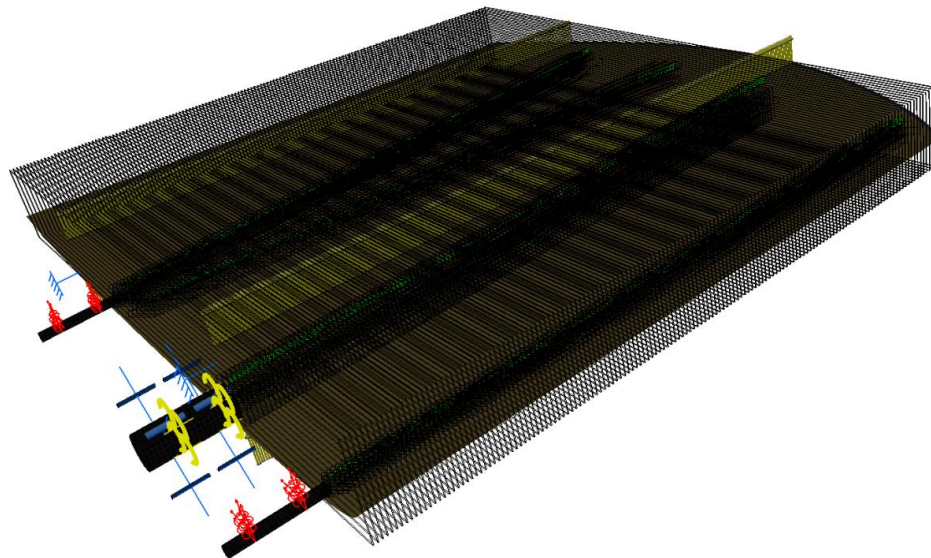


Figure 3.14 CATIA boundary conditions for morphing element.

After geometric modelling was completed, each configuration was imported into the ANSYS Static Structure Module. ANSYS structural software tools automatically detect and performed the setup for contacts between the parts of the assembly. Materials properties were then applied to the geometry. **Table 2** shows the material properties of the morphing components. Laser ply, Carbon Fibre and Raku-Tool WB-1700 were the materials used for the ribs, rods and main torsion tube, with end-bit section(tip) 3D printed.

Table 2 Summary of Material Properties

Materials	Tensile Strength, MPa
Raku-Tool WB-1700	85.00
Laser Ply Sheets	70.93
Carbon Fibre	600.00

Once the geometry and the materials were applied, ribs began to constraint. **Figure 3.15** depicts the boundary conditions applied to the winglet model. For each rib, sliding contact (no separation) properties were used to achieve the twist movements. In these contact properties, separation of the geometries in the contact is not allowed, but small amounts of frictionless sliding can occur along the contact geometries. Also, each rib was connected to the rods via the sliding contact, which provided free rotation during deformation. All three carbon rods were connected to the end section with bonded constraints, which enabled rotation of the end section and subsequent rib twist. In total 960 connections were used. To achieve twist deformation on the structure, 3.43 Nm torque was applied to the main carbon tube. Aerodynamic load was also applied to each rib.

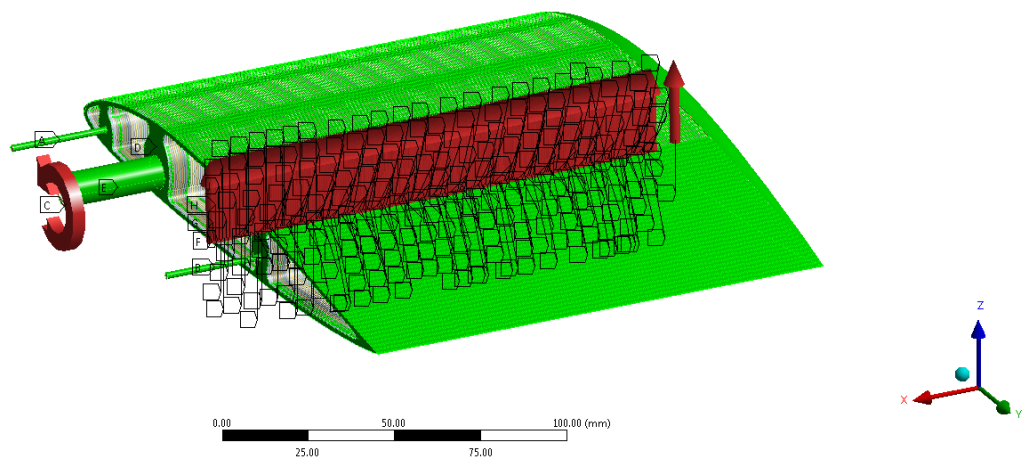


Figure 3.15 Boundary condition applied to a morphing structure.

3.3.5 Meshing Size and Approaches

Having chosen the element types and with the geometry complete, model meshing was performed. Mesh size is critical to achieving adequate and accurate results. ANSYS provides a wide range of highly robust automated meshing tools from tetrahedral meshes to pure hexahedral meshes, inflation layers, and high quality shell meshes.

Unstructured meshes tend to pose accuracy challenges in critical regions such as the boundary layer and typically require significantly more cells than their structured counterparts. Additionally, unstructured meshing is generally not as well suited to moving and/or deforming geometries [159], [160]. Therefore, structured fine meshes used for this analysis. Using structured meshes also provided minimum distortion for the end section solid geometry. An example of the final mesh applied is shown in **Figure 3.16**.



Figure 3.16 Applied appropriate meshing size to morphing elements.

To accomplish an accurate grid size and also to reduce computational memory and time required to run the simulation, a grid refinement study was performed. Various meshing sizes were examined via changing the total element numbers from 100000 to 900000 in steps of 50000 until the results exhibited insensitivity with further modification. Due to the computational memory and time requirements, 570000 elements were chosen as the final mesh size. These test results are illustrated in **Figure 3.17** and **Figure 3.18**.

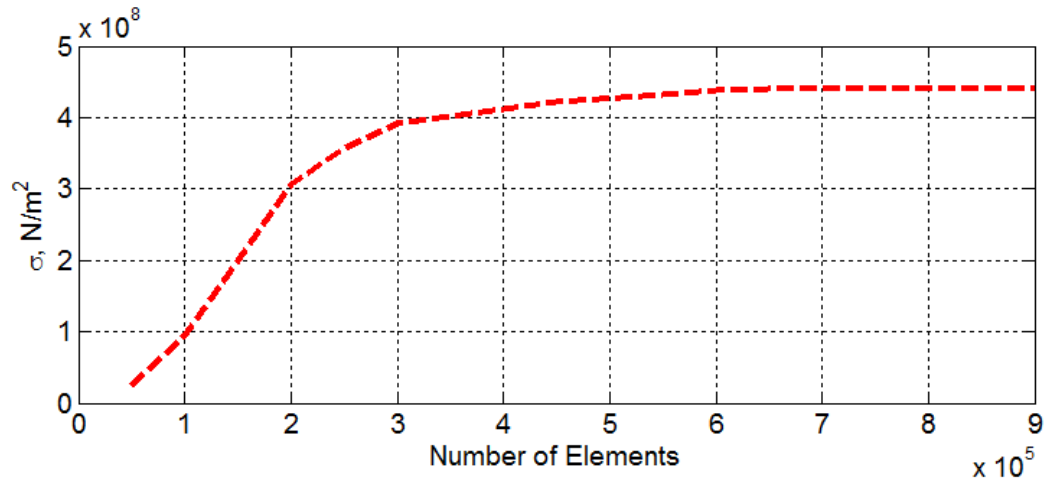


Figure 3.17 Mesh independent results for maximum stress occurred on morphing structure.

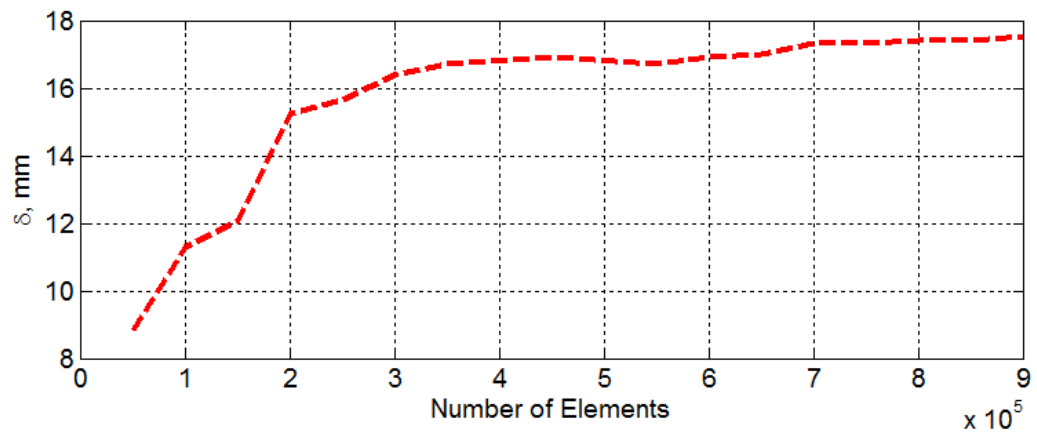


Figure 3.18 Mesh independent results for maximum deformation magnitudes occurred on morphing structure.

3.3.6 Solver Setup

Solver options are other important elements for ANSYS FEA solutions. **Table 3** depicts the ANSYS solver methods for different applications according to DOF (Degree of Freedom) size. The wing model as shown in **Figure 3.16** has up to 30 million DOF when the maximum meshing options are considered, which is too large. According to the design requirements, the sparse solver mention that 1120 MB RAM is needed for an in-core run. As Brunel University’s Cluster has 256 MB RAM and 600 GB disk space, the solver will not have enough core and hard disk space for the calculations. As the model is large, 600 GB disk space may also not be sufficient for the run.

Table 3 ANSYS Solver Options [161]

Solver	Model Size	Memory Use	Disk Use
Frontal Solver (direct elimination solver)	Under 50,000 DOFs	Low	High
Sparse Direct Solver (direct elimination solver)	10,000 to 500,000 DOFs (more for shell & beam models).	Medium	High
PCG Solver (iterative solver)	50,000 to 1,000,000+ DOFs	High	Low
ICCG (Iterative solver)	50,000 to 1,000,000+ DOFs	High	Low
JCG Solver (iterative solver)	50,000 to 1,000,000+ DOFs	Medium	Low

The disadvantages of the out of core run are very slow solution steps, so it is not recommended by ANSYS. One alternative is to use the iterative PCG solver, which requires less RAM. To do so, some commands embedded in an ANSYS input file under the pre-processor stage, will allow running of the model in-core configuration while specifying the memory size.

3.4 Computational Analysis of Prototype Model for Flight Testing

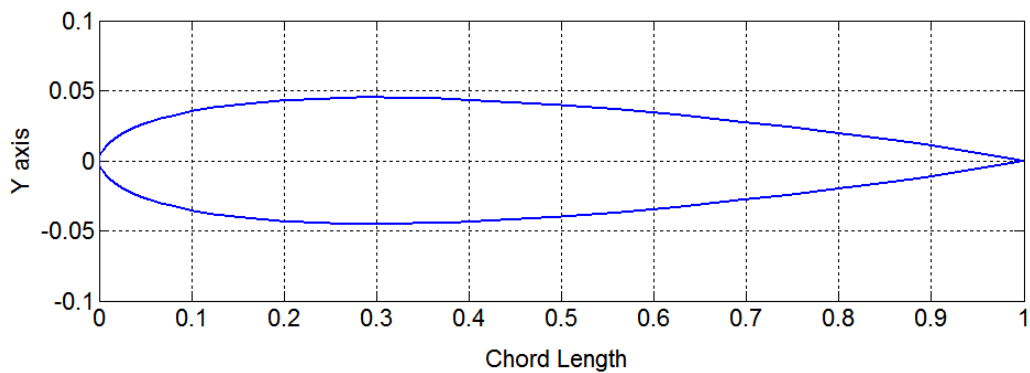
To validate the concept in a real flight environment, computational modelling also initially performed on the concept to evaluate possible performance metrics for a remote controlled aircraft. In this section, the design and analysis of the retro-fitted wings is described. Structural Modelling was carried out in ANSYS with aerodynamic load analysis performed by AVL.

3.4.1 Wing Geometry

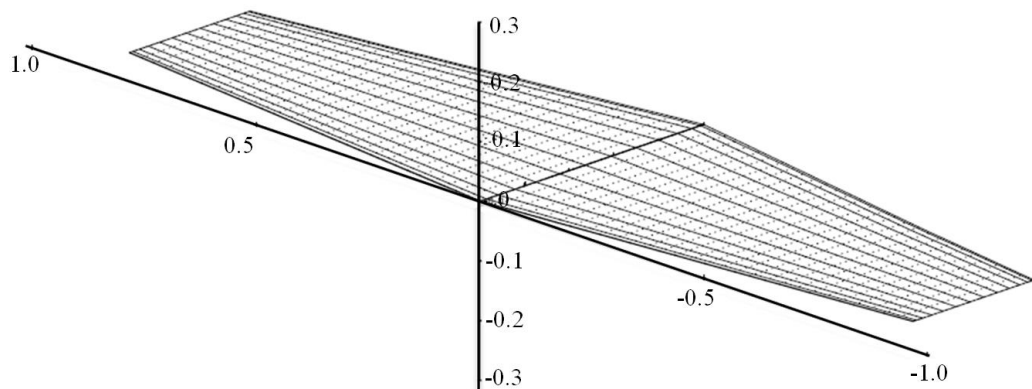
Within the final stages of the project, an Extreme flight Extra 300 with a 78-inch wingspan (**Figure 3.19 (a)**) was used as a testbed for the concept. The baseline wing for this aircraft comprised a proprietary airfoil section (**Figure 3.19(b)**), a 2.5° leading edge sweep, 1.980m wing span, a 0.5m root chord, a 0.27m tip chord, with aspect and tip ratios of 5.45 and 0.54 respectively. The fuselage was 1.930m long and the maximum thickness was 0.230 m. For this validation phase, the concept was 0.3m in span.

3.4.2 Aerodynamic Analysis of the RC Configuration

The aerodynamic loads acting on the RC prototype were calculated using AVL, as described in detail in **Section 3.2**. As no commercially data were available for the wing model's airfoil shape, airfoil sections coordinates were measured directly. The final section measured is shown in **Figure 3.19 (a)**. It can be seen that this was symmetrical airfoil which typically allows this plane type (aerobatic) to have similar performance whether upside down or right side up. To analyse the aerodynamic behaviour, XFLR software was used over sectional Reynolds numbers ranging from 10000 to 1000000. As can be seen from the results (**APPENDIX-A Figure A- 1** and **Figure A- 2**), the airfoil provided adequate lift production with a zero-lift drag coefficient of $C_{D=0.017}$. **Figure 3.19 (a)** illustrates the computational modelling of a completed wing configuration. For all of the simulations, the freestream velocity was set to



(a)



(b)

Figure 3.19 RC plane analysis: (a) Airfoil shape and (b) Schematic View of Wing Structures in AVL.

30m/s and all of the results were calculated without the influence of compressibility. As has been mentioned in previous sections, grid refinement study was also performed on the baseline configuration prior to widespread use of the developed model. Subsequent to this activity all of the computations were thereafter based on 20 horseshoe vortices along the wing and winglet chord, and 76 along the semi-span of the baseline wing and winglet. The lift force distribution versus angle of attack change is shown in **Figure 3.20** . According to the results, 250 N total forces were computed on the half-wing configuration.

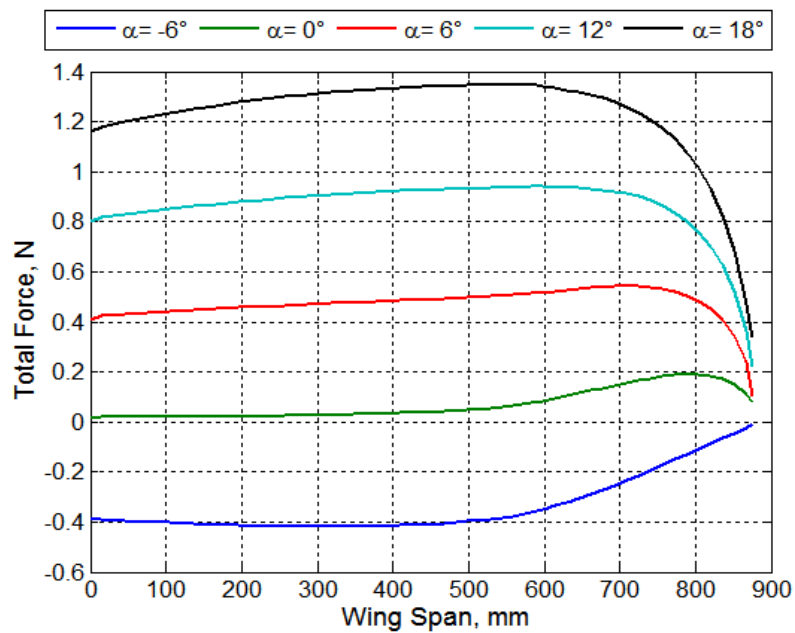


Figure 3.20 Aero load on wing structure.

3.4.3 Computer Aided Design (CAD) of RC Wing Prototype

The CAD modelling of the prototype wing is shown in **Figure 3.21**. In order to be computationally efficient as well as to reduce time, initially only the twistable wing section was considered as an ANSYS model. Due the weight requirements for an actual flight model, balsa wood sheets were used to construct the ribs (further described in **CHAPTER 5**). The final model consisted of 365 balsa wood ribs and eight small carbon rods (0.5mm diameter) distributed along the wing span. These rods produced an aerodynamically smooth surface while allowing wing twist with sufficient structural rigidity in bending. Two 1.5mm diameter carbon rods were also used at the origin of the wing chord. They provided durability to the wing structure and alignment together with the main carbon tube.

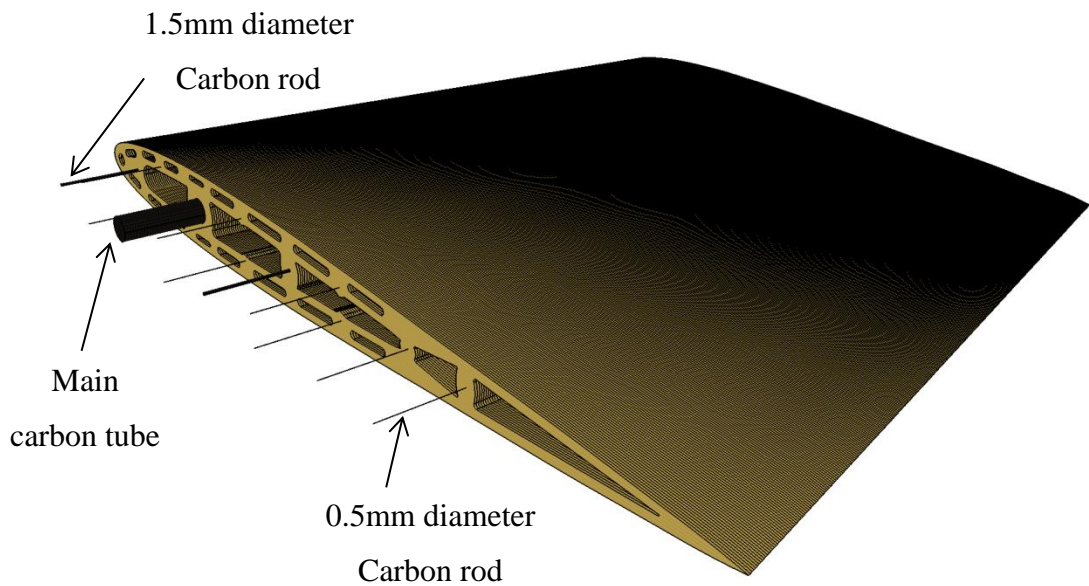


Figure 3.21 CAD for Extra300 Wing Twist Section.

3.4.4 Finite Element Modelling

For this prototype wing, a computational simulation was carried with ANSYS Structural Mechanics. In ANSYS, the winglet modelling was imported from the CatiaV5 CAD software with the constraints and connections as well as material properties and force acting on the wing structure (determined from AVL) was applied. **Table 4** shows the material properties of the morphing components.

Table 4 Summary of Material Properties

Materials	Tensile Strength, MPa
P400 ABS	56.58
Balsa Wood Sheets	30.00
Carbon Fibre	600.00

Figure 3.22 depicts the boundary conditions applied to the prototype wing model. For each rib, sliding contact properties were used to achieve twist movements. Also, each rib was connected to the rods via the sliding contact, which

provided free rotation during deformation. All of the carbon rods and the tube were connected to the end bits with bonded constraints. In total 4731 connections were

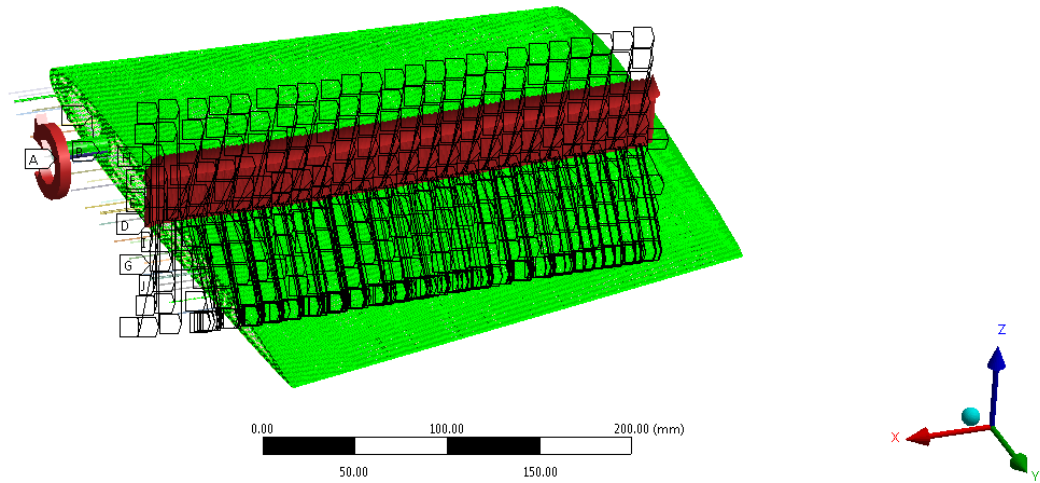
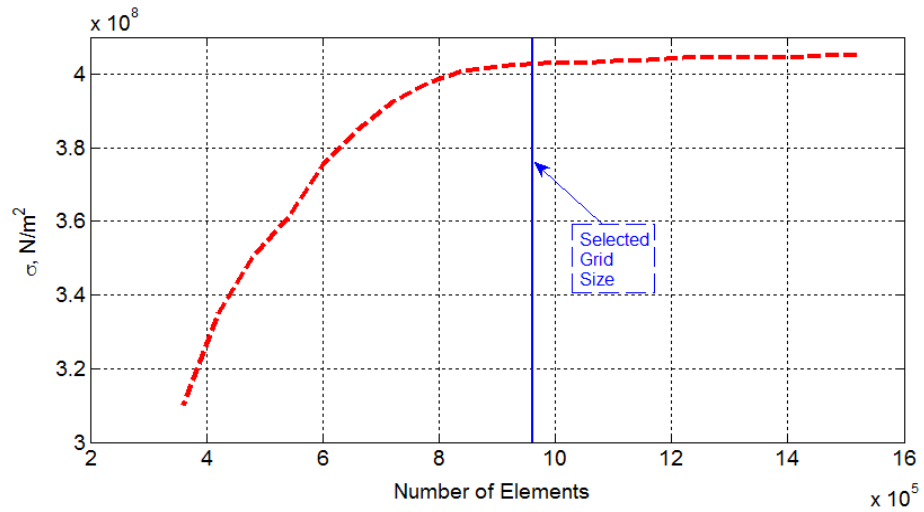


Figure 3.22 Load Applied the wing structure.

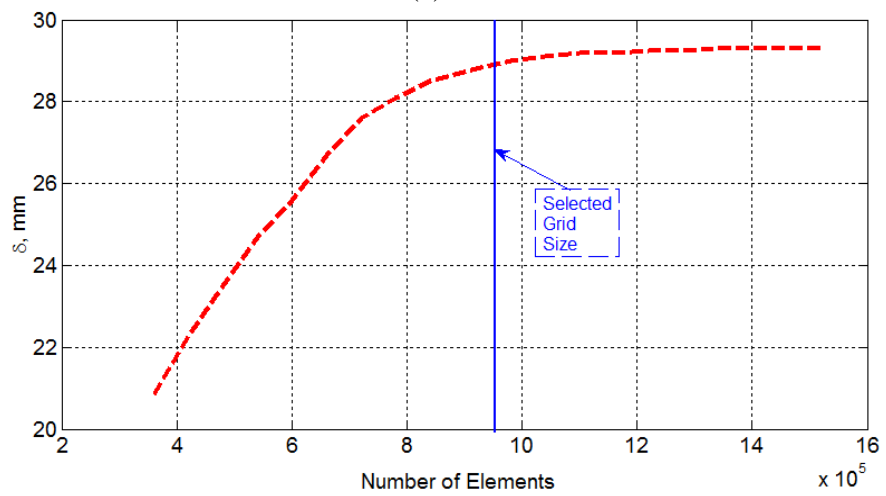
used. The first rib was clamped and a fixed support was also applied to the protruding carbon rods at the root. To achieve twist deformation, frictionless support was used for the carbon tube with 3.43 Nm of torque was applied. Aerodynamic load (total for complete structure = 80N) was applied to each rib from segmented data obtained from AVL (**Figure 3.20**). A pitching moment (5 Nm) was also added to accurately model the wing structure.

Structurally fine meshes were used for this analysis due to the need for accurate stress and deformation analysis. Only for the small carbon rods used were body size meshing options applied. This gives more accurate results for small surfaces and prevents over-meshing, which requires more computational power. A convergence study using a section of the wing was also performed to assess the suitability of the finite element model mesh (shown in **Figure 3.23 (a)** and **(b)**). Prior to this mesh refinement study, a different number of elements were applied to the wing structure (without applying any load factors) until the results revealed insensitivity with further modification. Although the result seemed to become insensitive after 1060000 elements, when the load factor was included in the structure, it was not possible to run the FEA simulation due to the computational memory requirements

of Brunel University Cluster's account, therefore a grid size of 950000 was selected. The final meshed structure is shown in **Figure 3.24**.



(a)



(b)

Figure 3.23 Mesh Refinement Test for RC Plane Wing: (a) Von-Mises Stress and (b) Deformation Magnitude with different number of elements.

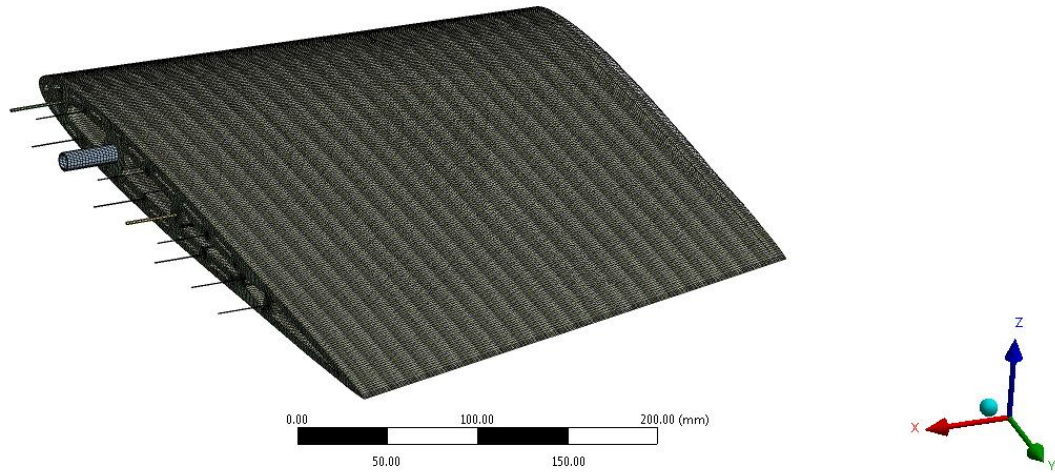


Figure 3.24 Final Mesh for Wing Structure.

3.5 Summary

This section presented the computational setups and methodologies used for the various phases of the development. A brief introduction to how the Vortex Lattice Method works in AVL together with information regarding FEA was provided. Both wind tunnel model and prototype model FEA analysis setup were also be described in detail. The results obtained from these computational studies will enable to compare with the experimental models. Description of the mesh refinement studies for each software element application (AVL and ANSYS Mechanical) was also presented and a Basic uncertainty analysis for the numerical design (AVL) was also provided.

CHAPTER 4 EXPERIMENTAL SETUPS AND METHODOLOGIES

4.1 Introduction

This chapter describes the experimental designs and methodologies used to construct the morphing concept developed. In sequence, **Section 4.2** describes the CAD design and manufacturing processes for the wind tunnel test model. Justification regarding to model length used for this study was also be described. In order to make a direct comparison and further validate the morphing concept and a traditional aileron system for roll control, six different ailerons ($\pm 10^\circ$, $\pm 20^\circ$ and $\pm 30^\circ$) was designed and manufactured. **Section 4.3** provides necessary information regarding the experimental procedure, instrumentation, calculation, calibration and uncertainty analysis and with **Section 4.4** detailing the development of the flying RC prototype construction and instrumentation used. Also, morphing twist system was presented and described in detail. A brief summary (**Section 4.5**) thereafter concludes this chapter.

4.2 Wind Tunnel Model Design and Manufacturing

For the design and development of the morphing concept, CATIA and ANSYS software packages were used. Depending on the configuration selected, structure weight, deflection magnitudes, skin deformation levels, and overall stresses were used in this section. The following sections provide details of these elements together in the design and integration of actuation mechanisms.

4.2.1 Computer Aided Design (CAD) and Analysis

CAD design was carried out using the CATIA V5. Initially, an appropriate wind tunnel model designed (**Figure 4.1**) to test the validity of the concept. According to standard wind tunnel blockage requirements where the wing is sized to span 70-75% wind tunnel cross sectional width(wind tunnel width= 0.457m) [162], a wing span of 315 mm was used. For simplicity and ease of manufacture and built, a straight wing

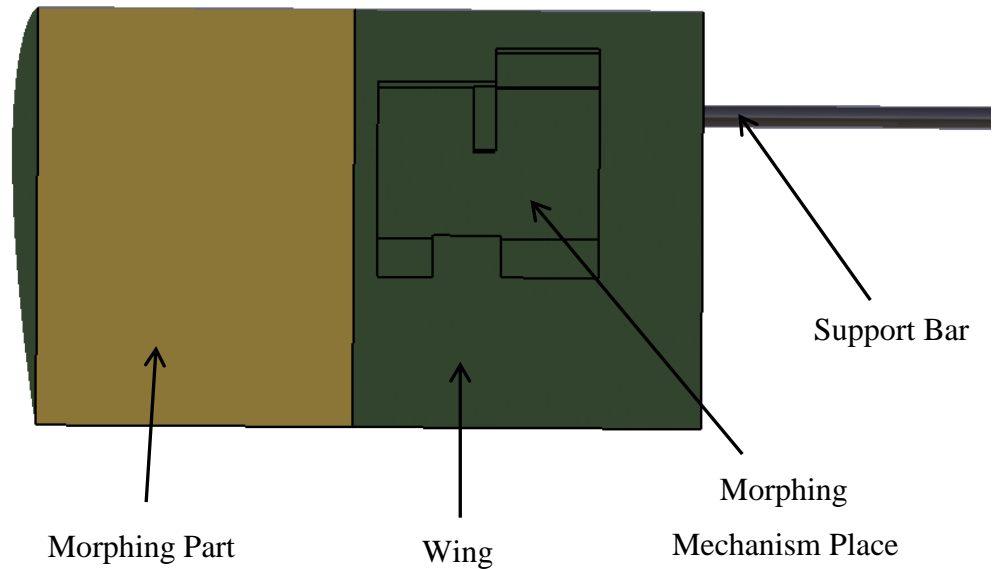


Figure 4.1 Wind Tunnel Model.

profile was chosen for this wind tunnel test prototype to validate the developed concept. Overall, this baseline wing configuration (without winglet) comprised a 12% thick, Zagi airfoil section, no leading edge sweep angle, a 0.165m semi-span, a 0.2m constant chord, with aspect ratios of 1.58. The morphing element also comprised the same airfoil section and subtended a span of 0.15m. In order to compare results to a baseline configuration (no morphing), another full wing was manufactured with a total span of 315mm as shown in **Figure 4.4 (b)**. To ensure these models could stand applied aerodynamic loads, a stress analysis was performed in CATIA V5 software package. For this analysis, the wing root was clamped and aerodynamic loads (total 165N obtained from the AVL simulation (as indicated in **Section 3.3.3, Figure 3.12**)) were distributed along the complete wing structure. **Figure 4.2** shows the results, it can be seen that the maximum stress was seen at the lower edge resulting in $\sigma = 1.14e+007 \text{ N/m}^2$ (**Figure 4.2 (a)**). As the wing material (Raku-tool wb1700) could carry stresses up-to $8.5e+007 \text{ N/m}^2$ before failure, the design was used. For maximum displacement, a maximum of 1.98mm deformation was obtained at the tip of the wing (**Figure 4.2 (b)**).

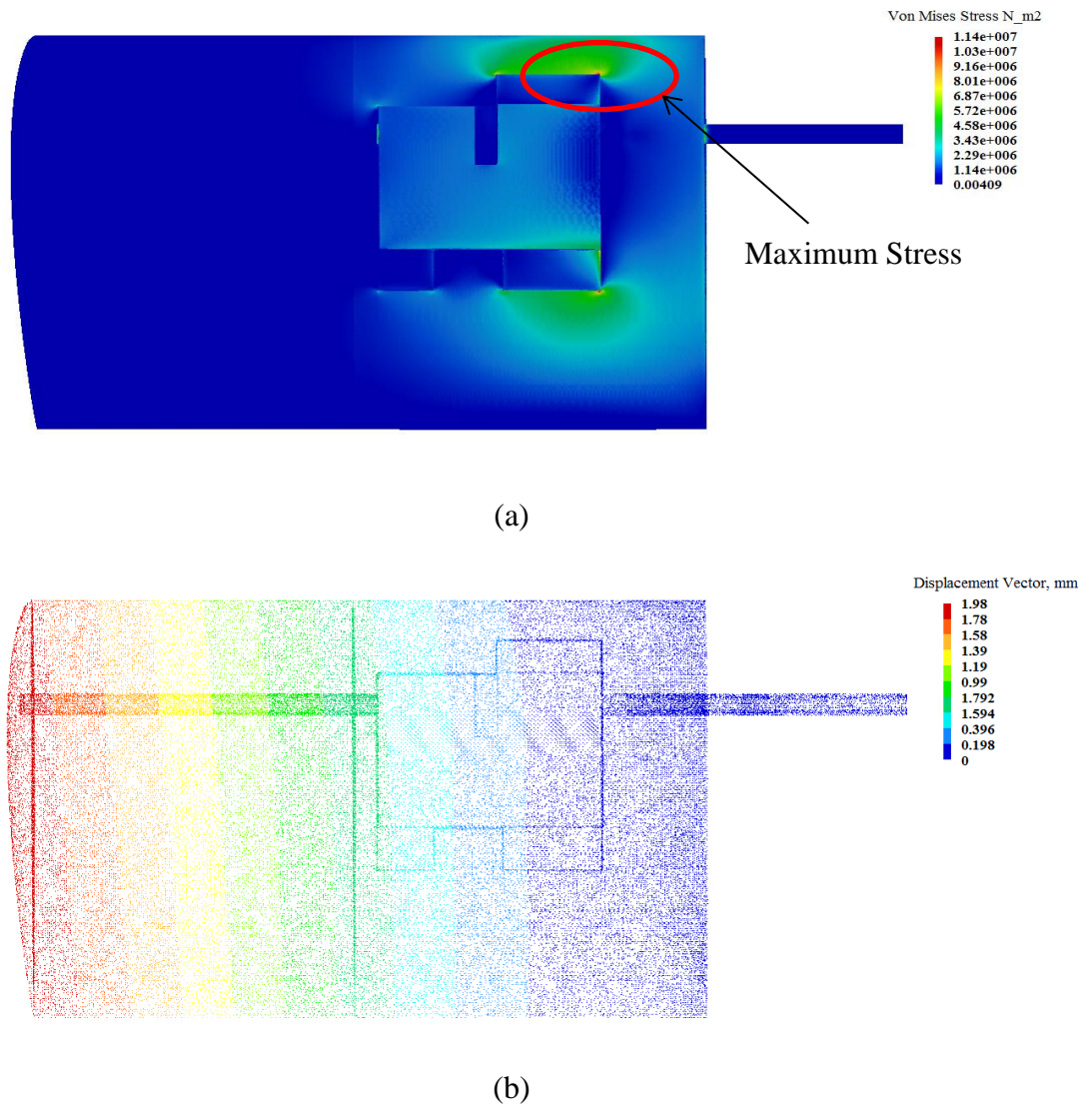


Figure 4.2 Structure Analysis of a wing: (a) Von-Mises Stress analysis of a wing under aerodynamic load and (b) Displacement vector of a wing under aerodynamic load.

4.2.2 Wind Tunnel Test Model and Twist Mechanism

As stated previously in **Section 2.9**, the morphing concept consists of several rib elements with the complete structure actuated by a servo motor and torque tube to create a twist distribution. **Figure 4.3** illustrates the design for this actuation mechanism. It can be seen that the servo was placed inside of an evacuated wing section and then fixed in place with additional screws.

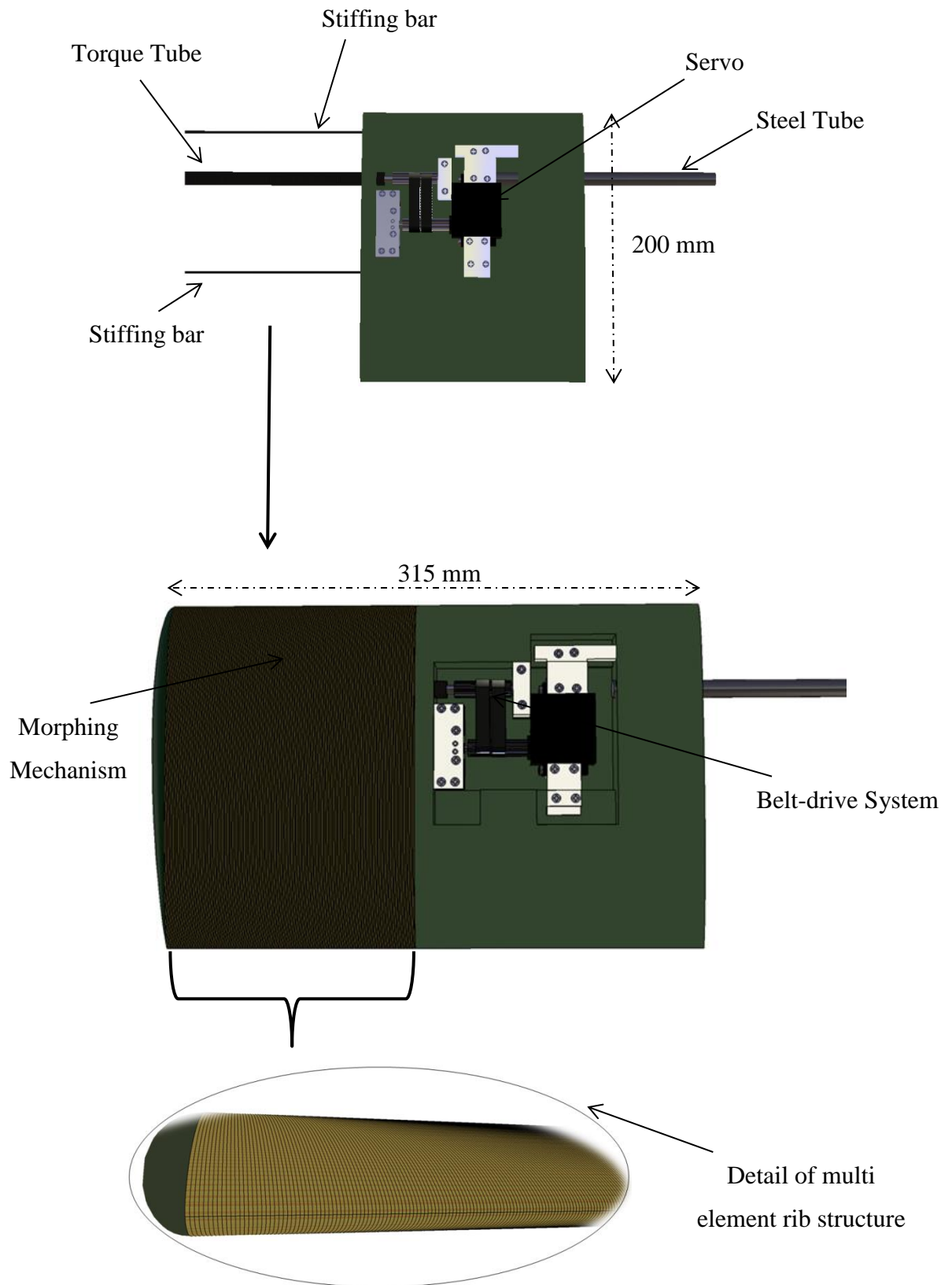
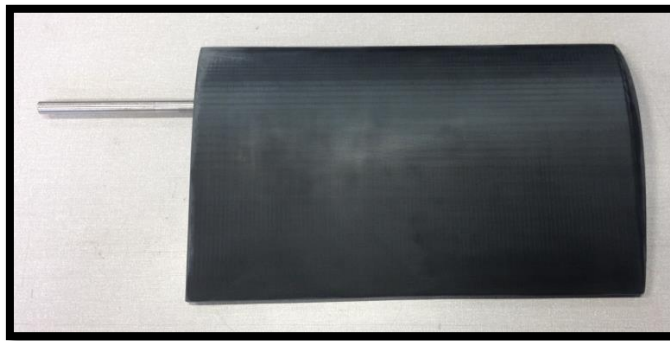


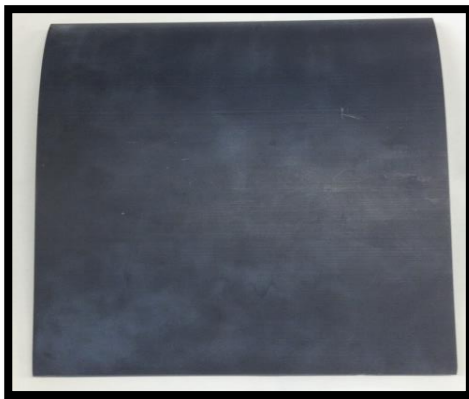
Figure 4.3 Design of a Morphing Twist Mechanism.



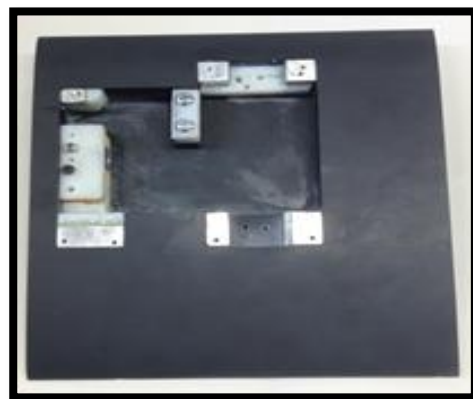
(a)



(b)



(c)



(d)

Figure 4.4 Manufacture of Raku-Tool WB-1700 Wing: (a) Wing manufacturing process, (b) Fixed baseline model for comparison, (c) Half wing profile, and (d) Removed bottom section of the wing and installed parts.

Figure 4.4 shows the morphing wing being manufactured. It can be seen that a rectangular wing platform was used as an experimental model. This wing model (made of Raku-Tool WB-1700) (**Figure 4.4 (c)**) was manufactured in the school's workshop using the Roland Modela Pro II MDX-540 Subtractive Rapid Prototyping (SRP) device machine.

The morphing actuation mechanism was critical for the concept to work adequately. It is also had to be integrated into the model seamlessly to minimise drag. Once the mechanism is working, the vibration needs to be minimal in order to achieve accurate system performance. To accommodate this system, a part of the bottom section of the wing was removed and an internal mechanism installed inside the wing. Some support parts were used to provide adequate housing support for the mechanism as is shown in **Figure 4.4 (d)**. The Carbon Fibre Torsion Tube was fixed to the main wing before installing the mechanism (**Figure 4.5**). On the other side of the carbon tube, an end support was fitted.

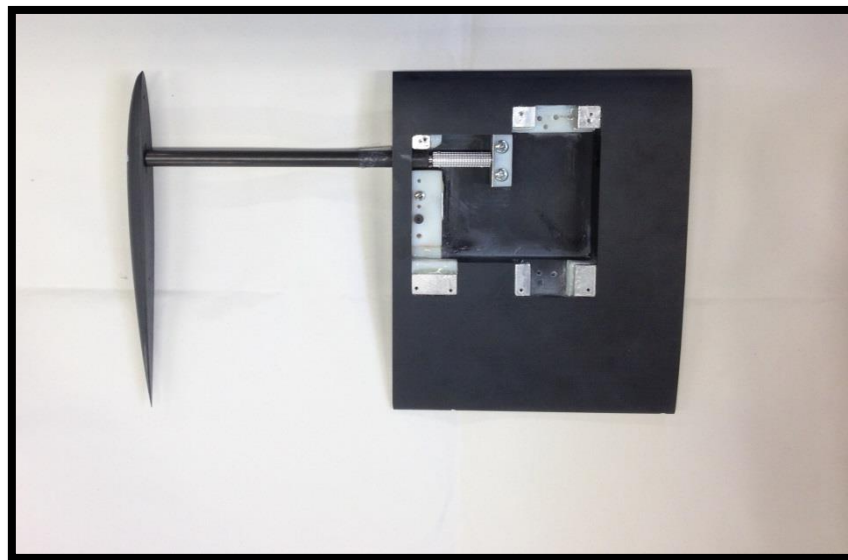


Figure 4.5 Wing and glued carbon fibre tube.

As stated in **Section 2.9**, to achieve the seamless twist, desired 239 ribs were used. ANSYS Mechanical tool was used for optimising the structure. **Figure 4.6** illustrates the morphing mechanism that was placed inside the wing profile. The twist mechanism encompassed one Hitec HS-7950 TH high voltage torque servo, which was a titanium gear coreless servo. It is rated at 3.43 N-m torque at 7.4 Volts, and was retrofitted with a belt drive system operating with a 1:1 gear ratio to rotate

the shaft, which was positioned at the quarter chord of the overall wing. When the servo torque was applied to this shaft to end-support would enact twist. A belt tensioning system was also set up inside the wing profile to allow belt tension adjustment. The system consisted of the ABS plastic boxes, which were glued to the bottom side of the wing and the top side of the system was free to slide and tension the belt. On this top surface, a bearing was used with a servo shaft connected to provide alignment and support structural bending. Once the belt system was tensioned, the top surface (plate) was screwed to the bottom side to maintain the aerodynamic shape.

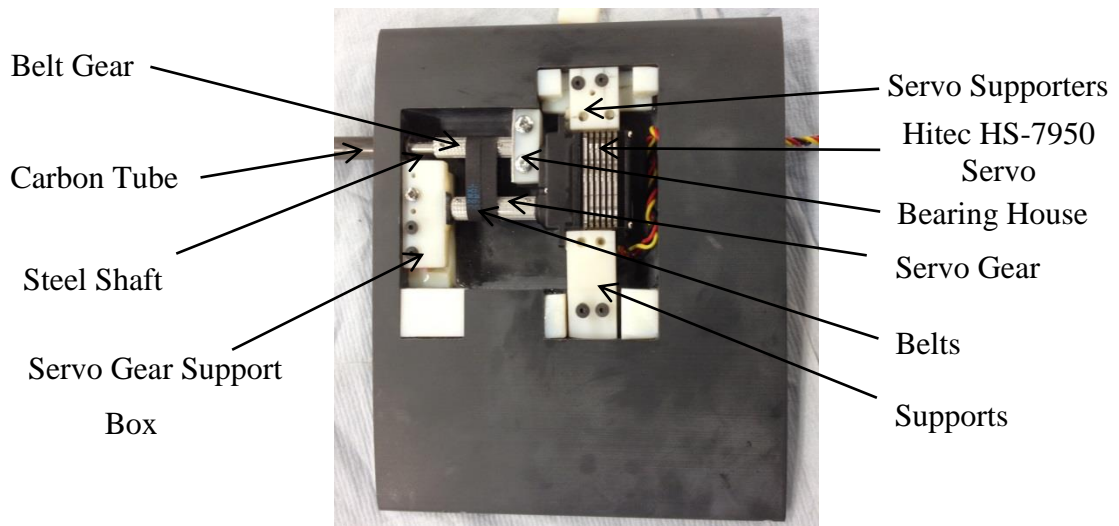


Figure 4.6 Morphing Twist Mechanism.

Similar to that described above, the shaft and the belt gear arrangement was also connected to a second bearing, which was positioned inside the ABS plastic support (Bearing House). This provided the rotation support and prevented any bending due to the applied actuated servo moment. Space was also left inside the wing section for the servo cable to exit the wind tunnel support and connect to the driving electronics. Additionally, in order to reduce vibration, additional support boxes were also fastened and glued to the inside of the wing profile to further support the servo as well as the gears.

Figure 4.7 illustrates the internal shaft mechanism and its connection to the end-section part. As can be seen the gear was fixed to one side of the steel rod with the other end of the rod connected to the end-section using an attachment pin. Through the belt drive system, the belt activates the end-section to create the twist motion. To

align the steel rod within the torsion tube and to minimise misalignment, inside the carbon tube, 3 bearings were positioned along the steel rod length.

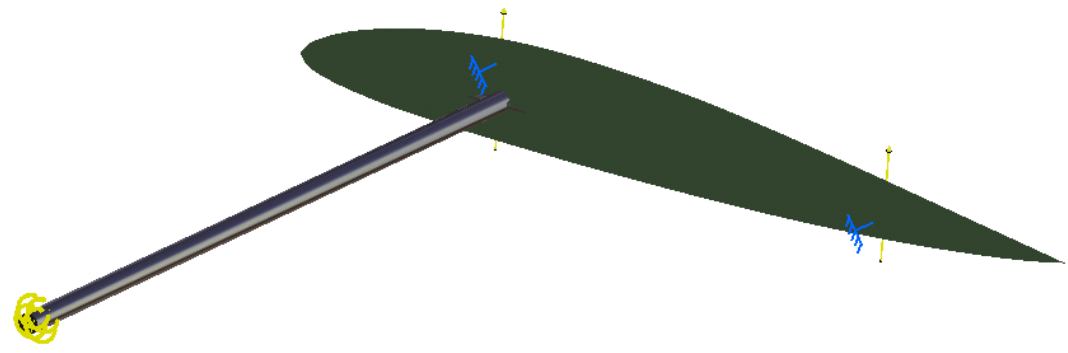


Figure 4.7 End-section and its mechanism.

To ensure that the end-section assembly could stand the high torque moments, structure testing was also done in CATIA V5. For these tests, the end-section was clamped and a torque applied to the steel bar (3.43 N-m). The results (**Figure 4.8 (b)**) indicated a maximum stress of $3.61e+008N/m^2$, which were below the tensile strength of the material ($4.0e+008N/m^2$).

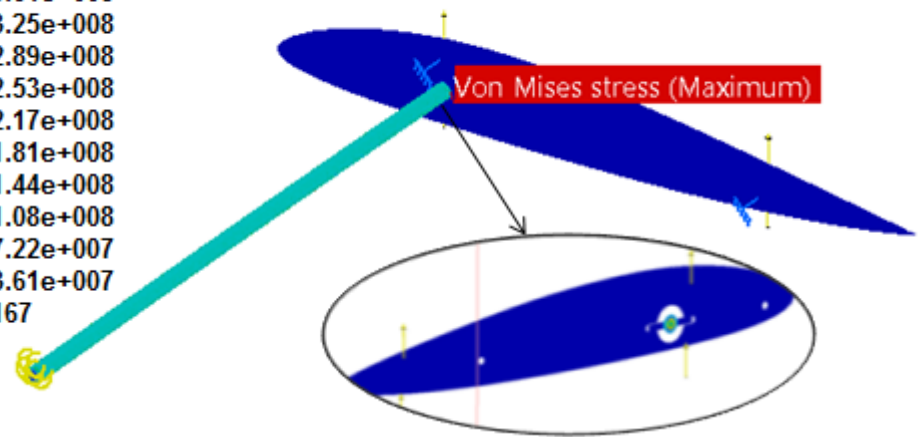
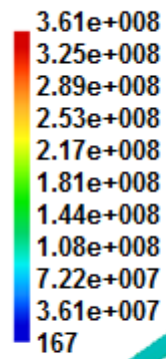
For the morphing section each of the 239 ribs were made from 0.6mm thick laser plywood sheet. For the combined morphing structure, CAD designs (CATIA V5) was imported into ANSYS to analyse structural performance to ensure it could withstand the required aerodynamic loads. Several rib designs and configurations were tested. After these exploratory investigations, it was decided that 2 carbon rods and one carbon tube would provide satisfactory stiffness to the concept. These lightweight and strong carbon fibre rods were both glued and screwed to the main wing. The torsion tube, which was a 10 mm diameter pultruded carbon fibre tube, was also glued to the wing **Figure 4.10 (a)**.

Traditionally, it has been difficult to develop a wing twist system that allows twist while maintaining a rigid aerodynamic surface to minimise the drag penalty, so after some initial quantitative inspection tests, surface deformation was found to be minimal using a 2mm edge thick (t) rib. This was chosen initially as the first point to manufacture and test.



(a)

Von Mises Stress N_m2

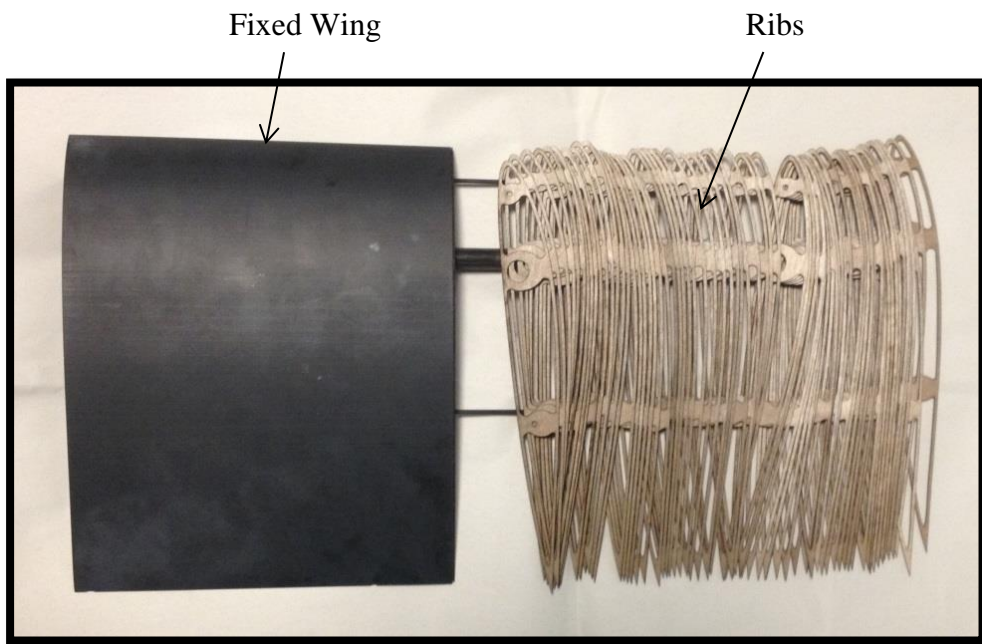


(b)

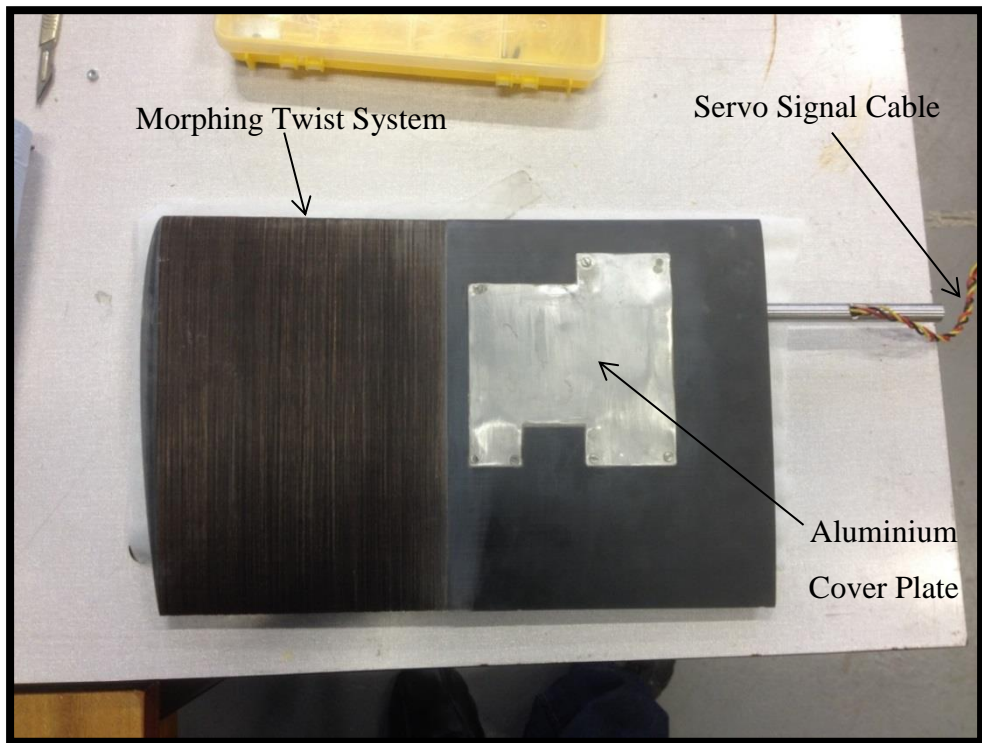
Figure 4.8 End-section structure stress analysis: (a) CAD modelling and (b) Stress result.



Figure 4.9 Laser Cutting Machine.



(a)



(b)

Figure 4.10 Morphing element construction: (a) assembly process for rib structures and (b) completed wing structure and aluminium cover for mechanism.

After installing the twist mechanism (inside wing section), the ribs were cut using a Laser Cutting Machine as illustrated in **Figure 4.9**. The parts were then assembled (the assembly process for rib structures is shown in **Figure 4.10 (a)**) and the end-section was mounted and screwed with nuts and grub screws. Cavities were filled and sanded to create an aerodynamically smooth surface finish. After assembly, the top and bottom sections of the rib surfaces were sanded in situ to ensure a smooth, aerodynamically clear surface (shown in **Figure 4.10 (b)**). The completed wing internal mechanism is indicated in **Figure 4.11**.

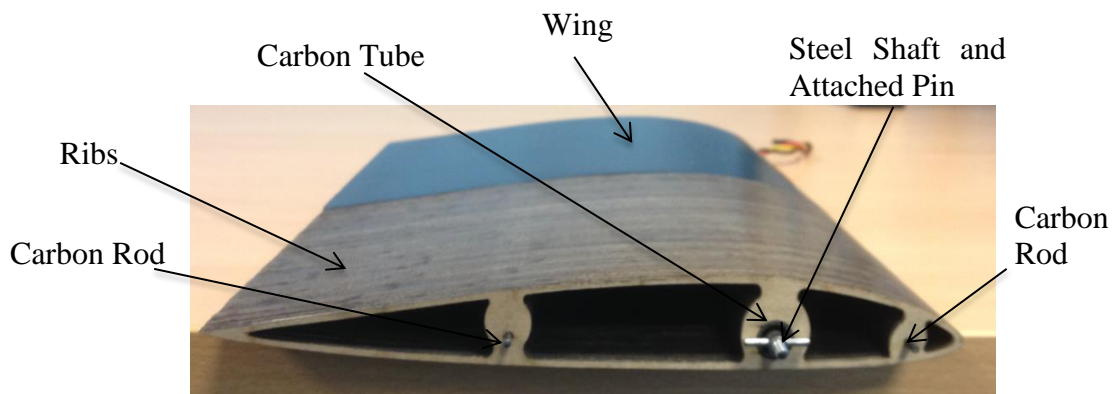
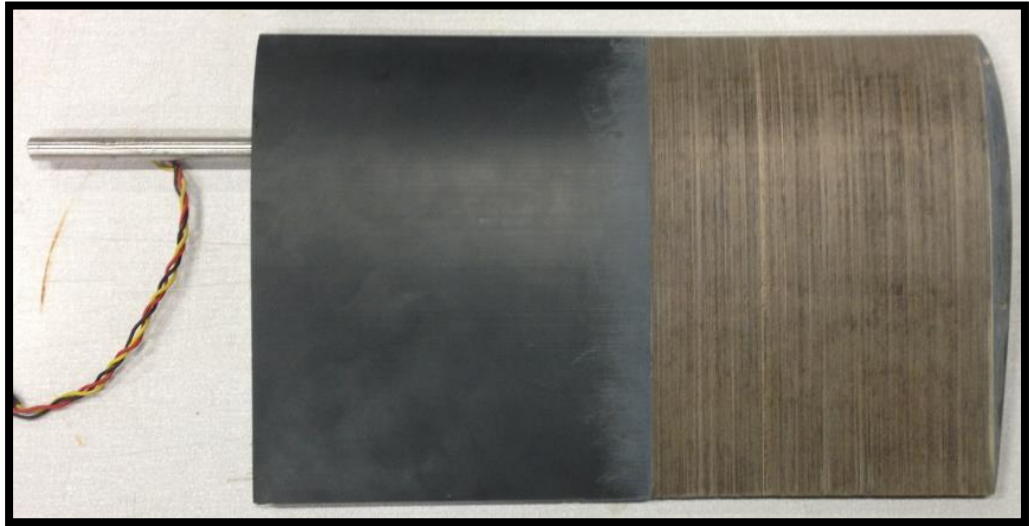


Figure 4.11 Internal mechanism of an active wing.

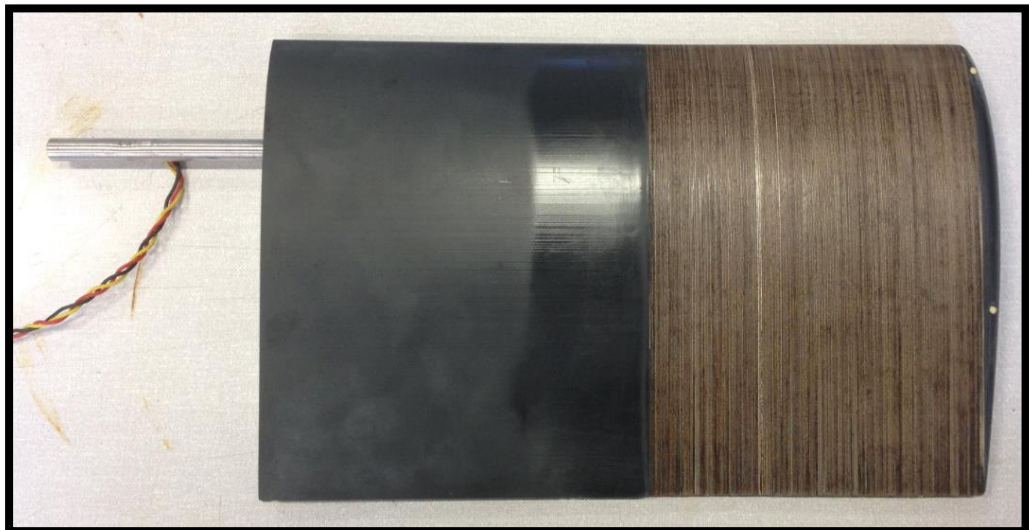
To attach the wing model to the wind tunnel, a 10mm diameter steel tube were also fastened and glued with epoxy resin at the quarter chord point of the wing model. The servo motor cable was then passed from the steel tube and pulled out from the holes created for this purpose on the steel tube. An aluminium cover was designed to enclose the top of the mechanism (as shown in **Figure 4.10 (b)**). To reduce any undue aerodynamic flow behaviour, the exposed part of the cover was trimmed and sanded back to the main wing surface creating an aerodynamic smooth surface finish.

As stated previously in **Section 4.2.1**, to compare the results of morphing concept, a full wing baselined-fixed was separately manufactured (as shown in **Figure 4.4 (b)**). Similar to the other configuration, the wing was made of Raku Tool WB-1700 with an identical span of 0.315m. Initial wind tunnel testing of the morphing concept was also conducted to investigate initially for comparison. This testing process consisted of the full and active wing model's aerodynamic behaviour at various angles of attack from -6° to 18° . The drag coefficient graph is shown in **Figure 4.13**. It can be seen that C_D was higher (the worst case is $\approx 15\%$ difference at

$\alpha = -6^\circ$). This was somewhat expected as the initially untreated plywood surface was rough. After these initial tests, the surface was sanded and sprayed with an Enamel Spray Paint Clear Lacquer to further smooth the surface (shown in **APPENDIX-A Figure A-4**). These two model states are indicated in **Figure 4.12**. After modifying the model, the experiments were conducted again for comparison. From **Figure 4.13** the lacquered model provided a lower drag performance and was near identical to that observed for full wing, fixed baseline model.



(a)



(b)

Figure 4.12 Complete active wing structure: (a) without lacquered skin and (b) lacquered skin.

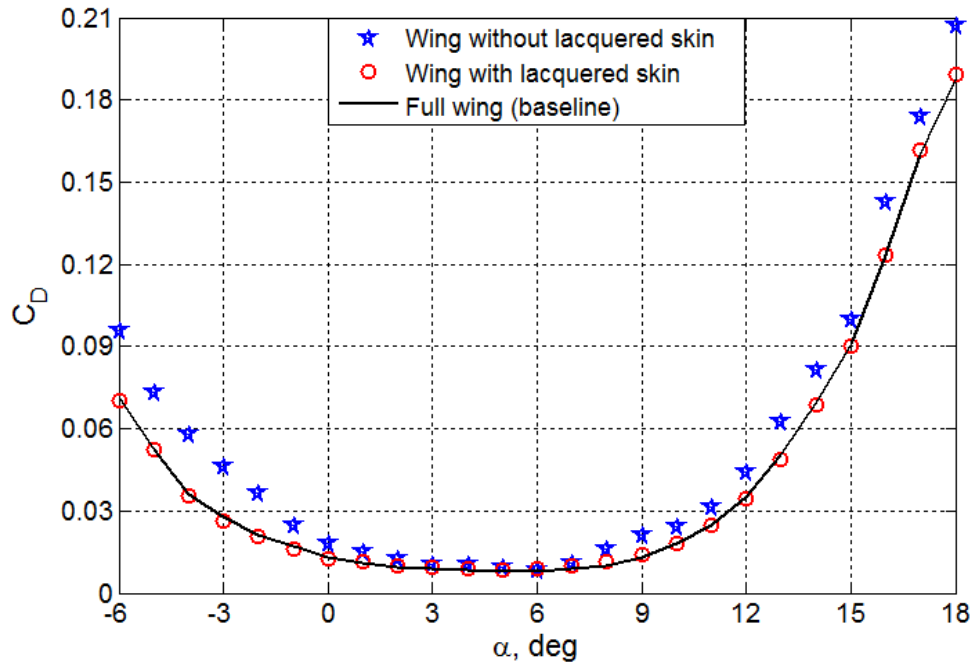


Figure 4.13 Effects of changing surface smoothness on drag coefficient (C_D) results.

4.2.3 Aileron Design and Comparison

In order to make a direct comparison and further validate the morphing concept and a traditional aileron system for roll control, six different ailerons ($\pm 10^\circ$, $\pm 20^\circ$ and $\pm 30^\circ$) was designed and manufactured (as shown in **Figure 4.15**), and then tested in a wind tunnel as illustrated in **APPENDIX-A Figure A- 7** to **Figure A- 12**. These angular ranges here were selected based on recommendations [163],[164] of conventional aircraft ailerons. The aileron was also placed outboard of the trailing edge of the wing with a size chosen at 50mm chord length (0.25% wing chord), and a span of 145 mm. The decision was made based on the standard aileron system [165] as well as the calculated twisted wing roll rate [166][167].

Each aileron (**Figure 4.15 (a)** and **(b)**) was made from a combination of 6mm thick elements in a combined linear array. Due to the high aerodynamic loading expected at high deflection angles as well as the additional pitching moment from the aileron deflection, the structure needed to be very rigid. To ensure satisfactory performance, structural analysis was performed in CATIA to ensure whether the aileron design was able to withstand the required loads and moments. An aerodynamic lift of 25N and a 0.5Nm pitching moment were applied to the aileron structure (**APPENDIX-A Figure A- 5**). The attachment pins for connection to the

main wing were clamped and fixed constraints applied. The results are shown in **Figure 4.14**.

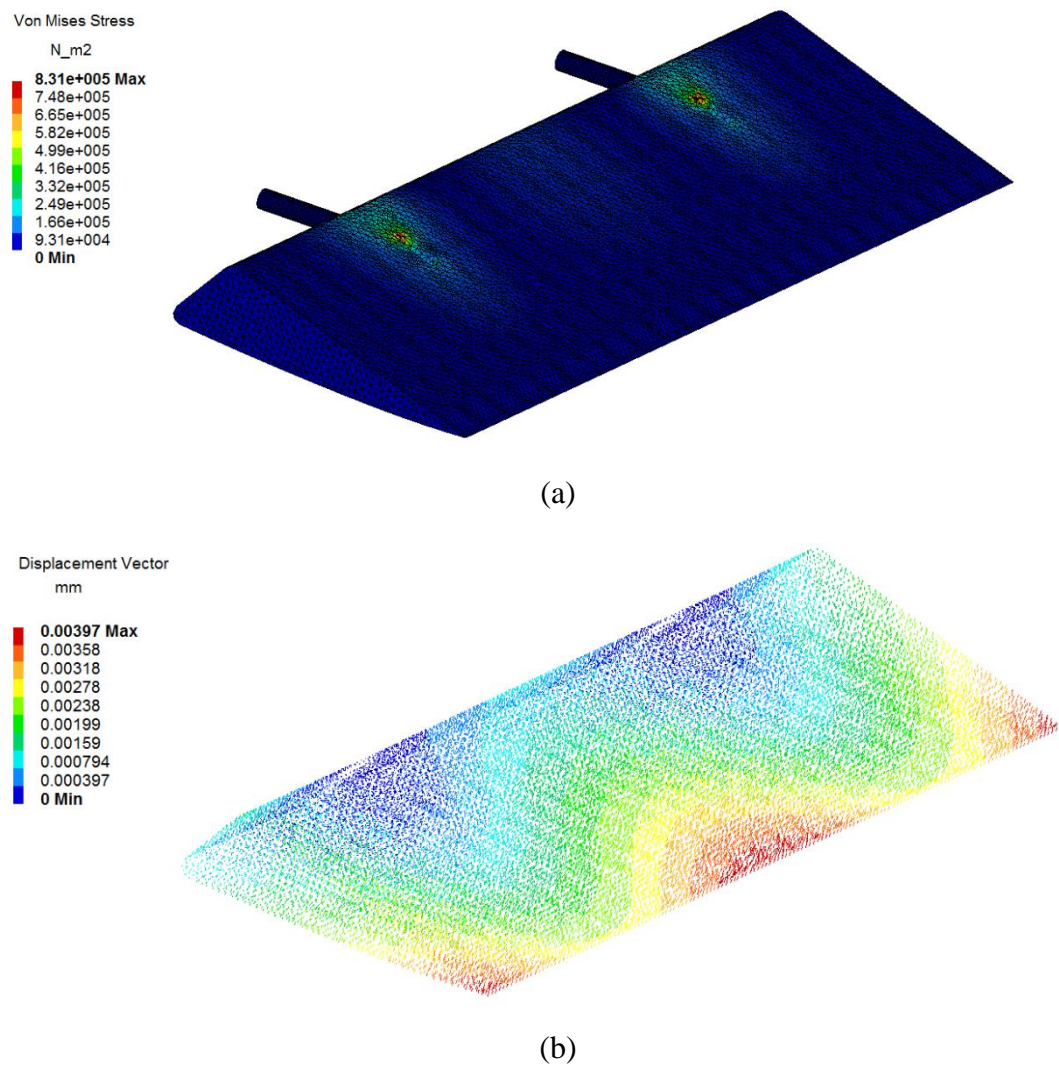


Figure 4.14 Structural Analysis for Aileron.

The results show each aileron has a maximum stress of $8.31e+005 N/m^2$, below the plywood yield stress ($70.93e+006 N/m^2$). Deformation magnitudes were measured at approximately 0.004mm. The structure was deemed adequate for the tests expected.

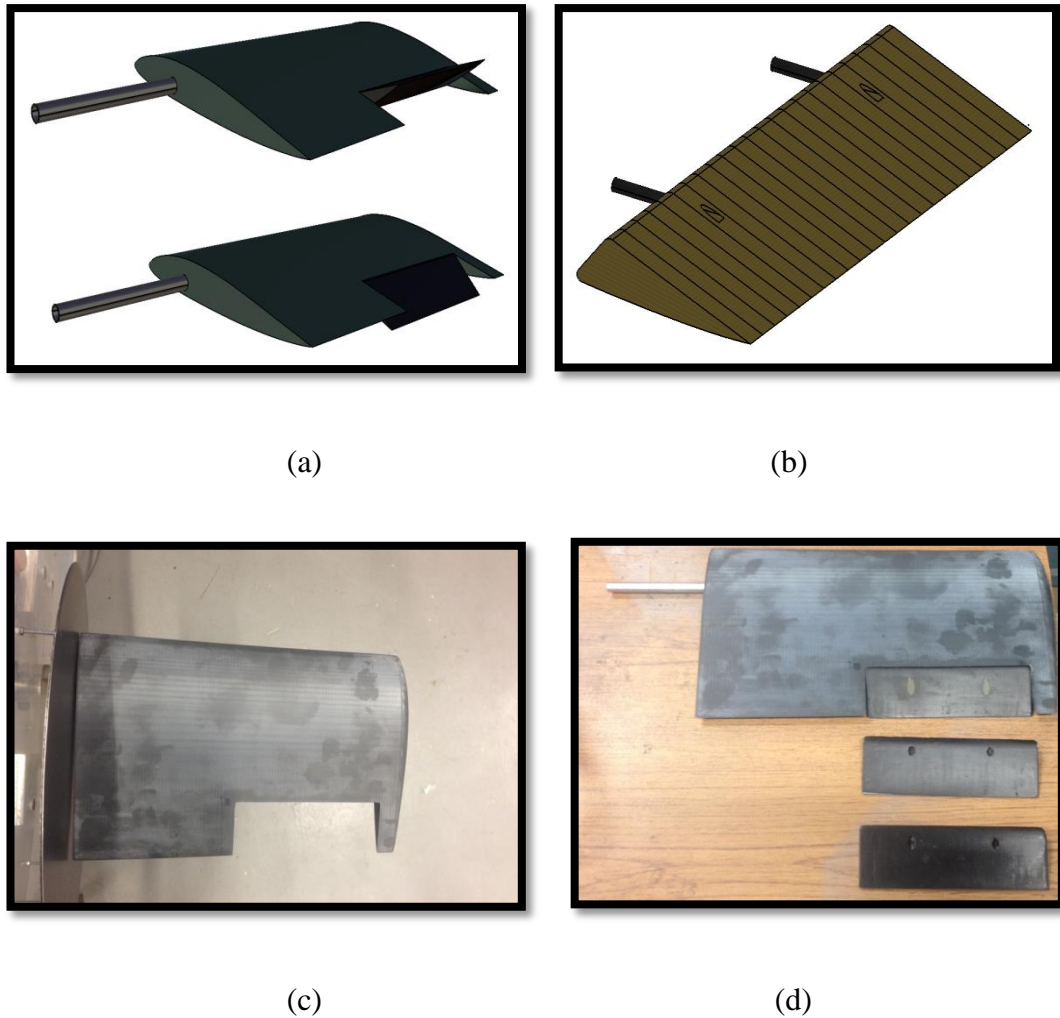


Figure 4.15 Aileron Configurations : (a) CAD design for full wing with an aileron, (b) CAD design for Aileron, (c) Manufactured wing profile and (d) Manufactured wing and ailerons.

The final model is shown in **Figure 4.15 (c) and (d)**. This configuration was CNC machined encompassing the aileron with the required space for the aileron removed. To provide an aerodynamic finish, the surface was sanded and coated with black paint. Two locating screws were used to fix the aileron to the wing structure. The screw holes were then filled with putty and sanded smooth. Similar manufacturing procedures were used to construct the other ailerons. In total, 3 different aileron angles were produced with each one providing both a negative and positive test case (a total of 6 configurations). Additionally, the gap between the aileron and the wing structure was sealed to minimise any flow discontinuities[168].

4.3 Wind Tunnel Setup and Apparatus

This section gives an overview and details of the wind tunnel preparation, the experimental procedures, the instruments, and the uncertainty for the model testing. All experimental wind tunnel testing was carried out on a 0.46m x 0.46m open circuit, low speed wind tunnel, with a maximum operating free stream velocity of 40 m/s (**Figure 4.16**). Before widespread testing, the flow quality was characterised using hotwire anemometry.



Figure 4.16 Brunel University Wind Tunnel Environment.

4.3.1 The Hotwire System

To characterise and obtain the baseline velocity and the turbulent intensity inside the wind tunnel, a Dantec hot wire anemometry system was used. A hotwire anemometer is a device that senses the changes in heat transfer from a small, electrically heated wire exposed to fluid motion. Its operation relies on the variation in the electrical resistance of the wire material with temperature. When the temperature and pressure of the fluid are constant, the only variable affecting heat transfer is the fluid velocity [169]. To obtain the results, two Streamline CTA Module signal conditioners A/D board NI e-series, and miniature X wire Probe (Dantec 55P61) was used (**Figure 4.18 (a)**).

To accommodate the hot wire probe and probe support, the tunnel top lid was machined into several (10.5m diameter) slots using (**Figure 4.17**). A small manual

traverse was used to move the probe to any position within a 0.30m x 0.30m x 0.30m grid (**Figure 4.18 (b)**) behind the model and perpendicular to the flow. A Digital Inclinometer was used to position the probe (maximum position error $\pm 0.05\text{mm}$). During the tests, in order to prevent any air leaking into the test section, the slots were covered with adhesive tape (**Figure 4.18 (b)**).

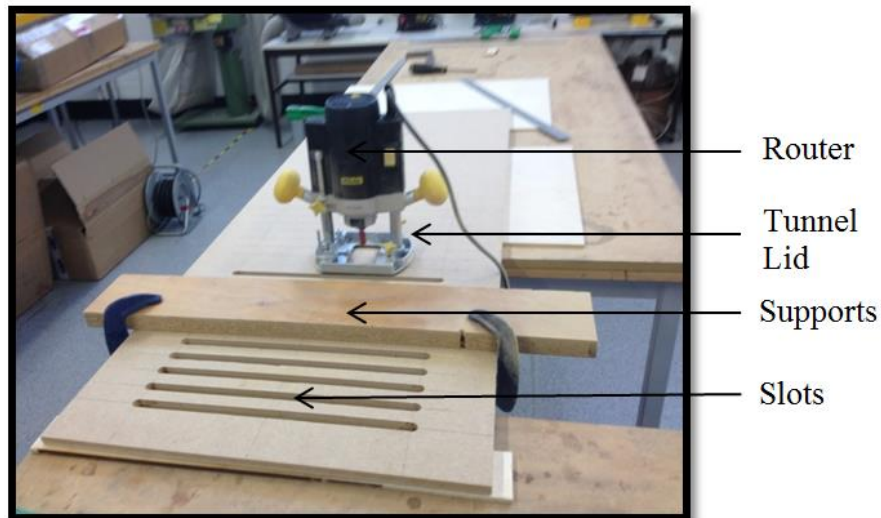


Figure 4.17 Router and slots for probe position.

Prior to conducting measurements, a calibration was done. For calibration, a Dantec Dynamics Hot-Wire Calibrator was used with the probe was installed on a pitch-yaw-roll manipulator (**Figure 4.19 (a)**). The sampling frequency was 1 kHz and 1024 samples per calibration velocity were recorded.

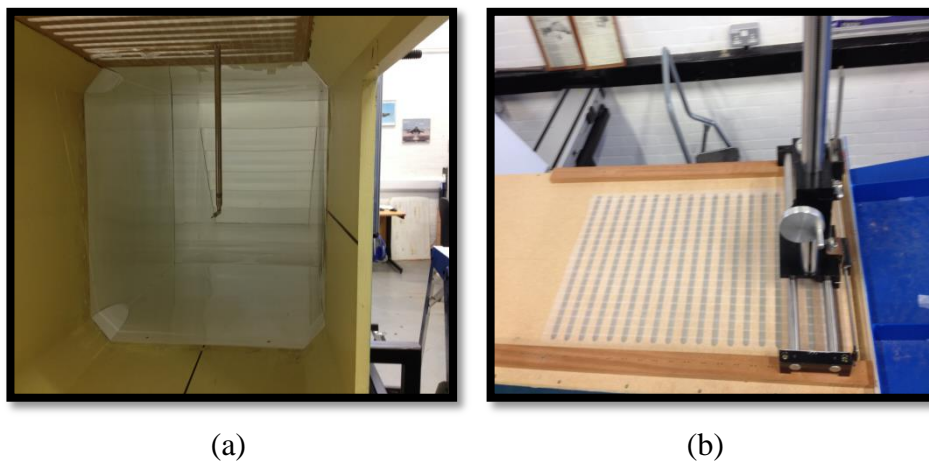
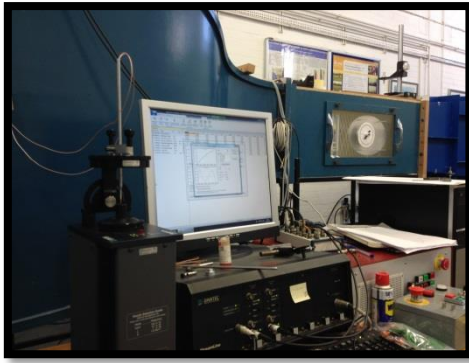
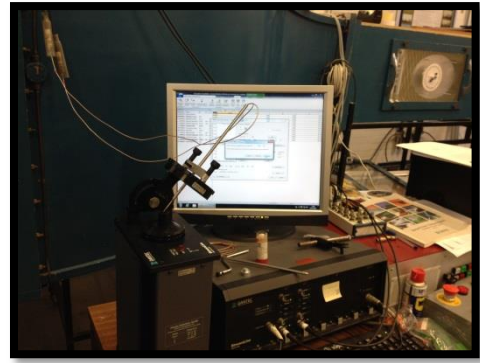


Figure 4.18 Hotwire probe setup: (a) Installed Probe and probe support bar and (b) Probe position slots and traverse.

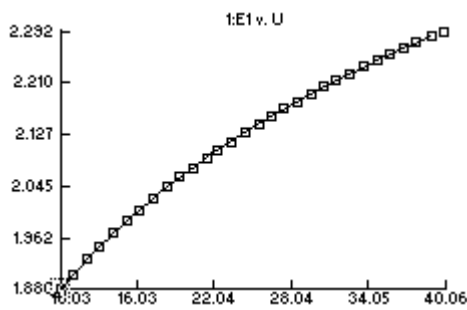


(a)

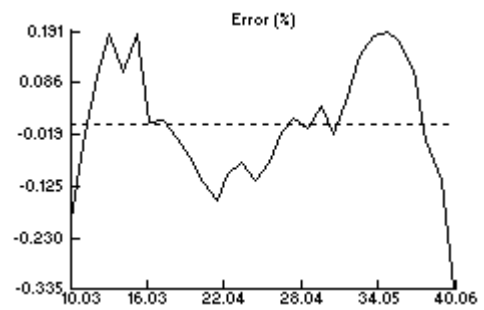


(b)

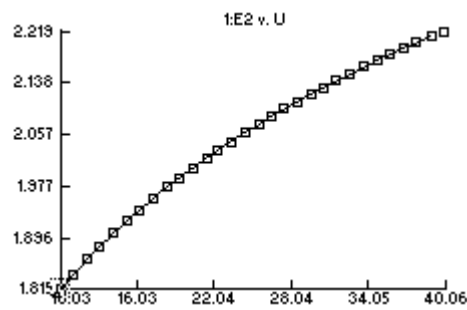
Figure 4.19 Hot Wire Probe Calibration Setup: (a) Velocity Calibration and (b) Angular Calibration.



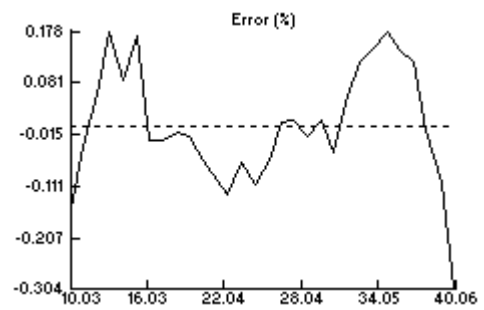
(a)



(b)



(c)



(d)

Figure 4.20 Hotwire anemometry calibration graphs: (a) sensor E1 versus velocity (U), (b) sensor E1 error rate, (c) sensor E2 versus velocity (U), and sensor E2 error rate.

The calibration was performed by placing the probe within the nozzle of the calibrator [169]. The speed was programmatically set the calibrator, with the corresponding hot-wire voltage output measured, averaged, and recorded automatically by the Streamline software (**Figure 4.20**). From this data, the best curve fit was created, which was used to correct measured voltage from the hot-wire probe. Corrections were automatically made to the signal to account for changes in temperature and density between the time the probe was calibrated and the time the measurements were made. A directional (positional) calibration was also conducted between -60° and 60° to ensure that in case of large flow misalignments, the hot wire would read accurately (the setup is shown in **Figure 4.19 (b)** and the graphs are shown in **APPENDIX-A Figure A- 6**).

4.3.2 Wake Surveys and Wind Tunnel Flow Quality Assessment

Before testing, wind tunnel wake surveys were conducted to measure and understand the qualities of the wind tunnel. Using hotwire, the velocity variation and turbulence intensity were measured. The formulas shown in **Equation (4-1)** were used [170].

$$TI(\%) = \frac{V'}{V} \times 100 \quad (4-1)$$

Where V' the root is the mean square of the velocity calculated from:

$$V' = \sqrt{\frac{1}{n} \sum_{i=1}^n (V_i - V)^2} \quad (4-2)$$

Initially, the empty section of the wind tunnel was measured at 40 m/s. The probe was traversed in the streamwise (x) direction through a longitudinal slot in the test section root and vertically (y), and transversely (z) between both the tunnel walls via a manually controlled traverse. Accurate positioning was manually controlled and measured using digital verniers. Averaged velocity data was recorded at each grid point through the Dantec Dynamic Streamline Software. After data at several streamwise locations had been taken, turbulent intensity was manually calculated. A turbulence intensity of 1% or less is generally considered low and turbulence intensities greater than 10% are considered high. The contour plots from **Figure 4.22** to **Figure 4.27** illustrate the velocity and turbulent intensity variation results for 3

different places (the front, middle, and rear of the test section, shown in **Figure 4.21**). Overall, It can be seen that the velocity was found to be low near the walls due to the wall effect [162]; hence the turbulence intensity in some places particularly for tunnel top and bottom wall was high. When the probe was positioned on the front side ($x=150\text{mm}$), TI was found to be less than 0.3% and the velocity variation was steady. Moving the probe from the front to the middle section ($x=0\text{mm}$) (**Figure 4.21**) where the wing was attached, a similar trend was observed. The average of wind tunnel TI was measured at 0.35-0.4%. For the rear side ($x=300\text{mm}$), the velocity variation was found to be much more varied compared to other positions, but still acceptable with a TI of 0.35% (**Figure 4.27**).

The boundary layer plate was also considered to see if it has any detrimental effect on the aerodynamics. The plate installation processes are described in detail in **Section 4.3.5**. The results show that the plate did not have any detrimental effect on the tunnel flow. Nevertheless, for some of the cases presented, when the probe was positioned in the middle of the plate ($x=0\text{mm}$), more steady flow behaviour was found to exist as shown in **Figure 4.24**.

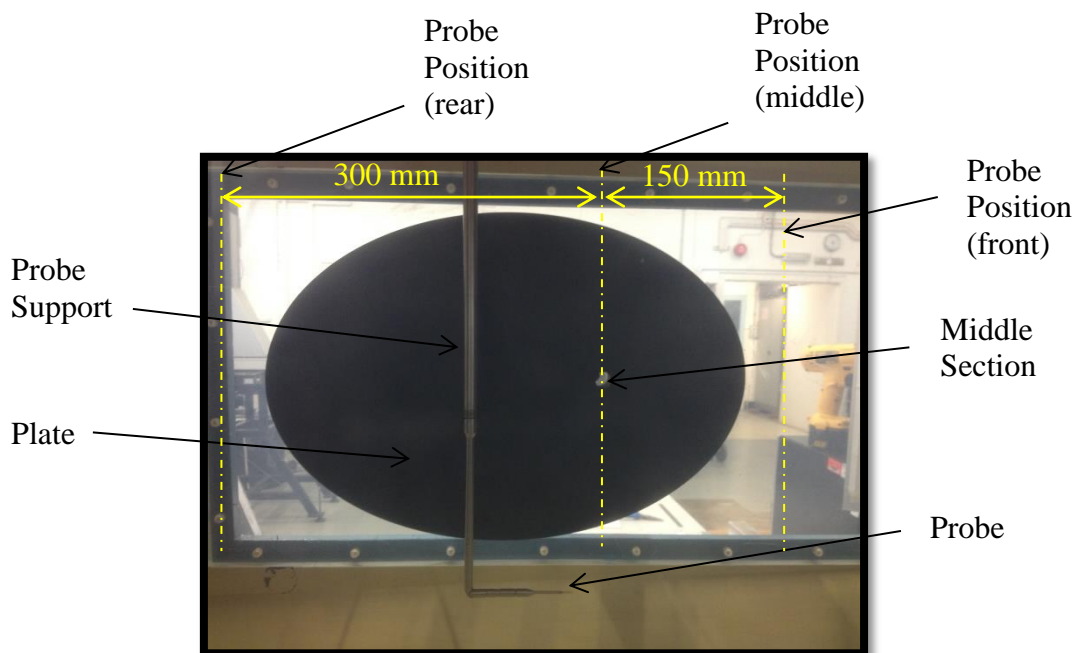


Figure 4.21 Hotwire probe position and the boundary layer plate.

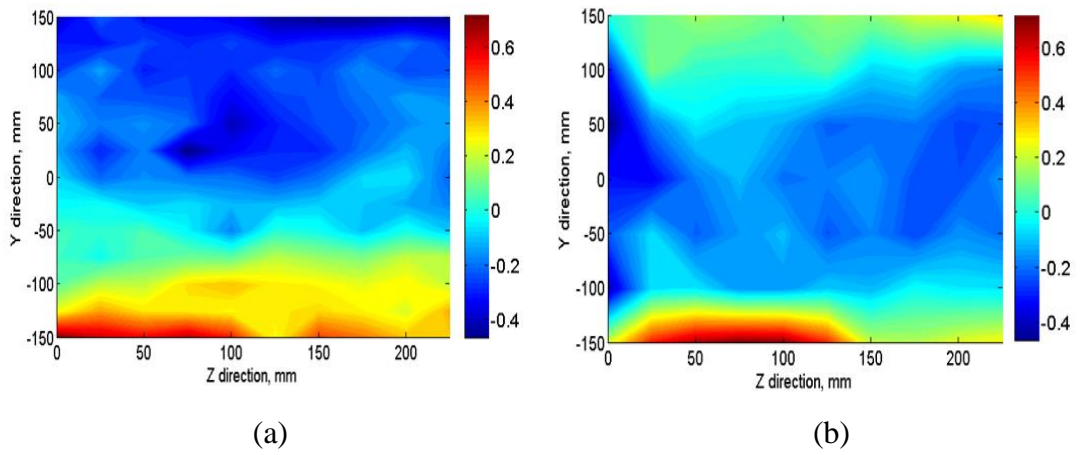


Figure 4.22 Velocity maps front side of the plate ($x=150\text{mm}$): (a) without plate and (b) with plate.

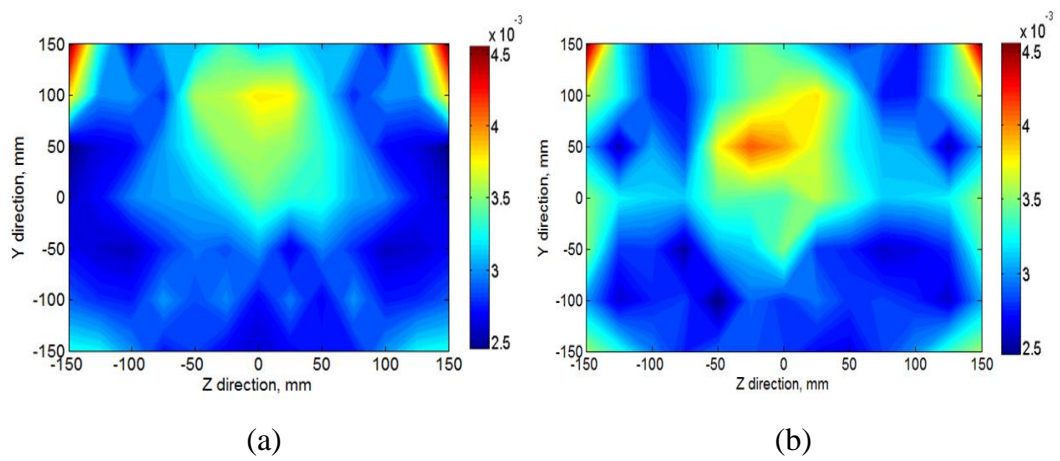


Figure 4.23 Turbulent intensity maps front side of the plate ($x=150\text{mm}$): (a) without plate and (b) with plate.

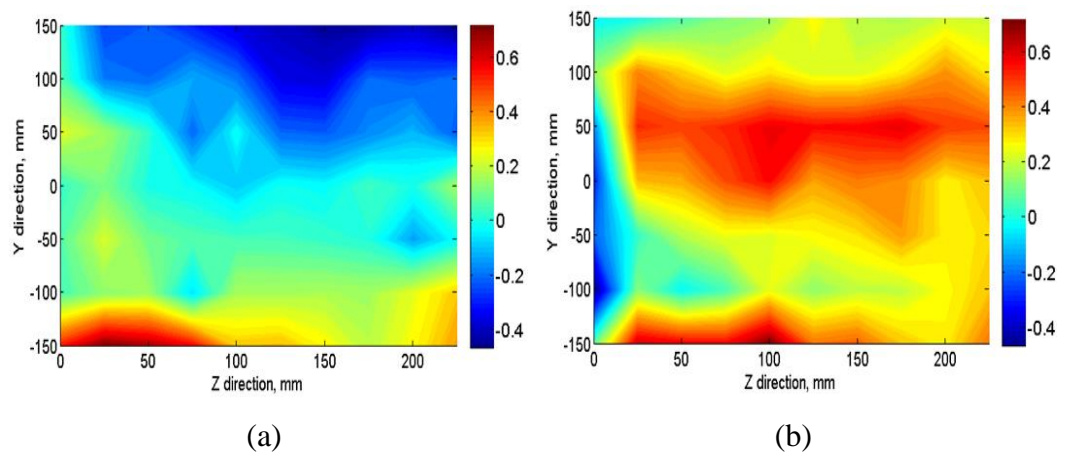


Figure 4.24 Velocity maps middle side of the plate ($x=0\text{mm}$): (a) without plate and (b) with plate.

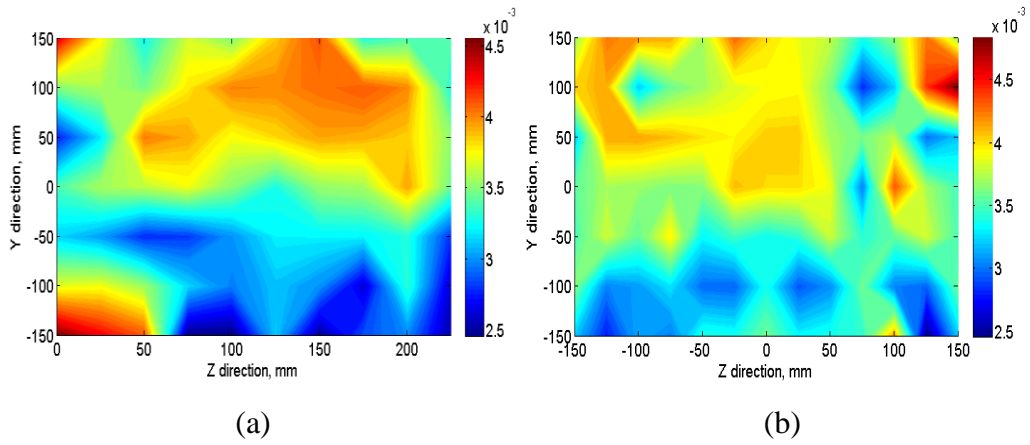


Figure 4.25 Turbulent intensity maps middle side of the plate ($x=0\text{mm}$): (a) without plate and (b) with plate.

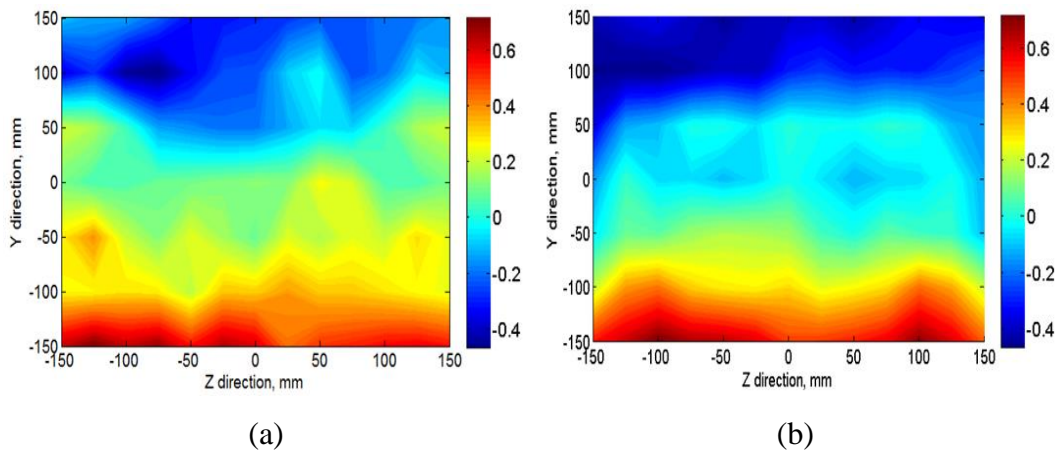


Figure 4.26 Velocity maps rear side of the plate ($x=-300\text{mm}$): (a) without plate and (b) with plate.

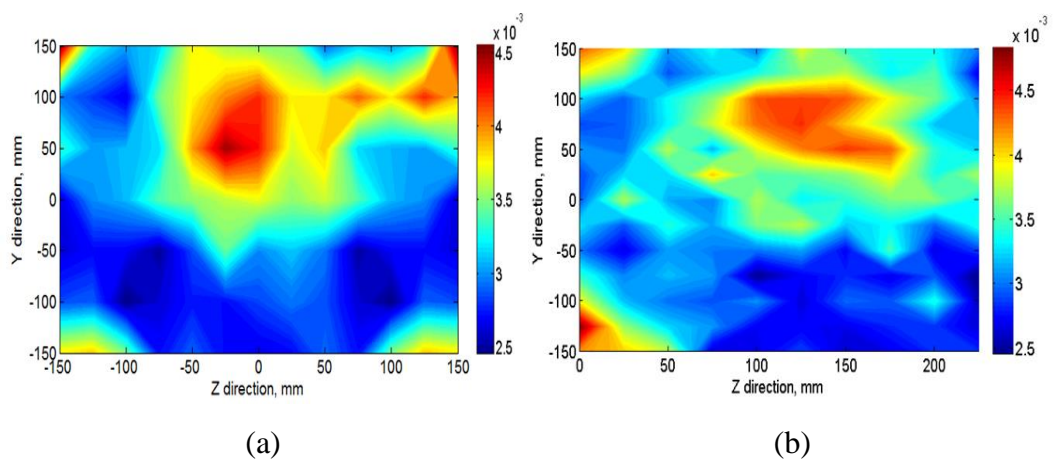


Figure 4.27 Turbulent intensity maps rear side of the plate ($x=-300\text{mm}$): (a) without plate and (b) with plate.

4.3.3 Force Balance Setup

The force and moment balance used to measure the performance of the wind tunnel models was an AMTI MC3A-500 (**Figure 4.29 (a)**). The MC3A is a compact, six-axis transducer with threaded inserts on its top and bottom surfaces. The measurements were made through integrated wheatstone bridges and by measuring the output voltage at the bridge output [171]. The body of the load cell was manufactured from a high-strength aluminium alloy with an anodised finish to protect the exterior from corrosion. Elastomeric O-ring seals provide internal protection of the strain gages and wiring from industrial environments and moisture exposure (the technical specifications of AMTI MC3A-500 M is described in **Table 5**). With the AMTI MC3A-500, a DigiAmp amplifier was used. This amplifier is a six channel Strain Gage Amplifier with analog and digital data output capabilities (**Figure 4.29 (b)**). The DigiAmp is designed to interface with AMTI's six-axis force platforms and transducers. These instruments measure the three orthogonal forces, F_x (Drag Force), F_y (Lift Force), F_z (Side Force) and three moments M_x (roll moment), M_y (yaw moment), and M_z (pitch moment) (illustrated in **Figure 4.28**). The DigiAmp provides bridge excitation, low level signal amplification and a suite of filters and signal conditioning algorithms designed to provide the highest quality signal with the lowest possible noise [172].

Table 5 Technical Specification of AMTI MC3A-500 M [173].

Channel	F_x	F_y	F_z	Units	M_x	M_y	M_z	Units
Capacity	222	222	445	N	11	11	5.6	N-m
Sensitivity	5.4	5.4	1.35	$\mu\text{v/v-N}$	266	266	213	$\mu\text{v/v-N-m}$
Natural frequency	-	-	-	Hz	300	300	-	Hz
Stiffness (X 105)	21.04	21.04	298	N/m	-	-	0.0226	

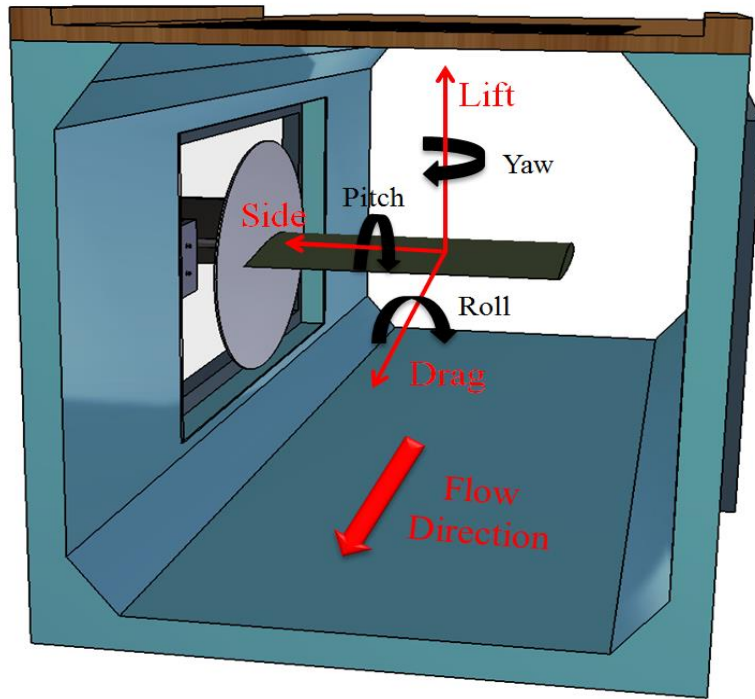


Figure 4.28 Wind tunnel balance.



(a)



(b)

Figure 4.29 Instrumentation to obtain results: (a) AMTI MC3A-500 Load Cell and (b) DigiAmp six channel strain gage amplifier.

To support the load cell on the wind tunnel, an aluminium balance support frame was manufactured and fixed to the tunnel wall (**Figure 4.30**). A spirit level and inclinometer were used to ensure that the load cell was level. The model support sting was then mounted to the active plate of the AMTI MC3A-500. To prevent any contact between the support sting and the tunnel wall, a clearance hole was cut out of the tunnel lid. A symmetrical airfoil shaped fairing was manufactured and bonded to the boundary layer plate (**Figure 4.31**). Calibration of the load cell was completed before testing and derivation was found to be less than $\pm 2.5\%$ of full scale output (details shown in **Section 4.3.6**).

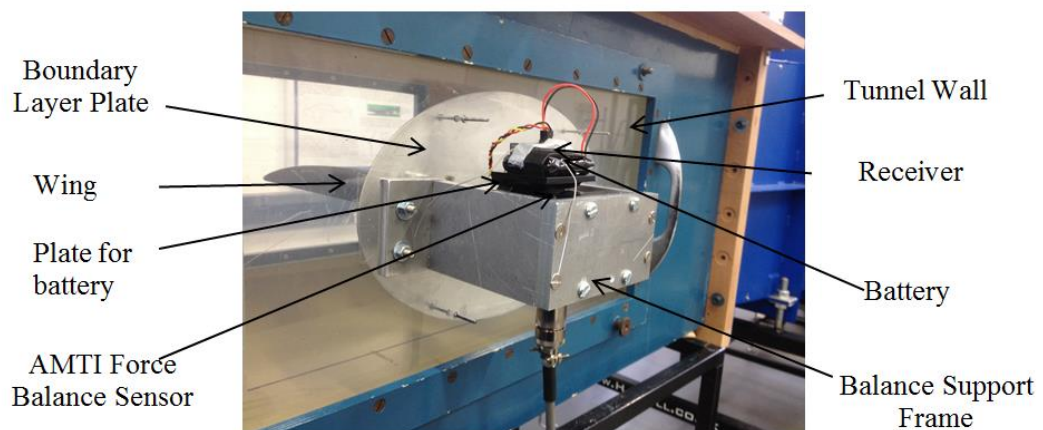


Figure 4.30 Force and Moment Balance Mechanism Setup.

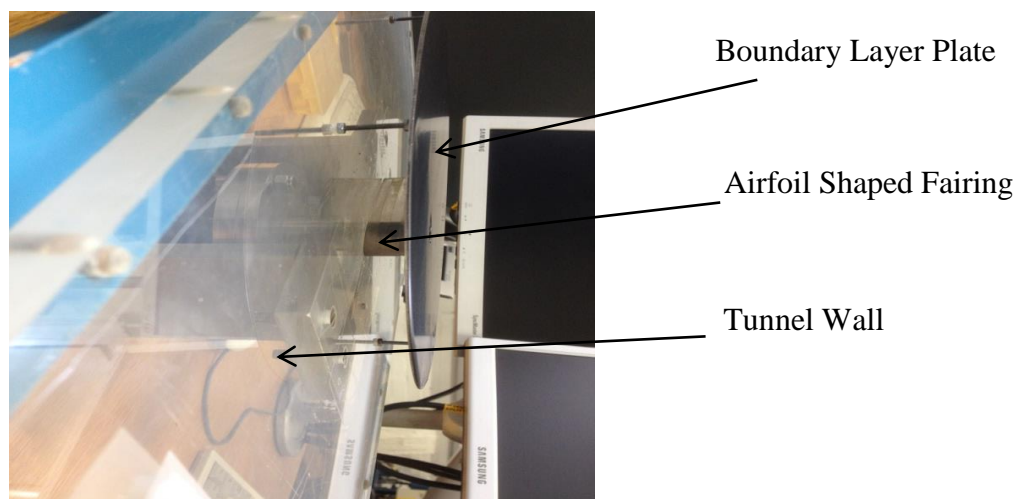


Figure 4.31 Installed boundary layer plate and the airfoil shaped fairing.

4.3.4 Servo Driver System and Angle of Attack Adjustment

A Futaba R617FS 2.4GHz FASST 7-Channel receiver and Futaba T10CG 2.4GHz 10-Channel T-FHSS radio system (transmitter) were used to control the servo motor of the morphing wing. The Hitec Servo within the model was connected to the receiver and a 6V NiMh battery was utilised as the power source.

To adjust the angle of attack of the wing configurations, a manual rotation stage was designed and attached to a support bar (shown in **Figure 4.32**). This manual rotation stage was also mounted directly onto the force and moment balance, which was connected to the support frame fixed to the outside test-section wall. Using additional bolts, the wing support sting could be adjusted in accordance with the oncoming flow. A digital inclinometer was used to calibrate the angle of attack mechanism (position error $\pm 0.5^\circ$).

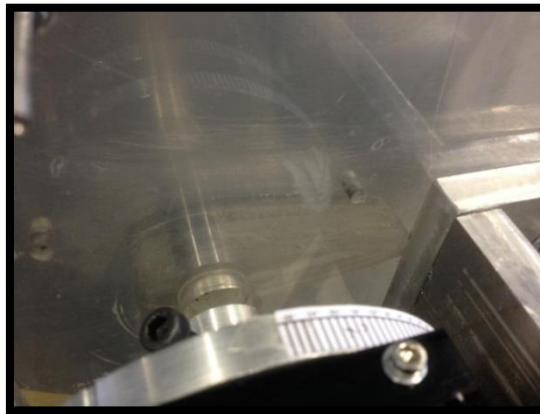


Figure 4.32 Manual Angle of Attack Mechanism

4.3.5 Model Installation and Testing Process

The models as shown in **Figure 4.34**, was installed in the middle of the test section. To reduce boundary layer wall effects, an end plate was used (0.37m x 0.25m) (**Figure 4.33**) according to the results of Barlow [162] and Kubo et al. [53]. They recommended that the end plates extend at least 4.28 times the model height downstream and at least 2.5 times the model height upstream. Also, with regard to the plate height, at least 8.5 times the height of the model is recommended. The end plates therefore, extended 60mm upstream of the leading edge of the model and 110mm downstream of the trailing edge. This plate was made of 2mm thick aluminium sheet. The distance between the tunnel wall and the plate was calculated

using boundary layer theory as described in **Equation (4-3)** [174]. Ultimately, the plate was installed 0.015m off the tunnel wall using adjustable threaded rods. The wing model was also placed 0.001m off the plate to allow free movement in accordance with Mueller et al. [175]. They showed that the gap size needs to be around 0.5% of the span to not have any interference on the results.

$$\delta_{turbulence} = \frac{0.37x}{(Re^{1/5})} \quad (4-3)$$

$$\delta^* = \int_0^{\infty} \left(1 - \frac{u(y)}{u}\right) dy \quad (4-4)$$

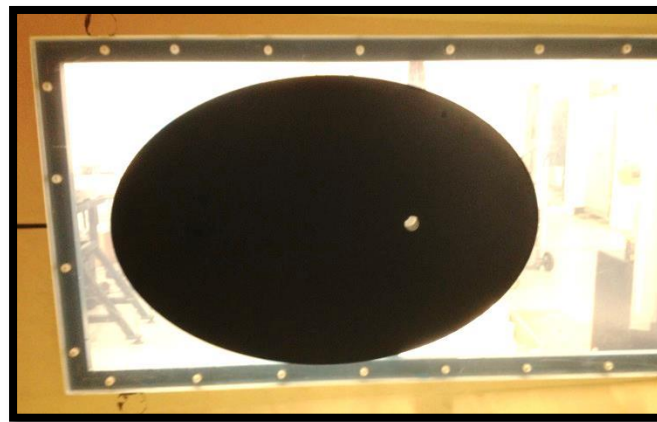


Figure 4.33 Boundary Layer Plate.

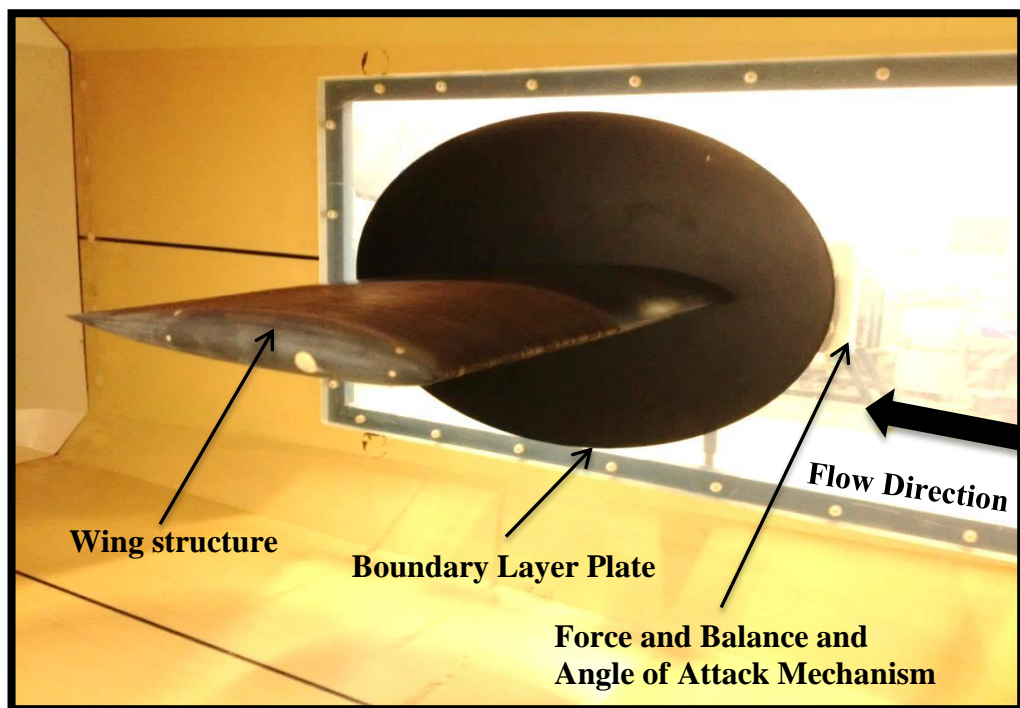


Figure 4.34 Experimental setup for Adaptive Wing Configuration.

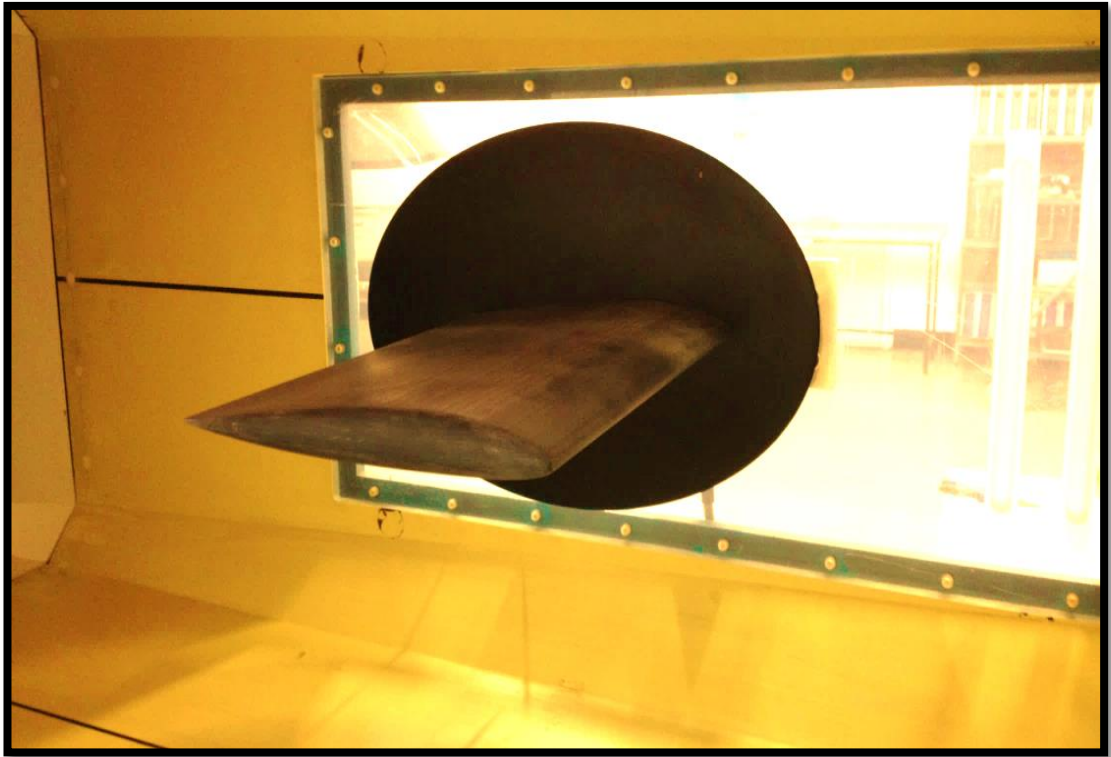


Figure 4.35 Experimental Setup for Full Wing Configuration.

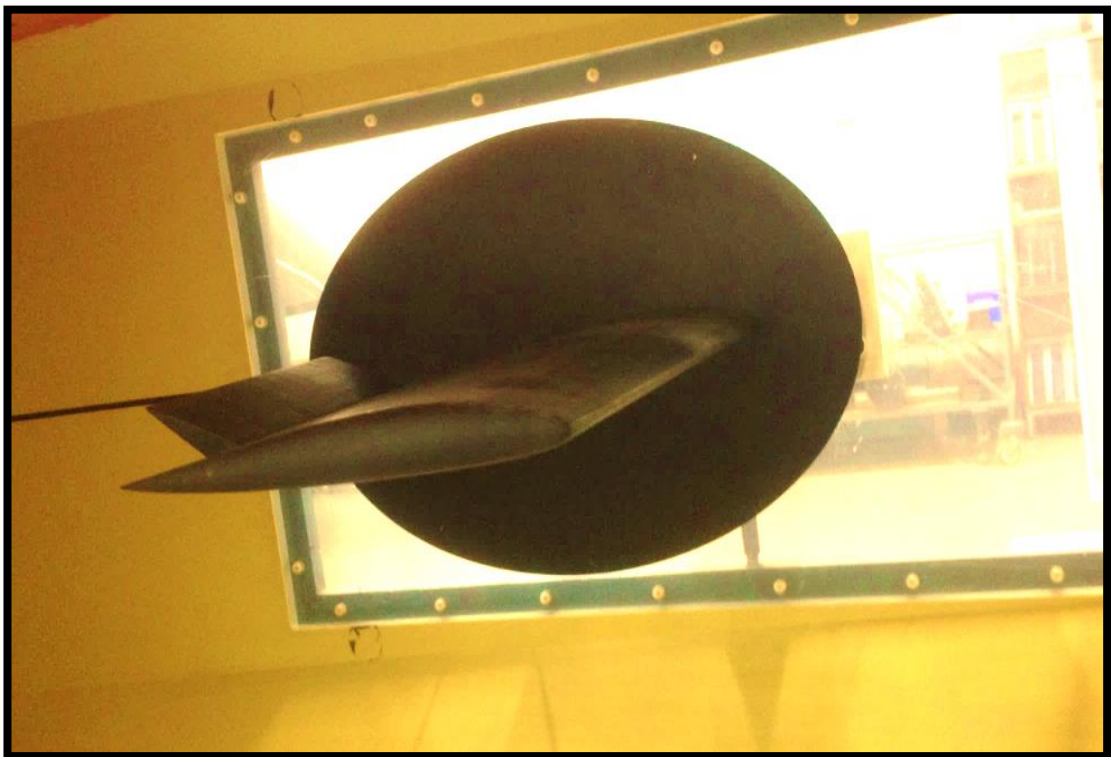


Figure 4.36 Wind Tunnel Setup for Aileron (-30°).

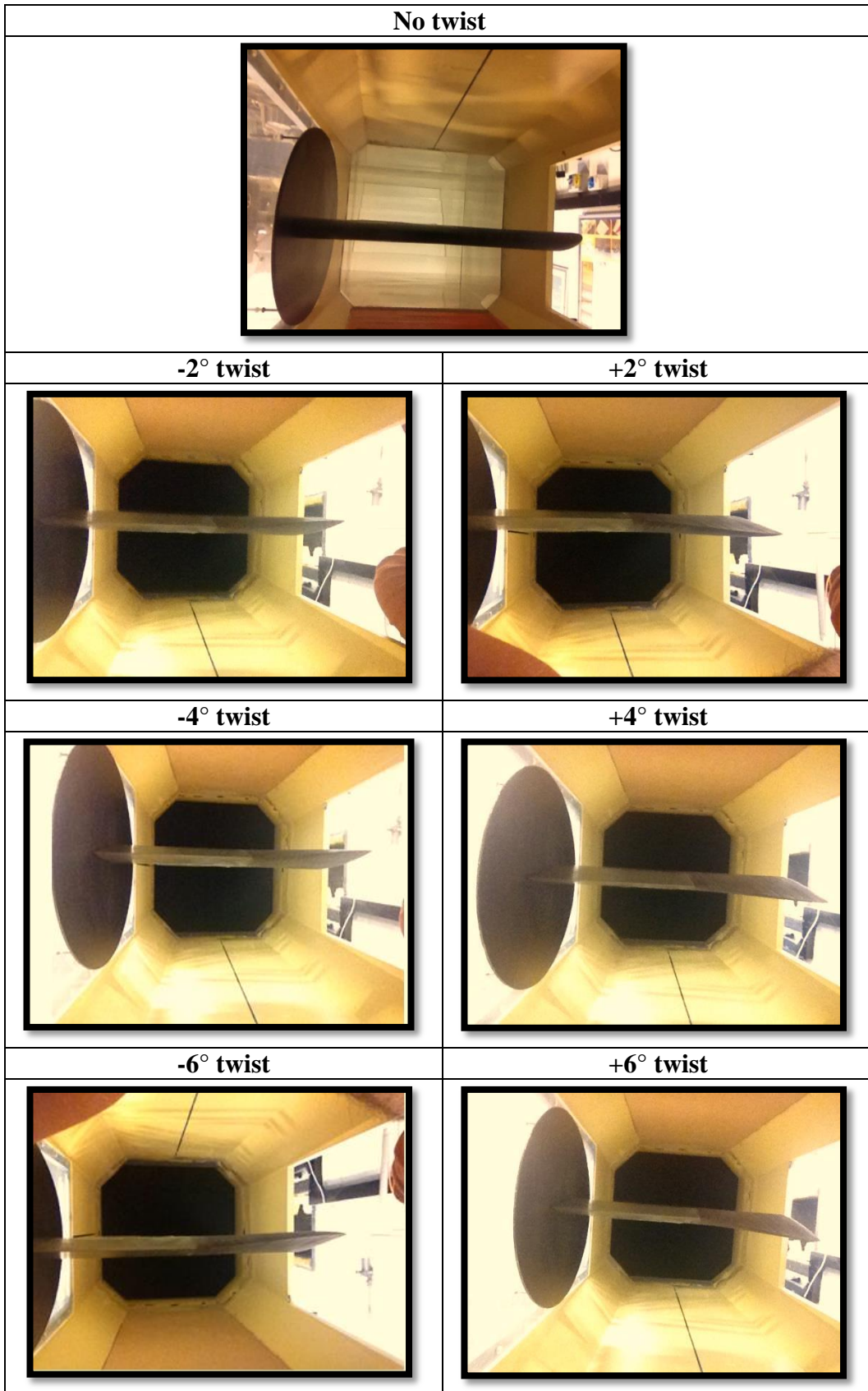


Figure 4.37 Twist cases for wind tunnel model.

4.3.6 Force Balance Calibration

To obtain final force and moment results, calibration was needed to convert the output voltage from the AMTI. Transducers are typically calibrated in eight different load locations, which provide data for F_x , F_y , F_z , M_x , M_y , M_z , $-M_x$ and $-M_y$. All loads and moments were applied in the same way. Prior to applying the load zeros were taken. The load was then slowly applied up to the maximum working load. As the load increased, the data was recorded and then the loads were released slowly. The load data during released was also recorded. In total 10 point calibrations were performed, which was the number recommended by the company [173]. For the moment calibrations, the distance between the applied load and the transducers was also measured and included in the calculation. The calibration equations are shown in **Table 6** (x =voltage and y = force). After completing the calibrations, the sensor was ready to measure the aerodynamic response of the wind tunnel models.

Table 6 AMTI Calibration Equations for Force and Moment

Force and Moments	Calibration Equations
Lift Force	$y = 0.0523x + 0.0028$
Drag Force	$y = 0.0512x + 0.0055$
Side Force	$y = -0.0139x - 0.0332$
Roll Moment	$y = -0.332x - 0.0046$
Yaw Moment	$y = 0.3299x - 0.0046$
Pitch Moment	$y = -0.2287x - 0.0033$

Due to the interface between the load cell and the Streamline Software, an additional calibration was required. A signal generator with an oscilloscope was used for each force and moment data. The signal generator (ISO-TECH GFG-8216A) used two outputs; one is connected to an oscilloscope to monitor the magnitude and the other unit is connected to streamline data acquisition system. Signals were produced by the signal generator with the data recorded from the oscilloscope and the Streamline software. The data were recorded with the calibration equations produced as shown in **Table 7**.

Table 7 Streamline Calibration Equations for Force and Moment

Force and Moments	Calibration Equations
Lift Force	$y = 0.610015x + 0.0003$
Drag Force	$y = 0.4713x + 0.00015$
Side Force	$y = 0.110x - 0.0026$
Roll Moment	$y = 0.8123x + 0.00052$
Yaw Moment	$y = 0.48x + 0.0001$
Pitch Moment	$y = 0.13251x - 0.0004$

4.3.7 Moment Data Reduction

Due to the distance between the load cell and the wing reference point, moment transfers were required to obtain final results. Frequent use is made of the relations from engineering statics, which give the rules for transferring forces and moments from one reference point to another. The rules contain the basic force, distance and moment relationships and assume that a system of forces produces a resultant Force F and a resultant moment M_1 relative point 1, and then an equivalent system acting at another point 2, is [162]:

$$F_1 = F_2 \quad (4-5)$$

$$M_2 = M_1 - (F_1 \times r_{12}) \quad (4-6)$$

Where r_{12} is the vector from point 1 to point 2. The existing resultant moment (M_1) was subtracted from the calculated new moment, which was obtained by multiplying the force and the distance between the load cell and the wing (**Equation (4-6)**).

4.3.8 Experimental Procedures and Data Processing

For all wind tunnel testing, a fixed experimental procedure was developed and applied. The following section summarises the experimental procedure applied.

Typical experimental procedure:

- Model installed and checking done for correct twist angle.

- The force-balance sensor was checked for response.
- Pressure and density temperature read before each tests. Using **Equation (4-9)** the density was calculated.

$$\rho = \frac{P}{R_0 \times T} \quad (4-7)$$

Using local density, the Reynold number was calculated using **Equation (3-12)**.

$$Re = \frac{\rho \times V \times x_l}{\mu} \quad (4-8)$$

- Prior to the start of every subsequent test, zero readings were obtained from the force balance both before and after each test so that the tare and zero effects could be corrected for in the final results.
- Then tunnel was run and the velocity was recorded.
- The angle of attack increased to 18°, then decreased to -6°. For every angle of attack, the velocity was recorded.
- After tunnel shut down, second a zero reading was recorded.

Data Processing:

All data was sampled at 100Hz for 10s and then averaged to get the mean value.

- Measured data from the load cell was recorded.
- Calibration curves were applied to the results.
- Corrected voltage results were converted to force and moment data using relevant calibration equations.
- Force and moment data were converted to coefficient data using the **Equations** from (3-6) to (3-12).

No wind tunnel blockage corrections and artificial transition fixing was used.

4.3.9 Experimental Uncertainty (Experimental Error)

It is important to consider uncertainty when experimental results are presented. Such an analysis provides one with a reliable way of assessing repeatability and

precision of the data [176]. This section will discuss the uncertainty analysis conducted to assess the errors associated in the experimental wind tunnel testing.

For a calculated parameter (y) which depends on n different measurements ($X_1, X_2, X_3 \dots X_n$) (expressed using the following **Equation (4-9)**). The total experimental

$$y = f(X_1, X_2, \dots X_n) \quad (4-9)$$

uncertainty consists of two types of errors; systematic and random errors. Systematic errors are fixed, repeatable and mostly arise from the instrumentation. These errors can be decreased by calibration. On the other hand, random errors are unknown entities that can be caused by anything, including for instance environmental conditions. They can be reduced by increasing the amount of data gathered. Coleman & Steele [177] proposed the following **Equation(4-11)** for finding the absolute uncertainty of a calculated parameter shown in **Equation ((4-9))**.

$$U_{abs} = \sqrt{\left(\frac{\partial y}{\partial X_1}\right)^2 (U_{X_1})^2 + \left(\frac{\partial y}{\partial X_2}\right)^2 (U_{X_2})^2 + \dots + \left(\frac{\partial y}{\partial X_n}\right)^2 (U_{X_n})^2} \quad (4-10)$$

In **Equation (4-10)**, U_{abs} is the absolute uncertainty of the calculated y value, $\partial y/\partial X_1$ is the derivative of y with respect to X_1 and U_{X_i} is the absolute uncertainty of measurement X_i . By dividing both sides of **Equation (4-10)** by y , the relative uncertainty (U_{rel}) of the calculated parameter in terms of % can be expressed using **Equation (4-11)**:

$$U_{rel} = \sqrt{\left(\frac{X_1}{y} \frac{\partial y}{\partial X_1}\right)^2 \left(\frac{U_{X_1}}{X_1}\right)^2 + \left(\frac{X_2}{y} \frac{\partial y}{\partial X_2}\right)^2 \left(\frac{U_{X_2}}{X_2}\right)^2 + \dots + \left(\frac{X_n}{y} \frac{\partial y}{\partial X_n}\right)^2 \left(\frac{U_{X_n}}{X_n}\right)^2} \quad (4-11)$$

Experimentally measured relative uncertainties, which come primarily from the instruments used, are listed in **Table 8**. The relative uncertainty of the measurements was determined through the calibration conducted in the laboratory as explained in **Section 4.3.6**. The relative uncertainty of the calculated parameters is discussed in detail and calculated by applying **Equation (4-10)** and **Equations (4-11)** as proposed in [177], [178] and [176] in conjunction with the information listed in **Table 8** and **Table 9**.

Table 8 Uncertainty values of devices

Instruments and Measurements	Accuracy
Hot Wire Probe Traverse Mechanism	± 0.05 mm
Angle of Attack Mechanism	$\pm 0.5^\circ$
Twist Angle	± 0.5 mm
Mercury Barometer	± 0.05 mmHg
Temperature Measurement	± 0.5 °C
Ruler Measurements	± 0.5 mm

Table 9 Uncertainty values of calculated parameters

Parameters	Accuracy	Error Rate (%)
Air Density	± 0.0029 gr/cm ³	$\pm 0.24\%$
Velocity	± 0.2 m/s	$\pm 0.25\%$

Table 10 Uncertainty values of measured force and moments

Force and Moments	Error Rate for Streamline Anemometer System	Error Rate for Load Cell	Total Error Rate
Lift Force	± 0.5 %	± 0.2 %	± 0.75 %
Drag Force	± 0.5 %	± 0.25 %	± 0.75 %
Side Force	± 0.25 %	± 0.2 %	± 0.5 %
Roll Moment	± 0.5 %	± 0.2 %	± 0.75 %
Yaw Moment	± 0.25 %	± 0.2 %	± 0.5 %
Pitch Moment	± 0.25 %	± 0.25 %	± 0.5 %

4.4 Design and Manufacturing of Prototype Wing for Flight Testing

In order to demonstrate the viability of the concept, prototype wings were made for flight testing. This section describes this setup and methodology. Various instrumentation used also described and presented.

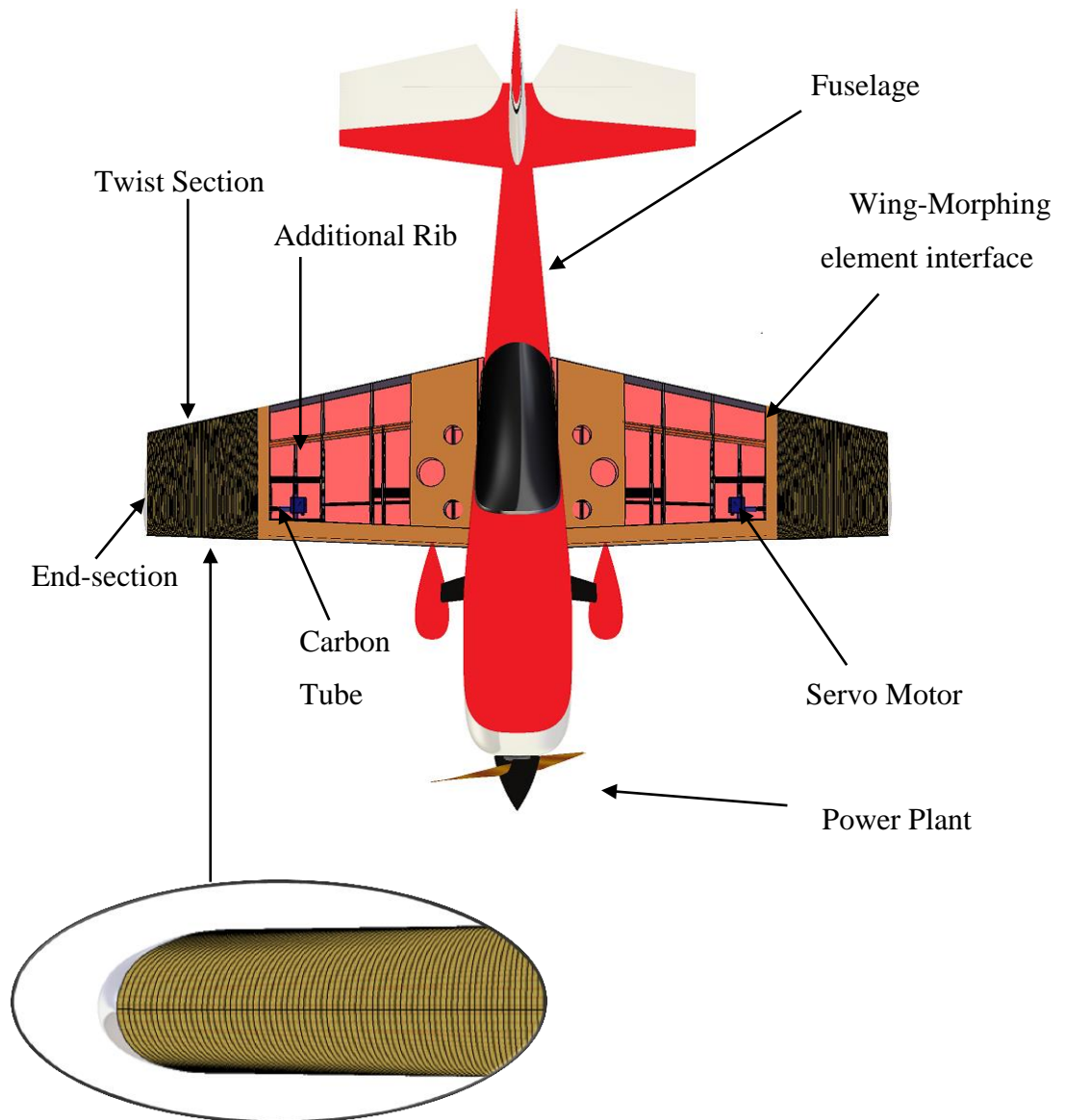


Figure 4.38 Schematic of the Extra 300-78inch aerobatic plane and prototype wing concept.

4.4.1 RC Plane Wing Manufacture and Implementation

The model chosen for this study was an Extreme flight Extra 300 with a 78-inch wingspan. The baseline wing configuration comprised a symmetrical airfoil section and a 2.5° leading edge sweep angle, a 1.980m wing span, a 0.5m root chord, and a 0.27m tip chord, with aspect and tip ratios of 5.45 and 0.54 respectively. The fuselage part was 1.930m long and the maximum thickness was 0.215m. In this study two wing sets (left and right wing) were used (the schematic view of the plane is shown in **Figure 4.38**). The wings had a fixed configuration with a full aileron section. It was decided to make the twistable wing sections 0.3m long according to initial morphing applications [179]. Most of the twist and control surfaces in aircraft are located in the outer 1/3 of the wing. Consequently the end part of 0.3m was cut and then modified to implement the designed morphing wing as shown in **Figure 4.39**.

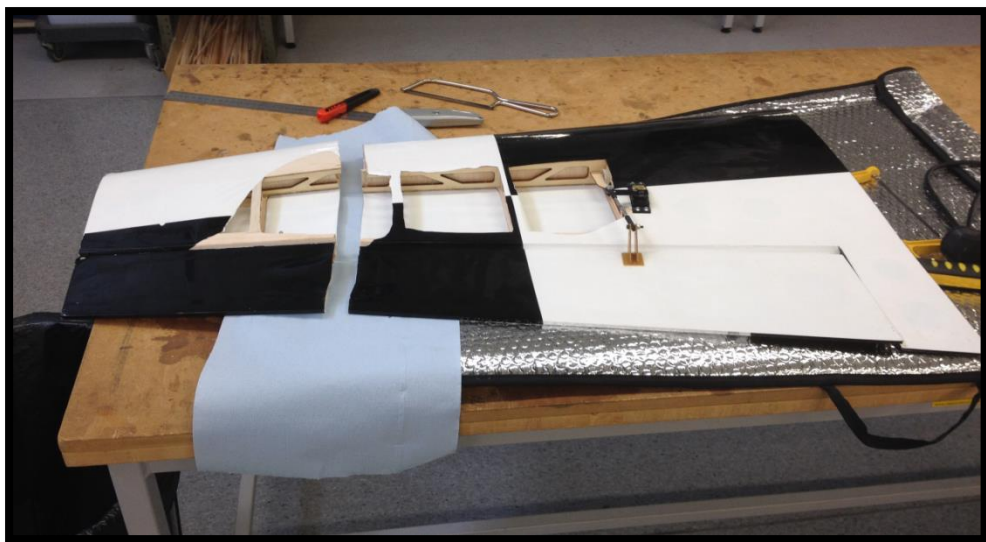


Figure 4.39 Full Wing was cut to implement novel design concept.

Before manufacturing, structural analysis for a full wing configuration was carried out using the ANSYS Mechanical Software. Prior to this, the wing CAD modelling was done in CATIA V5 and then imported into ANSYS to investigate the structural effects of the twisted wing configuration. For AVL, the required force and moment data (totally 250N) were applied to the structure. **Figure 4.40** depicts the structural analysis results for the wing configuration. It can be seen that the most stress occurred at the root of the wing around $\sigma = 28.2$ MPa and also in some places where the connections were added near the morphing element (**Figure 4.40 (a)**). According to the failure criteria, the wing should not exceed 30 MPa for balsa wood

and 70.93 MPa for plywood. Therefore the structure appeared to meet aerodynamic load and moment requirements. Additionally, **Figure 4.40 (b)** illustrates the deformation magnitudes of a wing. A displacement of about 5mm was measured under aerodynamic load, which occurred at the tip of the wing configuration.

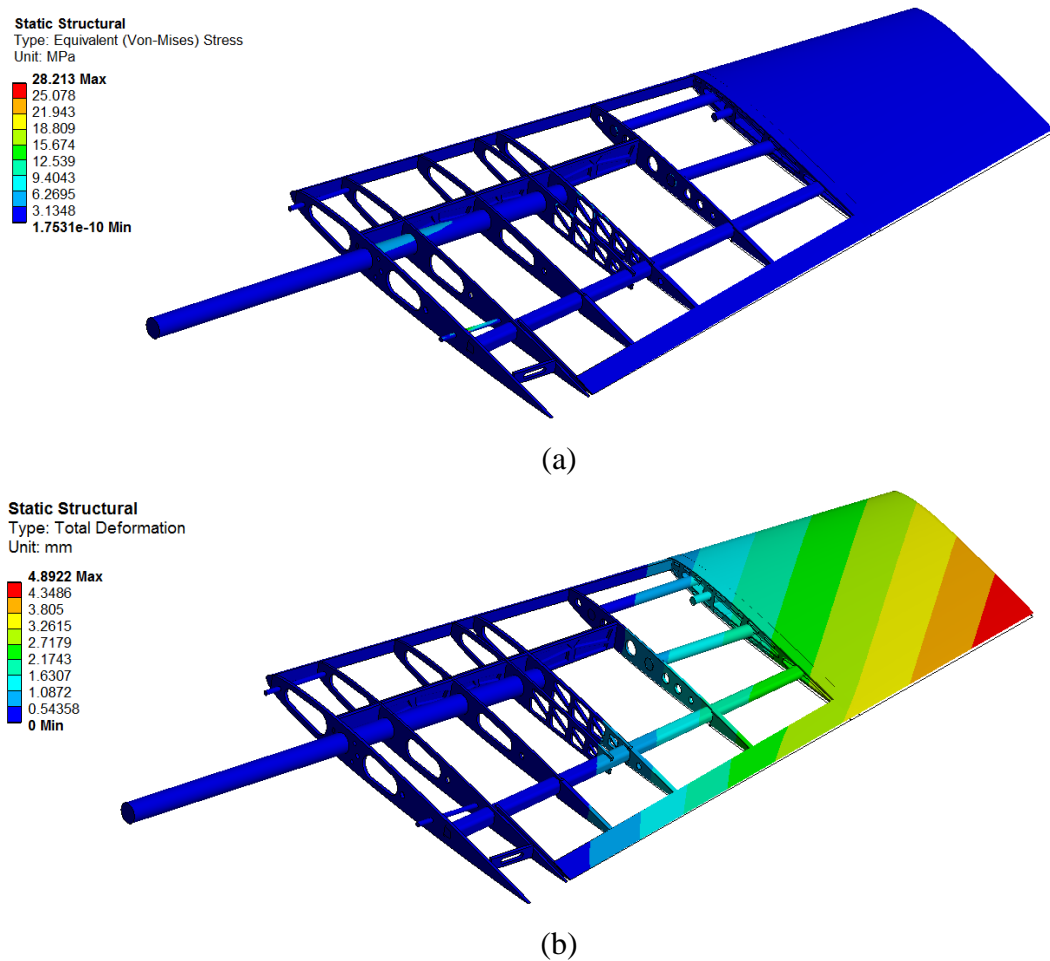


Figure 4.40 Structural analysis for full wing profile: (a) Von-Mises stress and (b) total deformation.

After completing the structural design, the wings were modified. Initially, as stated previously, the wing tip was cut to 0.3m long and the surface stripped. The configuration is shown in **Figure 4.41 (a)**. It can be seen that the structure has aileron elements that needed to be rigidly fixed. Therefore, the connection between the ailerons and the wing was fixed with balsa wood. Superglue was applied as illustrated in **Figure 4.41 (b)**.

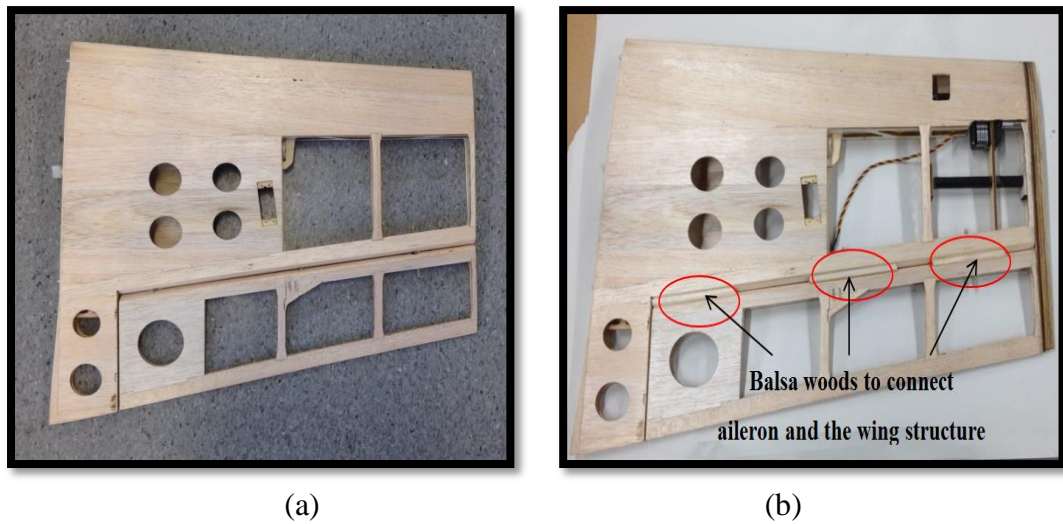


Figure 4.41 Full wing profiles: (a) normal wing structure and (b) Modified wing structure (bottom side).

While the wings were being manufactured, the assembly of the twist mechanism and the morphing parts began. As stated previously in **Section 3.4.3**, for the twist mechanism, due to the weight requirements for an actual flight environment, balsa wood sheets were used as the main material for the ribs and the inside of the rib sections (as described in **CHAPTER 5**). The number of stiffening rods selected was based on the achievable twist displacement. It can be seen from **Figure 4.43** that the final model consists of 365 balsa wood ribs, which were cut using a Laser Cutter machine. The active wing model also had eight small carbon rods (each with a 0.5mm diameter) that were distributed along the wing span. These rods produced an aerodynamic smooth surface while morphing as well as making the structure able to resist aerodynamic load. Additionally, two 1.5mm diameter carbon rods were used at the origin of the wing chord. These also aimed to provide durability to the wing structure. Furthermore, the main carbon tube (10mm outer-diameter) was used to align the ribs as well as to accommodate the internal shaft to rotate the end-section. Rib assembly process is shown in **Figure 4.42** and the internal mechanism is also shown in **Figure 4.44**.

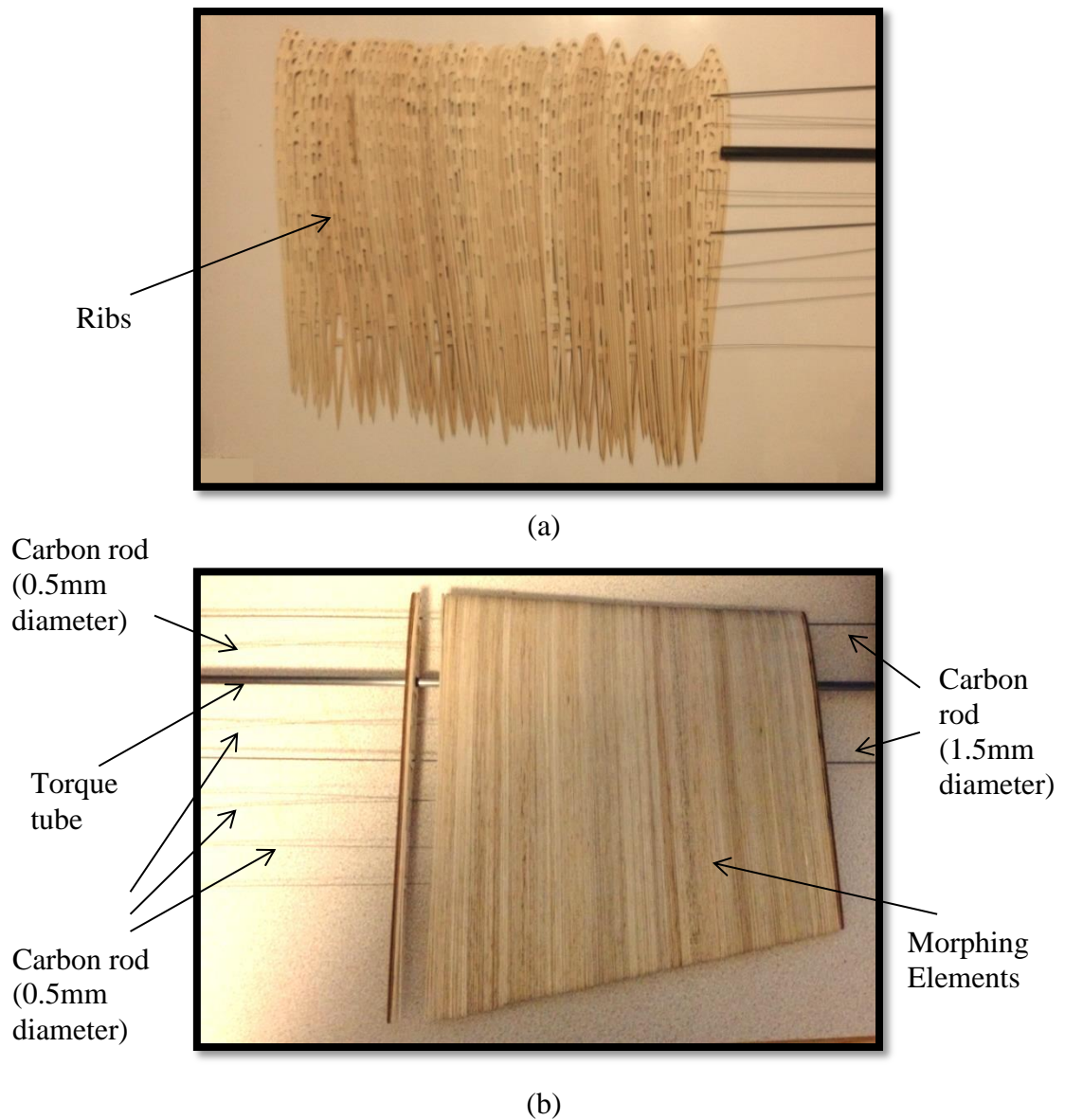
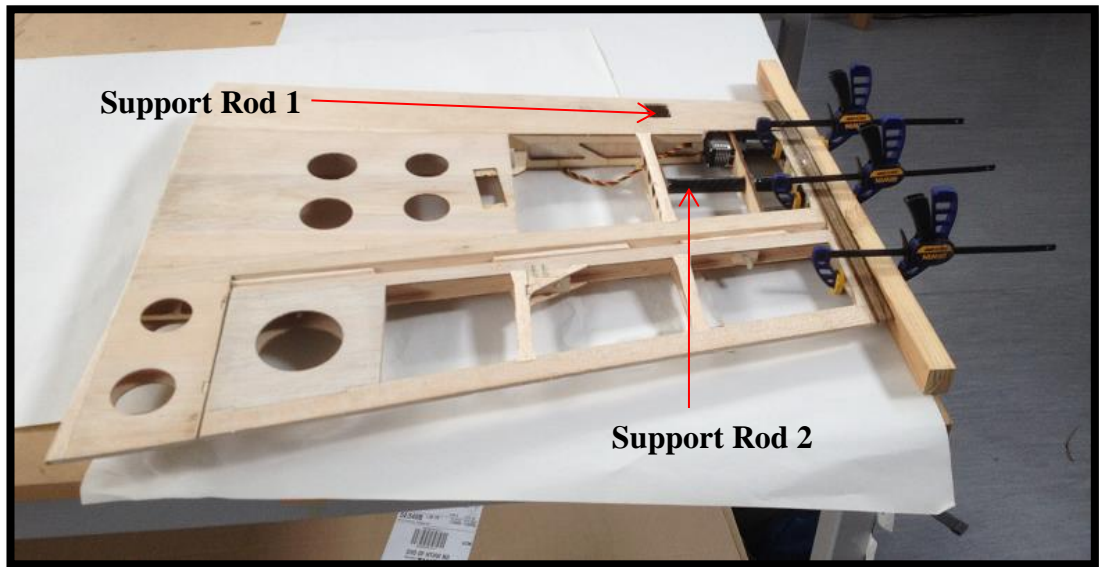
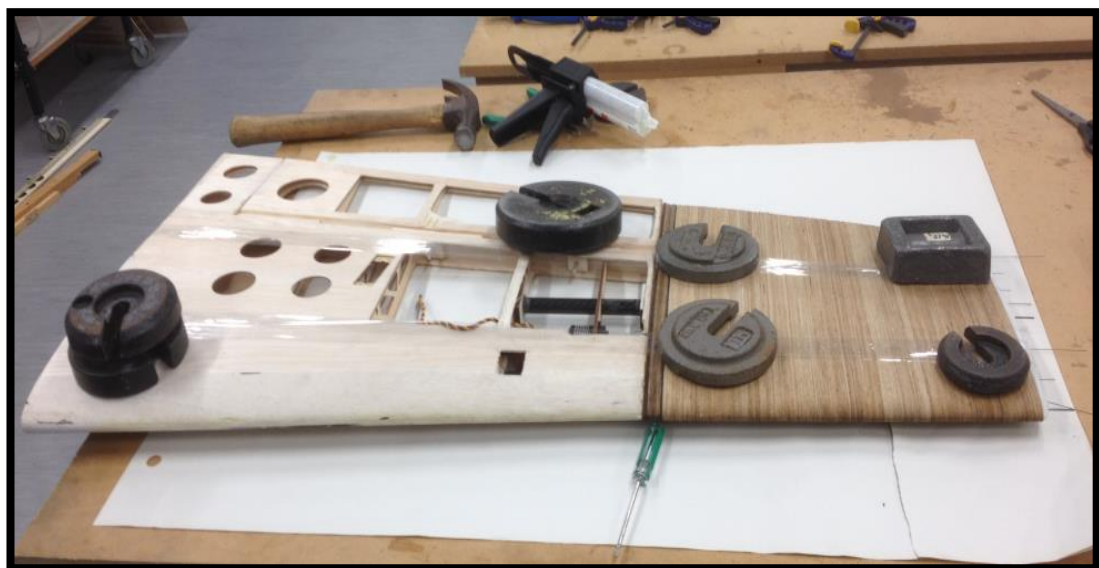


Figure 4.42 Morphing element design: (a) Rib assembly process and (b) completed morphing configurations.

It was found that, the tip of the wing structure was very weak. Additional parts were needed to increase the strength of the edge. Therefore 15mm ribs consisting of 1 piece of plywood (6mm thick) and 3 pieces of balsa wood (3mm thick) were glued to the end of the wing structure. A clamp was applied as shown in **Figure 4.43(a)** to hold the structures in position until the glue cured. Additionally, a carbon tube was used to increase the strength of the wing tip for both wings. This was important due to the morphing element creating additional load when the twist was rotated. The carbon rod tube was then glued to the main wing with the ribs able to rotate with the twist action. As shown in **Figure 4.43 (b)** weights were applied to the structure to ensure that the tube was positioned correctly.



(a)



(b)

Figure 4.43 Wing manufacturing: (a) Clamped the additional support ribs and (b) Glued active wing internal carbon tube to inside the wing model.



(a)



(b)

Figure 4.44 Internal structure of the morphing elements: (a) the point where the wing attached and (b) tip of the wing structure

The actuator mechanism for the twist movement consisted of a Hitec HS-7950 TH high voltage torque servo (which is a titanium gear coreless servo, 3.43 N-m maximum Torque at 7.4 Volt), a steel shaft, an attachment pin, bearings, a washer, nuts, and the ABS plastic made end-section. The steel shaft was positioned at the quarter chord of the wing over the span of the structure. The manufactured servo coupling held the connection between the servo motor and the steel shaft. The other side of the steel rod was connected to the end-section using a fitted attachment pin as well as additional nuts. Activating the servo rotated the end-section where all of the interconnection carbon rods were bonded. To align the steel rod with a carbon tube and to reduce any misalignment inside the carbon tube, four bearings were positioned and fixed to the steel rod. A 3mm plywood cut and was also glued to the required position inside the wing to support the servo (**Figure 4.46**). As is well known with regard to RC planes, weights play a significant role in obtaining good flight performance [180]. Taking this into account, the inside of the end section was carefully removed. It can be seen from **Figure 4.45** that maximum stress was 43.963MPa which is acceptable with a steel yield stress of 250MPa.

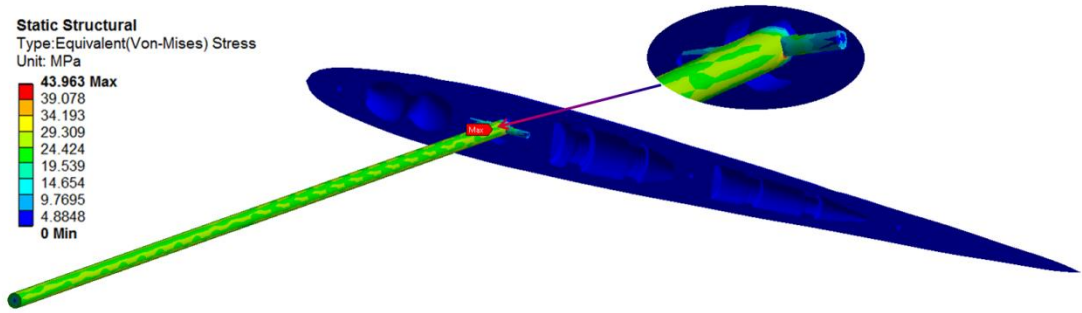


Figure 4.45 Stress Analysis of end-bit due to rotation.

The surface needed to be as smooth as possible, because discontinuities on the surface have a negative effect on the aircraft's performance. To prevent any undue aerodynamic flow behaviour, the complete morphing elements were sanded as shown in **Figure 4.46**. For the wing, the surface was covered with red adhesive plastic film. The final wing is shown in **Figure 4.47**.

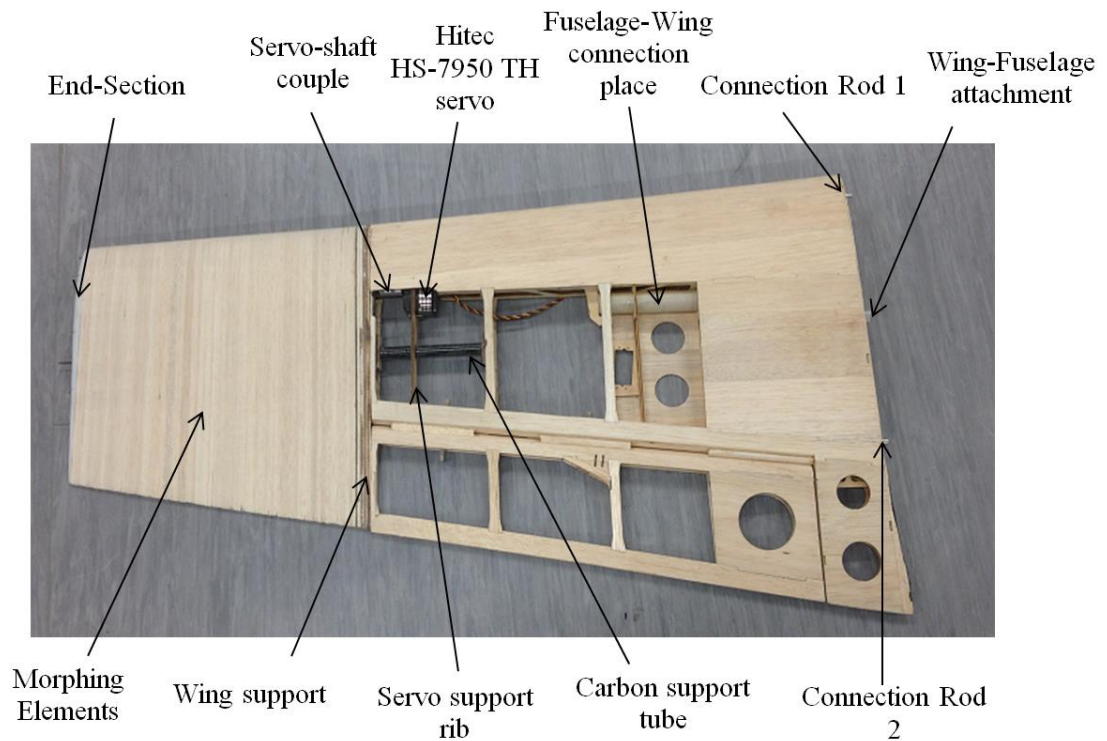


Figure 4.46 Final structure of a wing model.



Figure 4.47 Preparing wing for covering.



Figure 4.48 Wing Structures: Fixed wing with an aileron (top side) and wing with twist section (bottom side).

After installing all servo mechanisms, shafts and electrical connections, baseline and morphing concept were compared to investigate any differences between these two wing configurations. It can be seen in **Figure 4.49**, that the baseline wing was

lighter (54 gram less) than the morphing wing. The final installed morphing wing is shown in **Figure 4.53**.



(a)



(b)

Figure 4.49 Scale Measurements: (a) Fixed (baseline) wing and (b) morphing wing.

4.4.2 Instrumentation

Figure 4.51 illustrates the instrumentations used for flight testing. A Futaba R617FS 2.4 GHz FASST 7-Channel receiver was used as the main controlling device. Servo cables, which provide wing twist, pitch, yaw and thrust, were connected to the receiver. These control surfaces were controlled by the transmitter (Futaba T10CG 2.4GHz 10-Channel T-FHSS radio system) as shown in **Figure 4.50**. An Eagle Tree data flight recorder was used with a Seagull wireless data transmitter that used a static pressure / pitot tube/ transducer combination for flight

speed and pressure altitude, a magnetic RPM sensor for motor RPM, a thermocouple for temperature and a two axis accelerometer for g-forces in the rolling axis. Note that the G-force device was positioned on the plane's cg. The Eagle tree recorder also recorded the servo positions and control inputs from the radio. Data were recorded at 10 Hz and saved on an on-board computer. Velocity, altitude and signal strength were continuously transmitted to a ground station. The data recorder utilises a USB cord to communicate with the Eagletree software loaded on a laptop computer. RC Logger Video Telemetry and Orientation G-Force Module was also used to measure pitch angle, roll angle, direction, linear acceleration, angular position, and velocity during flight.



(a)



(b)

Figure 4.50 Futaba radio systems: (a) Transmitter and (b) Receiver.

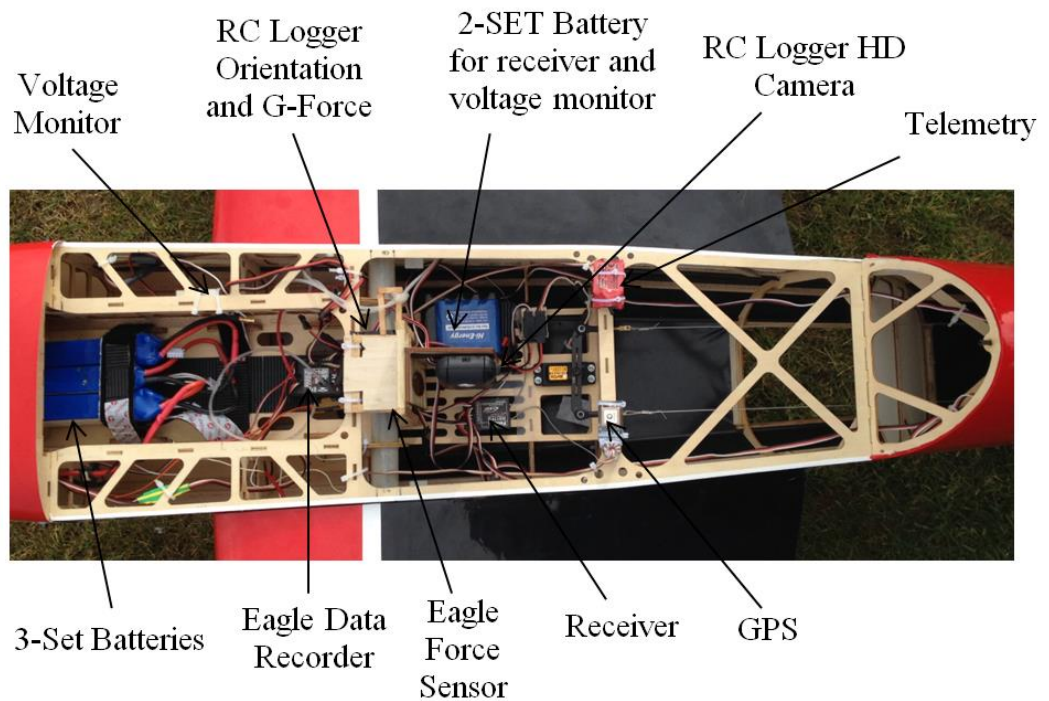


Figure 4.51 Aircraft Instrumentations.

4.4.3 Flight Environment and Testing procedures

The flying site used for this study was Little Harlington Playing Fields (**Figure 4.52**). The red line illustrates the circuit shape which was flown. In total 4 circuits were completed. Two of them were with a fixed wing configuration and the other two were with the morphing configuration. Flight data were recorded for each circuit and then analysed to investigate flight performance.



Figure 4.52 The flying site: Little Harlington Playing Fields

The testing procedure was as follows:

Before flight:

- Check environment to see if it is suitable to fly.
- Check the aircraft.
- Turn the transmitter power on before the receiver and connect the batteries to run the receiver.
- After running the electronics, check all of the control surfaces and make sure that the controls are working properly. Check the trim levers on the transmitter. Push the control sticks to the right and witness the rudder moving right and when the control stick moves to the left, the rudder moving left. Then, pull the control sticks to the up and observe the

elevator moving down and when down the elevator moving up. Similarly, check the twist moment. Here, push the control stick left and observe the washout effect on the left wing.

- Run the propeller and check that it is working properly.
- The data recorder was checked.



(a)



(b)

Figure 4.53 Flight Testing: (a) Wing with ailerons and (b) Wing with morphing concept.

During Flight:

- During the flight, the pilot control the aircraft and carry out basic manoeuvres to see if the morphing wing structure provided adequate roll control.
- While the pilot was controlling the plane, the required data was recorded by the ground station.

After flying:

- Once the flight circuit was completed, the flight battery was turned off and disconnected. Then the transmitter turned off.
- The recorded data were downloaded.

4.5 Summary

The experimental setups and apparatus used for testing were described in this chapter. This included the wind tunnel environment and the models used. Before tunnel use, the model was built based on the wind tunnel blockage requirements and then integrated with the morphing mechanism inside a baseline wing section. In order to make a direct comparison and further validate the morphing concept, a traditional aileron system for roll control with six different ailerons ($\pm 10^\circ$, $\pm 20^\circ$ and $\pm 30^\circ$) was also designed and manufactured. Following that, wind tunnel apparatus such as load cell, hotwire system, data acquisition systems, boundary layer plate, AOA mechanism, and AMTI support frame were described. Before testing, wind tunnel wake surveys were conducted to measure and understand the qualities of the wind tunnel. Using hotwire, the velocity variation and turbulence intensity was also measured before testing of by varying twist and aileron deflections.

CHAPTER 5 RESULTS AND DISCUSSION

5.1 Introduction

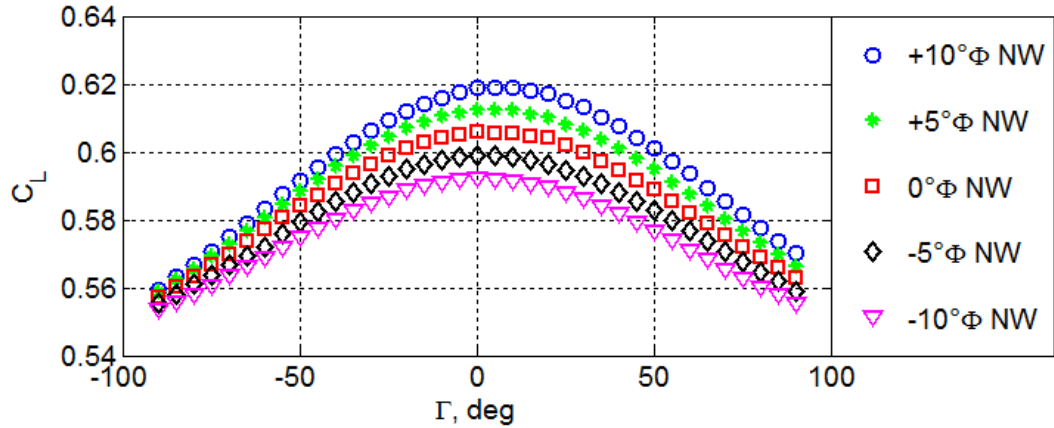
This chapter presents and discusses the computational and experimental results for morphing concept. The initial work involves investigating various swept wing and winglet configurations to gauge the possible benefits available. For this work, **Section 5.2** presents the computational analysis (Athena Vortex Lattice) for this configuration considering varying degrees of twist ($-10^\circ \leq \phi \leq 10^\circ$), sweep ($-40^\circ \leq \Lambda \leq 40^\circ$), and dihedral angle ($-90^\circ \leq \Gamma \leq 90^\circ$). From **Section 5.2.1** to **Section 5.2.4.1** provide details of the influence of these on the static force and moments. Using this data for insight, results from a simple wing with morphing concept is presented and discussed. These results included direct experimental comparison to a traditional aileron-based control system for roll control (**Section 5.3**). Finally, flight testing results were presented and discussed in **Section 5.4** with the chapter concluded with a brief summary (**Section 5.5**).

5.2 Initial Computational Results for Swept Wing/Winglet Configurations

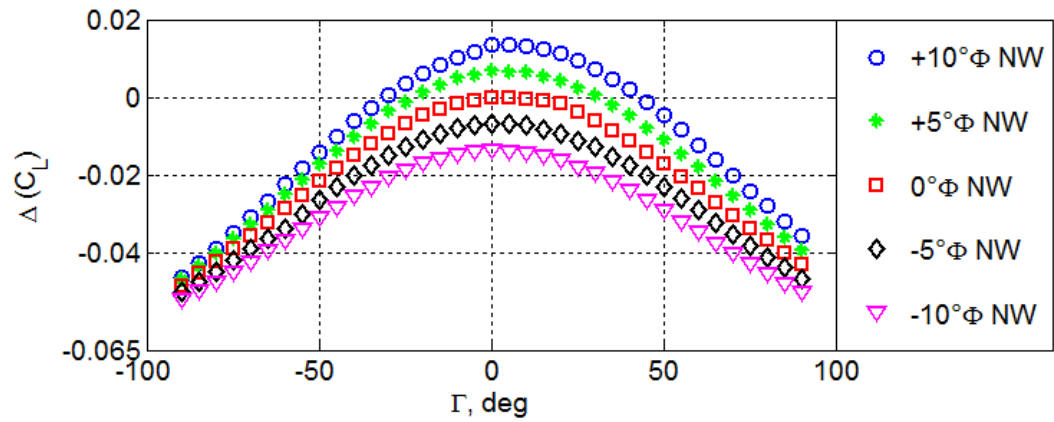
The concepts investigated in this exploratory investigated consist of various winglet configurations centred on a baseline swept wing. The impetus for the work was to identify winglet configurations that best to enhance the aerodynamic efficiency of a swept wing/winglet morphing aircraft configuration. The detail of the computational methodology and setup is shown in **Section 3.2**.

5.2.1 Effects of Changing Winglet Dihedral Angle on the Static Force and Moment Coefficients

The change in static force and moments coefficients obtained from single winglet (port side) deflection between $-90^\circ \leq \Gamma \leq 90^\circ$ are shown in **Figure 5.1**. From **Figure 5.1**, it can be clearly seen that deflecting the winglet through both $\Gamma < 0^\circ$ and $\Gamma > 0^\circ$ creates an overall reduction in lift coefficient which would shift of the aerodynamic



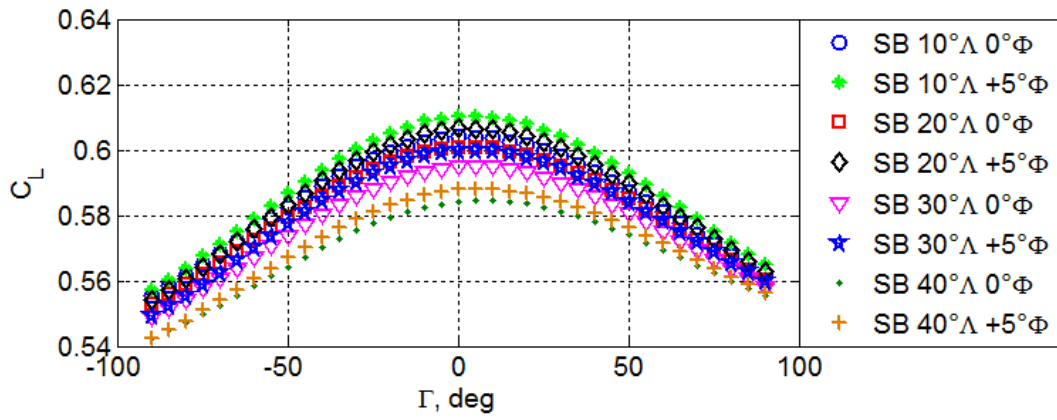
(a)



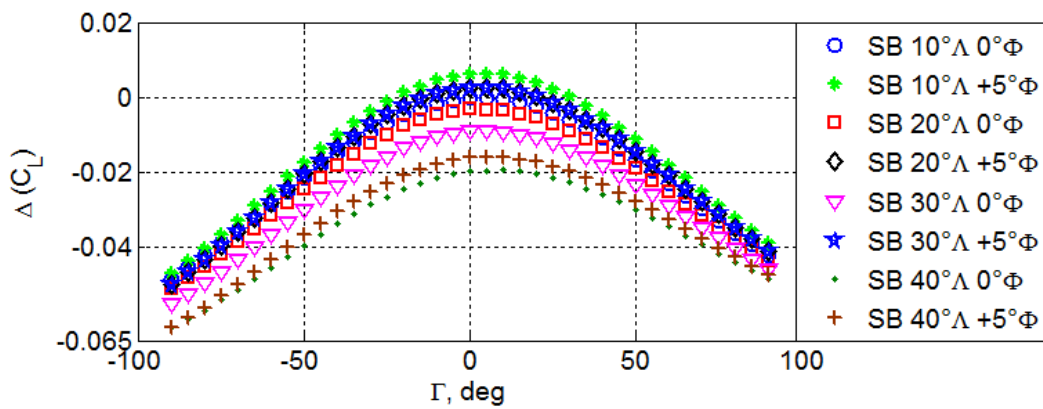
(b)

Figure 5.1 Effects of changing winglet dihedral and twist angle in normal winglet (NW) configuration at $C_{L_0} \cong 0.6$ (a) C_L and (b) ΔC_L .

load inboard (for $\Gamma = +90^\circ \Delta C_L = -0.043$, $\Gamma = -90^\circ \Delta C_L = -0.048$) in agreement with previous work [115], [131]. This mechanism is manifested through a reduction in effective lift production as the winglet rotates out of the wing plane [131]. Increasing the winglet's cant angle, also results in a reduction in lift curve slope.



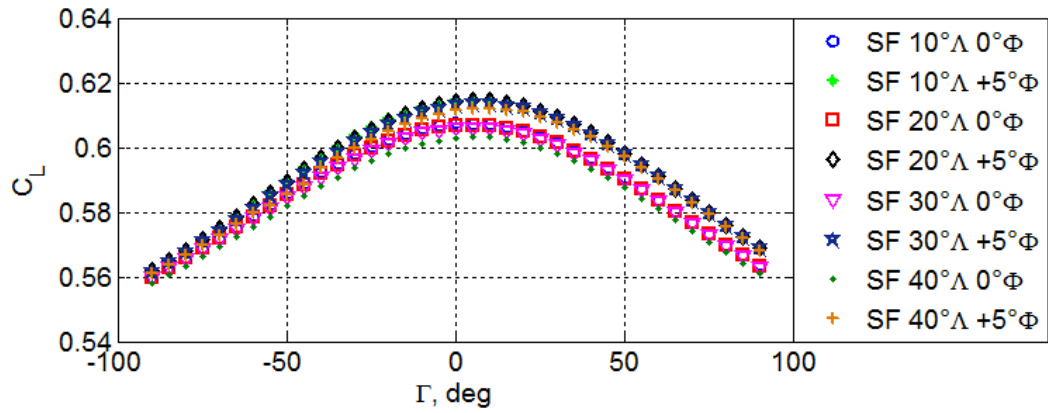
(a)



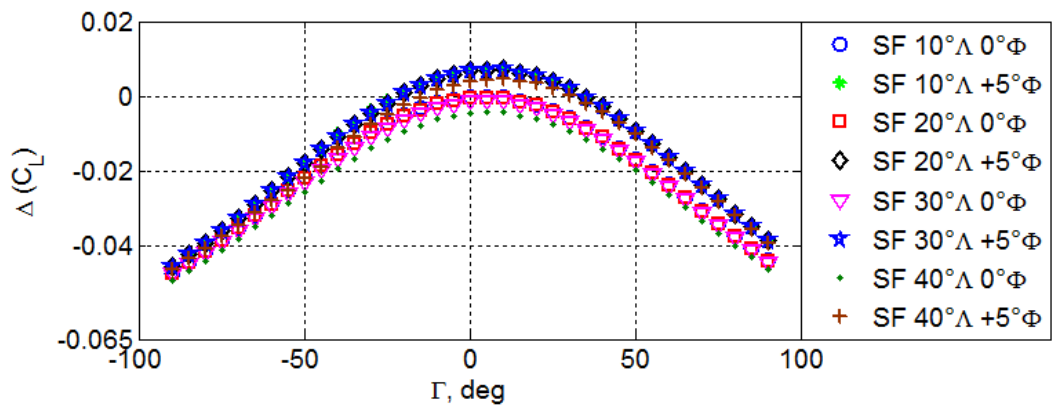
(b)

Figure 5.2 Effects of changing winglet dihedral, sweep, and twist angle in sweep back winglet (SB) configuration at $C_{L_0} \cong 0.6$ (a) C_L and (b) ΔC_L .

Moreover, in agreement with [131], there is also a tendency of asymmetrical lift reduction at $\Gamma = -90^\circ$ relative to $\Gamma = 90^\circ$ (NW), due to the use of an unsymmetrical airfoil shape. This lift coefficient reduction asymmetry (particularly evident at large winglet twist angles $\phi > 0^\circ$) is seen to favour movement to positive dihedral as both the flow is expected to more effectively maintain the upper surface low pressures as well as the loss of lift production effectiveness.



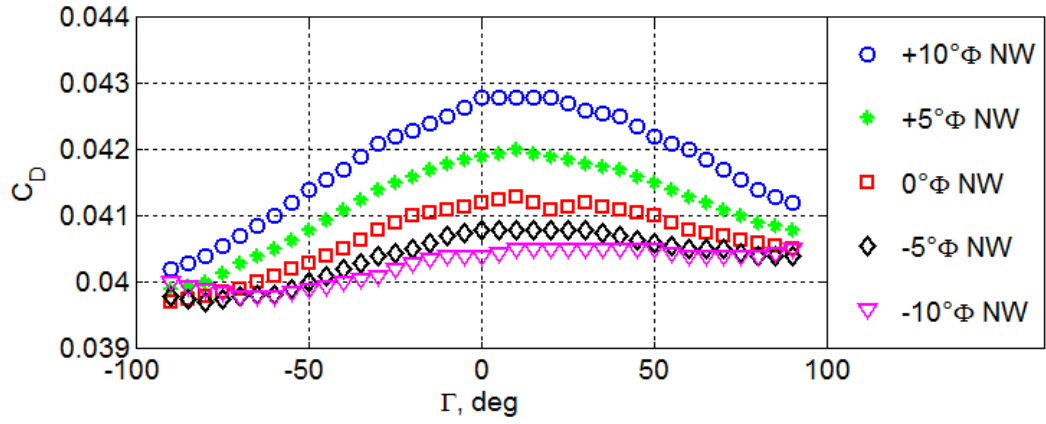
(a)



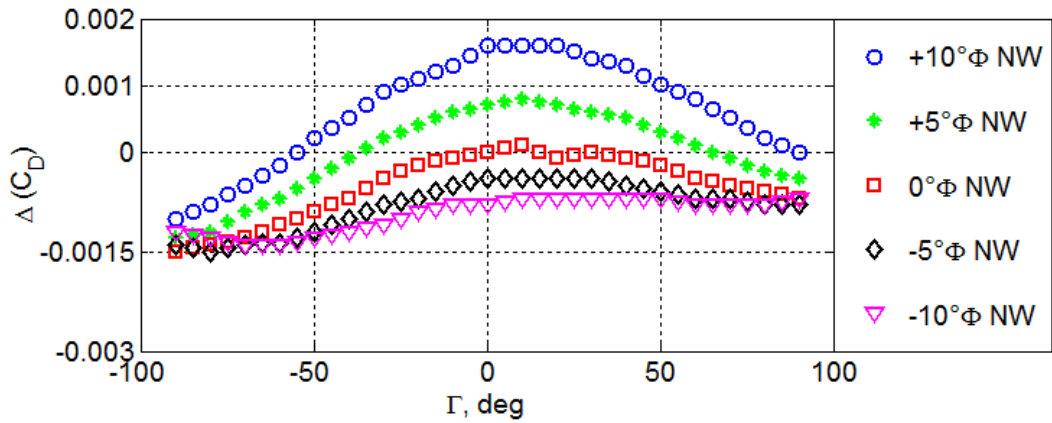
(b)

Figure 5.3 Effects of changing winglet dihedral, sweep, and twist angle in sweep forward winglet (SF) configuration at $C_{L_0} \cong 0.6$ (a) C_L and (b) ΔC_L .

Comparing **Figure 5.1**, with **Figure 5.2** and **Figure 5.3**, adding both sweepback and forward sweep to the winglet has a marked effect on wing performance. For the swept back configuration (**Figure 5.2**), the change in lift coefficient continues to show the trend seen in **Figure 5.1** with the asymmetric decrease with change in dihedral angle, favouring $\Gamma < 0^\circ$, however results for large angles of sweepback show this configuration with a maximum difference in ΔC_L from $\Gamma = -90^\circ$ to $\Gamma = 90^\circ$ of $\Delta C_L = -0.014$ asymmetric decrease was found to be further exacerbated over the normal winglet at $SB = 40^\circ$ $\phi = +5^\circ$ from $\Delta C_L = -0.010$ for NW at $\phi = +10^\circ$. For the forward swept winglet configuration (**Figure 5.3**), there seems to be much less of a variation when compared to the swept back configuration with maximum lift reduction asymmetry being $\Delta C_L = -0.044$ and $\Delta C_L = -0.047$ at $\Gamma = 90$ and $\Gamma = -90^\circ$



(a)

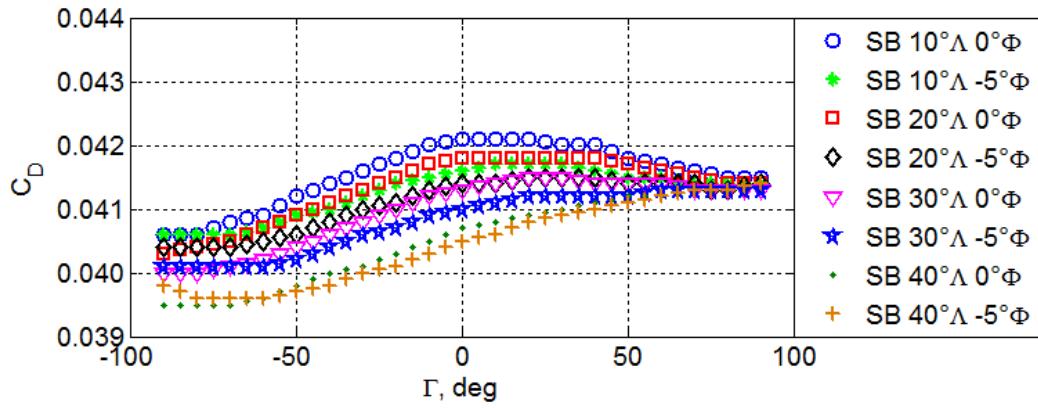


(b)

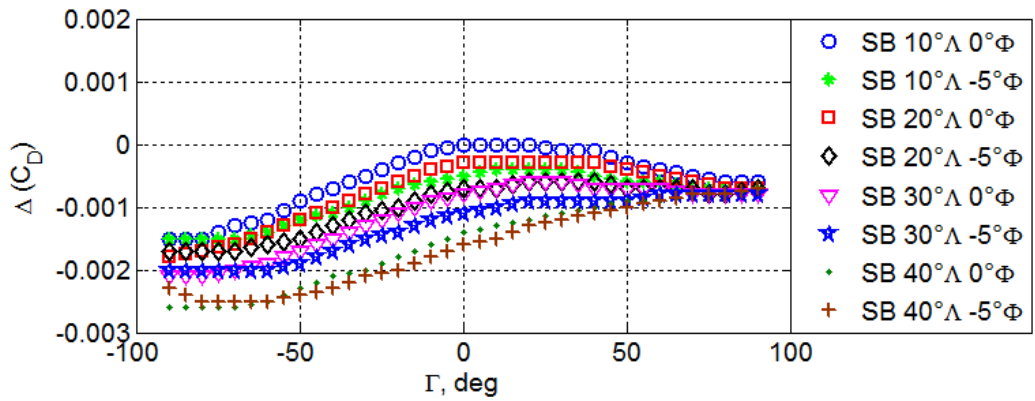
Figure 5.4 Effects of changing winglet dihedral and twist angle in normal winglet (NW) configuration at $C_{L_0} \cong 0.6$ (a) C_D and (b) ΔC_D .

respectively. One possible reason for this may lie in the increased effectiveness of sweptback winglets at interacting with the developed wingtip vortices [105].

Similar to ΔC_L , and in general agreement with [115], [131], overall drag (ΔC_D) reductions of up to 15 and 7 drag counts for $\Gamma = 90^\circ$ and $\Gamma = -90^\circ$ respectively were obtained for the normal winglet configuration (NW) shown in **Figure 5.4**. The influence of twist angle on change in drag coefficient for this configuration was also found to be substantial with maximum differences of more than 22 drag counts when winglet twist is varied from $-10^\circ < \phi < 10^\circ$. The characteristic asymmetric bias with winglet dihedral angle, evident in the results for ΔC_L , also seems to exist for ΔC_D ,



(a)

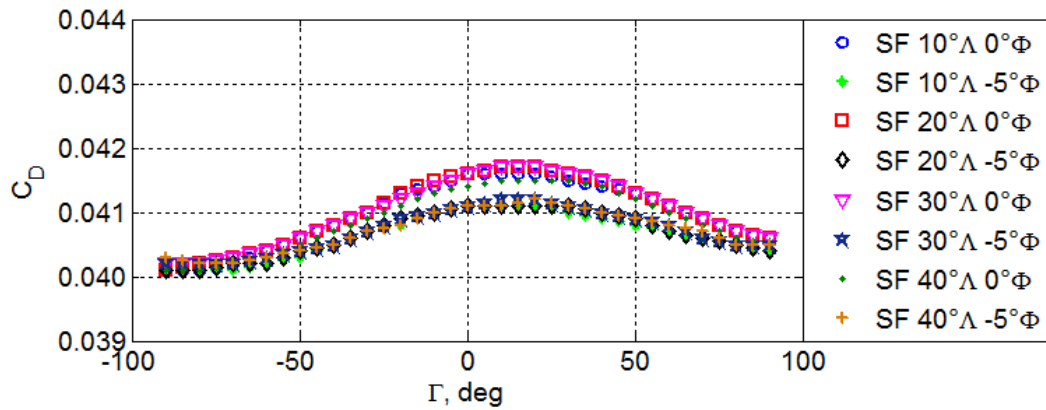


(b)

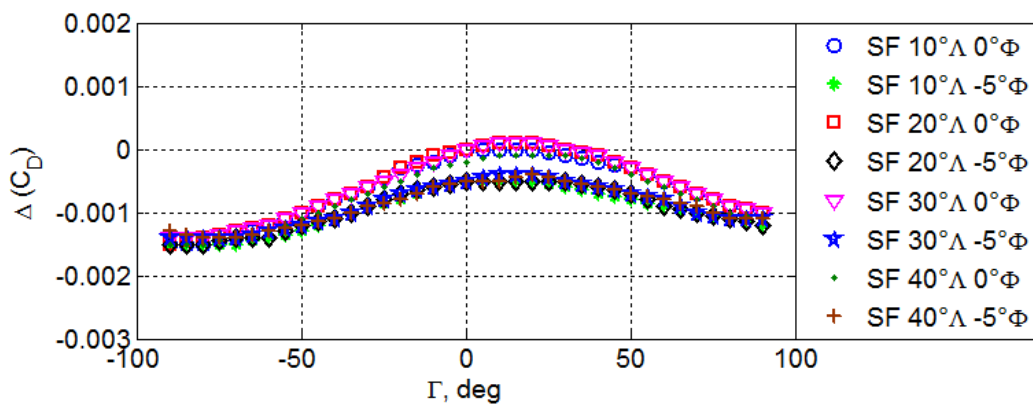
Figure 5.5 Effects of changing winglet dihedral, sweep, and twist angle in sweep back winglet (SB) configuration at $C_{L_0} \cong 0.6$ (a) C_D and (b) ΔC_D .

however the influence of a linear increase in winglet twist to maximum, as would be expected, clearly shows a non-linear dependency on ΔC_D , particularly as $\phi < 0^\circ$.

With the inclusion of both winglets swept forwards and/or backwards, similar behaviour with regards to drag reduction was observed relative to the normal winglet configuration. Comparing the normal winglet configuration to the swept back configuration (**Figure 5.5**), the degree of drag reduction has increased for most configurations at maximum negative dihedral angle position with the largest sweep angles, with no inherent twist, providing a maximum additional drag reduction of more than $\Delta C_D = 10$ drag counts. The influence of increasing sweep back angle at maximum positive winglet dihedral placement is also shown to be relatively



(a)

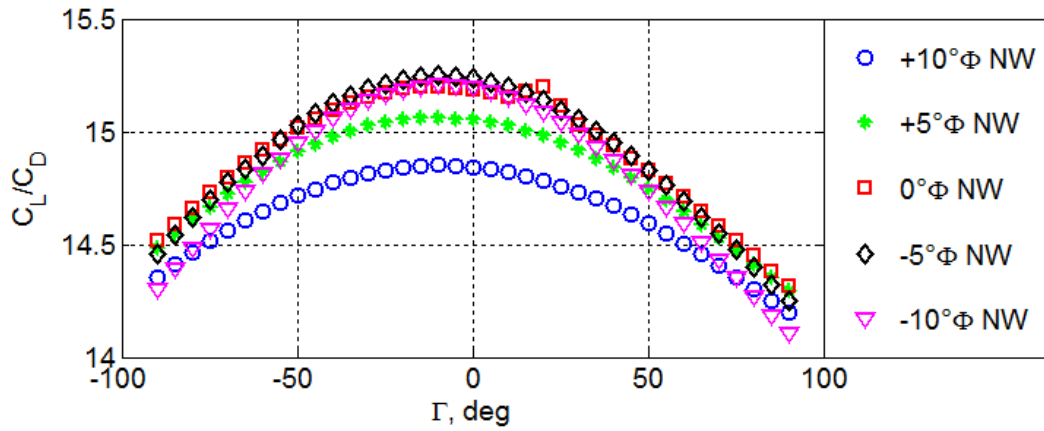


(b)

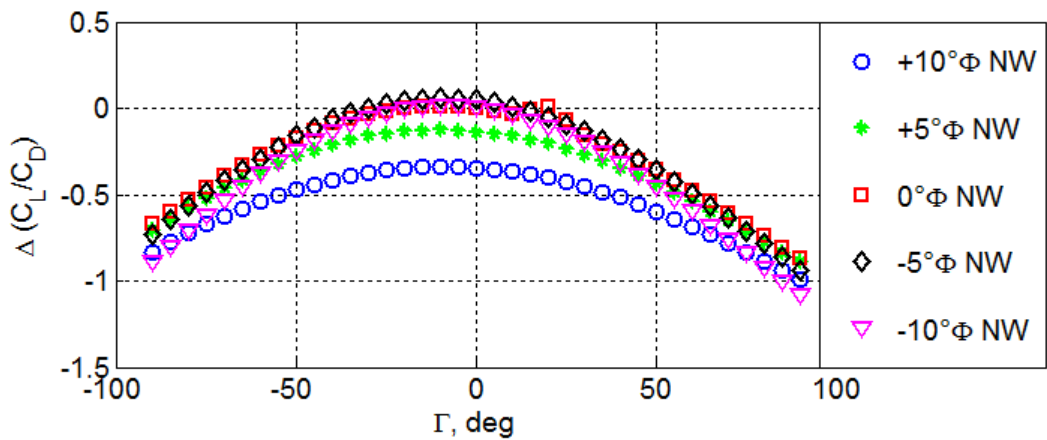
Figure 5.6 Effects of changing winglet dihedral, sweep, and twist angle in sweep forward winglet (SF) configuration at $C_{L_0} \cong 0.6$ (a) C_D and (b) ΔC_D .

insensitive to changes in drag for the cases presented. For the forward swept configuration, results from the analysis showed levels of drag reduction very similar to the normal winglet configuration with drag reductions (ΔC_D) of 15 and 12 drag counts found at $\Gamma = -90^\circ$ and $\Gamma = 90^\circ$ respectively ($\Lambda=20^\circ$ at $\phi = -5^\circ$ condition).

Lift to drag ratio plays significant role in the aerodynamic performance of an aircraft. **Figure 5.4**, **Figure 5.5**, and **Figure 5.6** detail the $\Delta C_L / C_D$ for normal winglet, swept back and swept forward configurations. In all of these configurations, and as would be expected, it can be clearly seen that the principle effect on C_L / C_D is one of a reducing magnitude with movement of dihedral angle away from planar configuration ($\Gamma = 0^\circ$). In saying this however, there exist subtle characteristics



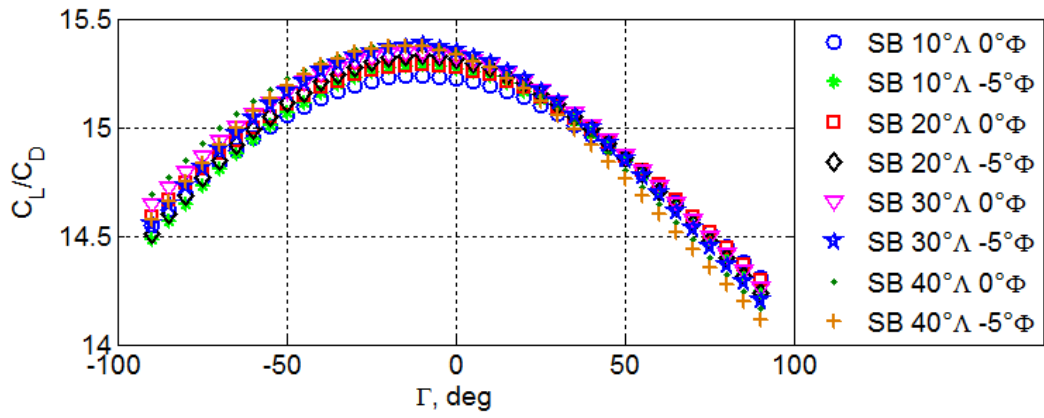
(a)



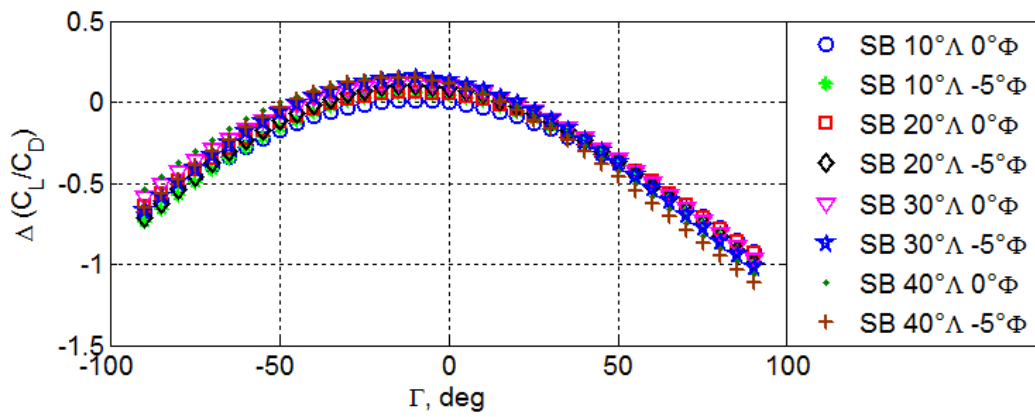
(b)

Figure 5.7 Effects of changing winglet dihedral and twist angle in normal winglet (NW) configuration at $C_{L_0} \cong 0.6$ (a) C_L/C_D and (b) $\Delta C_L/C_D$.

within the computed results that show a small degree of augmentation around this baseline planar flow case. In the region of dihedral angles from $-20^\circ < \Gamma < 0^\circ$, particularly for the sweptback configuration, there is evidence of an increase in C_L/C_D (SB= 30° , $\phi = -5^\circ$, $\Gamma = -10^\circ$) of approximately $\Delta C_L/C_D = 0.2$ (1.3%) over all other configurations tested. From **Figure 5.7** and **Figure 5.9**, there seems to be little extra benefit in terms of increased aerodynamic efficiency with either increasing wing twist or sweeping forward the winglet, however additional rearward sweep (**Figure 5.8**) does show nominal but discernible improvements in aerodynamic efficiency for most of the conditions included.



(a)

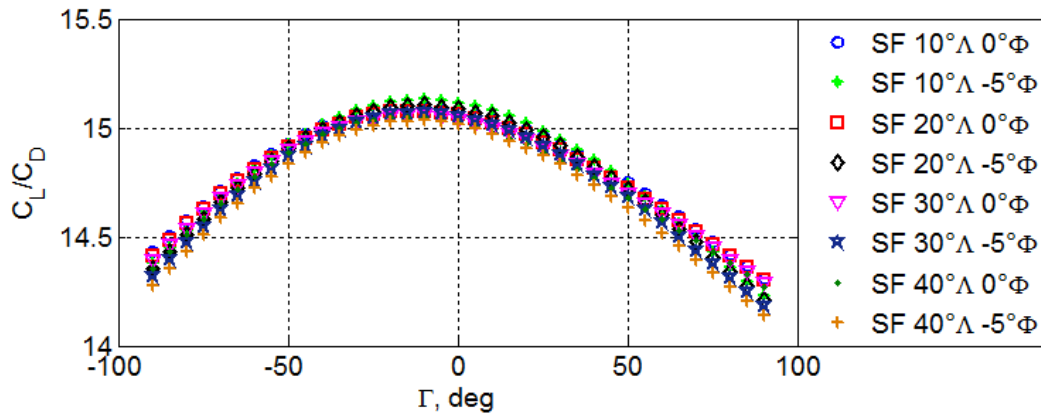


(b)

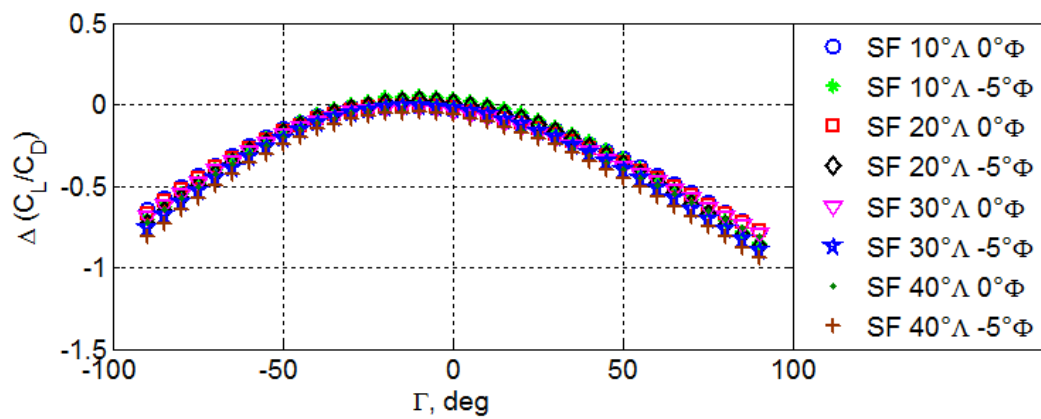
Figure 5.8 Effects of changing winglet dihedral, sweep, and twist angle in sweep back winglet (SB) configuration at $C_{L_0} \cong 0.6$ (a) C_L/C_D and (b) $\Delta C_L/C_D$.

Interestingly, the asymmetric bias evident for both the changes in lift and drag coefficient with increasing or decreasing dihedral angle has switched to favouring positive dihedral for $\Delta C_L/C_D$ with the degree of asymmetry reducing as the winglet is swept more forward. Similar results were also presented in [90]; with small dihedral angles resulting in the production of the lowest lift-induced drag.

Figure 5.10, **Figure 5.11** and **Figure 5.12** highlight the influences of dihedral angle change on the change in pitching moment coefficient. As can be seen in these figures, nose up pitching moments were the predominant action on the wing/winglet configuration with change in dihedral angle either side of the planar case ($\Gamma = 0^\circ$).



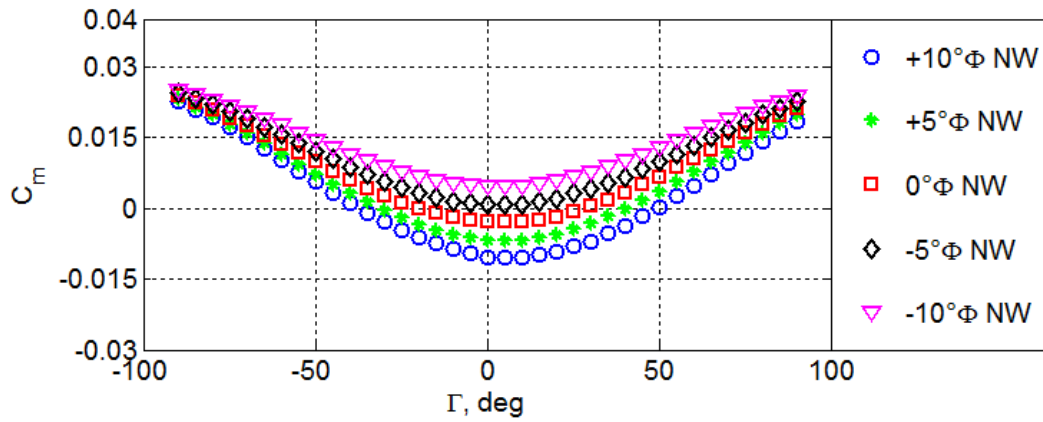
(a)



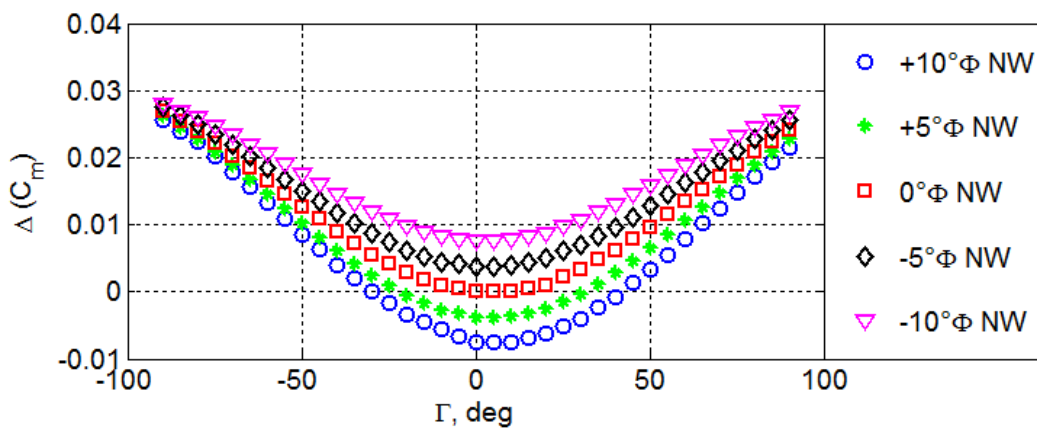
(b)

Figure 5.9 Effects of changing winglet dihedral, sweep, and twist angle in sweep forward winglet (SF) configuration at $C_{L_0} \cong 0.6$ (a) C_L/C_D and (b) $\Delta C_L/C_D$.

However, for some cases presented for the normal and swept back configurations, additional negative pitching moments were found to exist with both, with further increases in winglet twist (up to $\phi = 10^\circ$ for the NW case), as well as at increased, untwisted, values of sweepback ($\Lambda = 40$). This would be expected as winglet twist added at the near planar case would increase the pitching up moment as the winglets in this configuration are more effective at producing lift behind the c.g. Rotating the winglet from the near-planar case would therefore reduce this augmentation. Additional sweep back, observed to produce a similar result, has a comparable flow dynamic through the movement of the aerodynamic centre forward with dihedral angle increase. It is this behaviour that has been put forward as a possible means for aircraft pitch control augmentation [115].



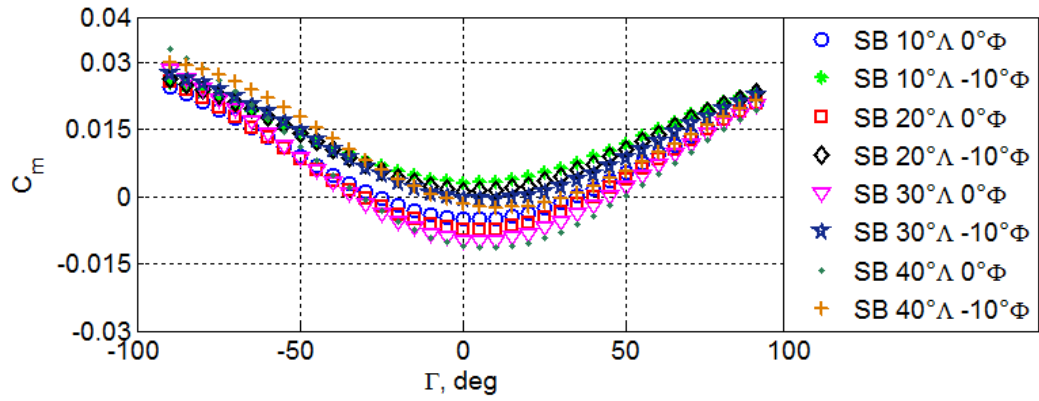
(a)



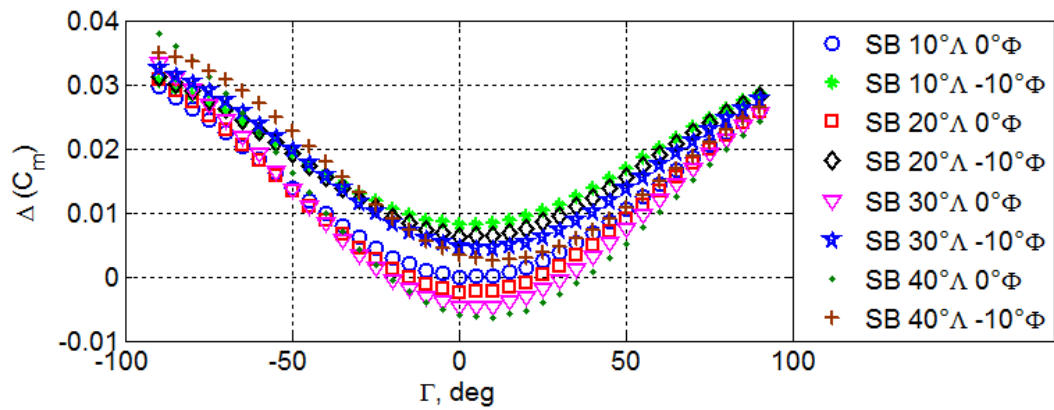
(b)

Figure 5.10 Effects of changing winglet dihedral and twist angle in normal winglet (NW) configuration at $C_{L_0} \cong 0.6$ (a) C_m and (b) ΔC_m .

Winglets have showed they are able to provide basic pitch control moments through changing dynamic static margin, quite contrary to the conventional elevator system which generates control moments by altering zero-lift pitching moment [114]. It can also be seen in **APPENDIX-A Figure A- 13**, a non-planar winglet are able to provide more nose up moment at a fixed angle of attack (the negative value of C_m is less and also with static margin reduced due to forward aerodynamic centre movements).



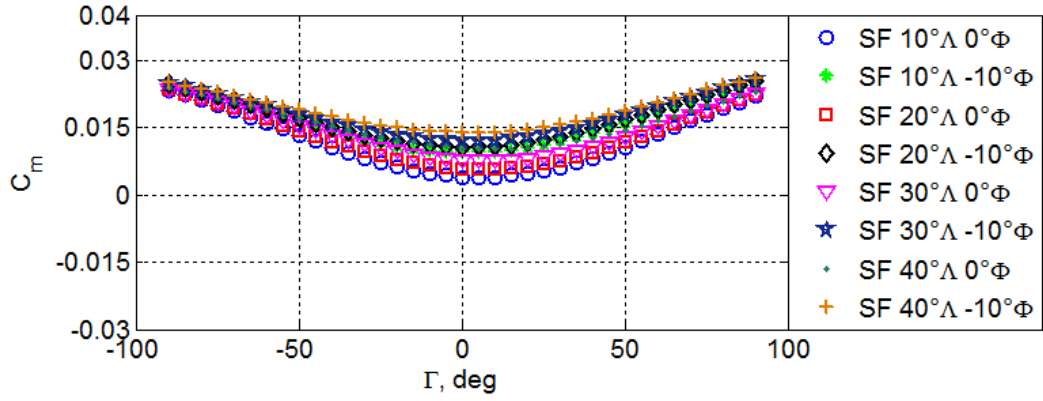
(a)



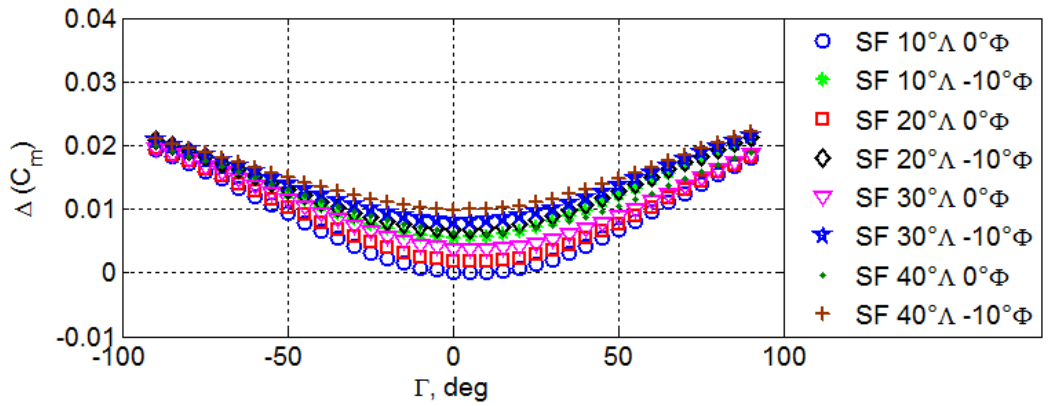
(b)

Figure 5.11 Effects of changing winglet dihedral, sweep, and twist angle in sweep back winglet (SB) configuration $C_{L_0} \cong 0.6$ (a) C_m and (b) ΔC_m .

It has also been shown previously that increases in winglet dihedral angle away from the planar configuration can provide substantial roll authority suitable for aircraft roll control [115]. **Figure 5.13(b)**, **Figure 5.14(b)** and **Figure 5.15(b)** illustrate the change in roll coefficient results for the three winglet configurations. As is shown in all of these figures, roll authority is significant with dihedral changes from $\Gamma = +90^\circ$ and $\Gamma = -90^\circ$ (max $\Delta C_l = 0.021$ NW $\phi = +10^\circ$ $\Gamma = -90^\circ$). Interestingly, for all three configurations, the maximum amount of roll coefficient change generated from dihedral angle movement is relatively invariant with either winglet sweep forward or back, however from **Figure 5.13**, for $-40^\circ < \Lambda < 40^\circ$, large levels of winglet twist angle are seen produce the opposite effect on change in rolling moment coefficient with the production of a roll moment component acting to oppose the



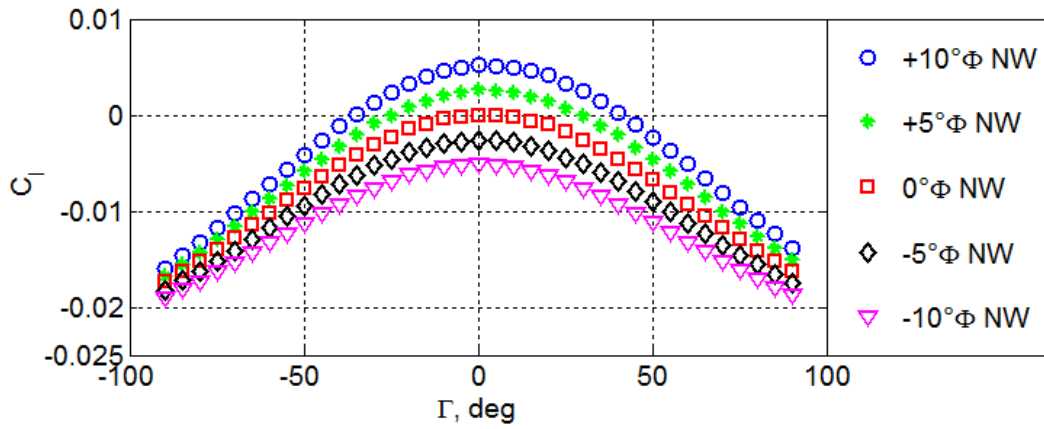
(a)



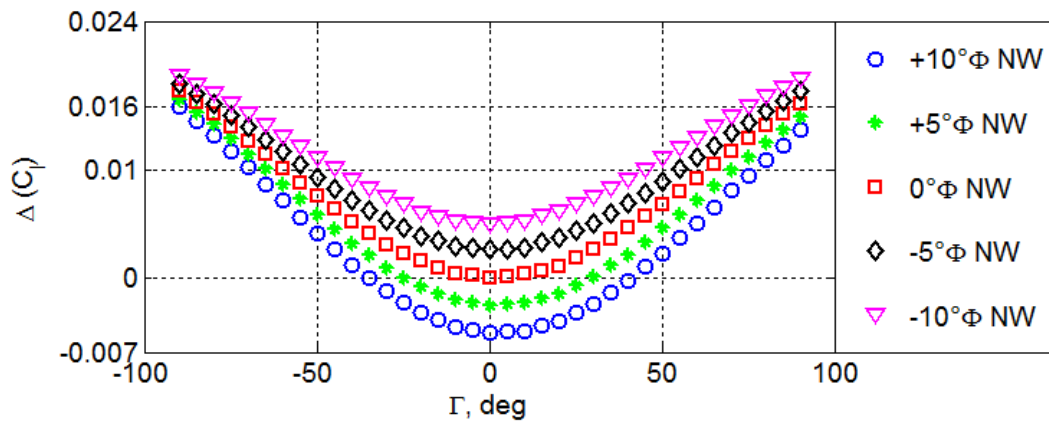
(b)

Figure 5.12 Effects of changing winglet dihedral, sweep, and twist angle in sweep forward winglet (SF) configuration $C_{L_0} \cong 0.6$ (a) C_m and (b) ΔC_m .

nominal winglet dihedral deflection dynamics at $\Gamma = -90$. Overall, however, results using this control methodology do show in agreement with [115], [131] in that comparable roll control moments relative to traditional aileron systems ($\Delta C_l = 0.0152$ - 0.0531 where $C_{L_0} \cong 0.6$) [167] can be produced. The change in yawing moment coefficient with dihedral angle change also show similar characteristics for the three main test cases considered (**Figure 5.16**, **Figure 5.17** and **Figure 5.19**). For the normal and swept forward winglet cases, there is again very little perceptible difference in the maximum control forces generated with ΔC_n being significantly larger for $\Gamma = 90^\circ$ than $\Gamma = -90^\circ$. Interestingly, for $\Gamma < 0^\circ$, the production of effective yawing moment change is much more varied than for $\Gamma > 0^\circ$, with a maximum



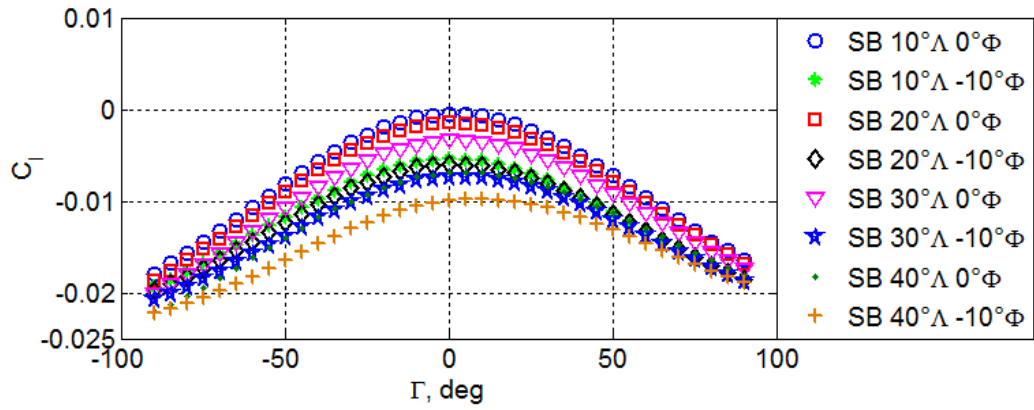
(a)



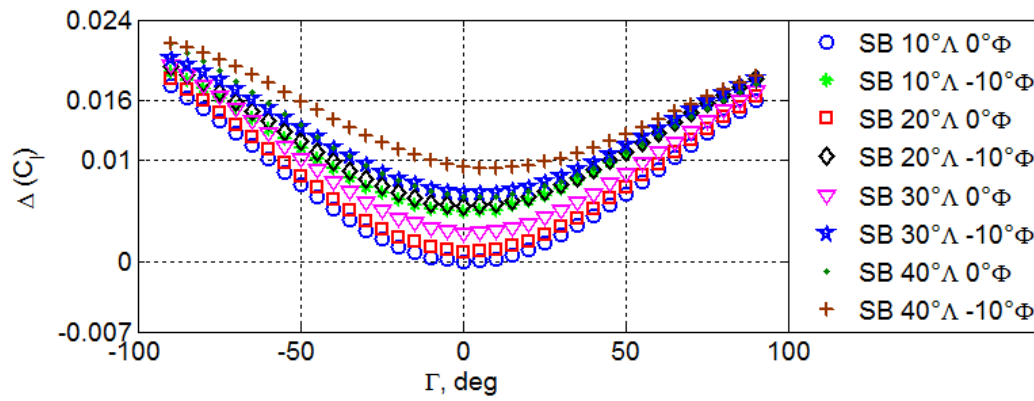
(b)

Figure 5.13 Effects of changing winglet dihedral and twist angle in normal winglet (NW) configuration $C_{L_0} \cong 0.6$ (a) C_l and (b) ΔC_l .

change generated at approximately $\Gamma = 45\text{-}50^\circ$ in agreement with previous studies [115]. For the swept back case, (**Figure 5.17**), values of change in yawing moment with winglet dihedral change were found to be markedly more scattered and of increased magnitude, particularly for $\Gamma < 0^\circ$ when compared other test cases investigation. Clearly, adding winglet sweepback, particularly with additional winglet twist, increases generated yawing moment due to the further rearward displacement of the aerodynamic centre behind the c.g.



(a)

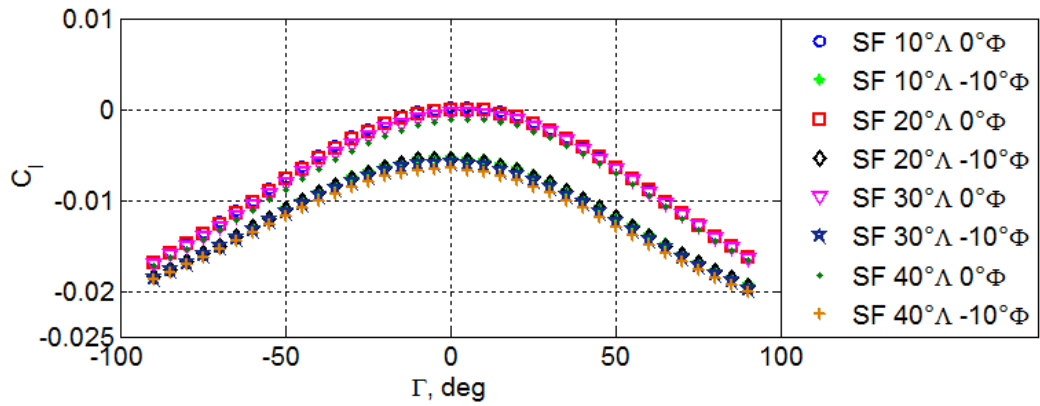


(b)

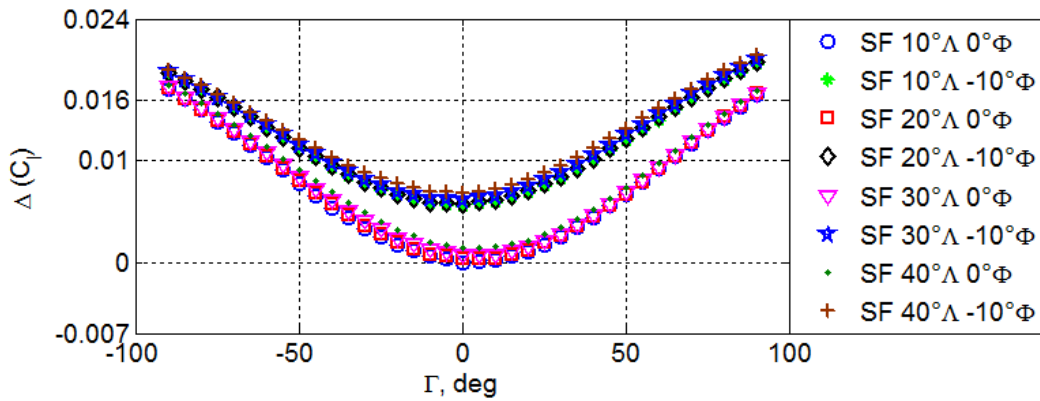
Figure 5.14 Effects of changing winglet dihedral, sweep, and twist angle in sweep back winglet (SB) configuration $C_{L_0} \cong 0.6$ (a) C_L and (b) ΔC_L .

5.2.2 Effects of Changing Winglet Twist Angle on Aircraft Control and Performance

Overall, high winglet twist angle performed well as a mechanism for control, and at up to winglet twist angles of $\phi = \pm 5^\circ$, good aerodynamic efficiency was achieved. With regards to ΔC_L , and as would be expected, positive twisted winglets provides good lift force production performance compared to negative twisted winglets, although, negatively twisted winglets to a small degree, do provide, in some cases, improved aerodynamic efficiency. As discussed already for ΔC_L and ΔC_D , winglet twist of $\phi = 10^\circ$ has a different impact on lift and drag with positive and negative dihedral angle change. This conflicting result when combined was found to reduce efficiency (3.8%).



(a)

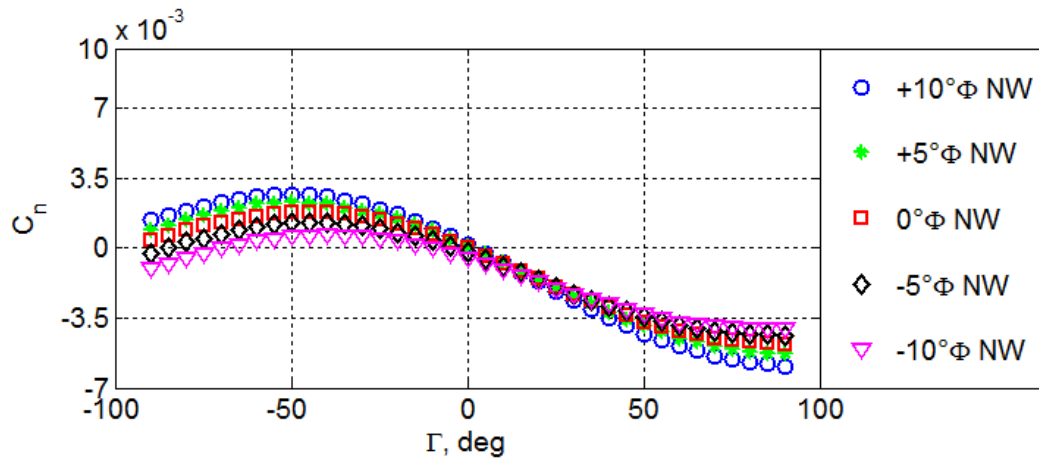


(b)

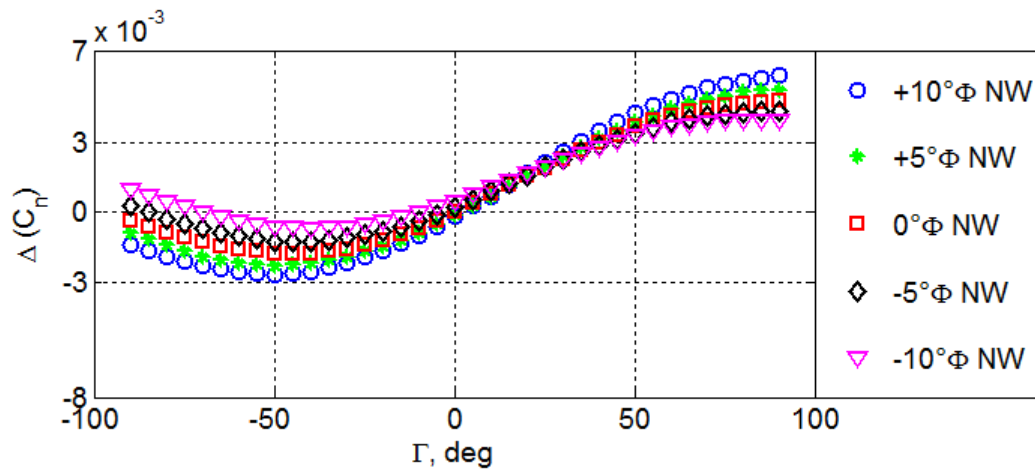
Figure 5.15 Effects of changing winglet dihedral, sweep, and twist angle in sweep forward winglet (SF) configuration $C_{L_0} \cong 0.6$ (a) C_l and (b) ΔC_l .

For some twist cases investigated, the overall lift characteristics could be reduced with negative twist ($\Delta C_L = -0.013$ NW at $\phi = -10^\circ$ $\Gamma=0^\circ$) and increased with positive twist angle ($\Delta C_L = 0.015$ NW at $\phi = +10^\circ$ $\Gamma=0^\circ$). Quite distinct from the swept back and normal winglet configurations, winglet twist for the swept forward configuration was found to have a minor influence on various aerodynamic and control metrics with the most notable contributions occurring at small levels of winglet twist angle $\phi = \pm 5^\circ$.

For the moment coefficient values, increasing winglet twist angle typically increases the degree of moments generated with maximum values occurring at maximum degrees of twist. Inducing additional winglet twist in the swept back and swept forward configurations has a similar influence as discussed for normal winglet



(a)



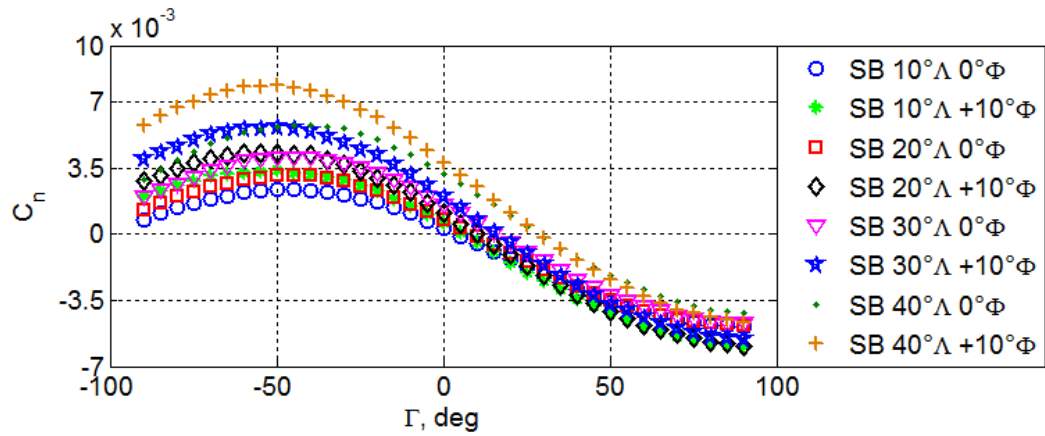
(b)

Figure 5.16 Effects of changing winglet dihedral and twist angle in normal winglet (NW) configuration $C_{L_0} \cong 0.6$ (a) C_n and (b) ΔC_n .

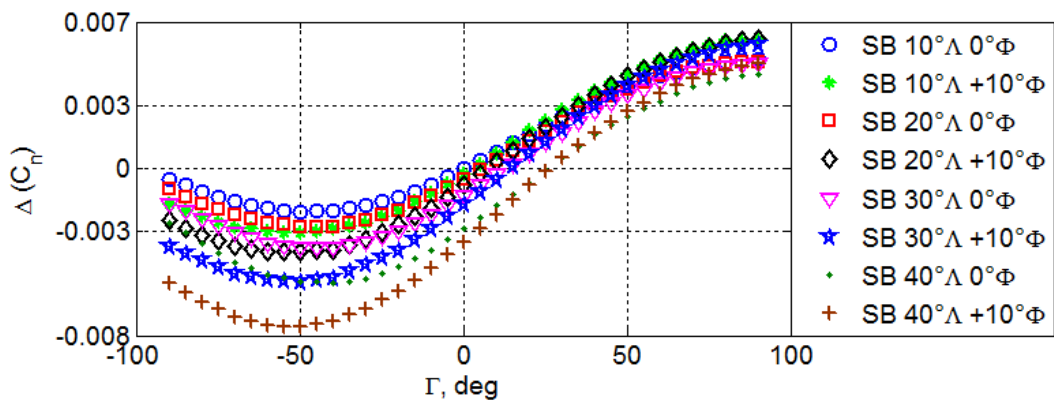
configuration in terms of control with increasing twist angle up to $\phi = \pm 10^\circ$ found to increase roll, pitch, and yaw moments. Overall, increasing winglet dihedral angle either side of the planar case, further increases the change in moment coefficient, however, the generation of maximum yawing moment coefficient does not occur at maximum winglet deflection, but at approximately -40° to -50 degrees from planar.

5.2.3 Effects of Changing Winglet Swept Angle on Control and Performance

For the most part, with respect to ΔC_L changing winglet sweep angle does have a detrimental effect on lift production with for the most part, a positive influence on



(a)

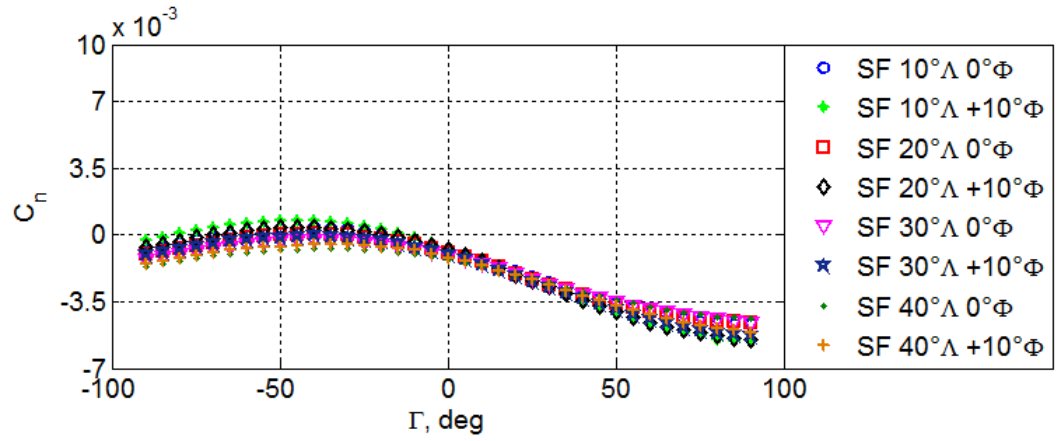


(b)

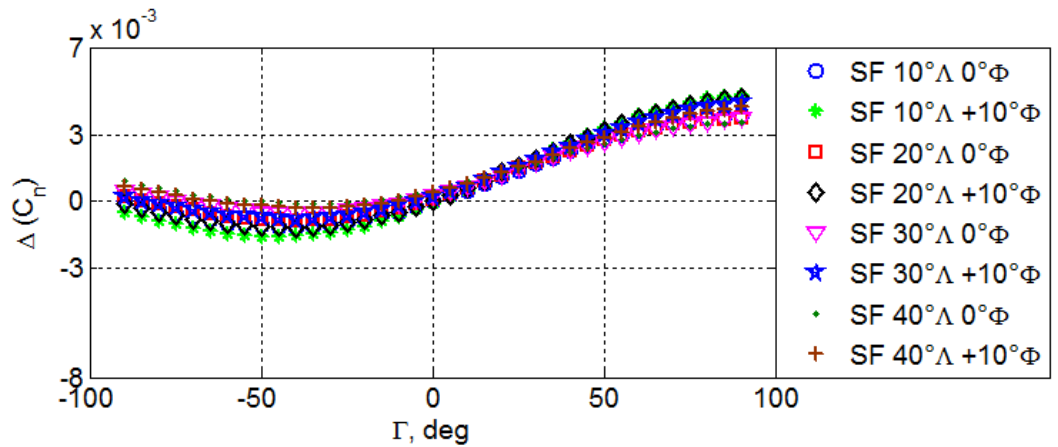
Figure 5.17 Effects of changing winglet dihedral, sweep, and twist angle in sweep back winglet (SB) configuration $C_{L_0} \cong 0.6$ (a) C_n and (b) ΔC_n .

drag with the highest $\Delta C_L / C_D$ found at $\Lambda = 30^\circ$ compare to other swept configurations. This is further supported by work done in [102] where different winglet sizes with different winglet sweep were investigated showing swept back winglets of approximately $\Lambda = 25^\circ$, gave the highest C_L/C_D .

With forward swept winglets, change in lift coefficient was found be reasonably invariant; however at this condition, increases in lift production were found at low to moderate sweep angles. Unlike the sweptback winglet configuration, forward sweep was also found not to yield a significant increase C_L/C_D with typically, an overall reduction evident.



(a)



(b)

Figure 5.18 Effects of changing winglet dihedral, sweep, and twist angle in sweep forward winglet (SF) configuration $C_{L_0} \cong 0.6$ (a) C_n and (b) ΔC_n .

From the perspective of control moment production, swept-back configurations offer augmented control moment generation with increasing sweep angle. For pitching moment in particular, the basic mechanism of increased pitch-up moment via changing dihedral angle from the planar configuration is evident.

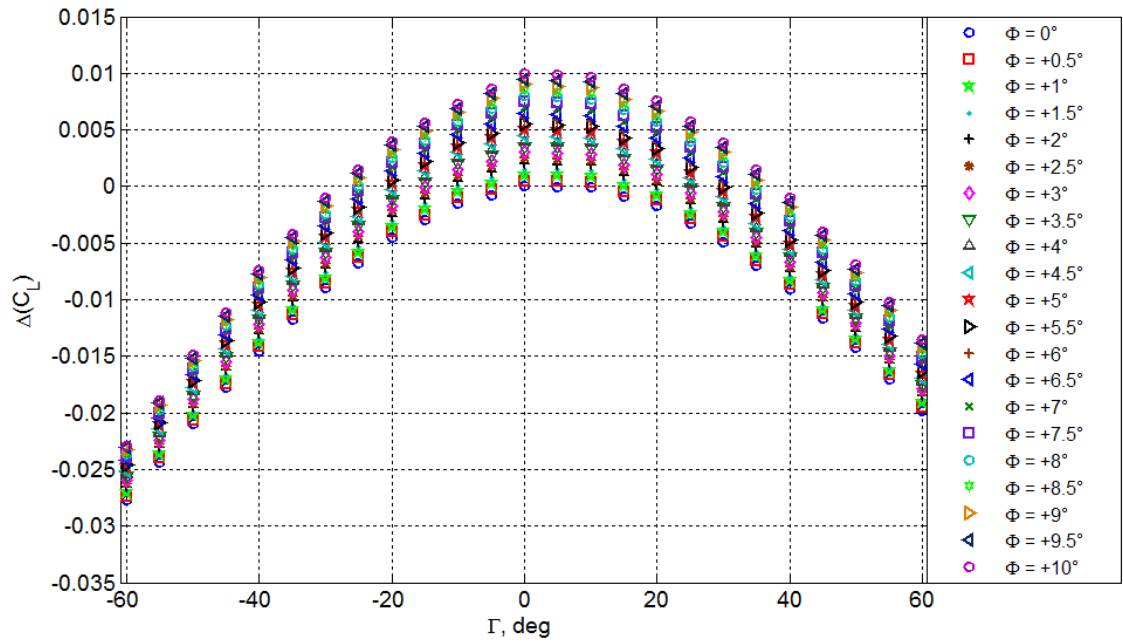
5.2.4 Optimized Winglet Sweep Angle and Twist Analysis

From the preceding analysis (From **Figure 5.8**), $\Lambda = 30^\circ$ swept winglets performed the best when compared to other swept cases presented. Therefore, in all subsequent analysis for winglet twist and dihedral angle, sweep angle was set at $\Lambda = 30^\circ$.

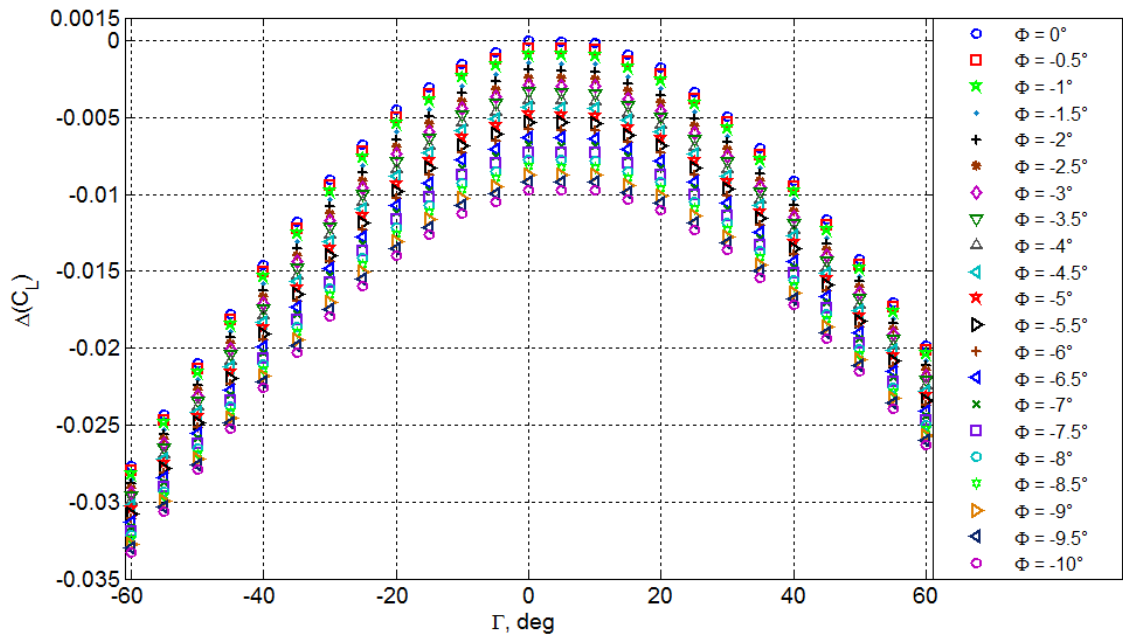
5.2.4.1 *Effects of Changing Dihedral Angle on Twisted Winglet Performance*

The change in static force coefficients and C_L/C_D obtained from the winglet deflection between $-60^\circ \leq \Gamma \leq 60^\circ$. It can be clearly seen from **Figure 5.19 (a)** that deflecting the winglet through both $\Gamma < 0^\circ$ and $\Gamma > 0^\circ$ in a positive-twisted configuration creates an overall reduction in lift coefficient (for $\Gamma = 60^\circ \Delta C_L = -0.02$, $\Gamma = -60^\circ \Delta C_L = -0.028$ at $\phi = +10^\circ$) in agreement with previous work [131]. As also be mentioned in **Section 5.2.1**, this mechanism is manifested through a reduction in effective lift production as the winglet rotates out of the wing plane [131]. Also, as would be expected, due to the use of a Zagi 12% airfoil shape within the swept wing configuration, there is a tendency of asymmetrical lift reduction at $\Gamma = -60^\circ$ relative to $\Gamma = 60^\circ$ ($\phi = -10^\circ \Delta C_L = 0.008$). This lift coefficient asymmetry is seen to reduce less for movement to positive dihedral angle as both a non-symmetrical airfoil was used and the flow is expected to be more effective at the maintaining the upper surface low pressures for $\Gamma = 60^\circ$. It can also be seen that the change in lift coefficient continues to show the trend seen in **Figure 5.19 (a)** with reductions in lift coefficient as dihedral angle increases or decreases. As would also be expected, results in **Figure 5.19 (b)** show overall net lift reductions ($\Delta C_L = -0.033$ at $\phi = -10^\circ$, $\Gamma = -60^\circ$) compared to **Figure 5.19 (a)** as less lift is produced in the negatively-twisted winglet configurations.

Similar to ΔC_L , and in general agreement with, [131], maximum overall drag (ΔC_D) reductions of up to 15 and 6 drag counts (for $\Gamma = -60^\circ$ and $\Gamma = 60^\circ$ respectively $\Gamma = 0^\circ$ baseline) were obtained for the $\phi = 10^\circ$ winglet configuration shown in **Figure 5.20 (a)**. When dihedral angle increases from $\Gamma = 0^\circ$ to 60° , winglet twist angles of up to $\phi = 3^\circ$ show little benefit in terms of drag reduction with further increase in twist angle ($\phi > 3^\circ$) tending to produce drag reductions of up to 6 drag counts at maximum dihedral angle ($\Gamma = 60^\circ$ relative to $\Gamma = 0^\circ$). This result gives some indication of the influence of the winglet's movement (at large twist angles) out of the wing plane on overall performance. However, there seems to be some exception to this finding, particularly for $\Gamma > 20^\circ$ (low twist) where the results seem to be relatively constant. Additionally for $\Gamma > 0^\circ$, there seems to be a much more subtle linear reduction in drag coefficient with dihedral angle change as opposed to

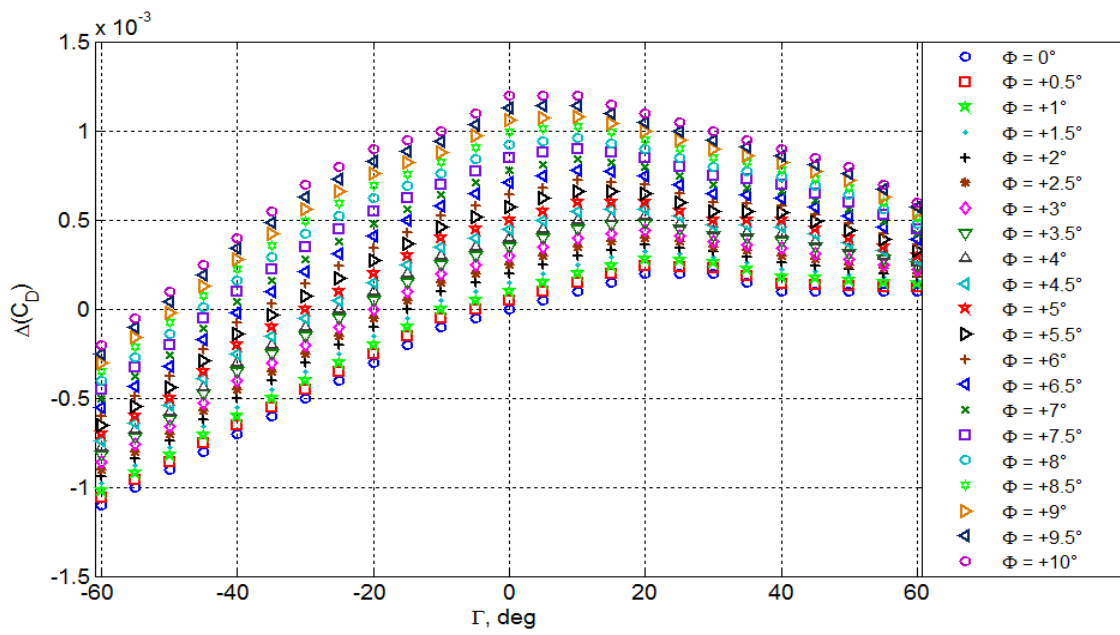


(a)

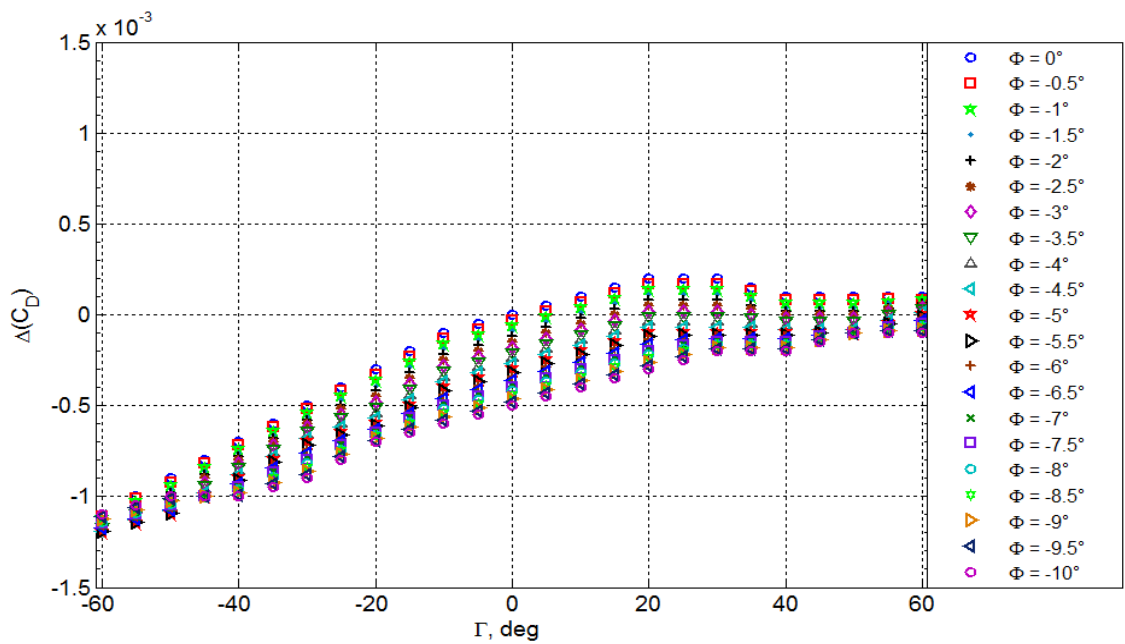


(b)

Figure 5.19 Effects of Changing Winglet Dihedral and Twist angle on Performance (ΔC_L) at $C_{L_0} \cong 0.6$: a) Wash-in (Positive Twist) and b) Wash-out (Negative Twist).

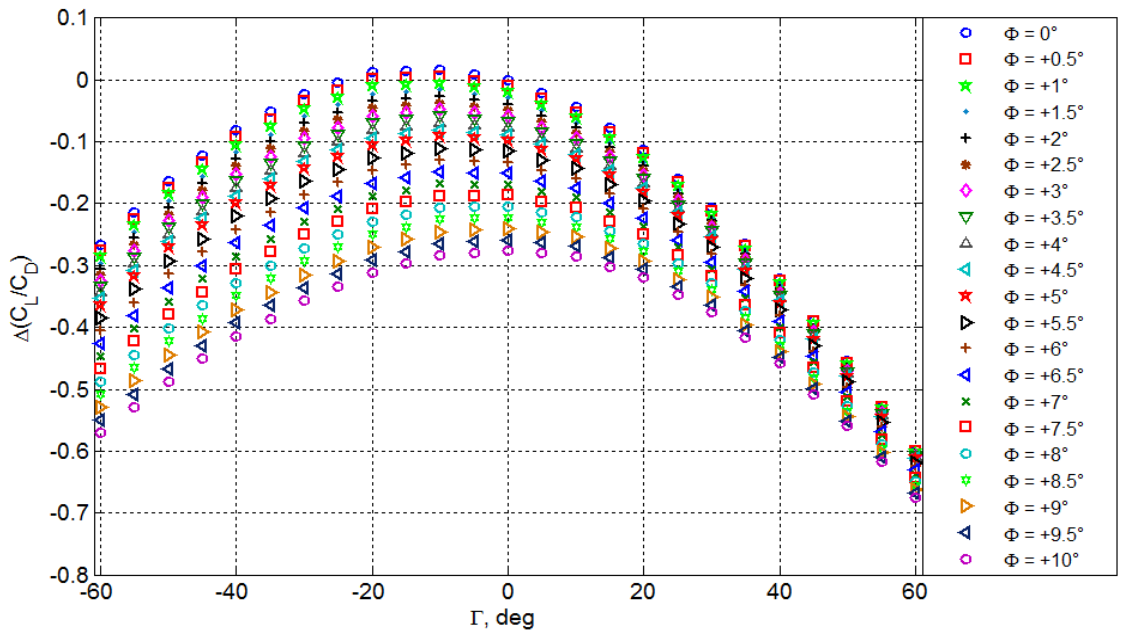


(a)

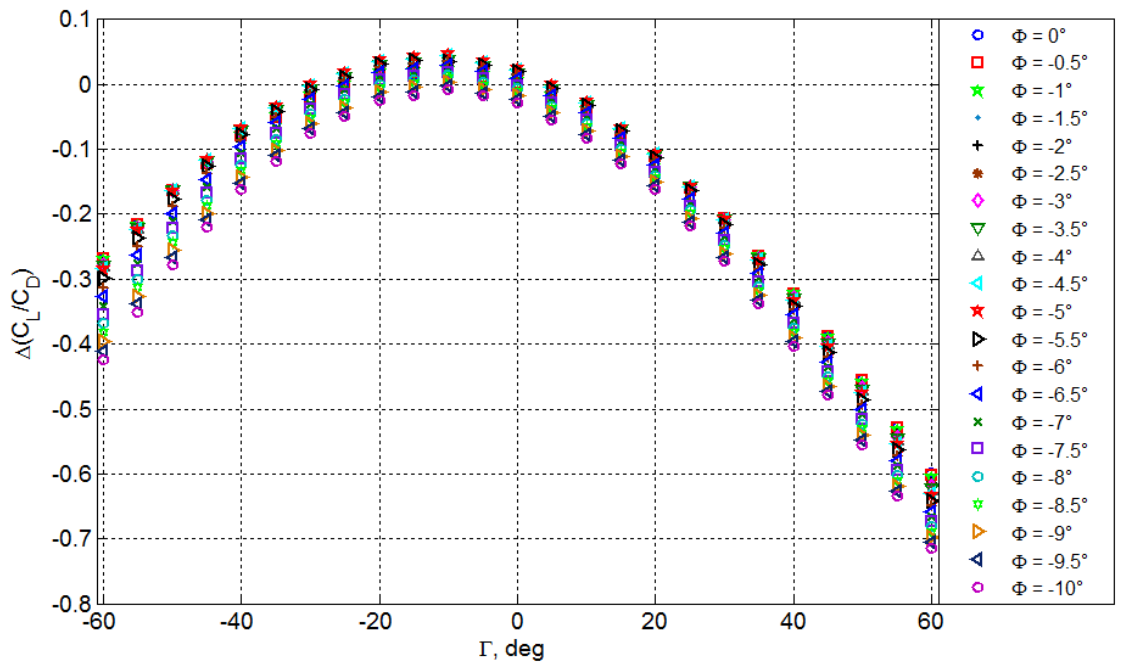


(b)

Figure 5.20 Effects of Changing Winglet Dihedral and Twist angle on Performance (ΔC_D) at $C_{L_0} \cong 0.6$: a) Wash-in (Positive Twist) and b) Wash-out (Negative Twist).



(a)



(b)

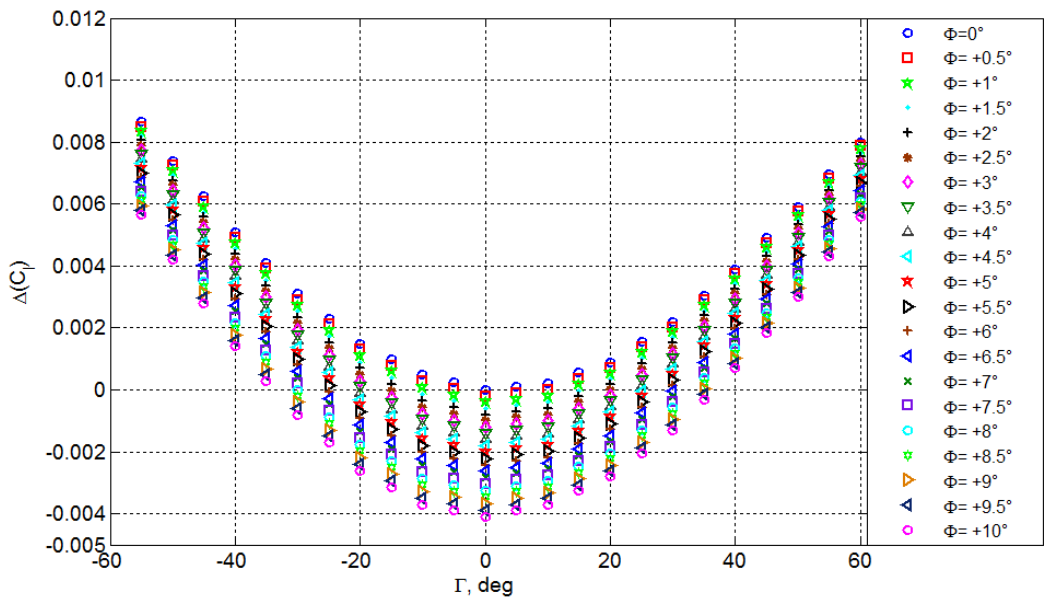
Figure 5.21 Effects of Changing Winglet Dihedral and Twist angle on Performance ($\Delta C_L/C_D$) at $C_{L_0} \cong 0.6$: a) Wash-in (Positive Twist) and b) Wash-out (Negative Twist).

the results shown for $\Gamma < 0^\circ$ where a maximum drag reduction of 15 drag counts at $\Gamma = -60^\circ$ ($\phi = 10^\circ$) exists.

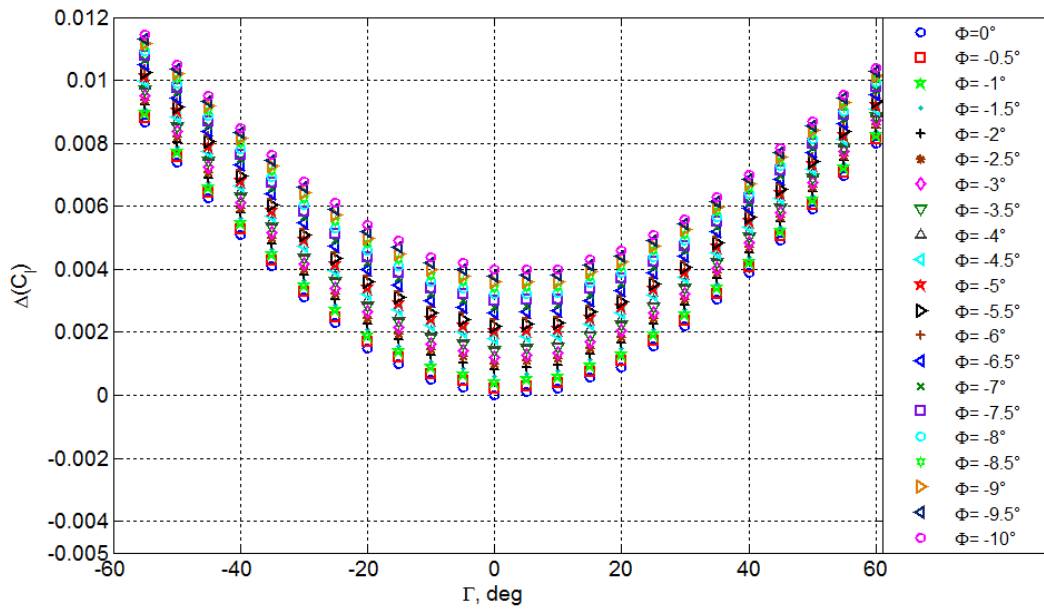
Considering results for $\phi < 0^\circ$ as shown in **Figure 5.20 (b)**, there seems to be much less of a variation in change in drag coefficient when compared to the $\phi > 0^\circ$ winglet configurations (**Figure 5.20 (a)**) with the influence of winglet twist angle being much less pronounced than that found for $\phi > 0$. One possible reason for this may lay in the increased effectiveness of negative twist winglets at both producing less overall lift (and therefore less lift-dependent drag) as well the ability of negatively-twisted winglet configurations to maintain lower effective angles of attack relative to the freestream flow. For all test cases presented negative dihedral angle seems to have a much more pronounced effect on changing the overall aerodynamic performance with (particularly for $\phi > 0^\circ$) large amounts of variation in drag coefficient with twist angle change. Results for $\Gamma > 60^\circ$ in both cases are much less variable.

Figure 5.21 (a) and **(b)** detail the change in C_L/C_D coefficients obtained from winglet deflection between $-60^\circ \leq \Gamma \leq 60^\circ$ for all the winglet configurations. In all of these configurations, and as would be expected, it can be clearly seen that the principle effect on C_L/C_D is one of a reducing magnitude with movement of dihedral angle away from planar configuration (maximum $\Delta C_L/C_D = -0.57$, $\Gamma = -60^\circ$ and $\Delta C_L/C_D = -0.72$ for $\Gamma = +60^\circ$). In saying this however, there exist subtle characteristics within the computed results that show a small degree of augmentation around this baseline planar flow case. In the region of dihedral angles from $-20^\circ < \Gamma < 0^\circ$, there is evidence of a small increase in C_L/C_D . Moreover, there is also a tendency for asymmetric $\Delta C_L/C_D$ reductions of up to $\Delta C_L/C_D = -0.1$ at $\Gamma = 60^\circ$ relative to $\Gamma = -60^\circ$ for $\phi > 0^\circ$ (**Figure 5.21 (a)**).

Figure 5.21 (b) highlights the change in C_L/C_D for negative twist winglet configurations. Similar to $\phi > 0^\circ$, in all of these configurations, and as would be expected, reductions were observed in the change of C_L/C_D when winglet dihedral angle deviates from the planar configuration ($\Gamma = 0^\circ$). Although globally, efficiency tends to reduce, as was the case for $\phi > 0^\circ$, for some local cases presented ($-20^\circ < \Gamma < 0^\circ$) for the negative winglet twist angle configurations, minor improvements ($\Delta C_L/C_D = 0.07$ at $\phi = -5^\circ$) over that observed from the baseline flow case exist. Similar results were also presented in [90], with in effect a small range of negative

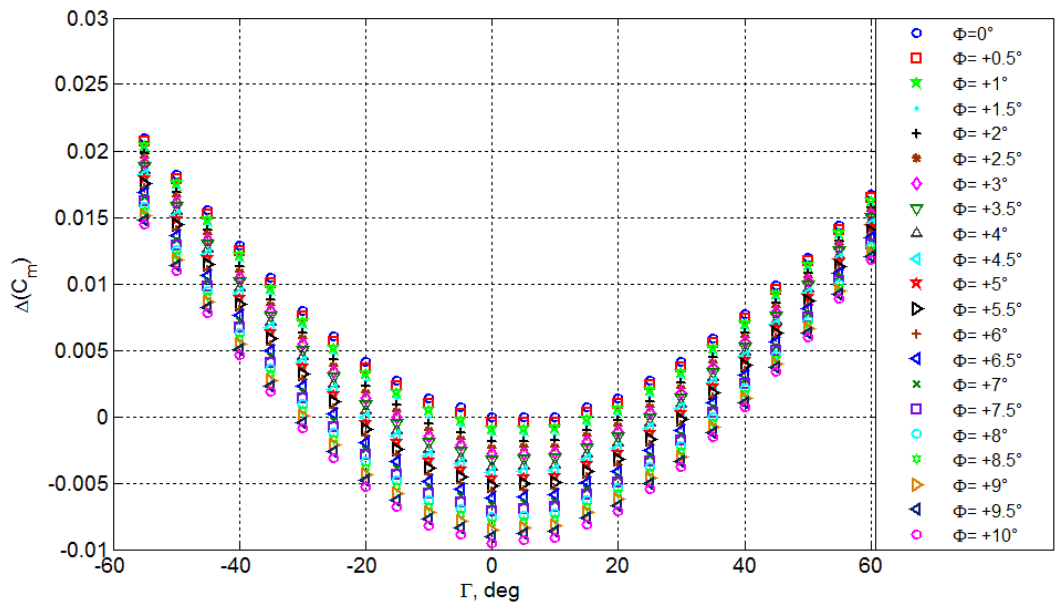


(a)

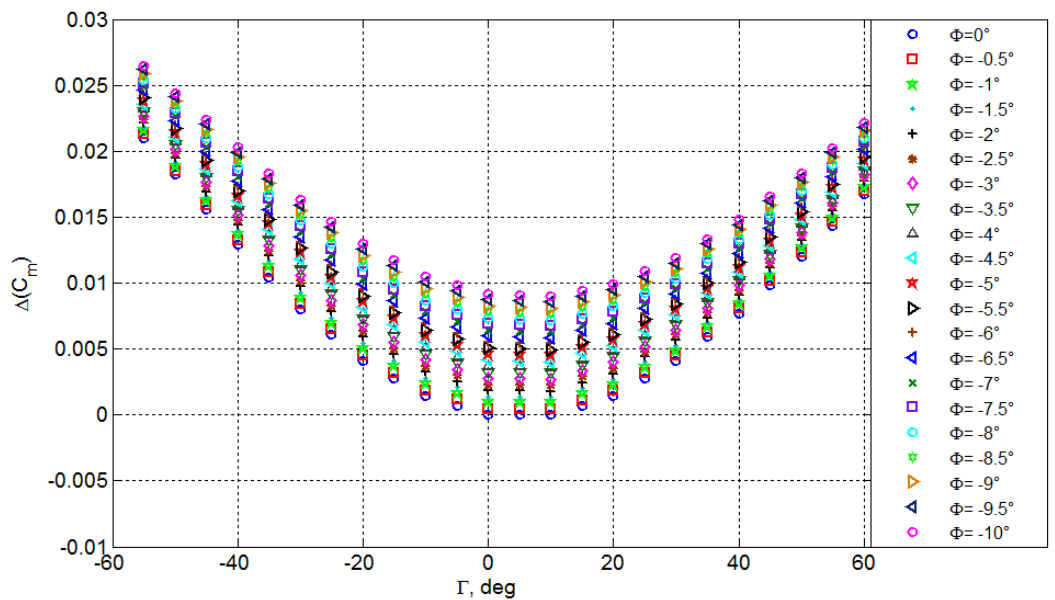


(b)

Figure 5.22 Effects of Changing Winglet Dihedral and Twist angle on Performance (ΔC_l) at $C_{L_0} \cong 0.6$: a) Wash-in (Positive Twist) and b) Wash-out (Negative Twist).



(a)



(b)

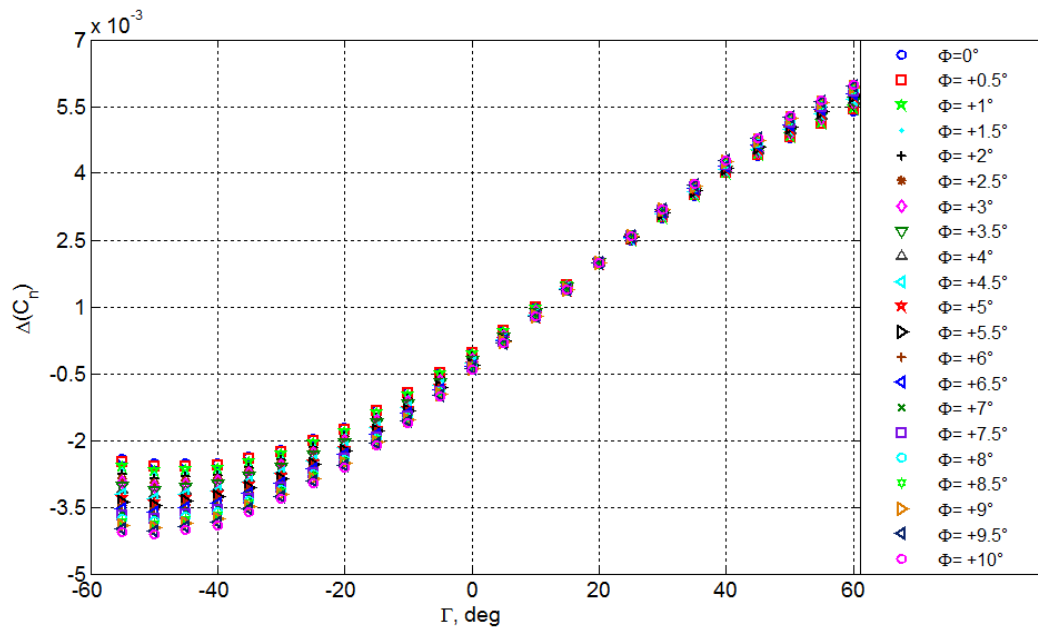
Figure 5.23 Effects of Changing Winglet Dihedral and Twist angle on Aircraft Performance (ΔC_m) at $C_{L_0} \cong 0.6$: a) Wash-in (Positive Twist) and b) Wash-out (Negative Twist).

dihedral angles resulting in the best values of C_L/C_D . Furthermore, the asymmetric bias evident in **Figure 5.21 (a)** for the change in C_L/C_D with increasing or decreasing dihedral angle also exists for negative twist winglet configurations (**Figure 5.21 (b)**) although for this case, the degree of asymmetry has tended to increase further with some examples showing differences of up to $\Delta C_L/C_D = -0.31$ ($\phi = -10^\circ$, $\Gamma = -60^\circ$ to 60°). Moreover, from comparing **Figure 5.21 (a)** and **(b)** directly, results do show much more variability with positive winglet twist (particularly for $\Gamma < 0^\circ$) on $\Delta C_L/C_D$ than that observed for the negatively twisted configurations. This is most notable when comparing results in **Figure 5.21 (a)** at $\Gamma = -60^\circ$.

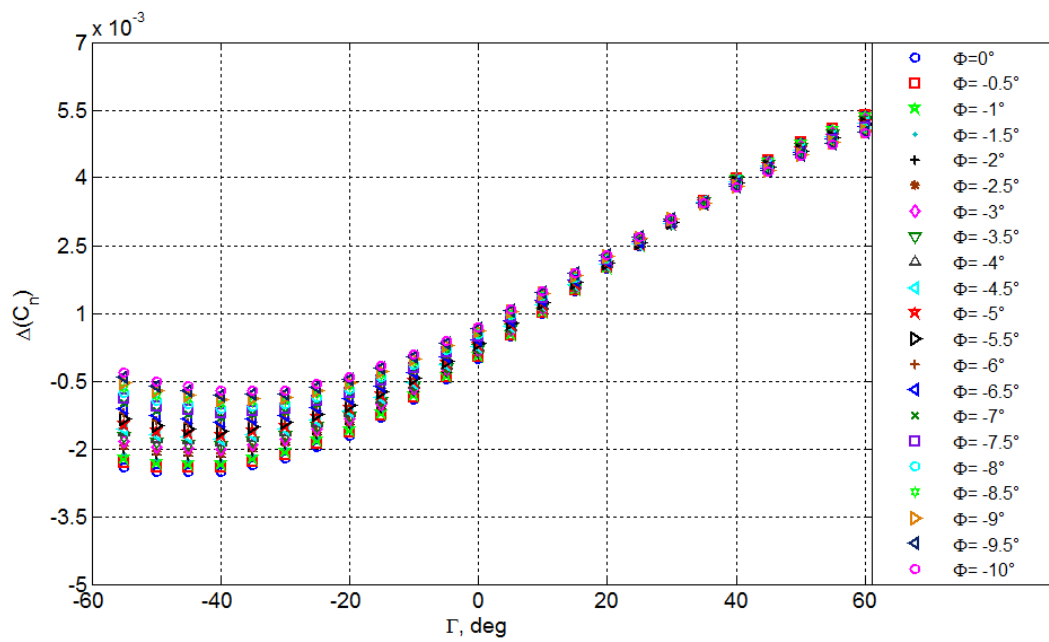
5.2.4.1 *Effects of winglet twist on Aerodynamic Performance and Control Moments*

From **Figure 5.19 (a)** and **(b)**, as winglet twist angle increases or decreases, the net effect on change in the lift coefficient varies almost linearly up to $\phi = \pm 10^\circ$ with the maximum changes with winglet twist occurring at the baseline flow case of $\Gamma = 0^\circ$ ($\Delta C_L = \pm 0.01$ $\phi = \pm 10^\circ$). This would be expected as the maximum effectiveness of winglet angle twist occurs at $\Gamma = 0^\circ$ and is the subsequent position of maximum lift enhancement. This effect reduces with change in dihedral angle from the planar case, due to both net reductions in effective angle of attack as the winglet moves out of the wing plane and the winglet contribution to overall lift development reduces.

Similar to ΔC_L , the influence of twisting the winglets has a marked influence on the production of drag, however in this particular case, there exists a very non-uniform degree of change that is heavily dependent on the degree of winglet dihedral angle. For positive winglet twist angles, there is a clear bias and significantly more influence on the drag with changing winglet twist angle for $\Gamma < 0^\circ$. The results in this case suggest that change in drag varies significantly less for $\Gamma > 0^\circ$. Maximum drag coefficient change for these conditions were obtained at a maximum twist angle of $\phi = 10^\circ$ and represented up to an additional 10 drag counts compared to non-twisting winglet configurations ($\Gamma = 0^\circ$). Comparing the features seen in **Figure 5.20 (a)** with negative twisted winglets (**Figure 5.20 (b)**), change in drag coefficient was found to be much less with winglet change from $\phi = \pm 10^\circ$ with maximum differences of approximately 5 drag counts with winglet variations from $\phi = 0^\circ$ to $\phi = -10^\circ$ ($\Gamma = 20^\circ$).



(a)



(b)

Figure 5.24 Effects of Changing Winglet Dihedral and Twist angle on Performance (ΔC_n) at $C_{L_0} \cong 0.6$: a) Wash-in (Positive Twist) and b) Wash-out (Negative Twist).

Together with these results, while **Figure 5.20 (b)** displays much more non-linear behaviour with change in dihedral angle, the influence of changing winglet twist angle still remains relatively linear at any particular dihedral angle when the winglet is twisted about $\phi = 0^\circ$ at that set dihedral angle. These effects are most notable at $\Gamma = 20^\circ$ to 40° with similar results also presented in [134].

As discussed previously, and confirmed in the results shown here, positive twisted winglets provide a greater lift force production capability than those obtained for negative twisted winglets. However, it should be noted that, under the same conditions, the influence on drag coefficient is much more complex [134] with the overall result, for the majority of test cases considered, representing a reduction in aerodynamic efficiency. However, according to the results presented here, increases in aerodynamic efficiency were achieved up to twist angles of $\phi = -5^\circ$ ($-20^\circ < \Gamma < 0^\circ$) with these winglet angle configurations seeming to give some enhancement of $\Delta C_L / C_D$. Similar results were also presented in [134] with small twist angles resulting in the production of the lowest lift-induced drag. However, considering further increases in twist angle, this influence tended to diminish the aerodynamic performance (**Figure 5.21**).

As far as moment coefficient values are concerned, winglet twist angle has noticeable influences on roll, pitch, and yaw moments. With increases the degree of moments generated with maximum values occurring at maximum degrees of twist and maximum roll and pitching moments were obtained with increasing twist angle up to $\phi = \pm 10^\circ$. Overall, increasing winglet dihedral angle either side of the planar case, further increases the change in moment coefficient. Moreover, the generation of maximum yawing moment coefficient was also achieved at maximum winglet deflection (**Figure 5.24**).

5.3 Prototype Wind Tunnel Model FEA and Experiments results

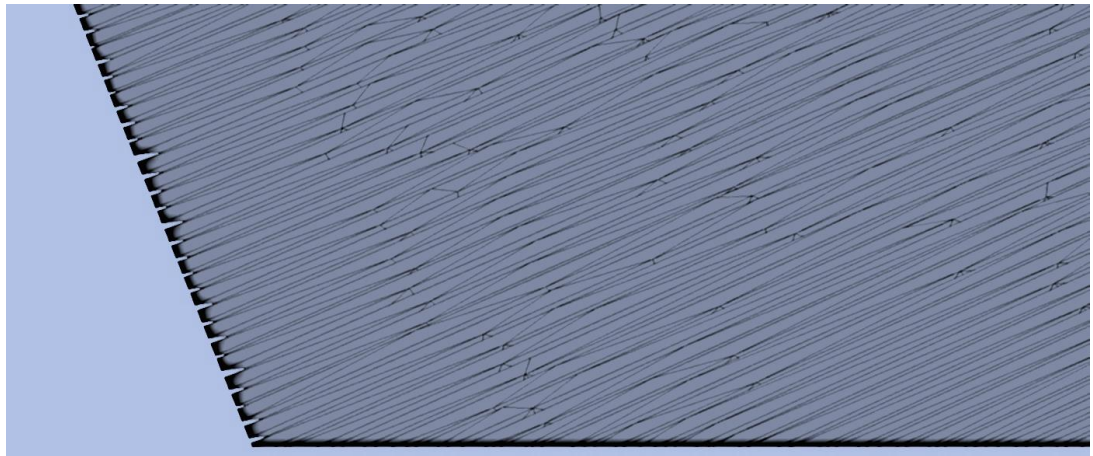
Having investigated possible benefits from morphing swept wing and winglet configurations, attention is now turned to using these insights into the investigation at the morphing concept. This section describes the finite element analysis of this concept. The structural results obtained from ANSYS Mechanical with some optimisation are included. Wind tunnel results including aerodynamic force and moment results are also discussed, as are comparisons to a traditional wing-aileron system to ascertain any performance enhancements.

5.3.1 Finite Element Analysis and Rib Shape Optimisation

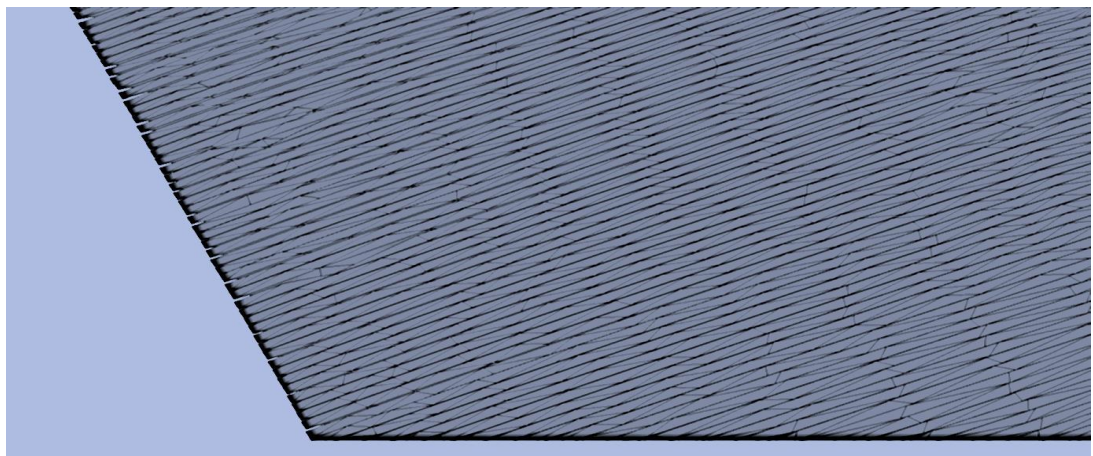
For the morphing concept, optimising weight with an aerodynamically smooth surface finish were the main priorities. To assist in achieving these goals, several structural configurations were tested (details of the computational setup and methodologies expressed in **CHAPTER 3**). Assessments also needed to be made about overall strength as well.

It is very important to define the best rib structure with low wrinkling rate in order to achieve minimal or less drag influences due to surface. In this regard, maximum deformation criteria for a skin were defined based on boundary layer theory for a wing structure. According to this theory, surface would move within a limit in the direction perpendicular to its normal vector to give the same flow rate as occurs between the surface and the reference plane in a real fluid. Using **Equation (4-4)** in **CHAPTER 4 Section 4.3.5**, maximum displacement was calculated and set as 0.594mm. Based on these criteria, optimisation required for rib structures were done in ANSYS.

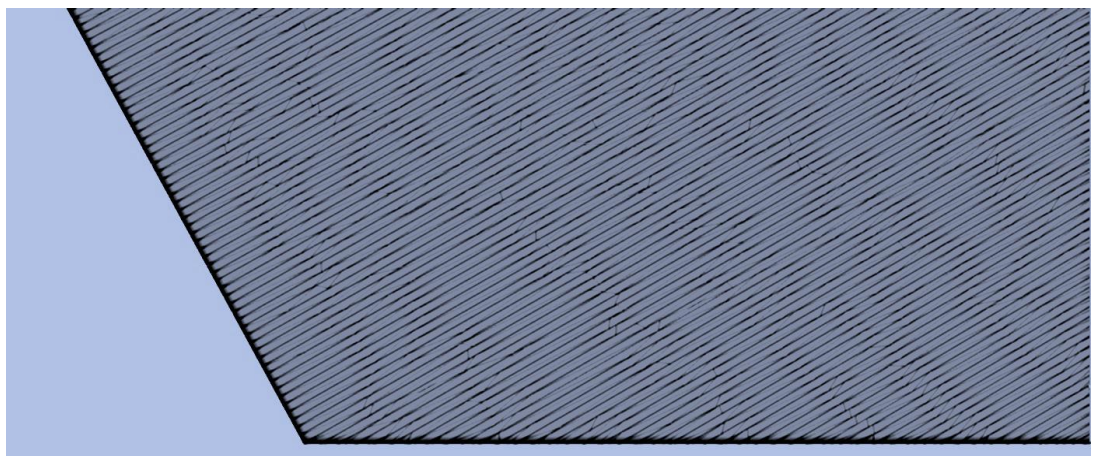
Figure 5.25 illustrates 3 different rib thickness designs investigated. Individual rib thicknesses were set to 1mm, 0.8mm, and 0.6mm respectively, totalling 150 ribs, 187 ribs and 250 ribs. According to the results, very little differences were observed for stress and deformation. However, a subtle change exists for the 1mm condition, when twist movements are applied. The last rib moved up to 0.693mm (maximum) relative to the other ribs, which is deemed not acceptable. The two other thickness ribs performed quite similarly, however as the 0.6mm thick rib gave ultimately the best surface finish, this was chosen.



(a)



(b)



(c)

Figure 5.25. Trailing edge deformation for three different rib designs near the wing tip under twist deformation: (a) rib thickness is 1mm and the maximum gap between two ribs is 0.635mm, (b) rib thickness is 0.8mm and the maximum gap between two ribs is 0.496mm, and rib thickness is 0.6 mm and the maximum gap between two ribs is 0.212mm.

Table 11 Deformation and Stress on Carbon rods for Various Rod Sizes

Rod size, r_1 and r_2 , mm	Wash-out σ_{max} , MPa	Wash-out δ_{max} , mm	Wash-in σ_{max} , MPa	Wash-in δ_{max} , mm
1	1045.70	25.803	959.15	23.121
1.5	696.02	20.052	628.06	18.916
2	441.04	19.336	324.42	17.488
2.5	406.51	16.238	316.62	15.004

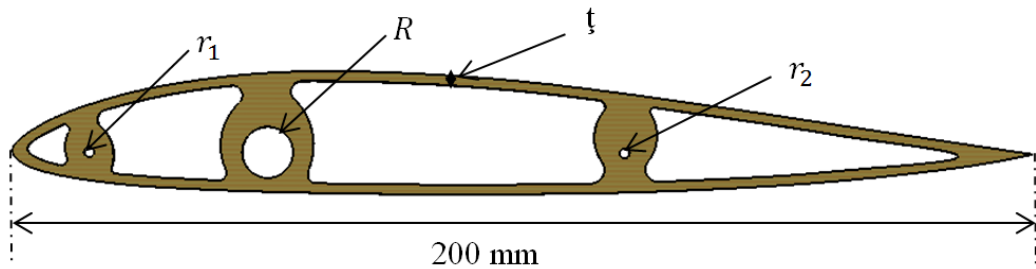


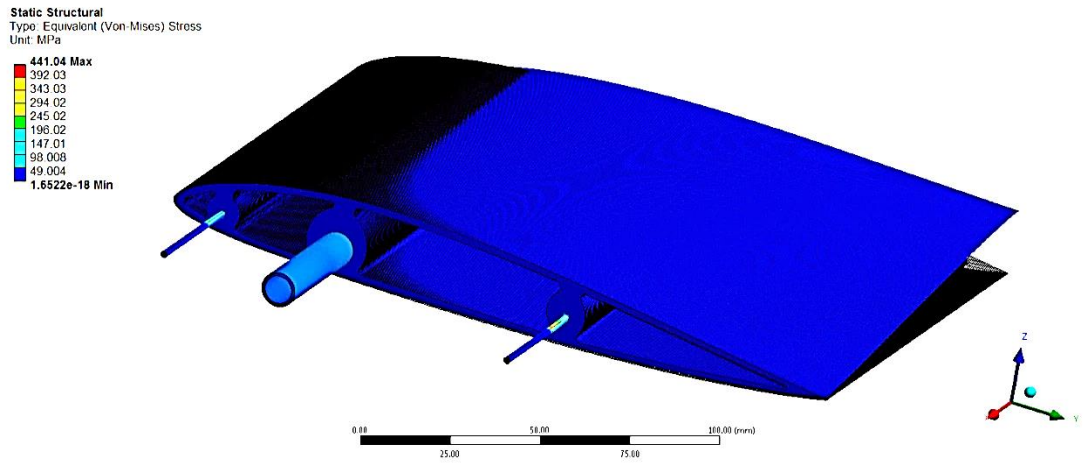
Figure 5.26 Optimised rib structure with parameters ($r_1=2\text{mm}$, $r_2=2\text{mm}$, $R = 10\text{mm}$, and $t=2\text{mm}$).

Table 11 summarises how changing the supporting rod parameters effect stress and deformation magnitudes. It can be seen that increasing the rod size, in both wash-in and wash-out cases, tends to reduce the stress occurring in the carbon rods. However, it reduces twist displacement. Using a yield stress (carbon) of 600MPa, for r_1 or $r_2 < 2\text{mm}$, the structure does appear to fail, so a rod size of be 2mm was chosen (the figures of stress and deformation magnitudes are shown in **Figure 5.27** and **APPENDIX-A** from **Figure A- 14** to **Figure A- 25**).

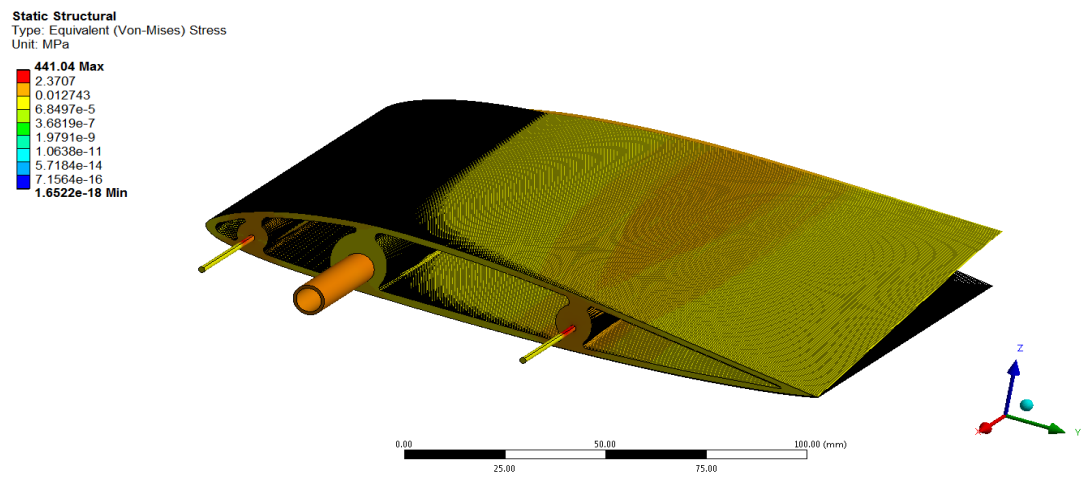
Figure 5.26 illustrates an individual rib structure and its defining parameters. Five different rib configurations were analysed with the final design chosen for use. **Figure 5.28** and **Figure 5.29** illustrate the deformation analysis for five different configurations (from $t = 3\text{mm}$ to $t = 1\text{ mm}$ steps of 0.5mm) which were chosen as cases to optimise the rib structure, and **Table 12** summarises the stresses on the carbon rods. Morphing twist angle was determined by measuring the relative displacement of the wing-tip trailing edge. Overall, the magnitudes of the total deformation in both wash-in and wash-out cases increased with reduced rib edge thicknesses (t).

Contour plots (**Figure 5.28**) illustrate the wash-out effects of 5 different wing configurations. For reasons of clarity, the un-deformed geometries are also shown (details can be seen in **APPENDIX-A Figure A- 26** to **Figure A- 34**). It can be seen that when the $t = 3\text{mm}$ case is considered (**Figure 5.28 (a)**), 17.013 mm wing twist deflection was obtained, much less than the other cases presented. As is shown in **Figure 5.30 (e)**, rib analysis also suggests almost no deformation (maximum of 0.49mm) on the rib structure. The maximum $\sigma = 339.85\text{ MPa}$ for this case was obtained on the rear carbon rod, well within the yield stress ($\sigma = 600\text{ MPa}$). Similar results were obtained for $t = 2.5\text{mm}$ **Figure 5.28 (b)**. The deformation magnitude of twist has increased to 17.98 mm from 17.03 mm with maximum stress of 417.14 MPa. Moreover, it can also be seen from **Figure 5.30 (d)**, rib (skin) displacement was found to be 0.524mm which is still acceptable for a wind tunnel model.

Comparing **Figure 5.28 (c)**, with **Figure 5.28 (a)** and **Figure 5.28 (b)**, reducing rib edge thickness to 2mm continues to show the trend seen in **Figure 5.28 (b)** with an augmented deformation magnitude (19.336 mm) It can be seen from **Table 12** that maximum stress was 441.04 MPa which is acceptable with a carbon yield stress of 600MPa. The maximum displacement occurred on morphing surface is also acceptable with 0.56mm deformation **Figure 5.30 (c)**. The tendency of linearly increased twist deformation with further reduced rib edge thicknesses seems to be continued for $t = 1.5\text{mm}$ and $t = 1\text{mm}$. As stated previously, morphing skin needs to be smooth enough to keep drag level the same or lower. Conversely, although the influence of the twist deformation for $t = 1\text{mm}$ and $t = 1.5\text{mm}$ was found to be substantial with maximum displacement of 21.13mm and 21.8 mm respectively, abnormal deformation exists on the rib structure, not giving a smooth aerodynamic finish. As can be seen in **Figure 5.30 (b)**, when rib shape has $t = 1.5\text{mm}$, 1.07mm maximum bending occurred on the rib structure which is out of the boundary layer thicknesses rule (needs to be maximum 0.59mm), hence increasing overall drag. Similar results also exist for $t = 1.0\text{mm}$, with 1.51 mm maximum bending deflection obtained.



(a)



(b)

Figure 5.27 Von-Mises Stress for $t=2\text{mm}$: (a) Von-Mises stress analysis and (b) Detail surface analysis of morphing concept.

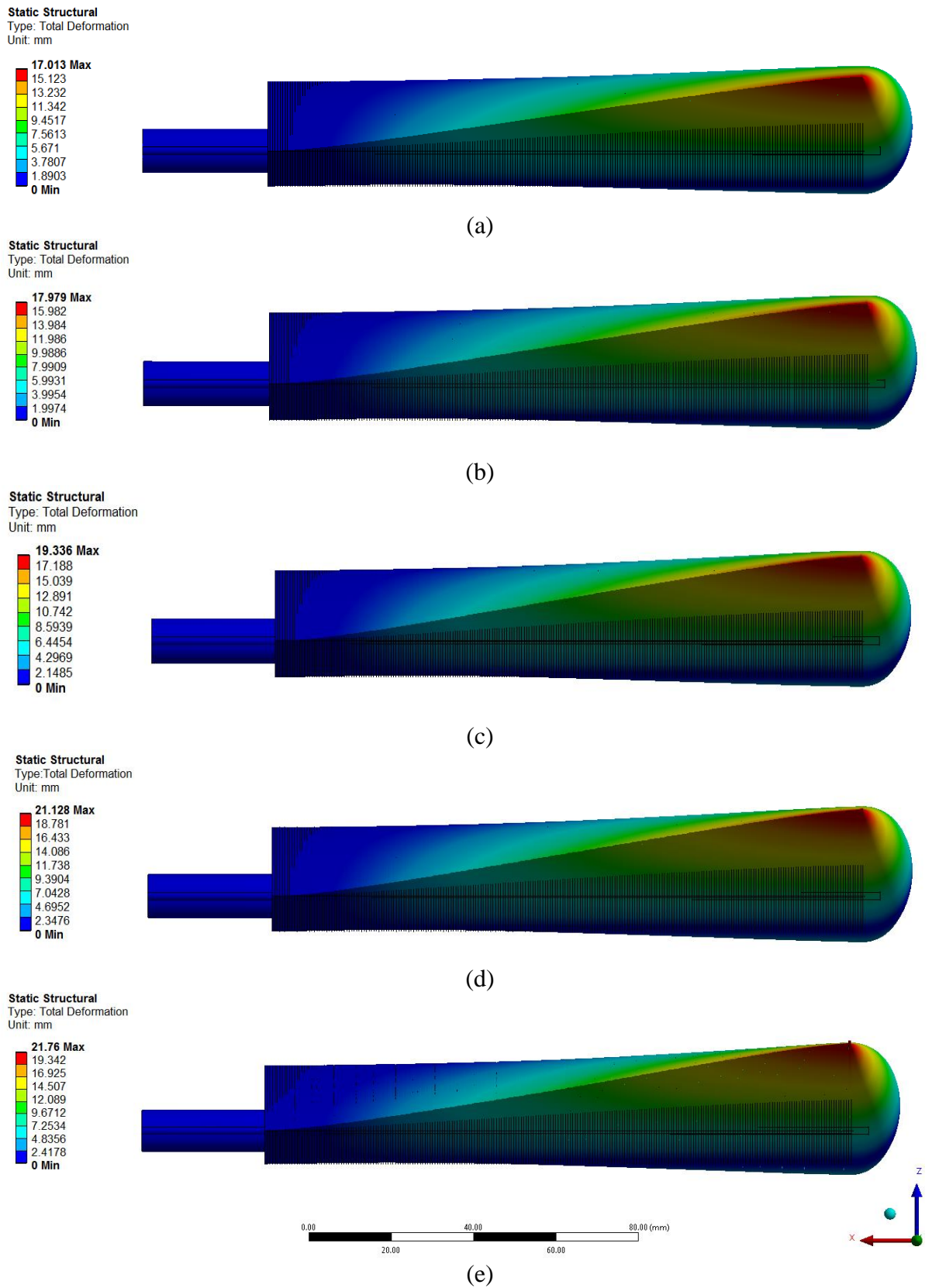


Figure 5.28 Total twist deformation on morphing concept (Wash-out): (a) $t=3\text{mm}$, (b) $t=2.5\text{mm}$, (c) $t=2\text{mm}$, (d) $t=1.5\text{mm}$, and (e) $t=1\text{mm}$.

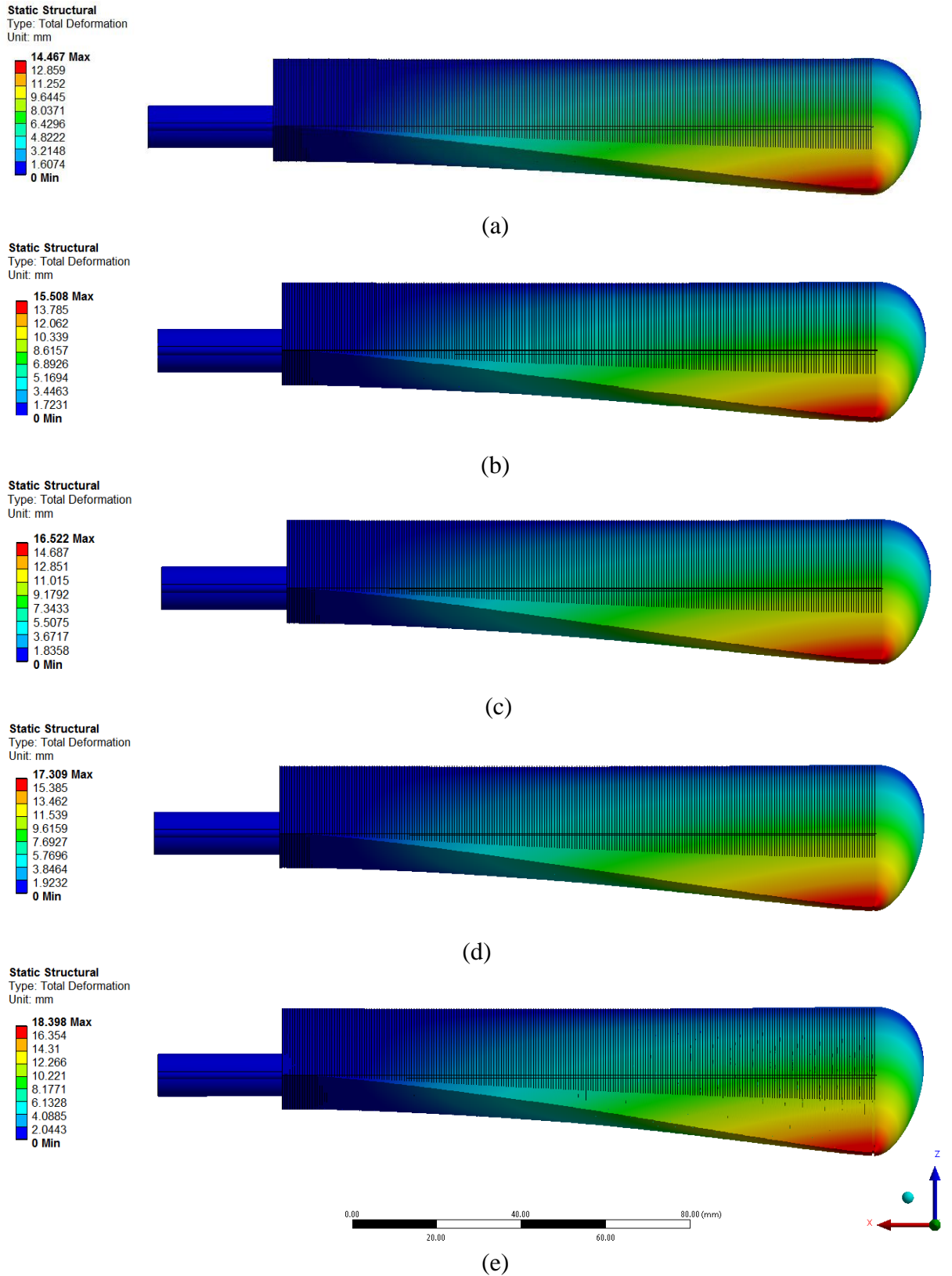


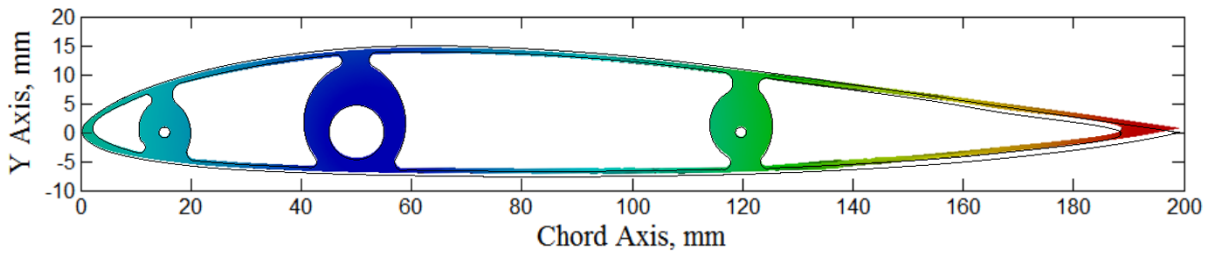
Figure 5.29 Total twist deformation on morphing concept (Wash-in): (a) $t=3\text{mm}$, (b) $t=2.5\text{mm}$, (c) $t=2\text{mm}$, (d) $t=1.5\text{mm}$, and (e) $t=1\text{mm}$.

Similar to the wash-out effects, wash-in twist displacement continues to show the trend seen in **Figure 5.29** with a linear increase with reducing rib edge thicknesses. As is shown in **Figure 5.29 (a)**, when $t = 3$ mm is considered, the expected low displacement value was obtained (14.5mm) due to the increased overall weight of the wing structure. Comparing this wash-in effect with wash-out effects of a model, reduced total deformation value was visible (from 17mm to 14.5mm). Interestingly, the bending value was reduced compared to the wash-out effects (maximum 0.33mm as shown in **Figure 5.31(e)**). One possible reason for this may lay in the reduced twist deformation on the wing's structure resulting in low bending movements on the rib structure. When total stress is considered, similar to other configurations, 290.19 MPa stress was observed on the rear carbon rod.

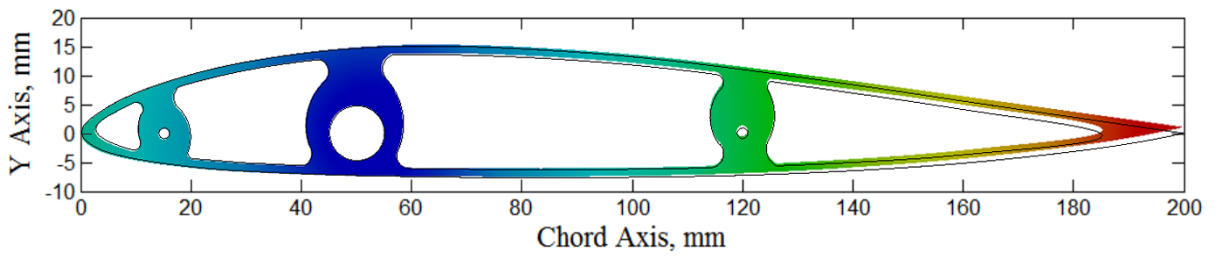
Table 12 Summary of Stress on carbon rods for various rib designs.

Rib Edge Thickness, t, mm	Wash-out σ_{max}, MPa	Wash-in σ_{max}, MPa
1	463.14	350.47
1.5	454.19	340.75
2	441.04	324.42
2.5	417.14	307.35
3	339.85	290.19

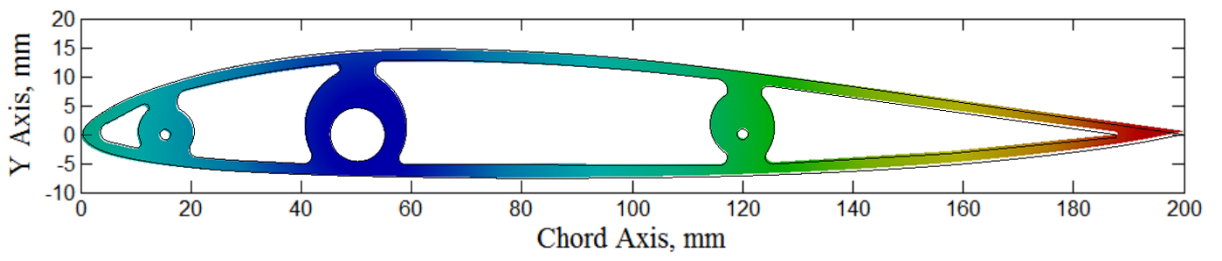
Figure 5.29 (b) depicts another rib configuration ($t=2.5$ mm) and which achieved a maximum 15.508mm deflection, 2.471mm less than negative twisted morphing elements (**Figure 5.28 (b)**). Also, this configuration gave a maximum stress of $\sigma = 307.35$ MPa. For the third wing configuration investigated ($t=2$ mm) (**Figure 5.29 (c)**), the rib configuration increased further (maximum deformation of 16.522 mm) in contrast to that discussed for **Figure 5.29 (b)** and **Figure 5.29 (a)**. The maximum stress is also $\sigma = 324.42$ MPa. Like negative twist effect, the maximum skin deformation was found to be acceptable with 0.49mm.



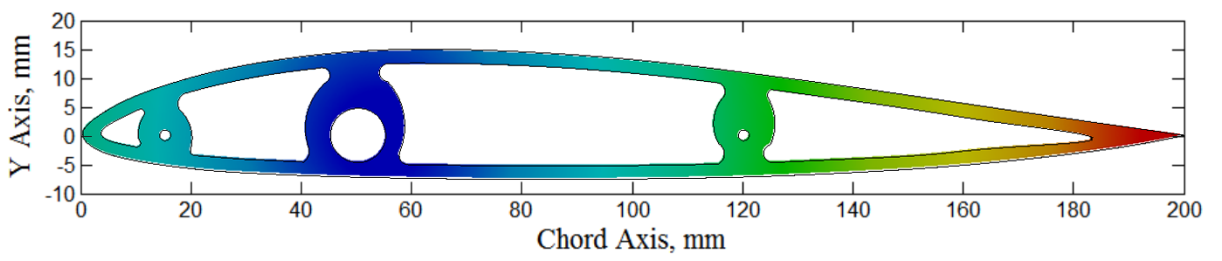
(a)



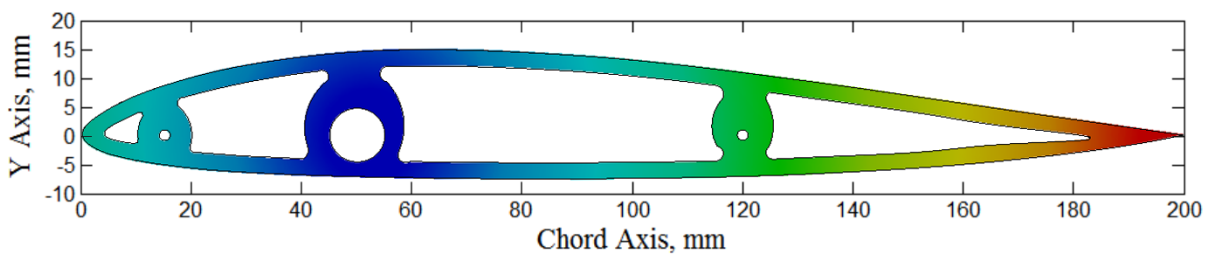
(b)



(c)

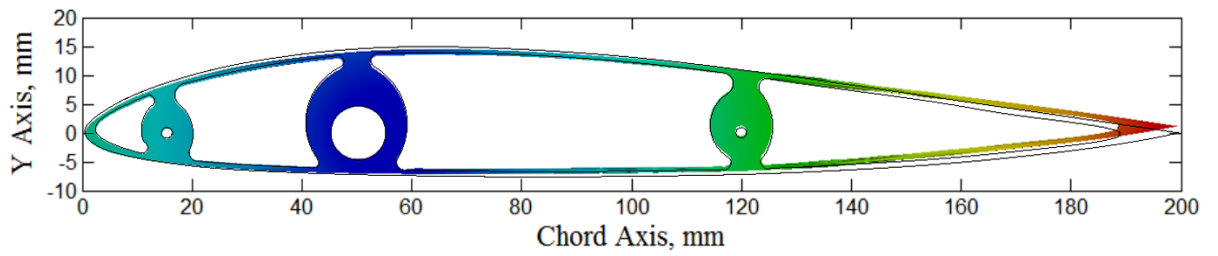


(d)

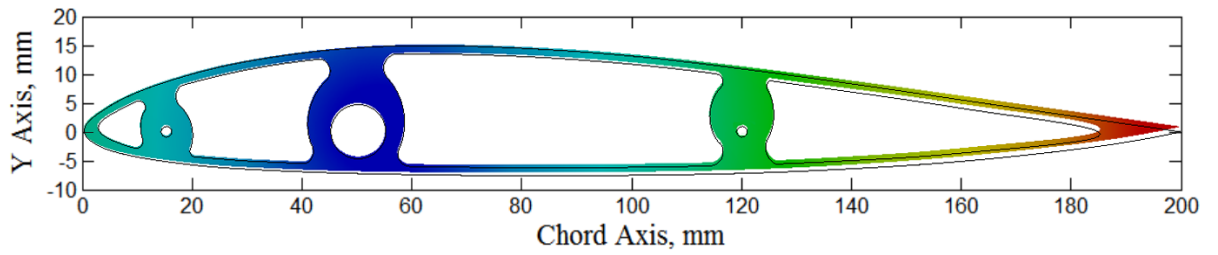


(e)

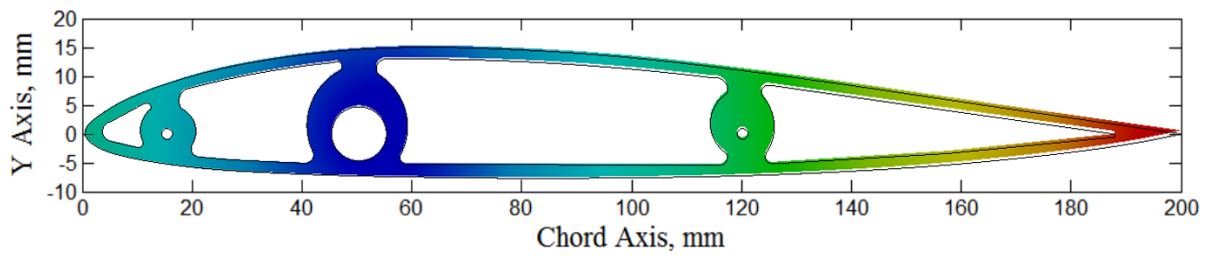
Figure 5.30 Rib deformation under aerodynamic load (wash-out): (a) $\zeta=1\text{mm}$, (b) $\zeta=1.5\text{mm}$, (c) $\zeta=2\text{mm}$, (d) $\zeta=2.5\text{mm}$, and (e) $\zeta=3\text{mm}$.



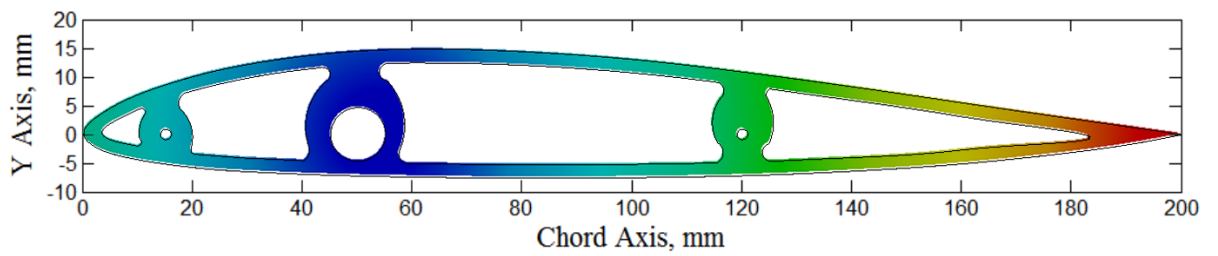
(a)



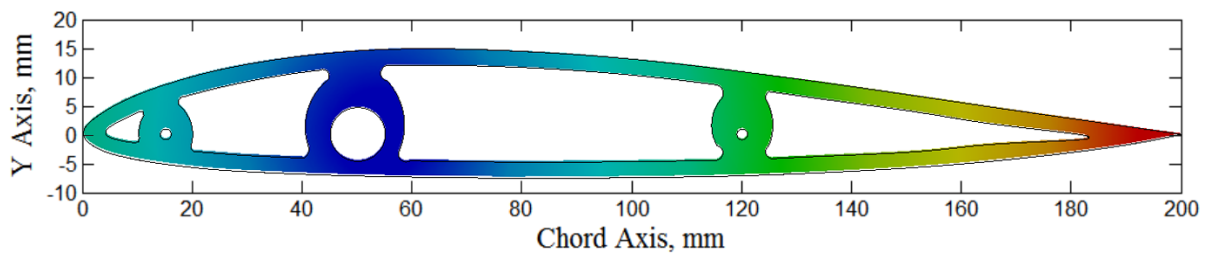
(b)



(c)



(d)



(e)

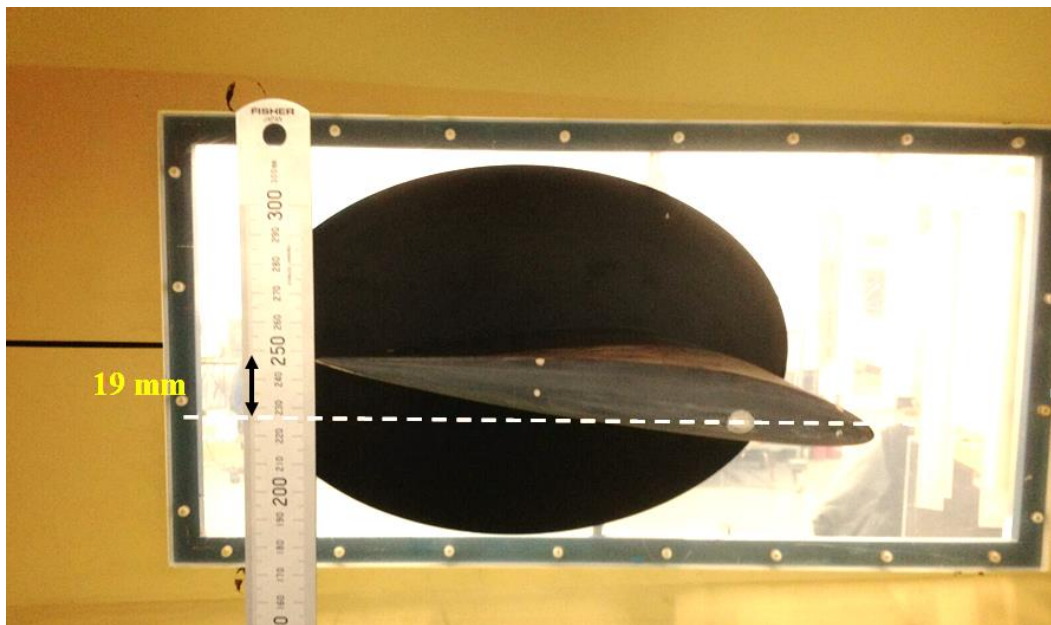
Figure 5.31 Rib deformation under aerodynamic load (wash-in): (a) $\zeta=1\text{mm}$, (b) $\zeta=1.5\text{mm}$, (c) $\zeta=2\text{mm}$, (d) $\zeta=2.5\text{mm}$, and (e) $\zeta=3\text{mm}$.

With further reduction of rib thickness to 1.5mm (**Figure 5.29(d)**), the displacement reduces to 17.309mm, which was lower than the other twist configurations tested except for $t=1$ mm. This configuration also appears to remain intact with a maximum stress of $\sigma = 340.74$ MPa. Although, the stress and twist deformation study showed that this wing structurally performed well, skin deformation was seen to be high (0.825mm) (**Figure 5.31 (b)**) and above the limit set of 0.594.

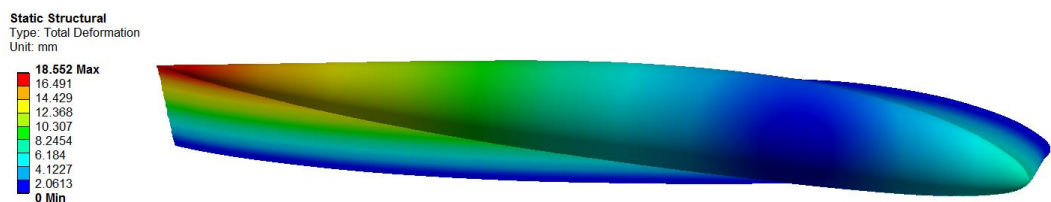
Further reduction of rib edge thickness to 1mm resulted in large degrees of wing twist deflection (18.398mm), with a maximum stress of $\sigma = 350.47$ MPa, the highest obtained. This configuration however, seems to result in an excessively deformed rib structure (maximum 1.16 mm) as shown in **Figure 5.31 (a)**. In summary for both wash-out and wash-in cases, a 2mm wing configurations was found to perform best and was selected for use.

5.3.2 Experimental and Numerical Analysis of Wind Tunnel Model

The results taken from ANSYS for the FEA model was compared directly to results from the experimental model under no-wind condition (shown in **Figure 5.32 (a)** and **Figure 5.32 (b)**). It can be seen from **Figure 5.32** that there is good agreement between the numerical and experimental model for wash-out (negative twist) deflection (negative twist) with maximum tip deflection was found to be 19mm compared to 18.552mm in from ANSYS.



(a)



(b)

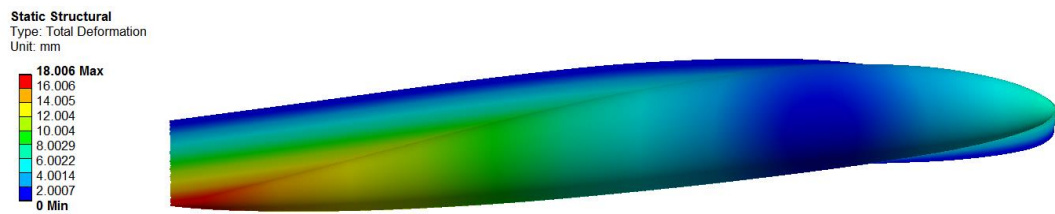
Figure 5.32. Maximum negative twist (wash-out) of the morphing concept without any flow interaction: (a) Experimental model twist and (b) Numerical modelling twist movement.

With wash-in (positive twist) deflection (**Figure 5.33**), the comparisons between the computational and experimental model gave differences of approximately 0.5mm. A maximum 18.5mm deflection was measured at the tip with the numerical

model giving 18.006mm. A few differences could be due to un-modelled friction factors between the components.



(a)



(b)

Figure 5.33 Maximum positive twist (wash-in) of the morphing concept without any flow interaction: (a) Experimental model twist movement and (b) Numerical modelling twist movement.

5.3.3 Static Forces and Moments

The static force and moment results produced through wing twist between $-6^\circ < \phi < 6^\circ$ versus angle of attack are shown from **Figure 5.34** to **Figure 5.37**. The first aerodynamic measurement on the morphing concept was conducted to understand the effects of the sliced ribs mechanism on static force and moment coefficients compared to a full span (baseline) wing model. In general, results show adequately the trends with varying angle of attack and are consistent with well-known wing aerodynamics [168]. The results for different twist configurations also show significant aerodynamic benefits in terms of efficiency and control compare to the

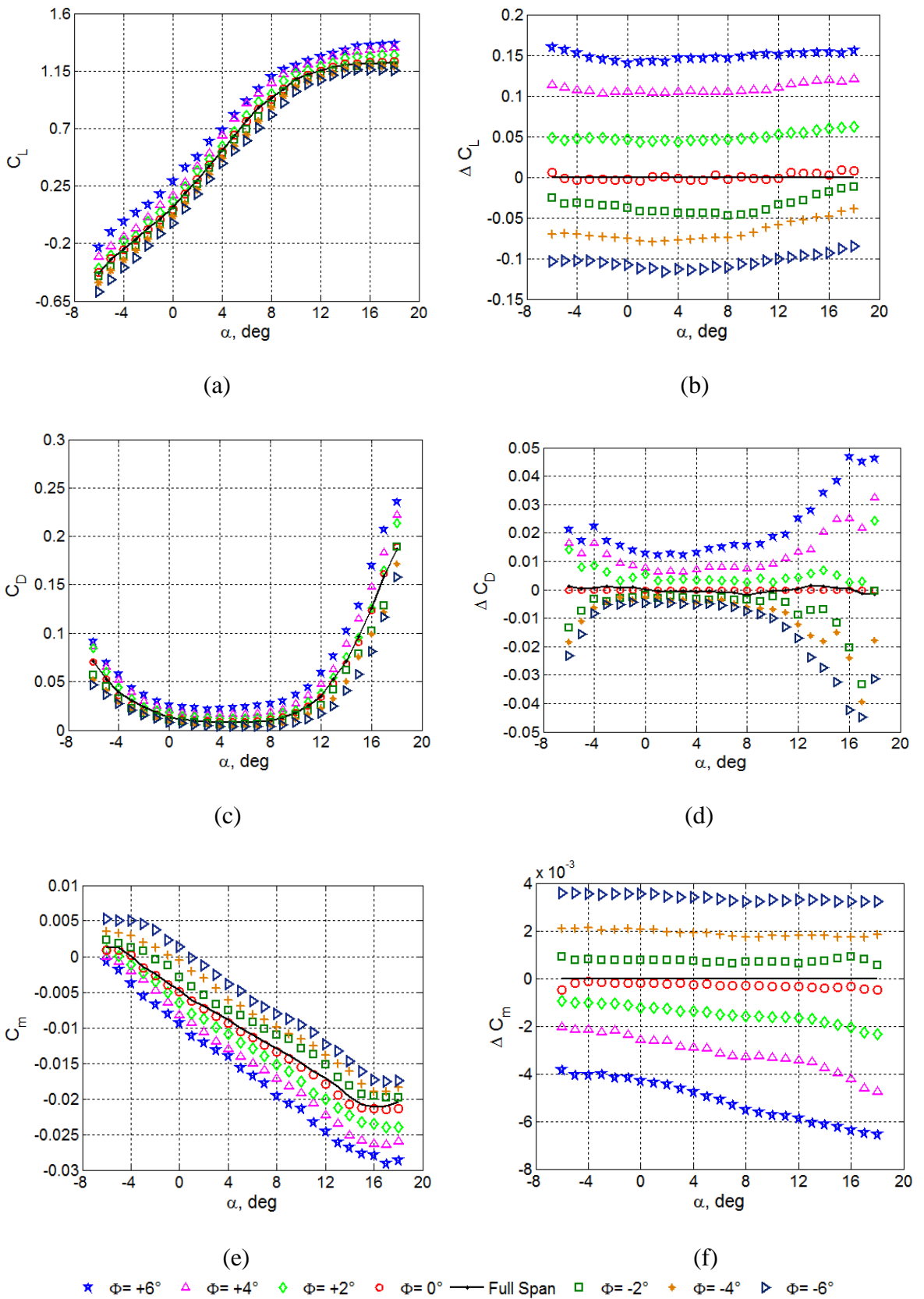


Figure 5.34 . Effects of changing twist angle on the longitudinal static forces and moments, $Re_n = 3.85 \times 10^5$.

baseline model.

Figure 5.34 (a) shows lift coefficient results for various twist configurations. It can be seen that increasing the twist angle to 6° tends to increase lift in agreement with [134] and, also as would be expected, the lift curve slope increases with angle of attack increases to maximum (maximum $\Delta C_L = 0.23$ (13%) compare to un-twisted wing configuration at $\alpha = 18^\circ$). Conversely, reductions are seen as twist angle decreases to $\phi = 4^\circ$ and $\phi = 2^\circ$ with maximum ΔC_L being 0.146 and 0.091 respectively. When negative twist configurations are considered, lift coefficient results were reduced further. When the twist angle varied to $\phi = -6^\circ$, a maximum reduction of $\Delta C_L = -0.145$ was found compared to the untwisted configuration (around 15.4% less compared to $\phi = 6^\circ$). This would be expected due to both net reductions in effective angle of attack as the wingtip moves out of the wing plane and contribution to overall lift production reduces [64]. Similar results were found in [134] where experimental results present greater C_L for higher positive twist angles. Direct comparison between the morphing concept and the full-span baseline wing are also illustrated in **Figure 5.34 (a)** and **(b)**. Similar trends are shown with a maximum $\Delta C_L = 0.022$ at maximum angle of attack ($\alpha = 18^\circ$).

Considering further with increasing angle of attack, overall drag increases can also be seen (**Figure 5.34 (c)** and **(d)**). The experiments show this drag increase to be more effective at $\phi = 6^\circ$ ($\Delta C_D = 0.049$ (20.6% higher than $\phi = 0^\circ$, at $\alpha = 18^\circ$). When $\phi = 4^\circ$ and $\phi = 2^\circ$ are considered, the results still show reasonable drag increases in contrast to $\phi = 0^\circ$ with a maximum increase at $\alpha = 18^\circ$ with $\Delta C_D = 0.031$ (16.4%) and $\Delta C_D = 0.025$ (11.1%) for $\phi = 4^\circ$ and $\phi = 2^\circ$ respectively. On the other hand, the influence of negative twist angle on drag reduction was found to be significant with maximum $\Delta C_D = -0.031$ (19.6% at $\alpha = 12^\circ$) when wing twist varied from $\phi = 0^\circ$ to $\phi = -6^\circ$. As reducing the twist angle to $\phi = -4^\circ$ and $\phi = -2^\circ$, drag reduction was also decreased, but still less drag increase compare to $\phi = 0^\circ$ with 9.88% and 1.37% respectively. This result gives some indication of the influence of large twist angles out of the wing plane on overall performance. This does however, seem to be some exceptions to this finding, particularly for $0^\circ < \alpha < 5^\circ$ where the results seem to be relatively low due to a lower increase in angle of attack. Due to increased sensitivity to the onset tip flow separation on wing after $\alpha = 12^\circ$, a dramatic drag increase was seen in most of the twist cases presented. A similar trend was observed both

computationally and experimentally [134] where there is a link between a reduction in C_D with negative twist variation to a maximum. Moreover, the un-twisted configuration of the morphing concept and full span baseline wing cases show very similar drag level trends (maximum $\Delta C_D = 0.001$ at $\alpha = 18^\circ$) implying adequate simulate between these two configurations under these conditions.

Figure 5.34 (e) and **(f)** illustrates the pitching moment coefficient results for various wing configurations. It can be clearly seen that nose down pitching moments are the predominant action on the wing twist change. This was expected due to the use of the reflexed trailing edge of the 12% Zagi airfoil. It can also be seen from plot C_m (**Figure 5.34 (e)**), at $\phi = -6^\circ$ that the pitching moment is positive ($\alpha < 0^\circ$) signifying the effectiveness of the trailing edge at producing stabilising nose-up moments with increasing the angle of attack, a maximum negative pitching moment was observed. In general, trends between the twist cases are very similar. At $\phi = +6^\circ$, results showed that the aerodynamic centre translation aft is much more than other cases presented with a maximum difference of $\Delta C_m = -0.0067$. Reducing the twist angle to $\phi = -6^\circ$, pitching moment coefficient still shows the trend as seen in $\phi = +6^\circ$, representing a 40% decrease compared to $\phi = 0^\circ$ ($\Delta C_m = 0.0037$).

Further comparisons between the full span baseline wing and the $\phi = 0^\circ$ twist configurations are shown in **Figure 5.34 (f)**. It can be clearly seen that there is strong evidence that both cases perform the same for most aerodynamic metrics (maximum $\Delta C_m = 0.001$ at $\alpha = 11^\circ$).

For side force coefficients, there is a linear trend with an augmented side force coefficient with varying angle of attack and twist angle to a maximum (both positive and negative side **Figure 5.35 (a)** and **(b)**). As would be expected, no side force was seen at $\phi=0^\circ$ or for the full span wing model (**Figure 5.35 (b)**) in all ranges of angles of attack. As twist increased, the side force increased and augmented with further increase in angle of attack ($C_Y = -0.0072$ and $C_Y = 0.0068$ for $\phi=6^\circ$ and $\phi=-6^\circ$ respectively at $\alpha=16^\circ$). Furthermore, due to the unsteady vortex bursting phenomenon[181], after $\alpha=16^\circ$ the results started become more stable, and began to reduce at $\phi = -6^\circ$. As corresponding twist angles of $\phi=4^\circ$ and $\phi=-4^\circ$, clear reduction was observed compared to $\phi= \pm 6^\circ$, with 42% and 35% respectively at $\alpha=18^\circ$.

The influence of twist on the rolling moment coefficient for both positive and negative twist is presented in **Figure 5.35 (c)** and **(d)**. As is well known, Prandtl's classical lifting-line theory and the Fourier coefficients [65], have shown previously that increases in wing twist away from the planar configuration can provide substantial roll authority suitable for aircraft roll control [182], [183]. As can be seen from **Figure 5.35 (c)** and **(d)**, rolling moments achieved through increasing twist angle to $\pm 6^\circ$ were maximum at $\Delta C_l = 0.0079$ and $\Delta C_l = -0.0099$ ($\alpha = 18^\circ$) for $\phi = -6^\circ$ and $\phi = 6^\circ$ respectively. As would be expected, negative roll moments were achieved for $\phi > 0^\circ$ due to increased lift force over the morphing element that tends to roll aircraft left. At $\phi = -4^\circ$ and $\phi = +4^\circ$, maximum roll coefficients of $\Delta C_l = 0.0057$ (30% less than $\phi = -6^\circ$) and $\Delta C_l = -0.0066$ (34.4% less than $\phi = -6^\circ$) at $\alpha = 18^\circ$ respectively were found and reducing to $\Delta C_l = 0.0035$ and $\Delta C_l = -0.0045$ for $\phi = -2^\circ$ and $\phi = +2^\circ$ respectively.

The yaw moment coefficient with different twist cases versus angle of attack is presented in **Figure 5.35(e)** and **Figure 5.35 (f)**. It can be seen that the general trend shows positive yawing moments exist for $\phi = -2^\circ$ and $\phi = -4^\circ$, at $\alpha > 15^\circ$. When $-2^\circ \leq \phi \leq 2^\circ$, the results suggest a limited effects on C_n with a maximum $\Delta C_n = 1 \times 10^{-4}$ at $\phi = +2^\circ$. Increasing twist angles to a maximum, C_n was found to be more effective with a maximum $\Delta C_n = 1.4 \times 10^{-4}$ and $\Delta C_n = 3.4 \times 10^{-4}$ for $\phi = 6^\circ$ and $\phi = -6^\circ$ respectively. As can also be seen yaw moments seem to be insensitive to changing angle of attack ($-6^\circ < \alpha < 12^\circ$) in all twist cases presented. This situation does change as further aerodynamic loading increases on wing the model and the results become more pronounced for $\alpha > 12^\circ$. This would be expected as increased wing drag level becomes more substantial after $\alpha = 12^\circ$ as seen in **Figure 5.34 (c)**.

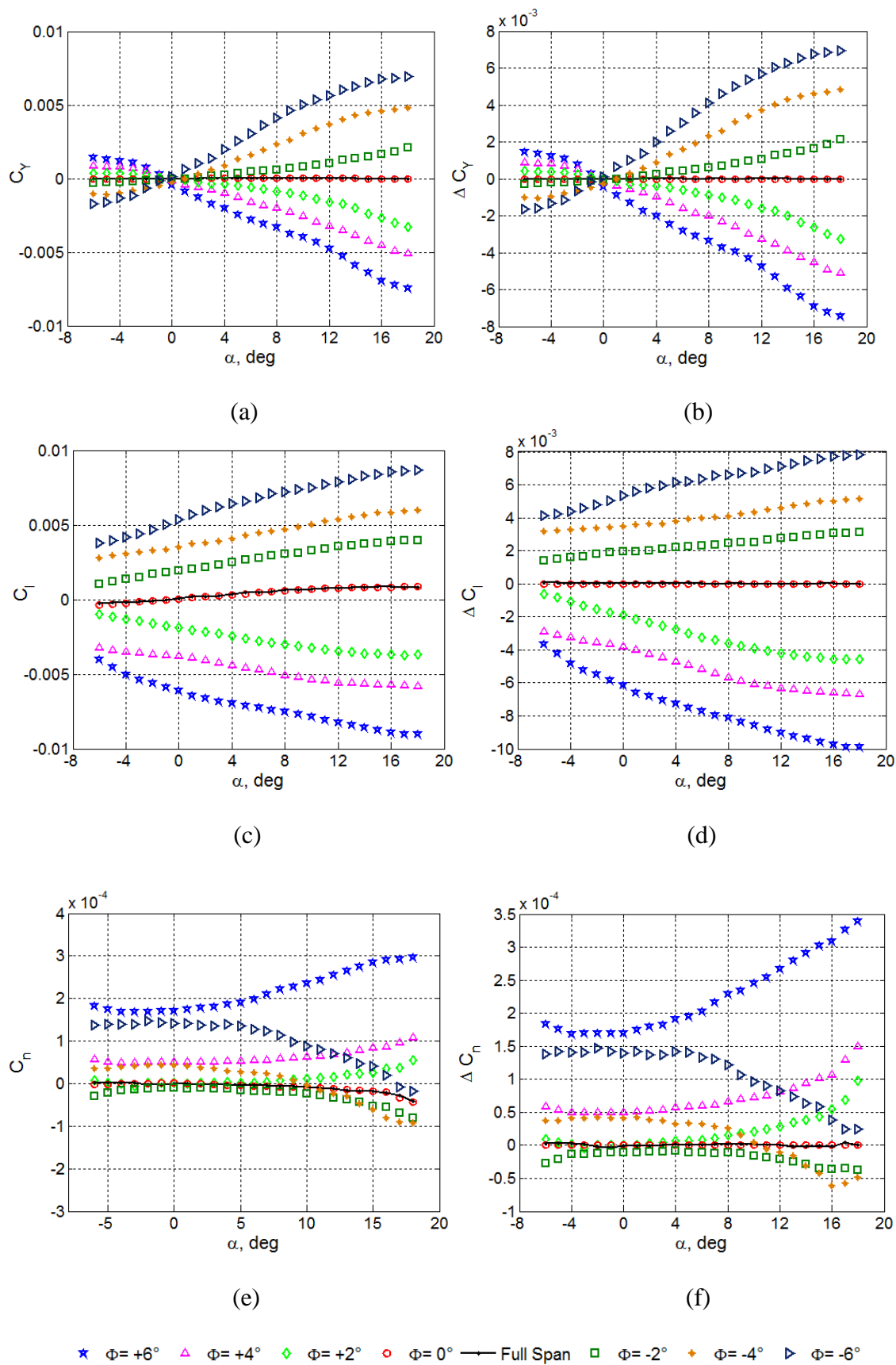


Figure 5.35 Effects of changing twist angle on the lateral static forces and moments, $Re_n = 3.85 \times 10^5$.

5.3.4 Influence of Reynold Number on Aerodynamic Response of Wing Twist

With the decision to introduce no artificial boundary layer tripping to the model, a study of the influence of the Reynolds number on the static force and moment characteristics was conducted to investigate any changes in the results in this transitional flow regime. **Figure 5.36** and **Figure 5.37** illustrate the results for twist at $Re_n = 5.14 \times 10^5$. It can be clearly seen that the basic aerodynamic trends were observed to be the same as seen for $Re_n = 3.85 \times 10^5$. For C_L , the twist cases ($\phi > 0^\circ$) presented do provide effective lift production compared to $\phi < 0^\circ$. This would be expected as increased angle of twist at the wing-tip tends to increase the lift force. Comparing this lift production with $Re_n = 3.85 \times 10^5$, the results seem to be slightly increased approximately $\Delta C_L(max) = 0.04$ (2.75%) for $\phi = 6^\circ$ at $\alpha = 18^\circ$ (**Figure 5.36 (a)** and **(b)**). This highlights that the increased Reynolds number provides additional lift force, as reducing the twist angle to -6° , similar to $\phi = 6^\circ$, the influence of Re_n has a very minor influence on the lift coefficient results. As would be expected, the magnitude of lift coefficient is reduced and compared to $Re_n = 3.85 \times 10^5$, $\Delta C_L(max) = 0.05$ (3%) is obtained for $\phi = -6^\circ$ favouring $Re_n = 5.14 \times 10^5$. In addition, the lift coefficient of a full span wing model is also presented and it can be seen that there is good agreement between full span wing and zero twisted wing modelling. This indicates that the twist mechanism works as normal as a full span wing.

Similar to C_L , there is a reasonably coherent influence of Reynolds number with general magnitudes increasing with increasing Re_n . It can be seen from **Figure 5.34(c)** that significant drag increase was obtained when $\alpha = 18^\circ$ due to increased sensitivity to the onset flow separation on the wing structure after $\alpha = 12^\circ$. This increase is further exacerbated by increasing Re_n ($\Delta C_D = 0.025$ compared to $Re_n = 3.85 \times 10^5$) for $\phi = 6^\circ$ at $\alpha = 18^\circ$ as shown in **Figure 5.36 (c)**. Changing the incidence angle of a wing has the similar trend as seen for $Re_n = 3.85 \times 10^5$. The overall coefficient magnitudes were reduced with reduced angle of attack. In saying this however, there exists subtle characteristics within the results that indicate a small degree of reduction particularly for $0^\circ < \alpha < 5^\circ$.

Similar circumstances are discussed for $Re_n = 3.85 \times 10^5$, here for $Re_n = 5.14 \times 10^5$, considering the results for $\phi < 0^\circ$ as shown in **Figure 5.36 (d)**, there

seems to be much less of a variation in change in drag coefficient when compared to the $\phi > 0^\circ$ configurations, with the influence of the twist angle being much less pronounced than that found for $\phi > 0^\circ$. One possible reason for this may lay in the increased effectiveness of negative twist angles at producing less overall lift (and therefore less lift-dependent drag) as well the ability of negatively-twisted morphing configurations to maintain lower effective angles of attack relative to the freestream flow. Furthermore, the full span wing drag coefficient results are also illustrated and it is clearly seen that the twist mechanism does not have any detrimental effect on the aerodynamic performance of the plane.

Figure 5.36 (e) and (f) highlight the results for C_m versus angle of attack. It can be seen that as the twist angle increases from -6° to 6° , the effective pitching moment coefficient reduces, as with the similar trend seen in **Figure 5.34(e)**. Comparing **Figure 5.34(e)** with **Figure 5.36 (e)**, results for C_m indicate that higher Re_n produces lower magnitudes of pitching moment coefficient.

For C_Y , the influence of Re_n is the increased effectiveness to produce side force as clear deviation is seen in C_l as well. It can be seen from **Figure 5.37 (a) and (b)** that negative and the positive twist configurations have completely opposite effects on the aerodynamic. This would be expected as increased lift force on positive twist configurations tends to have negative side effects, and positive side effects for $\phi < 0^\circ$. The trend between the small angles of twist ($\phi > 0^\circ$) and the larger twist is increased as the angle of twist increases and when negative twisted morphing configurations are considered, similar to $\phi > 0^\circ$, the side effects are a little increased, but in a negative direction. Comparing this feature with the low Reynolds number, similar results were obtained. Although similar trends were obtained, in most cases as would be expected there is a slightly augmentation in terms of side force. As far as $\phi = 6^\circ$ is considered there is a $\Delta C_Y = 0.001$ between $Re_n = 3.85 \times 10^5$ and $Re_n = 5.18 \times 10^5$ and this rate is further amplified to $\Delta C_Y = 0.0020$ at $\phi = -6^\circ$ (due to asymmetrical airfoil shape, negative and positive side twist performs differently). Reducing the twist angle to 2° and -2° , the magnitudes are also reduced to $\Delta C_Y = 7 \times 10^{-4}$ and $\Delta C_Y = 5 \times 10^{-4}$ respectively.

Figure 5.37 (c) illustrated C_l results for different angles of twist versus angle of attack at $Re_n = 5.18 \times 10^5$. It can be clearly seen that negative roll moments were achieved at $\phi > 0^\circ$ as increased lift force over the morphing elements that tends to

roll aircraft left. In contrast, a positive roll moment is produced in $\phi < 0^\circ$ that is the wing will roll in the right direction. Moreover, as expected, the results for ΔC_l show an almost symmetrical deviation with variation in twist angle due to the inherent connection between ΔC_L and ΔC_l . In general, the roll moment coefficient was slightly increased with the increased Reynolds number and maximum ΔC_l was found to be 0.001 and 0.0004 for $\phi = 6^\circ$ and $\phi = -6^\circ$ respectively.

For C_n , results show a similar trend as discussed for lift, pitching moment, and rolling moment coefficients for $\alpha < 12^\circ$ (**Figure 5.37 (e)**). However, after this angle of attack, the yawing moment coefficient is seen to increase markedly as the dependence on increasing wing drag levels becomes more and more significant. Comparing this to $Re_n = 3.85 \times 10^5$, the yawing moment coefficients showing almost steady performance with $\Delta C_n = 6.3 \times 10^{-6}$ at $\phi = -6^\circ$.

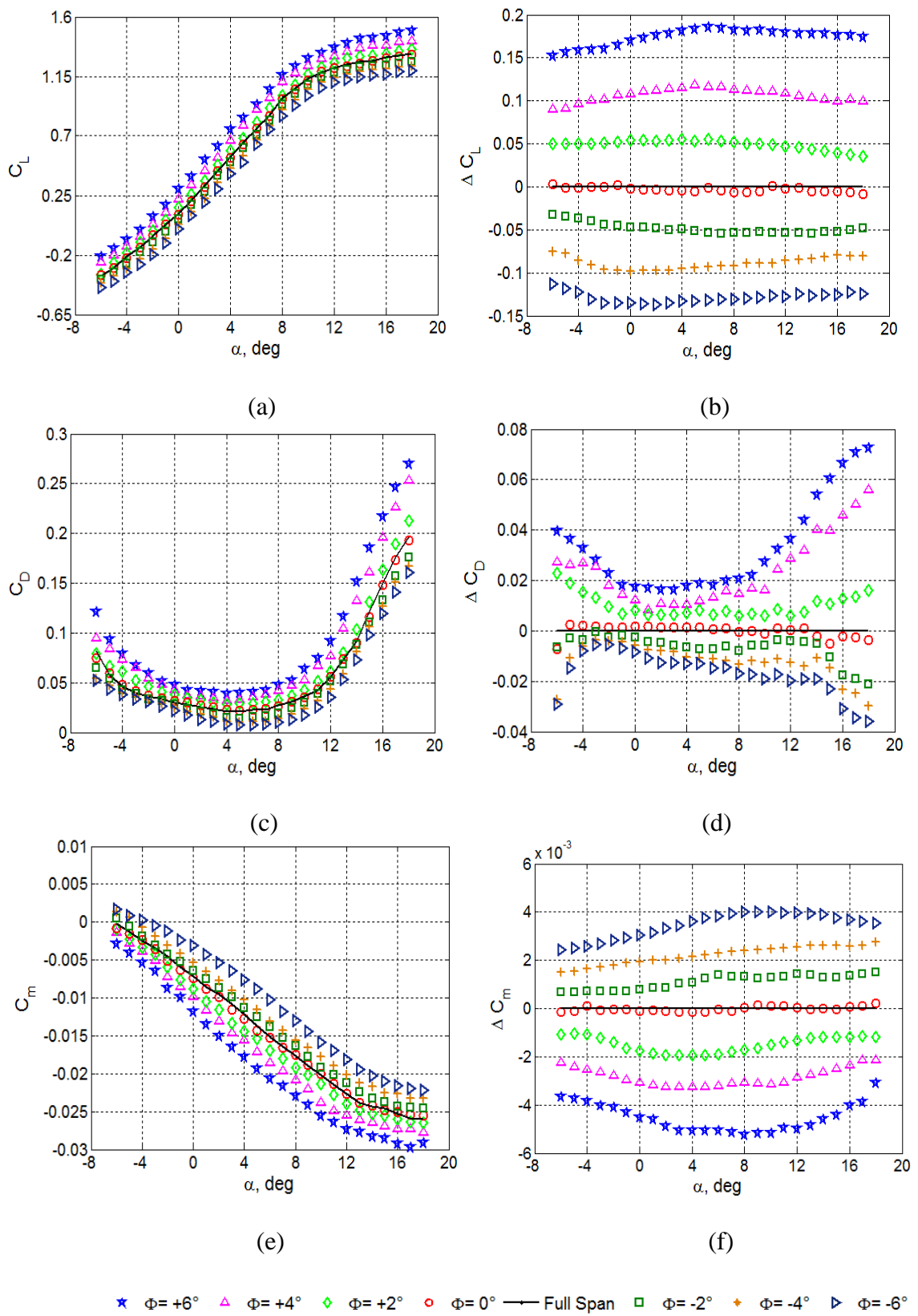


Figure 5.36 Effects of changing twist angle on the longitudinal static forces and moments, $Re_n = 5.14 \times 10^5$.

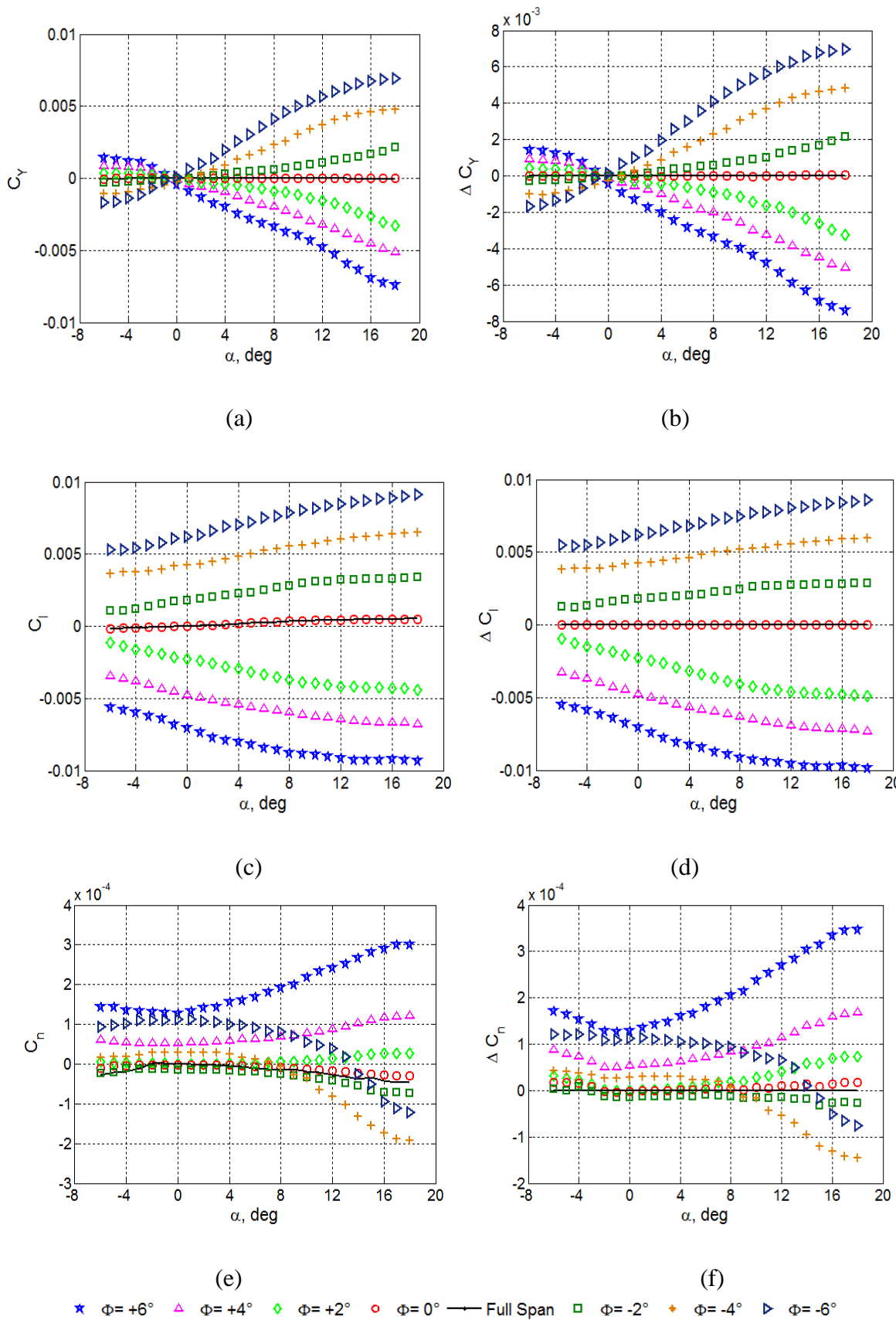


Figure 5.37 Effects of changing twist angle on the lateral static forces and moments, $Re_n = 5.14 \times 10^5$.

5.3.5 Comparison between Standard Aileron and Morphing Concept

Figure 5.38 compares between the standard aileron model and morphing concept. These results were performed at a $Re_n = 5.14 \times 10^5$. As mentioned in **Section 4.2.3**, the aileron angles were -30° to 30° in steps of 10° with the twist angle of the morphing concept, varied from -6° to 6° in steps of 2° . The lift coefficient results are presented in **Figure 5.38 (a)**. It can be seen that deflecting aileron angle to $\gamma > 0^\circ$ resulting in an increase in lift at a given angle of attack. Maximum lift coefficient, up until $\gamma = 30^\circ$, where only a small lift increment is seen over $\gamma = 20^\circ$ (7.6% at $\alpha=9^\circ$). Comparing these aileron models with twist configurations, the morphing concept shows very similar lift results (the differences between the $\phi = 6^\circ$ and $\gamma = 30^\circ$ configuration of $\Delta C_L = 0.03$ (2%) at $\alpha=9^\circ$). A lower deflection magnitudes, a small reduction in the lift curve slope was measured with the $\gamma = 20^\circ$ and $\gamma = 10^\circ$ configurations, almost equivalent in performance to the $\phi = 4^\circ$ and $\phi = 2^\circ$ respectively.

For negative angles, the lift becomes lower for reducing angle to $\gamma = -30^\circ$ and $\phi = -6^\circ$. This would be expected as reducing the effective incidence angle of the surface to decrease the lift force. Contrary to positive angles, variation between the negative twisted morphing concept and aileron configurations are slightly less and twisted concept was found to produce more lift than aileron deflections with $\Delta C_L = 0.03$ (4.5%) at $\phi = -6^\circ$ ($\alpha=9^\circ$) compare to $\gamma = -30^\circ$. Reducing the angle of twist and aileron deflection angle, similar characteristics were seen with ΔC_L is 0.05(5%) and 0.01(1%) for $\phi = -4^\circ$ and $\phi = -2^\circ$ respectively compare to $\gamma = -20^\circ$ and $\gamma = -10^\circ$.

For drag coefficient, there is a clear difference between the aileron and morphing concept model at large deflection angles. For the twisted morphing configuration at $\phi = 6^\circ$, same the highest drag coefficients were measured only to be supposed by the aileron configuration at $\gamma = 30^\circ$. It can also be seen from **Figure 5.38(b)** that the minimum drag coefficient is higher for the aileron configuration (23.9%) compared to the morphing concept (compare to $\phi = 6^\circ$ with $\Delta C_D = 0.055$ at $\alpha=18^\circ$). These differences exist at lower angles, but reduce in magnitude. For $\gamma = 20^\circ$, the drag coefficient results are still larger (15.4% and 24% high drag production compare to $\phi = 6^\circ$ and $\phi = 4^\circ$ respectively). This trend was continued for $\gamma = 10^\circ$ with 14% drag increase over $\phi = 2^\circ$. These would be expected due to the aileron configuration generating significant flow separation.

Considering the results for $\gamma < 0^\circ$ and $\phi < 0^\circ$ as shown in **Figure 5.38 (b)**, overall, there appears to be less of a variation in change in drag coefficient for comparable angles of attack comparing to the $\gamma > 0^\circ$ and $\phi > 0^\circ$ configurations. One possible reason for this may lay in the increased effectiveness of both negative twist and negative aileron configurations at producing less overall lift (and therefore less lift-dependent drag) as well the ability of negatively-twisted morphing configurations to maintain lower effective angles of attack relative to the freestream flow. When comparing the aileron configuration with the negative twist configuration, 3.5% higher drag was found to exist for $\gamma = -30^\circ$ over $\phi = -6^\circ$ at $\alpha=18^\circ$. This trend can be seen for $\gamma = -20^\circ$ with 2.79% drag increase over $\phi = -4^\circ$, and 1.15% for $\gamma = -10^\circ$ compare to $\phi = -2^\circ$. These results indicate that twist configuration produce less drag in all over aileron deflection angle, which tend to increase the flight envelope.

Figure 5.38 (e) highlights the influence of changing twist and aileron angle on the pitching moment coefficient. Increased negative pitching moment is the predominant result for all cases presented. Comparing these aileron angles with twist cases, the results for the aileron configuration had similar performance as that seen for twist cases between $-6^\circ \leq \alpha \leq 0^\circ$. This situation does change as aerodynamic loading increases with the reduction in C_m with deflection either in twist or aileron deflection angle, becoming more pronounced for $\alpha > 0^\circ$. When comparing directly the pitching moment coefficient between these two configurations, maximum ΔC_m between $\gamma = 30^\circ$ and $\phi = 6^\circ$, and $\gamma = -30^\circ$ and $\phi = -6^\circ$ were found to be 0.0064 and 0.0048 respectively, introducing that aileron deflection is more effective at pitching moment production.

For the side force coefficient, a similar trend was observed for both the aileron and morphing configurations with possible exception of $\phi = 2^\circ$ and $\phi = -4^\circ$. It can be seen from **Figure 5.38 (c)**, when the aileron configuration is deflected to $\gamma = 30^\circ$, negative side force is obtained with a magnitude much larger than when the deflection angle is reduced to 10° . Contrary to the morphing configuration, at $\gamma = 30^\circ$, $\Delta C_Y = 0.0003$ (3.5%) compare to $\phi = 6^\circ$, this rate is less pronounced between $\phi = 4^\circ$ and $\gamma = 20^\circ$, where ΔC_Y was found to be 0.001(2.2%) and seen to favour movement to $\phi = 4^\circ$ (which indicated $\phi = 4^\circ$ produce more side force than $\gamma = 20^\circ$). When negative angles are considered for $\phi = -4^\circ$ and $\gamma = -20^\circ$, the results seem to be

shifted to the aileron configuration ($\gamma = 20^\circ$ produced more side force than $\phi = 4^\circ$). Moreover, the variations between these angles are minimal with $\Delta C_Y = 0.0001$ (0.1%).

Figure 5.38 (d) illustrates the roll coefficient results for the various twist and aileron configurations. As is shown in all of these trends, roll authority is significant with both aileron and twist changes. This would be expected due to increases in the lift distribution increases roll moment. Comparing the twist with aileron configurations directly, very similar trends were observed. It can be seen that the aileron at $\gamma = 30^\circ$ produces a similar roll coefficient with $\phi = 6^\circ$. For these cases ($\gamma = 30^\circ$), the produced roll moment appears to be slightly more than $\phi = +6^\circ$ (maximum ΔC_l is 0.0004 (4.6%) at $\alpha = 18^\circ$). When reducing the angle of aileron deflection to 20° , the roll coefficient performed similar to results for $\phi = 4^\circ$, although at higher angles of attack there is a large moment generated from the aileron configuration than for the morphing configuration ($\Delta C_l = 0.0015$). For negative deflection ranges, similar trends as discussed for positive deflection seem to exist. It can be seen that the difference between the $\gamma = -30^\circ$ and $\phi = -6^\circ$ shows an advantage of $\Delta C_l = 0.002$. For morphing concept $\phi > 6^\circ$ with this advantage decreasing with further in negative angles of aileron deflection ($\gamma = -20^\circ$ and $\gamma = -10^\circ$) and twist ($\phi = -4^\circ$ and $\phi = -2^\circ$) ($\Delta C_l = 0.0011$ and $\Delta C_l = 0.0009$ respectively). In general, in both cases presented here, roll authority was achieved and compared well to both aileron and twist morphing configurations. The similar roll moments obtained implies that the morphing concept could possibly replace a traditional aileron with less drag penalty.

Comparing C_n results between the ailerons and morphing configurations, there appears to be much more variation compared to the other aerodynamic coefficients already discussed. It can be seen from **Figure 5.38 (e)** that, for some cases presented linearly increasing yawing moments were found to exist up to $\alpha \cong 12^\circ$. For $\alpha > 12^\circ$, the yawing moment coefficient is seen to deviate markedly in both cases as the dependence on increasing wing drag and propensity for stall becomes more and more significant. For positive aileron configuration, positive yawing exists with comparisons between $\gamma = 30^\circ$ and $\phi = 6^\circ$, show results higher by $\Delta C_n = 5 \times 10^{-5}$ (14%). The deviation was found to increase with decreasing aileron deflection angle

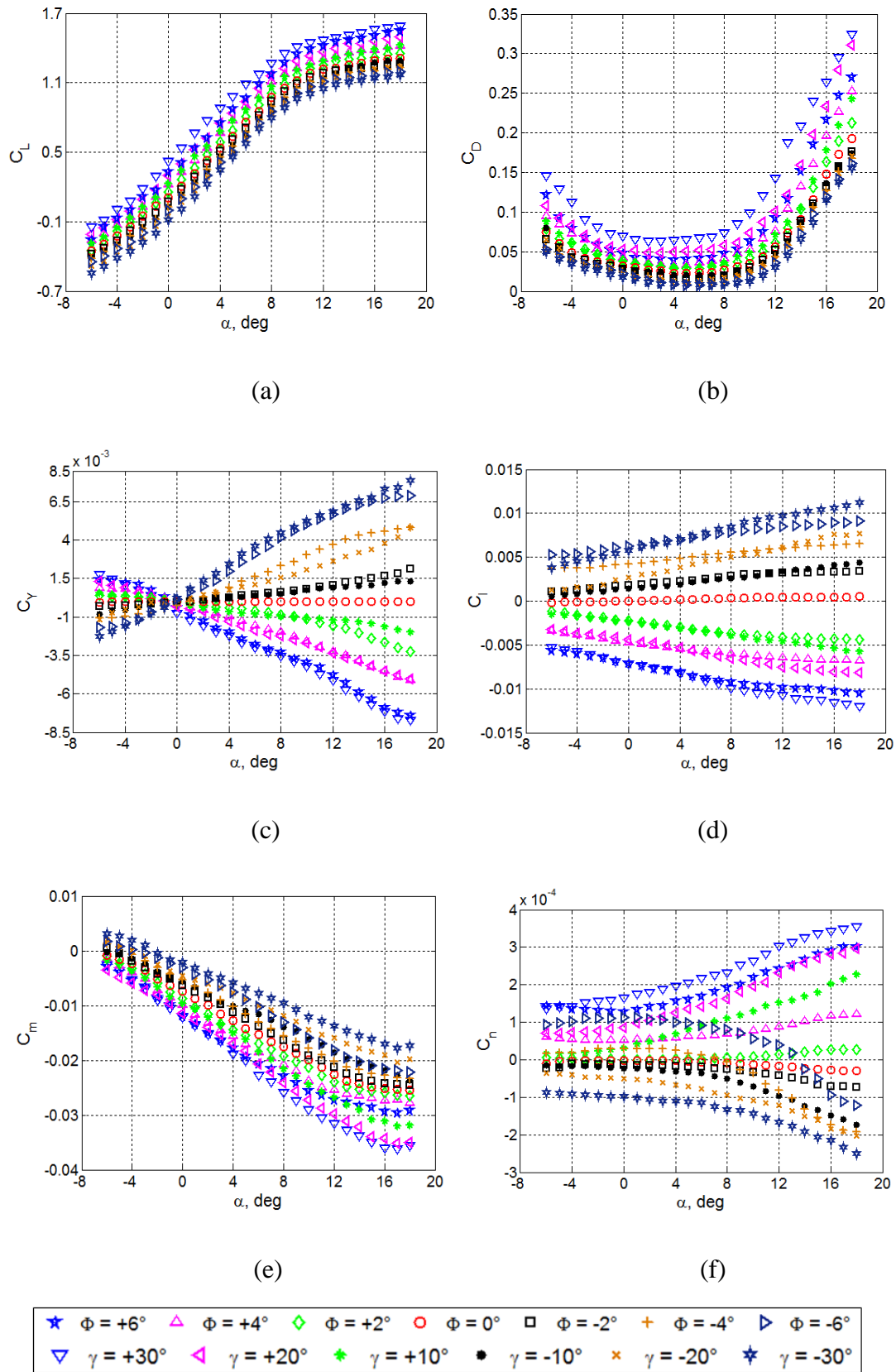


Figure 5.38 Comparison between plain aileron and twist configuration: (a) C_L , (b) C_D , (c) C_Y , (d) C_l , (e) C_m , and (f) C_n

at $\gamma = 20^\circ$. Similar to $\gamma = 30^\circ$ here, the results show the same trend seen for $\gamma = 30^\circ$, however comparing the results with $\phi = 4^\circ$, the ΔC_n variation increased further to 1.75×10^{-4} (more than 80% less performance compare to $\gamma = 20^\circ$). For negative deflection, results for morphing configurations are more promising with 15% differences at between $\gamma = 20^\circ$ and $\phi = 4^\circ$.

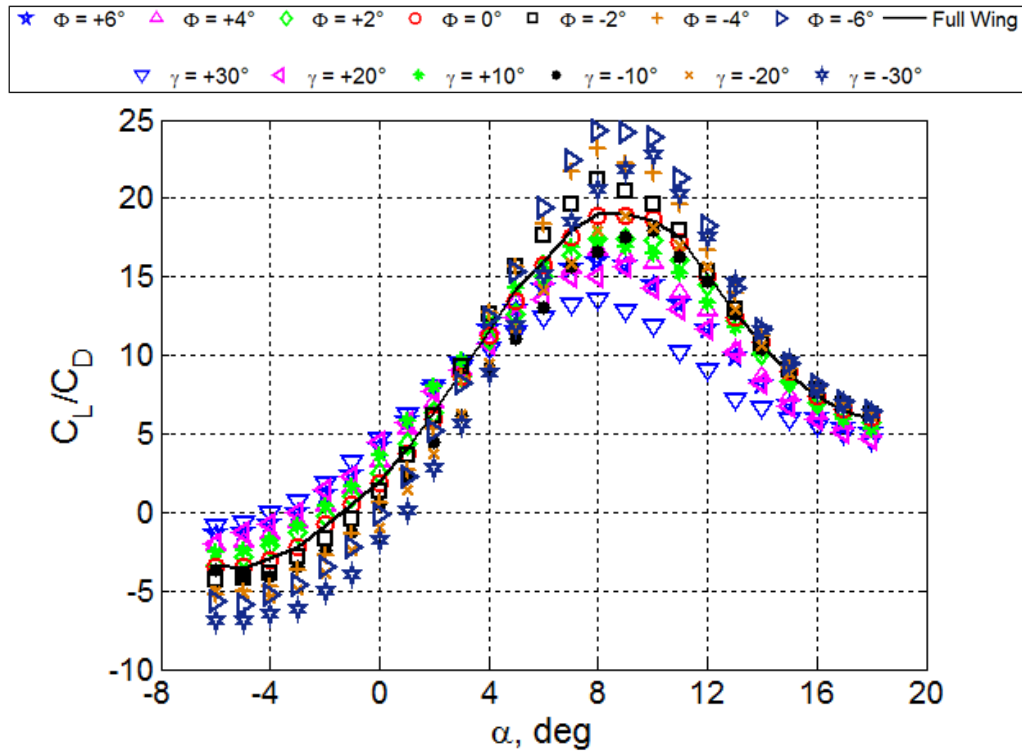


Figure 5.39 Lift to drag ratio for wing twist and aileron configurations.

The combined effects of lift and drag can be usefully combined by plotting the lift to drag ratio versus angle of attack (aerodynamic efficiency). To further discuss the advantage of the morphing system compared to a traditional aileron system C_L/C_D will be used. This is shown in **Figure 5.39**. Since the range of lift coefficient obtainable is very similar for both morphing and aileron configurations, drag coefficients are far difference and dictated C_L/C_D . In all of these configurations, and as would be expected, it can be clearly seen that the best C_L/C_D occurred in $8^\circ \leq \alpha \leq 10^\circ$ and the principle effect on C_L/C_D is one of a reducing magnitude with movement of aileron deflection magnitude and twist with positive deflection. With deflection of $\gamma=30^\circ$, appear to show the worst with comparison to $\phi = 6^\circ$, $\Delta(C_L/C_D)$ found to 17.5% less. In overall, performance is reduced 28.7% at $\alpha = 8^\circ$ compare to full wing baseline model. This would actually be expected due to severe flow separation at the

sudden and sharp discontinuity in ailerons. With further decrease aileron deflection angle to $\gamma=20^\circ$, appear to be much closer producing 1.8% and 6.25% less performance than $\phi = 6^\circ$ and $\phi = 4^\circ$ respectively. This also shows how standard aileron systems decrease the aerodynamic efficiency of an aircraft over morphing twist. For $\gamma=10^\circ$, interestingly similar trend was observed compare to $\phi = 2^\circ$ with reduction of 0.5% ($C_L/C_D=17.4$ at $\alpha = 9^\circ$). This also initiates that the small degree of deflection has small detrimental effects on aerodynamic performance.

To further quantify this improvement and through comparing positive and negative deflection for both aileron and morphing configurations, there is a significant improvement in terms of efficiency. For $\phi = -6^\circ$ configuration, best (C_L/C_D) is obtained as 24.3 at $\alpha=8^\circ$ and C_L/C_D shows 18.3% improvement over aileron configuration ($\gamma=-30^\circ$). This rate was 22% contrary to full baseline wing model. This reduces by reducing twist angle to -4° with the efficiency reducing to 23.16 (4.7%). However, it is also promising the advantage over the aileron configuration of $\gamma=-20^\circ$. Overall 22.66% improvements achieved at $\alpha = 8^\circ$ and with further increase in angle of attack to $\alpha = 10^\circ$, as expected improvement rate is reduced to 17.84%, which is still high. Interestingly, the $\gamma=-20^\circ$ configuration performed similarly to a full span (zero-twist) wing profile due to low lift coefficient. As mentioned previously for a small positive angle of deflection ($\gamma=10^\circ$) and twist $\phi = 2^\circ$ have minor effect on aerodynamic performance, but in here, for negative angle configurations, 10.5% improvement was seen at $\phi = -2^\circ$ ($\alpha = 8^\circ$) compare to full baseline wing model. Comparing $\phi = -2^\circ$ with $\gamma = -10^\circ$, 12% improvement was achieved. Thus, this smooth and continuous morphing concept appears to be more aerodynamic efficiency than the use of a standard aileron design.

Lastly, to compare the effectiveness of the two concepts, the roll/drag coefficient ratio is shown in **Figure 5.40**. It can be clearly seen that increasing aileron and twist angles in both the positive and negative side increase the magnitudes of moments generated with maximum values occurring at maximum degrees of twist or aileron deflections. However, this ratio provides further insight into how the drag coefficient influences the efficiency of two configurations. This improved performance over the aileron configuration is seen at $\phi = -6^\circ$ with the results showing (C_l / C_D) approximately 14.95% ($\alpha = 6^\circ$) higher than $\gamma=-30^\circ$. This implies that morphing concept with $\phi = -6^\circ$ can provide similar roll moment like aileron ($\gamma=-30^\circ$), but

superior aerodynamic efficiency compare to aileron deflection. As far as $\phi = -4^\circ$ is concerned, 50% improvements are seen over $\gamma = -20^\circ$. This would be expected because twist configurations do provide effective drag reduction while generating significant roll moments compared to standard aileron configurations. Further reduction in twist angle to $\phi = -2^\circ$, similar scenario as seen at $\phi = -4^\circ$ is continued with 38.6% improvement over $\gamma = -10^\circ$. Thence, the negative twisted morphing concepts showed substantial improvement for C_l/C_D in all cases presented over aileron configurations.

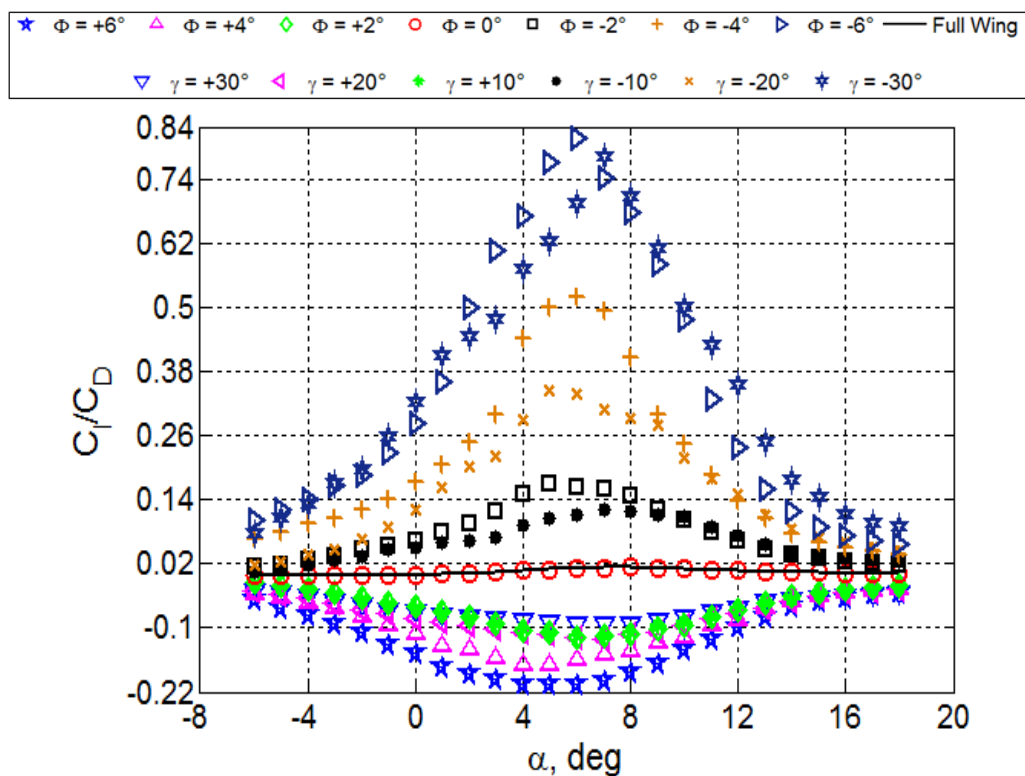


Figure 5.40 Rolling moment Coefficient versus drag coefficient.

Considering the positive angle deflection in aileron and twist configurations, it can be seen from **Figure 5.40**, the highest C_l/C_D value was obtained at $\phi = 6^\circ$. Comparing this with $\phi = -6^\circ$, due to drag increase in positive twist configuration tend to reduce the efficiency. Although efficiency is low, it still has reasonable improvements over the aileron configurations with 44% ($\alpha = 6^\circ$) (compare to $\gamma = 30^\circ$). Interestingly, maximum C_l/C_D was not occurred at maximum aileron deflection angle due to high lift-dependent drag at $\gamma = 30^\circ$. For $\phi = 4^\circ$ configuration, maximum C_l/C_D was found at $\alpha = 4^\circ$ with 63% improvement over $\gamma = 20^\circ$. As far as $\phi = 2^\circ$ considered, minor enhancement (1%) is obtained compare to $\gamma = 10^\circ$. As a results of

this C_l/C_D comparison clearly showed that the morphing configuration either in negative and positive twist provides substantial improvements in contrast to aileron configuration due to low drag coefficient.

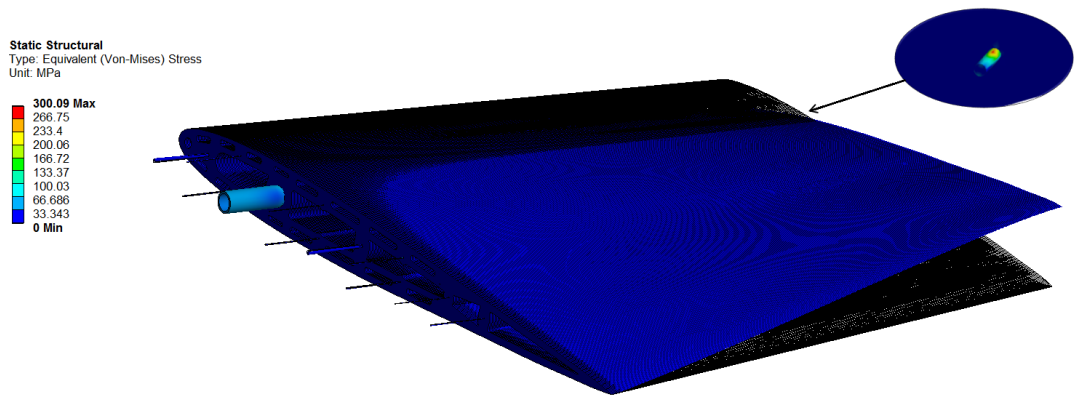
5.4 Flight Testing

As mentioned in **CHAPTER 3**, the morphing concept was adapted to an Extreme Flight Extra 300 RC aircraft with a 78-inch wingspan to validate the concept in a real flight environment. This section initially describes the FEA results for the design from a computational structural analysis with thereafter experimental flight test results presented and discussed.

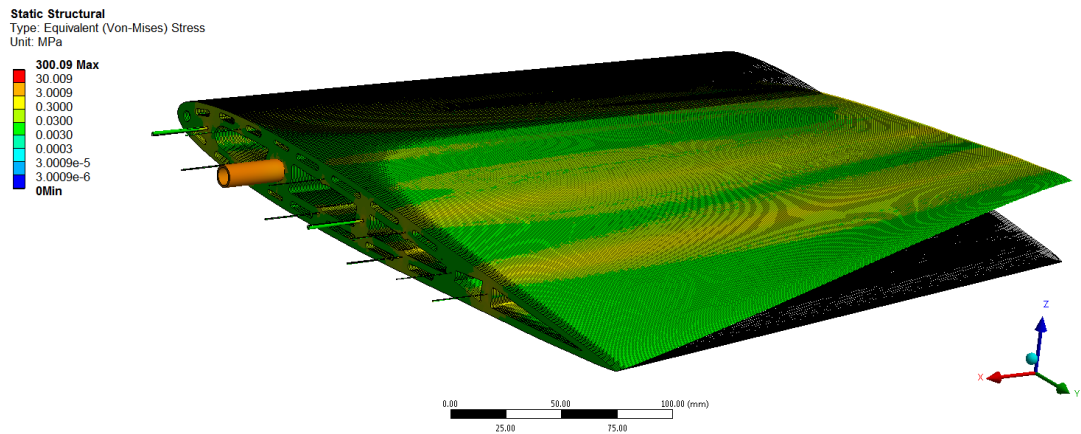
5.4.1 FEA of the Concept for Flight Testing

To design a morphing concept for flight testing needed to consider weight, skin deformation, mechanism suitability and structure durability. Weight was considered the most significant considerations when designing the concept for flight testing phase. Initially different configurations were designed and imported into ANSYS to conduct stress and deformation analysis. Skin deformation was also carefully monitored to ensure an aerodynamically smooth surface.

As the morphing concept adapted for flight testing was 0.3m long and additional rods were needed to maintain the surface smoothness. It can be seen from **Figure A-35** through **Figure A-49**, different numbers of the rods were analysed in order to meet the minimum required angular deformation of $\pm 6^\circ$. Another goal was to optimise the structure to reduce weight. It can be seen from **APPENDIX-A**, that initially 21 rods were tried with subsequent reductions to 11. This was expected as increasing the number of rods tends to increase stress magnitudes and resistance to twist. In some cases presented for these structures, the stresses incurred within these rods were acceptable but for the corresponding balsa rib failed. These cases were discarded. Furthermore, deformation magnitudes are considered as well (as shown from **APPENDIX-A Figure A-42** through **Figure A-49**) and decreased with increasing rod size, leading to a trade-off between structural compliancy, weight and ultimate strength.



(a)



(b)

Figure 5.41 The wingtip structure for flight testing: (a) Von-Mises Stress of structure and (b) Detail analysis of surface Von-Mises stress.

After the optimisation processes, the final structure selected for the prototype wings with the results shown in **Figure 5.41** (summarised in **Table 13**). It can be seen that the maximum stress occurred in the carbon rod (300 MPa) which was acceptable (600MPa Yield Stress) with the maximum stress on any balsa rib structure found to be 20MPa. This was deemed acceptable as the failure criteria for the balsa wood used was 30MPa.

Table 13 Stress and Deformation of a morphing structure

Cases	σ_{max} , MPa	δ_{max} , mm
Wash-out	300.09	44.516
Wash-in	291.5	32.892

Ultimately, this design enables deformation magnitudes in twist of up to 38.704 mm for both wash-in (positive twist) and wash-out (negative twist) twist cases.

These results were without the application of any aerodynamic load. When aerodynamic load and pitching moments are considered, these deflections were found to be 44.52mm (negative twist) and 32.89mm for positive twists cases (as illustrated in **Figure 5.42**). These difference between the negative and positive twist cases were expected as aero load tends to assist twist in negative twist cases and limited twist for positive twist cases. Rib deformation due to twist is also shown in **Figure 5.43**. This is important as it dictates the surface finish. It should be noted that if this value exceeds the boundary thickness displacement rule, surface drag increases. The boundary layer displacement thickness was calculated as 0.64mm [162]. It can be seen that the structure could deforms 0.40mm and 0.36mm (maximum) for positive and negative twist angles respectively. This implies the morphing concept with these design attributes should not have any detrimental effect on aerodynamic performance. It can also be seen that there was a variation in skin deformation between positive and negative twist cases with the differences of 0.16mm favouring to negative twist case. This would be expected because the aerodynamic load acting on morphing structure is against for the wash-in cases and during the twist action stress that occurs on the rib structure is more compared to wash-out cased, hence the increased skin wrinkle rate. Although, it is higher than the wash-out case, it is still lower than the boundary layer conditions.

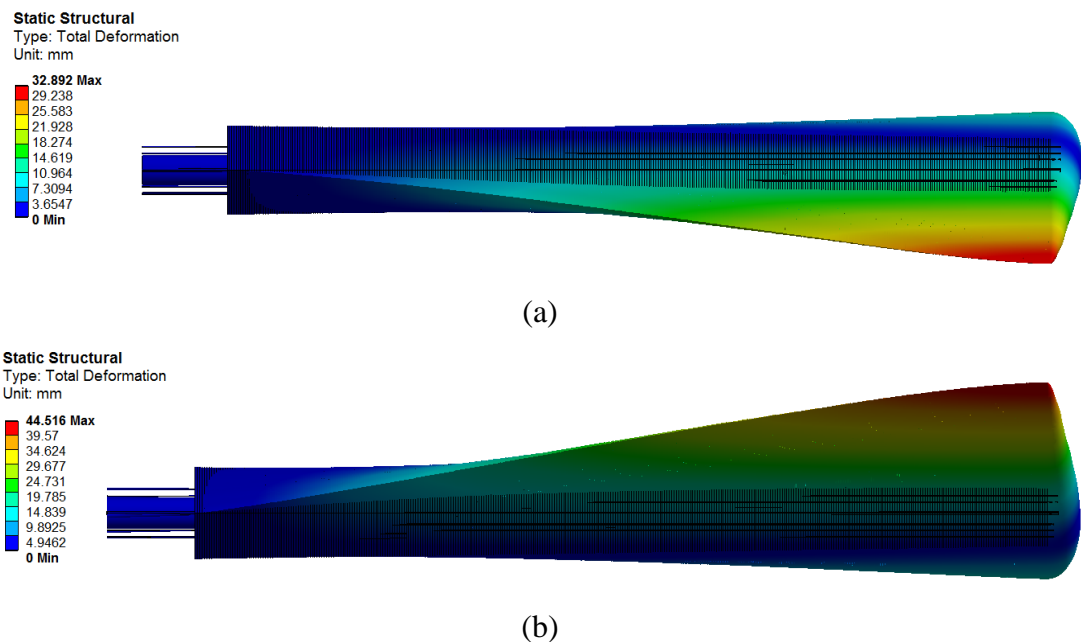
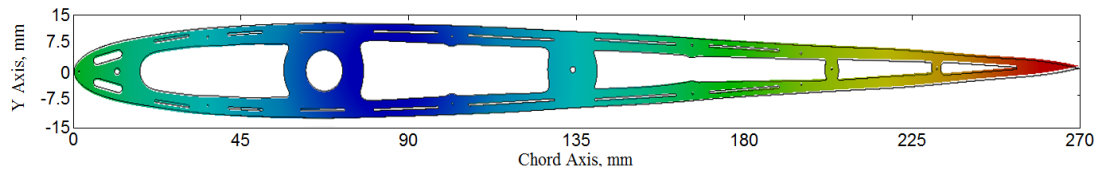
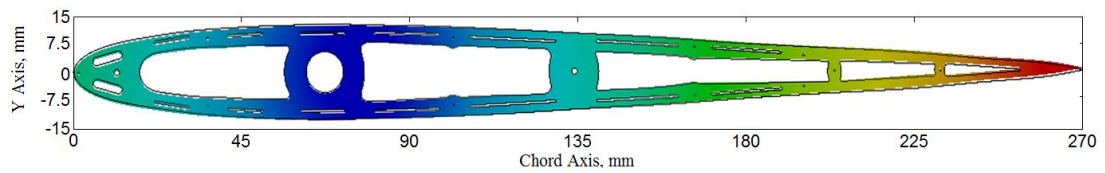


Figure 5.42 Displacement magnitudes of morphing concept: (a) Washin case (positive twist) and (b) Washout case (negative twist).



(a)

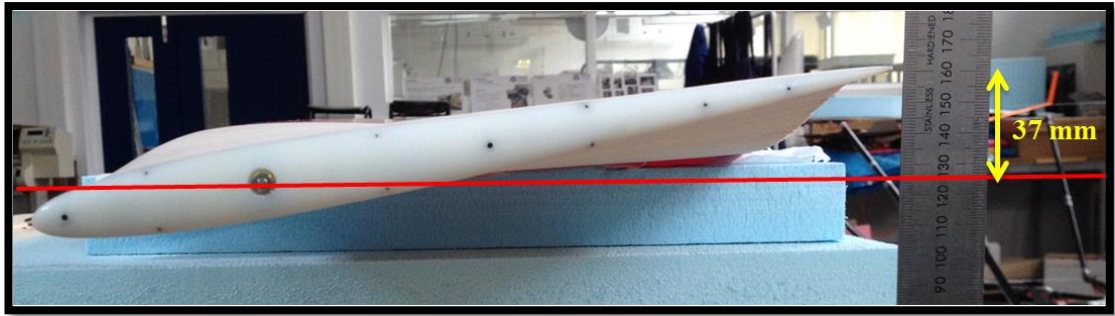


(b)

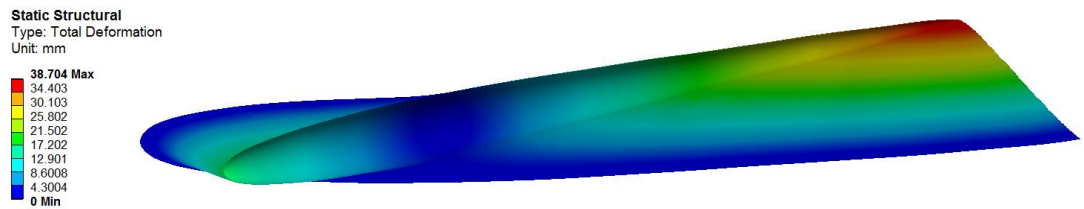
Figure 5.43 Skin (rib) displacement under aerodynamic load: (a) wash-in case (positive twist) 0.40mm and (b) washout case (negative twist) 0.36mm.

5.4.2 Structural Comparison between FEA and Prototype Morphing Wing

The structural deformation magnitudes without aero-load cases are shown in **Figure 5.44** and **Figure 5.45**. In general, there is good agreement between the computational and experimental results. It can be seen that the displacement magnitude in experimental modelling was 37 mm (**Figure 5.44(a)**) and compare to 38.7mm for the FEA (**Figure 5.44 (b)**). Similar results were also seen for negative twist configurations as shown in **Figure 5.45**. It can be clearly seen that the negative twist (max) deformation magnitudes were 38.7mm and 37mm for the FEA and the experimental models respectively. As would be expected, there are slight differences between these two approaches ± 2.5 mm thought mainly to originate from unmodelled friction forces between the ribs and elements.

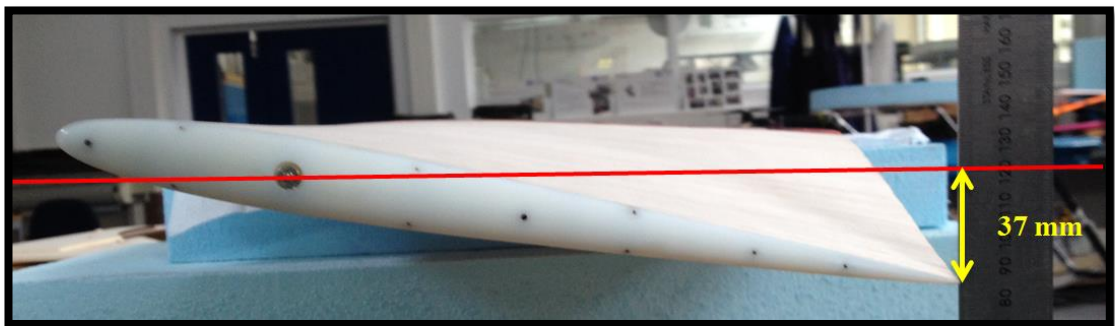


(a)

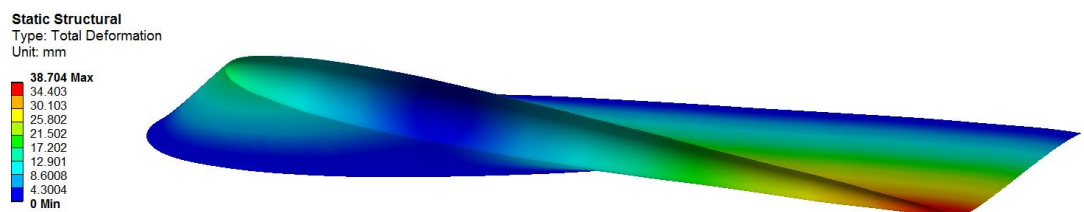


(b)

Figure 5.44 Maximum twist of the morphing concept without any flow interaction: (a) Experimental model twist movement (wash-out) and (b) Numerical modelling twist movement (wash-out).



(a)



(b)

Figure 5.45 Maximum twist of the morphing concept without any flow interaction: (a) Experimental model twist movement (wash-in) and (b) Numerical modelling twist movement (wash-in).

5.4.3 Rolling Rate comparison between the traditional wing structure and prototype morphing wing concept

Actual flight testing of the concept was performed to demonstrate the viability of the concept. Both full wing with aileron (unmodified baseline wing) modified wings (morphing concept) were tested and compared.

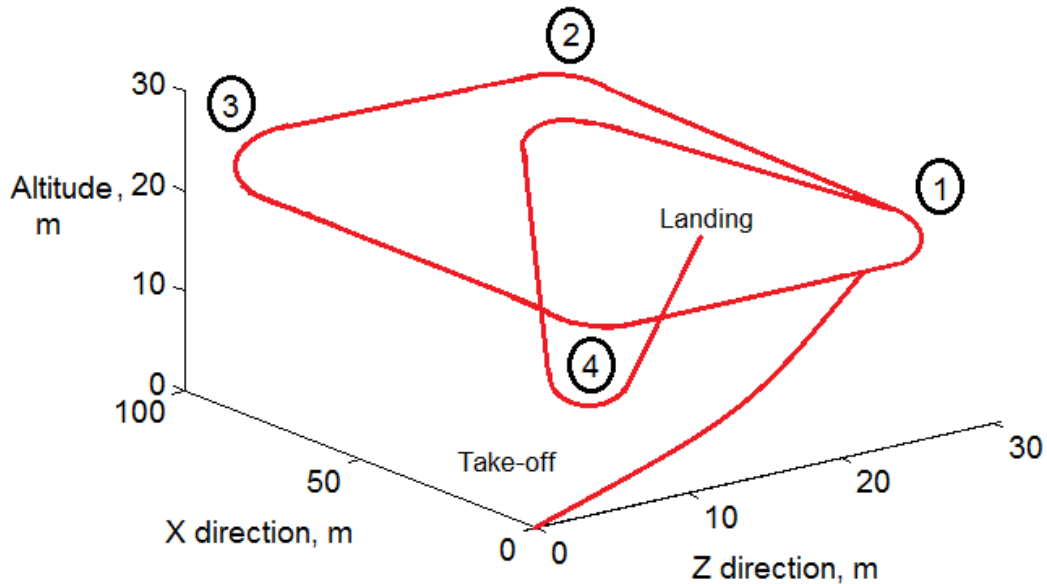
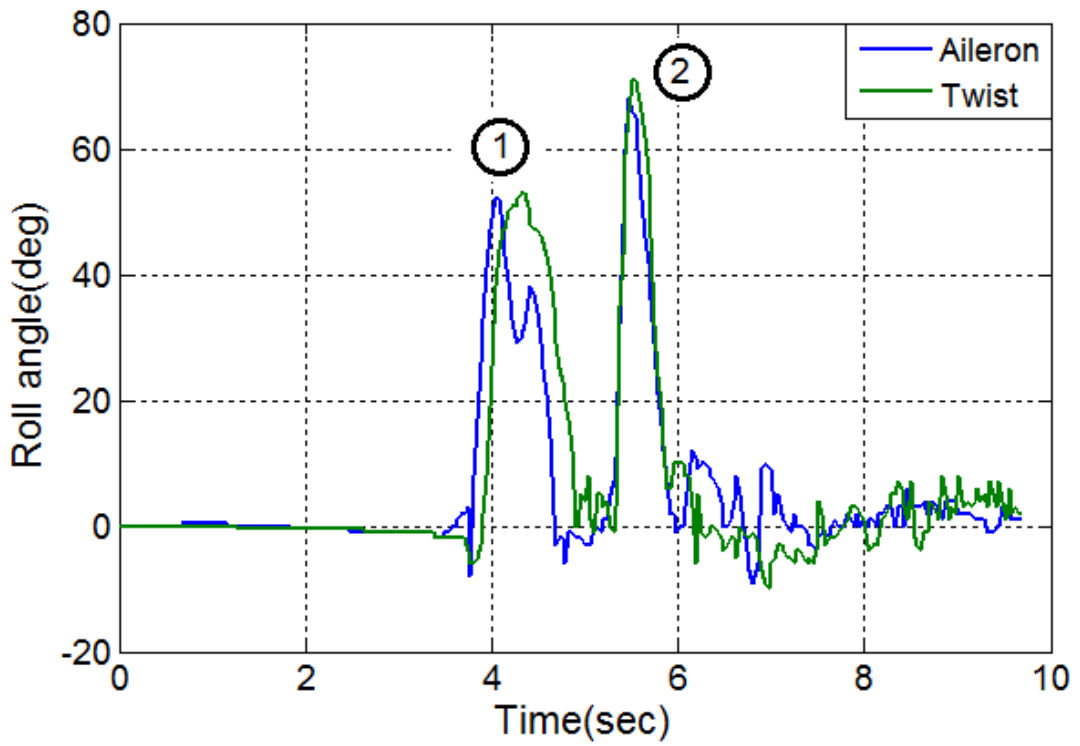


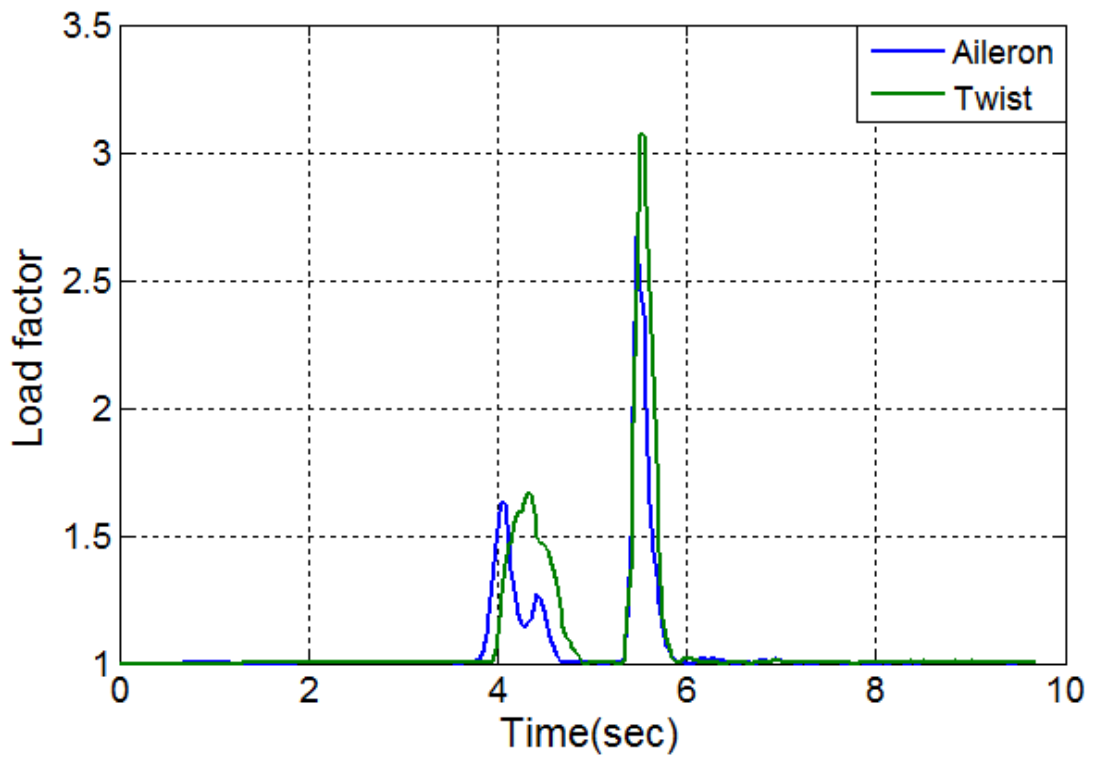
Figure 5.46 Altitude and Approximate Flight Path.

The altitude and flight paths adapted shown in **Figure 5.46**. Here, it can be seen that the pilot tried to do close approximations for both configurations. On the day of flight, the temperature was 6° and the wind speed nominally 5mph. The flight testing started with a take-off position and climbed the desired altitude (30m). Then the basic roll manoeuvring was followed as numbered from 1 to 4. After the 4th roll, the aircraft was landed. It should be also noted that, before and after each test, zero readings were obtained in order to achieve accurate results.

Figure 5.47 and **Figure 5.48** illustrate the basic roll angle achieved for both morphing and baseline wing configurations. It can be seen that the achieved roll angle for both designs is very similar for number 1 and 2 (**Figure 5.47 (a)**). Comparing these results with **Figure 5.48(a)**, similar results were obtained; nevertheless, the variation is less than the 1st and 2nd roll. Overall, results indicated that the morphing concept provides adequate roll moments and performance compared to traditional control surfaces.

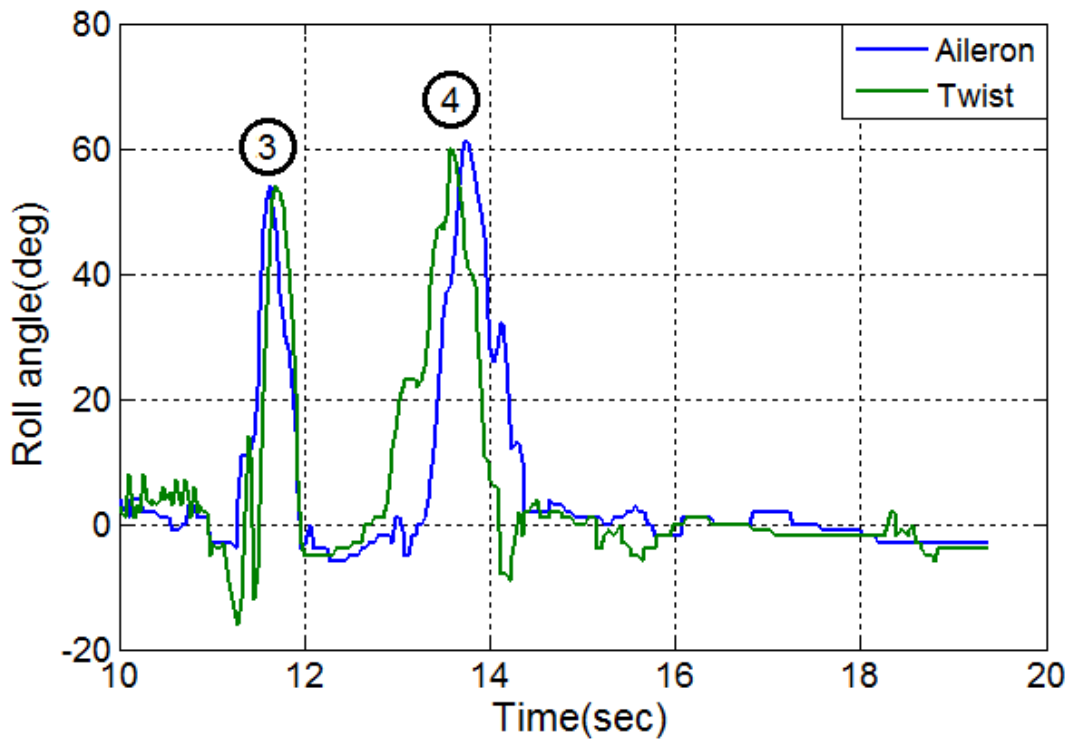


(a)

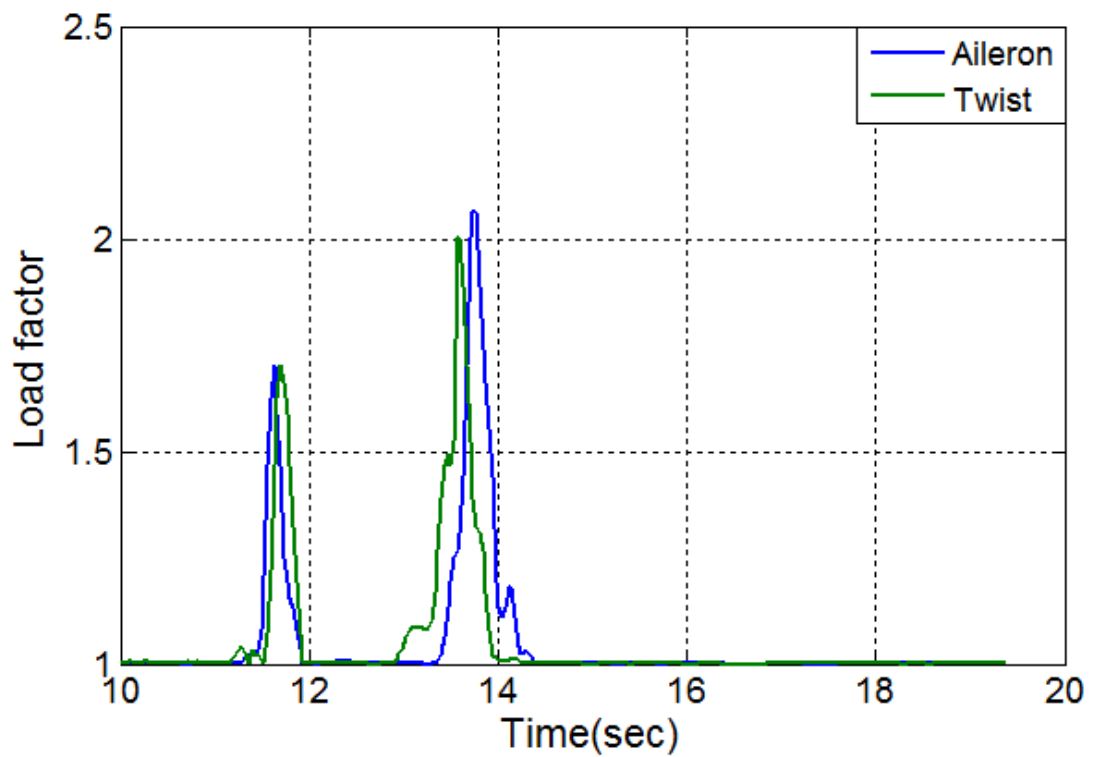


(b)

Figure 5.47 Flight Data for baseline (aileron) and morphing (twist) configuration: (a) Roll angle for rotation 1 and 2 and (b) Load factor for rotation 1 and 2.



(a)



(b)

Figure 5.48 Flight Data for baseline (aileron) and morphing (twist) configuration: (a) Roll angle for rotation 3 and 4 and (b) Load factor for rotation 3 and 4.

Load factors for both the baseline (aileron) and morphing (twist) configurations are presented in **Figure 5.47** and **Figure 5.48**. The load factor (n) is defined as the ratio of the lift of the aircraft to its weight (Total weight baseline = 5.698 kg morphing concept = 5.805 kg). This dictates the load factor. It can be seen from **Figure 5.47(b)** and **Figure 5.48 (b)** that the morphing concept produced more lift force than the baseline wing for this particular manoeuvre. Although the overall weight of the morphing wing structure is heavier than the baseline, it performed comparably for these tests.

In order to measure the efficiency of the morphing concept at rolling, the velocity was measured during the flight. This would provide some insight into relation drag increase in the turn. The velocity plot for both the morphing and baseline configurations is shown in **Figure 5.49**. It can be clearly seen that, during the rotation, a high velocity was achieved for morphing wing configuration, implying less drag production than the baseline (aileron) configuration. According to data, the velocity for the twist wing is 15% higher than the baseline configuration at time=7.5sec.

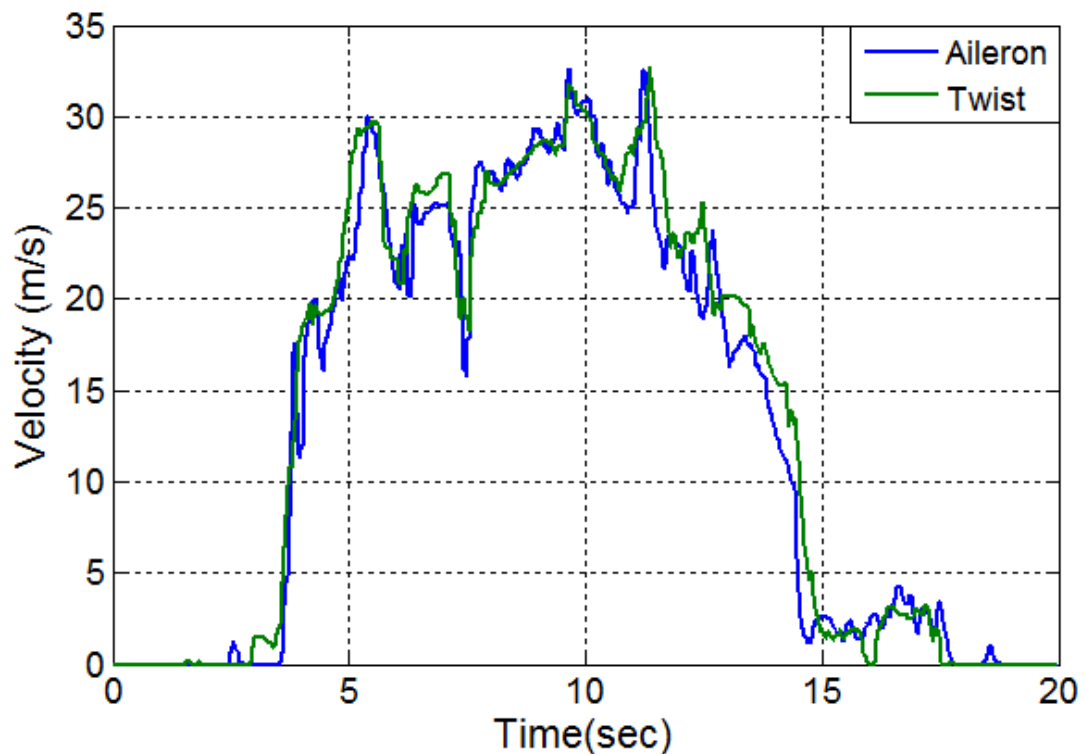


Figure 5.49 Velocity profile for baseline (aileron) and morphing (twist) configurations.



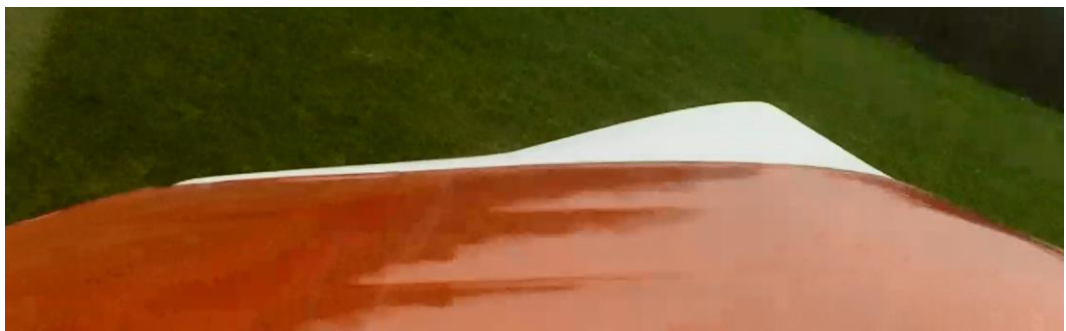
(a)



(b)



(c)



(d)

Figure 5.50 Morphing concept during flight: (a) and (b) washout, and (c) and (d) washin cases.



Figure 5.51 Morphing concept after flight testing.

According to the Pilot (Dr Alvin Gatto):

“Both configurations were able to achieve the basic manoeuvring. However, it was noticeable that the morphing wing enhanced performance without losing excessive velocity profile in the turn”.

In addition to all this, as is a well-known concept for morphing systems, it is very important that skin remain smooth. **Figure 5.51** illustrates the skin of the morphing concept after testing. It was clearly seen that no undue deformation existed and the configuration survived the flight. Further indications of performances can be gained from detailed flight pictures obtained during the test flights via a HD Rc Logger in-flight camera (**Figure 5.50**). It can be clearly seen that the wash-in and wash-out configurations performed very well with smooth surface changes (**Figure 5.51**) with no large undesired structural separations and/or surface wrinkling.

5.5 Summary

This section presented the computational and experimental results for the morphing concept developed within this work. Prior to the experimental results, a computational study of various winglet concepts was investigated with varying angles of dihedral, sweep, and twist. The impetus for the work was to identify and optimise winglets gauge the degree of enhanced controllability and the aerodynamic efficiency available to such at platform. Subsequent to this, further work illustrated the structural analysis of concept with stress, deformation and skin analyses

completed together with structural optimisation. Based on these results, the investigation a prototype wind tunnel model was developed and tested. In the tunnel, the twist angle was varied from -6° to $+6^\circ$ in steps of 2° and also compared to a traditional aileron baseline configuration with deflection of the aileron configurations from -30° to $+30^\circ$ in steps of 10° . According to the results, the morphing concept was found to provide adequate control moments compared to aileron baseline configurations. Moreover, in some of the twist cases presented, the aerodynamic efficiency was found to be higher than the aileron configurations which show that the morphing concept worked well. Finally, structural analysis and flight test results were presented. The roll rate and efficiency of the concept was compared with positive impact results compared to baseline configurations demonstrated.

CHAPTER 6 CONCLUSION AND FUTURE WORK

The motivation of this study was to explore novel concept for morphing aircraft control and performance. The primary variables investigated involved changing angles of twist with the main aim to use both experimental and numerical techniques to develop a flying prototype. A wind tunnel model and prototype test wings were designed and built. Further, this investigation was also aimed at producing a viable alternative approach for the morphing skin. The main findings of these works are as follows:

- Computational analysis of swept wing and winglet study;
 - Various winglet shapes provide good evidence for morphing aircraft control philosophies. Overall, increasing the winglet dihedral angle either side of the planar case further increases the change in roll moment coefficient. Based on $\Gamma = \pm 90^\circ$, the maximum roll was achieved at SB $\Lambda = 40^\circ$ $\phi = \pm 10^\circ$ $\Gamma = 90^\circ$ (max 15.5% at $\Gamma = \pm 90^\circ$)
 - High winglet twist angle performed well as a mechanism for control, and at winglet twist angles of up to $\phi = \pm 5^\circ$, comparable to good aerodynamic efficiency was achieved.
 - In the region of dihedral angles from $-20^\circ < \Gamma < 0^\circ$, particularly for the sweptback configuration, there is evidence of an increase in $\Delta C_L / C_D$ (SB = 30° , $\phi = -5^\circ$, $\Gamma = -10^\circ$) of approximately $\Delta C_L / C_D = 0.2$ (1.3%) over all other configurations tested.
 - Changing winglet sweep angle has a positive influence on drag (3.7% reduction at SB $\Lambda = 40^\circ$ $\phi = -10^\circ$ $\Gamma = 60^\circ$).

Subsequently, a wind tunnel model was built and a series of experiments were conducted with different angles of twist ($\pm 6^\circ$ in steps of $\pm 2^\circ$) and aileron deflection

angles ($\pm 30^\circ$ in steps of $\pm 10^\circ$). The conclusions of the experimental results can be summarised as follows:

- FEA of the wind tunnel model;
 - Various rod and rib size were investigated and the model was set to $\pm 6^\circ$ of twist change.
 - Skin deformation study was also being done in ANSYS to reduce any wrinkling occurred on surface.
 - Moreover, the weight of the structure was reduced in ANSYS while checking stress and deformation magnitudes.
 - Model showed good agreements with ANSYS FEA result.
- Wind tunnel testing;
 - According to the results, increasing the positive twist angle ($\phi = 6^\circ$ at $\alpha=18^\circ$) was found to increase the lift coefficient (13%), but also increase the drag acting on a structure (20.6%). Similarly, the controllability of the plane was also increased.
 - However, when the negative twist angle ($\phi = 6^\circ$) was considered, a dramatic reduction was seen in drag (19.6%) at $\alpha=18^\circ$ which improved the aerodynamic efficiency of the plane. In order to test the twist mechanism effects, the full wing profile was also manufactured and no negative influences were obtained. This is a good indication that the mechanism works without causing any additional drag.
 - Subsequent to this study, the aileron configurations were built and the investigation showed that the twist configurations could provide similar roll moments like aileron and one important feature for twist configurations was that the drag coefficients were too low compared to aileron (16.7%) at $\phi = -6^\circ$ compare to $\gamma=-30^\circ$, hence they improved efficiency of the plane.
 - For $\phi = -6^\circ$ configuration, the best (C_L/C_D) is obtained at $\alpha=8^\circ$ and it shows 18.3% improvement over aileron configuration ($\gamma=-30^\circ$). This rate was 22% contrary to full baseline wing model.

- With deflection of $\gamma=30^\circ$, appear to show the worst with comparison to $\phi = 6^\circ$, $\Delta(C_L/C_D)$ found to 17.5% less. In overall, performance is reduced 28.7% at $\alpha = 8^\circ$ compare to full wing baseline model.
- Improved performance over the aileron configuration is seen at $\phi = -6^\circ$ with the results showing (C_L/C_D) approximately 14.95% ($\alpha = 6^\circ$) higher than $\gamma=-30^\circ$. This implies that morphing concept with $\phi = -6^\circ$ can provide similar roll moment like aileron ($\gamma=-30^\circ$), but superior aerodynamic efficiency compare to aileron deflection.
- As far as $\phi = -4^\circ$ is concerned, 50% improvements are seen over $\gamma=-20^\circ$.
- The highest C_L/C_D value for positive deflection was obtained at $\phi = 6$ with improvements over the aileron configurations with 44% ($\alpha = 6^\circ$) (compare to $\gamma=30^\circ$).
- For $\phi = 4^\circ$ configuration, maximum C_L/C_D was found at $\alpha = 4^\circ$ with 63% improvement over $\gamma=20^\circ$.

After completing the wind tunnel testing, the flight model was designed and built. The findings from flight testing can be summarised as follows:

- FEA of the prototype morphing concept;
 - The optimisation process was carried out in ANSYS and the best structure modelling was decided.
 - Similar to wind tunnel model, $\pm 6^\circ$ of twist change was aimed and prior to that structure was set while checking the stress and deformation magnitudes.
 - Comparison between the prototype and ANSYS FEA showed good agreements.
- Flight testing study;
 - Flight testing was conducted and according to the results, the twist shape does provide effective roll moments, the same as the aileron configurations. Moreover, the velocity due to rotation was found to be

high (15% at $t=7.5$) compared to aileron which indicates that the twist system produced a low drag profile.

- It was clearly seen that no undue deformation existed on surface and the configuration survived the flight.

According to the experience acquired from experimental investigations, the following recommendations can be made for future studies:

- To simulate the configurations with fully frictional constraints in ANSYS. Although in this model the friction effects are negligible due to small surface area between each rib and the interface between the ribs and rods, it is important to estimate the effects of high AR models.
- A Manual Angle of Attack mechanism was used to change the angle of the wing twist. This again required an excessive amount of work since several angular positions were involved in the study. Such a workload can easily lead to human errors during processing. In order to overcome these problems and improve the efficiency and accuracy of the data processing stage, a mechanism with an automated capability can be employed.
- For the wind tunnel model, instead of using plywood, aluminium or carbon materials can be investigated to increase the strength as well as the surface smoothness.
- For the flight prototype, the internal mechanism could be replaced with a servo driven system to reduce mechanism weight.
- Finally, obtained experimental force and moment data can be compared with high fidelity computational results.

REFERENCES

- [1] D. McRuer and D. Graham, “Flight Control Century: Triumphs of the Systems Approach,” *J. Guid. Control. Dyn.*, vol. 27, no. 2, pp. 161–173, 2004.
- [2] F. E. C. Culick, “The Wright Brothers : First Aeronautical Engineers,” vol. 41, no. 6, pp. 8–11, 2003.
- [3] A. K. Jha and J. N. Kudva, “Morphing Aircraft Concepts, Classifications, and Challenges,” vol. 5388, pp. 213–224, Jul. 2004.
- [4] G. Murray, F. Gandhi, and C. Bakis, “Flexible Matrix Composite Skins for One-dimensional Wing Morphing,” *J. Intell. Mater. Syst. Struct.*, vol. 21, no. 17, pp. 1771–1781, 2010.
- [5] K. R. Olympio, F. Gandhi, L. Asheghian, and J. Kudva, “Design of a Flexible Skin for a Shear Morphing Wing,” *J. Intell. Mater. Syst. Struct.*, vol. 21, no. 17, pp. 1755–1770, 2010.
- [6] E. a. Bubert, B. K. S. Woods, K. Lee, C. S. Kothera, and N. M. Wereley, “Design and Fabrication of a Passive 1D Morphing Aircraft Skin,” *J. Intell. Mater. Syst. Struct.*, vol. 21, no. 17, pp. 1699–1717, 2010.
- [7] I. Dayyani, S. Ziaei-Rad, and M. I. Friswell, “The mechanical behavior of composite corrugated core coated with elastomer for morphing skins,” *J. Compos. Mater.*, vol. 48, no. 13, pp. 1623–1636, 2013.
- [8] A. D. Shaw, I. Dayyani, and M. I. Friswell, “Optimisation of composite corrugated skins for buckling in morphing aircraft,” *Compos. Struct.*, vol. 119, pp. 227–237, Jan. 2015.
- [9] P. H. F., “The Parker Variable Camber Wing,” Washington, 1920.
- [10] V. J. Burnelli, “Burnelli GX3,” 1,917,428.
- [11] J. A. D. Ackroyd and N. Riley, “Hermann Glauert FRS , FRAeS (1892 – 1934),” vol. 1, pp. 22–73, 2011.
- [12] W. Document, “Makhonin’s -telescoping-wing.” [Online]. Available: <http://www.wv2aircraft.net/forum/other-mechanical-systems-tech/makhonine-telescoping-wing-8527.html>. [Accessed: 01-Dec-2013].
- [13] John Valasek, *Morphing Aerospace Vehicles and Structures*, 1st ed. West Sussex: John Wiley and Son Ltd, 2012.
- [14] V.B.Shavrov, “History of aircraft construction in the USSR,” vol. 2, pp. 118–120.
- [15] National Museum of the United States Air Force, “REPUBLIC XF-91 THUNDERCEPTOR.” .
- [16] Y. G. and B. Dunbar, “NASA Armstrong Fact Sheet: X-5 Research Aircraft,” NASA. .

- [17] T. A. Weisshaar and T. H. E. M. Challenge, "Morphing Aircraft Technology – New Shapes for Aircraft Design," 2006.
- [18] R. J. H., "Mission Adaptive Wing Camber Control Systems for Transport Aircraft," *AIAA Pap.*, pp. 85–5006, 1985.
- [19] V. K. K. & L. J. Y. R. Zheng Min, "Aircraft morphing wing concepts with radical geometry change," *IES J. Part A Civ. Struct. Eng.*, vol. 3, no. 3, pp. 188–195, 2010.
- [20] "MiG 105-11," *Encyclopedia Astronautica*. .
- [21] P. W. Merlin, "A new twist in flight research: the F-18 active aeroelastic wing project," in *nasa aeronautics book series*, 2013.
- [22] R. W. DeCAMP, "Mission Adaptive Wing Research Programme," *Aircr. Eng.*
- [23] H. R. J. Norman D.K, Gangsaas D., "An integrated maneuver enhancement and gust alleviation mode for the AFTI/F-11 MAW aircraft," in *AIAA Guidance, Navigation and Control Conference and Exhibit*, 1983, vol. 83, p. 2217.
- [24] J. W. Smith, W. P. Lock, and G. a. Payne, "Variable-camber systems integration and operational performance of the AFTI/F-111 mission adaptive wing." 1992.
- [25] E. W. Pendleton, D. Bessette, P. B. Field, G. D. Miller, and K. E. Griffin, "Active Aeroelastic Wing Flight Research Program: Technical Program and Model Analytical Development," *J. Aircr.*, vol. 37, no. 4, pp. 554–561, 2000.
- [26] D. Voracek, E. Pendleton, E. Reichenbach, K. Griffin, and L. Welch, "The Active Aeroelastic Wing Phase I Flight Research Through January 2003," no. April, 2003.
- [27] J. N. Kudva, "Overview of the DARPA Smart Wing Project," *J. Intell. Mater. Syst. Struct.*, vol. 15, no. 4, pp. 261–267, 2004.
- [28] B. P. Kudva, J. N., Martin, C. A., Scherer, L. B., Jardine, A. P., McGowan, A. R., Lake, R. C., Sendekyj, G. P., and Sanders, "Overview of DARPA/AFRL/NASA Smart Wing Program," 1997, pp. 230–236.
- [29] NASA, "21st Century Aerospace Vehicle, Morphing Airplane." .
- [30] T. G. Ivanco, R. C. Scott, M. H. Love, S. Zink, and T. a. Weisshaar, "Validation of the Lockheed Martin morphing concept with wind tunnel testing," vol. 23, p. 26, 2007.
- [31] T. a. Weisshaar, "Morphing Aircraft Systems: Historical Perspectives and Future Challenges," *J. Aircr.*, vol. 50, no. 2, pp. 337–353, 2013.
- [32] K. Joshi, S. P., Jha, A. K. Rodrian, J. E., Alphenaar, R. A., and Szema, "Design of the NextGen MorphingWingWind Tunnel Model," *AIAA Pap. 2007*, p. 1731.
- [33] D. J. Anderson, G. R., Cowan, D. L., and Piatek, "Aeroelastic Modeling,

- Analysis and Testing of a Morphing Wing Structure,” in *48th AIAA/ASME/ASCE/AHS/ASC Structures, Structural Dynamics and Materials Conference*, p. 1734.
- [34] A. Y. N. Sofla, S. a. Meguid, K. T. Tan, and W. K. Yeo, “Shape morphing of aircraft wing: Status and challenges,” *Mater. Des.*, vol. 31, no. 3, pp. 1284–1292, Mar. 2010.
- [35] S. P. Joshi, Z. Tidwell, W. A. Crossley, S. Ramakrishnan, P. Engineer, and S. Engineer, “Comparison of Morphing Wing Strategies Based Upon Aircraft Performance Impacts,” no. April, pp. 1–7, 2004.
- [36] B. D. Roth and W. A. Crossley, “AIAA 2003-6733 AIAA 2003-6733 Application of Optimization Techniques in the Conceptual Design of Morphing Aircraft,” no. November, pp. 1–11, 2003.
- [37] E. T. Martin and W. A. Crossley, “AIAA 2002-5859 Multiobjective Aircraft Design to Investigate Potential Geometric Morphing Features,” no. October, pp. 1–8, 2002.
- [38] S. Ricci and M. Terraneo, “Application of MDO techniques to the preliminary design of morphed aircraft,” no. September, pp. 1–14, 2006.
- [39] R. De Breuker, M. Abdalla, Z. Gürdal, and D. Lindner, “Energy-Based Aeroelastic Analysis of a Morphing Wing,” vol. 6523, no. 0, pp. 652308–652308–12, Apr. 2007.
- [40] C. Thill, J. Etches, I. Bond, K. Potter, and P. Weaver, “Morphing skins,” no. 3216, pp. 1–23, 2008.
- [41] A. V. and L. Z. Ignazio Dimino, Monica Ciminello, Antonio Concilio, Rosario Pecora, Francesco Amoroso, Marco Magnifico, Martin Schueller, Andre Gratias, “Distributed Actuation and Control of a Morphing Wing Trailing Edge,” *Smart Intell. Aircr. Struct. Proc. Final Proj. Conf.*, 2016.
- [42] D. Moorhouse, B. Sanders, M. Von Spakovsky, and J. Butt, “Benefits and design challenges of adaptive structures for morphing aircraft,” *Aeronaut. J.*, vol. 110, no. 1105, pp. 157–162, 2006.
- [43] J. R. Butt, “A Study of Morphing Wing Effectiveness in Fighter Aircraft using Exergy Analysis and Global Optimization Techniques,” p. 141, 2005.
- [44] B. Sanders, “Aerodynamic and Aeroelastic Characteristics of Wings with Conformal Control Surfaces for Morphing Aircraft Introduction,” vol. 40, no. 1, 2003.
- [45] J.-S. Bae, T. M. Seigler, and D. J. Inman, “Aerodynamic and Static Aeroelastic Characteristics of a Variable-Span Morphing Wing,” *J. Aircr.*, vol. 42, no. 2, pp. 528–534, Mar. 2005.
- [46] J. Wittmann, H. Steiner, and A. Sizmann, “Framework for Quantitative Morphing Assessment,” *50th AIAA/ASME/ASCE/AHS/ASC Struct. Struct. Dyn. Mater. Conf.*, no. May, pp. 1–18, 2009.

- [47] S. Barbarino, O. Bilgen, R. M. Ajaj, M. I. Friswell, and D. J. Inman, "A Review of Morphing Aircraft," *J. Intell. Mater. Syst. Struct.*, vol. 22, no. 9, pp. 823–877, Aug. 2011.
- [48] J. C. Gomez and E. Garcia, "Morphing unmanned aerial vehicles," *Smart Mater. Struct.*, vol. 20, no. 10, p. 103001, Oct. 2011.
- [49] M. I. Friswell, "The prospects for morphing aircraft," pp. 1–14.
- [50] D. A. Neal and H. Robertshaw, "Design, Control, and Experimental Modelling of a Morphing Aircraft Configuration," pp. 1–10.
- [51] J. Blondeau, J. Richeson, D. J. Pines, and A. Norfolk, "Design, development and testing of a morphing aspect ratio wing using an inflatable telescopic spar 44th AIAA / ASME / ASCE / AHS Structures, Structural," *Aerosp. Eng.*, vol. 1718, no. April, pp. 1–11, 2003.
- [52] J. B. Samuel and D. J. Pines, "Design and Testing of a Pneumatic Telescopic Wing for Unmanned Aerial Vehicles," *J. Aircr.*, vol. 44, no. 4, pp. 1088–1099, 2007.
- [53] Y. Kubo, M. Miyazaki, and K. Kato, "Effects of end plates and blockage of structural members on drag forces," *J. Wind Eng. Ind. Aerodyn.*, vol. 32, no. 3, pp. 329–342, Oct. 1989.
- [54] R. D. Vocke, C. S. Kothera, B. K. S. Woods, and N. M. Wereley, "Development and Testing of a Span-Extending Morphing Wing," *J. Intell. Mater. Syst. Struct.*, vol. 22, no. 9, pp. 879–890, 2011.
- [55] R. M. Ajaj, E. I. Saavedra Flores, M. I. Friswell, G. Allegri, B. K. S. Woods, a. T. Isikveren, and W. G. Dettmer, "The Zigzag wingbox for a span morphing wing," *Aerosp. Sci. Technol.*, vol. 28, no. 1, pp. 364–375, 2013.
- [56] R. M. Ajaj, E. I. S. Flores, M. I. Friswell, and B. K. S. Woods, "Structural Design and Modelling of the Zigzag Wingbox for Span Morphing Wing," pp. 1–18, 1931.
- [57] D. A. Perkins, "Adaptive wing structures," *Proc. SPIE*, vol. 5762, pp. 132–142, 2005.
- [58] R. Jones, "Wing Planforms for High-Speed Flight," 1945.
- [59] N. Marmier, P., Wereley, "Morphing Wings of a Small Scale UAV Using Inflatable Actuators for Sweep Control," in *44th AIAA/ASME/ASCE/AHS/ASC Structures, Structural Dynamics, and Materials Conference*.
- [60] D. A. N. Iii, D. J. Inman, and C. Woolsey, "Design, Development, and Analysis of a Morphing Aircraft Model for Wind Tunnel Experimentation by Design, Development, and Analysis of a Morphing Aircraft Model for Wind Tunnel Experimentation," 2006.
- [61] F. Mattioni, A. Gatto, P. Weaver, M. Friswell, and K. Potter, "The application of residual stress tailoring of snap-through composites for variable sweep wings," *47th AIAA/ASME/ASCE/AHS/ASC Struct. Struct. Dyn. Mater. Conf.*

- 14th AIAA/ASME/AHS Adapt. Struct. Conf. 7th*, no. May, pp. 1–12, May 2006.
- [62] J. J. Joo, “Optimal actuator location within a morphing wing scissor mechanism configuration,” *Proc. SPIE*, vol. 6166, no. May 2012, pp. 616603–616603–12, 2006.
- [63] L. Prandtl, “Application of Modern Hydrodynamics to Aeronautics,” *Naca*, vol. 116, no. 116. 1923.
- [64] W. F. Phillips, “Lifting-Line Analysis for Twisted Wings and Washout-Optimized Wings,” *J. Aircr.*, vol. 41, no. 1, pp. 128–136, 2004.
- [65] W. F. Phillips, N. R. Alley, and W. D. Goodrich, “Lifting-Line Analysis of Roll Control and Variable Twist,” *J. Aircr.*, vol. 41, no. 5, pp. 1169–1176, 2004.
- [66] R. Barrett, “Active aeroelastic tailoring of an adaptive Flexspar stabilator,” *Smart Mater. Struct.*, vol. 5, no. 6, pp. 723–730, 1996.
- [67] D. Sahoo and C. Cesnik, “Roll maneuver control of UCAV wing using anisotropic piezoelectric actuators,” *43rd AIAA/ASME/ASCE/AHS/ASC Struct. Struct. Dyn. Mater. Conf.*, no. April, pp. 1–11, 2002.
- [68] H. Garcia, M. Abdulrahim, and R. Lind, “Roll Control for a Micro Air Vehicle Using Active Wing Morphing,” in *AIAA Guidance, Navigation and Control Conference (Austin, TX)*, 2003, pp. 1–12.
- [69] B. Stanford, M. Abdulrahim, R. Lind, and P. Ifju, “Investigation of Membrane Actuation for Roll Control of a Micro Air Vehicle,” *J. Aircr.*, vol. 44, no. 3, pp. 741–749, 2007.
- [70] M. Abdulrahim, H. Garcia, G. F. Ivey, and R. Lind, “Flight Testing A Micro Air Vehicle Using Morphing For Aeroservoelastic Control,” *J. Aircr.*, vol. 42, N^o 1, no. January- February, pp. 1–17, 2005.
- [71] M. Majji, O. Rediniotis, and J. Junkins, “Design of a Morphing Wing : Modeling and Experiments,” *AIAA Atmos. Flight Mech. Conf. Exhib.*, pp. 1–9, Aug. 2007.
- [72] R. Vos, Z. Gurdal, and M. Abdalla, “Mechanism for Warp-Controlled Twist of a Morphing Wing,” *J. Aircr.*, vol. 47, no. 2, pp. 450–457, Mar. 2010.
- [73] D. M. Elzey, A. Y. N. Sofla, and H. N. G. Wadley, “A bio-inspired, high-authority actuator for shape morphing structures,” *Proc. SPIE*, vol. 5053, pp. 92–100, 2003.
- [74] A. Y. N. Sofla, D. M. Elzey, and H. N. G. Wadley, “Two-way Antagonistic Shape Actuation Based on the One-way Shape Memory Effect,” *J. Intell. Mater. Syst. Struct.*, vol. 19, no. 9, pp. 1017–1027, 2008.
- [75] H. Lv, J. Leng, and S. Du, “A Survey of Adaptive Materials and Structures Research in China,” in *50th AIAA/ASME/ASCE/AHS/ASC Structures, Structural Dynamics, and Materials Conference*, 2009, no. May, pp. 1–8.

- [76] M. Abdulrahim and R. Lind, "Flight Testing and Response Characteristics of a Variable Gull-Wing Morphing Aircraft," no. August, 2004.
- [77] M. Majji, "Robust Control of Redundantly Actuated Dynamical System," Texas A&M University, 2006.
- [78] J. E. Cooper, "Adaptive Stiffness Structures for Air Vehicle Drag Reduction," *Multifunct. Struct. Sensors Antennas, Meet. Proc. RTO-MP-AVT-141*, pp. 15.1 – 15.12, 2006.
- [79] K. E. Griffin and M. a. Hopkins, "Smart Stiffness for Improved Roll Control," *J. Aircr.*, vol. 34, no. 3, pp. 445–447, 1997.
- [80] P. C. Chen, D. Sarhaddi, R. Jha, D. D. Liu, S. Antonio, R. Yurkovich, and T. B. Company, "Variable stiffness spar approach for aircraft manoeuvre enhancement using ASTROS," *J. Aircr.*, vol. 37, no. 5, 2000.
- [81] R. M. Ajaj, M. I. Friswell, W. G. Dettmer, G. Allegri, and a. T. Isikveren, "Performance and control optimisations using the adaptive torsion wing," *Aeronaut. J.*, vol. 116, no. 1184, pp. 1061–1077, 2012.
- [82] R. M. Ajaj, "Roll control of a Male UAV using the adaptive torsion wing," no. 3809, pp. 299–314, 2013.
- [83] R. M. Ajaj, M. I. Friswell, D. D. Smith, G. Allegri, a T. Isikveren, A. Concepts, D. Chief, and T. Officer, "Roll Control of a UAV Using an Adaptive Torsion Structure," *Aerosp. Eng.*, no. April, pp. 1–15, 2011.
- [84] R. M. Ajaj, M. I. Friswell, W. G. Dettmer, G. Allegri, a T. Isikveren, A. Concepts, D. Chief, and T. Officer, "Conceptual Modeling of an Adaptive Torsion Wing Structure," *Aerosp. Eng.*, no. April, pp. 1–15, 2011.
- [85] S. Barbarino, E. I. S. Flores, R. M. Ajaj, I. Dayyani, and M. I. Friswell, "A review on shape memory alloys with applications to morphing aircraft," *Smart Mater. Struct.*, vol. 23, no. 6, p. 063001–, 2014.
- [86] D. J. Hartl and D. C. Lagoudas, "Aerospace applications of shape memory alloys," *Proc. Inst. Mech. Eng. Part G J. Aerosp. Eng.*, vol. 221, no. 4, pp. 535–552, 2007.
- [87] N. C., C. A., and K. Y, "Application of shape memory alloy (SMA) spars for aircraft maneuver enhancement," in *Smart Structures and Materials*, 2002, pp. 226–23.
- [88] J. D. Jacob, A. Simpson, and S. Smith, "Design and Flight Testing of Inflatable Wings with Wing Warping," *SAE World Aerosp. Congr.*, pp. 1–3392:1306–15, 2005.
- [89] B. K. Woods, O. Bilgen, and M. I. Friswell, "Wind tunnel testing of the fish bone active camber morphing concept," *J. Intell. Mater. Syst. Struct.*, vol. 25, no. 7, pp. 772–785, Feb. 2014.
- [90] R. Eppler, "Induced drag and winglets," *Aerosp. Sci. Technol.*, vol. 1, no. 1, pp. 3–15, 1997.

- [91] R. T. Whitcomb, "Wind Tunnel Subsonic Mounted Approach Results Speeds For and At Selected Wing-tip Winglets National Aeronautics and Space Administration •," Washington D. C., 1976.
- [92] R. Hallion, "NASA's Contributions to Aeronautics: Aerodynamics, Structures, Propulsion, and Controls," Washington, 2010.
- [93] J. M. Kuhlman and P. Liaw, "Winglets on low-aspect-ratio wings," vol. 25, no. 10, pp. 932–941, 1988.
- [94] A. P., L. Smrdek, and F. N. Coton, "Aerodynamic design and experimental investigation of the sailplane wingtip devices," *Acta Polytech.*, vol. 43, no. 3, 2003.
- [95] M. R. Soltani, K. Ghorbanian, and M. Nazarinia, "Experimental Investigation of The Effect of Various Winglet Shapes On The Total Pressure Distribution Behind a Wing."
- [96] M. Nazarinia, M. R. Soltani, and K. Ghorbanian, "Experimental Study of Vortex Shapes behind a Wing Equipped with Different Winglets," vol. 3, no. 1, pp. 1–15, 2006.
- [97] I. Kroo, "Nonplanar Wing Concepts For Increased Aircraft Efficiency Introduction -- Why Nonplanar Wings? What is possible? Assessing the Potential," pp. 1–29, 2005.
- [98] A. Ning and I. Kroo, "Tip Extensions, Winglets, and C-wings: Conceptual Design and Optimization," *26th AIAA Appl. Aerodyn. Conf.*, Aug. 2008.
- [99] M. I. Inam, M. Mashud, A. Al-Nahian, and S. M. S. Selim, "Induced drag reduction for modern aircraft without increasing the span of the wing by using winglet," *Int. J. Mech. Mech. Eng.*, vol. 10, no. 3, pp. 69–74, 2010.
- [100] A. Hossain, P. Raj, A. Rahman, and A. Aziz, "Analysis of Longitudinal Aerodynamic Characteristics of an Aircraft Model with and Without Winglet," vol. 2, no. 3, pp. 143–150, 2008.
- [101] R. Babigian and S. Hayashibara, "Computational Study of the Vortex Wake Generated by a Three-Dimensional Wing with Dihedral, Taper, and Sweep," in *27th AIAA Applied Aerodynamics Conference*, 2009, no. June, pp. 1–13.
- [102] J. F. Halpert, D. H. Prescott, T. R. Yechout, and M. Arndt, "Aerodynamic Optimization and Evaluation of KC-135R Winglets , Raked Wingtips , and a Wingspan Extension," no. January, 2010.
- [103] G. Heller, P. Kreuzer, S. Dirmeier, and F. D. Gmbh, "Development and Integration of A New High Performance Wingtip Device For Transonic Aircraft," pp. 1–7, 2002.
- [104] A Beechook and J. Wang, "Aerodynamic Analysis of Variable Cant Angle Winglets for Improved Aircraft Performance," no. September, pp. 13–14, 2013.
- [105] S. C. Yen and Y. F. Fei, "Winglet Dihedral Effect on Flow Behavior and

- Aerodynamic Performance of NACA0012 Wings,” *J. Fluids Eng.*, vol. 133, no. 7, p. 071302, 2011.
- [106] P. Gerontakos and T. Lee, “Effects of Winglet Dihedral on a Tip Vortex,” vol. 43, no. 1, pp. 2–9, 2006.
- [107] R. Faye and Micheal Winter, “Blended winglets,” *Boeing*, no. 17, 2012.
- [108] AIRBUS, “Airbus launches Sharklet retrofit for in-service A320 Family aircraft.” .
- [109] AIRBUS, “AIRBUS A350 XWB,” 2015. .
- [110] H. G. Klug and P. E. F. Peters, “Auxiliary wing tips for an aircraft,” 1988.
- [111] V. Tucker, “Gliding birds: reduction of induced drag by wing tip slots between the primary feathers,” *J. Exp. Biol.*, vol. 180, no. 1, pp. 285–310, 1993.
- [112] M. J. Smith, N. Komerath, R. Ames, O. Wong, and J. Pearson, “Performance Analysis Of A Wing With Multiple Winglets,” 2001.
- [113] S. G and S. B., “Experimental Investigation on the Effect of Multi-Winglets,” *Int. J. Mech. Ind. Eng.*, vol. 1, no. 1, pp. 43–46, 2011.
- [114] P. Bourdin, A. . Gatto, and M. Friswell, “The Application of Variable Cant Angle Winglets for Morphing Aircraft Control,” in *24th Applied Aerodynamics Conference*, 2006, no. June, pp. 1–13.
- [115] P. Bourdin, A. Gatto, and M. I. Friswell, “Aircraft Control via Variable Cant-Angle Winglets,” *Journal of Aircraft*, vol. 45, no. 2. pp. 414–423, 2008.
- [116] P. Bourdin, A. Gatto, and M. I. Friswell, “Potential of Articulated Split Wingtips for Morphing-Based Control of a Flying Wing,” in *25th AIAA Applied Aerodynamics Conference*, 2007, no. June, pp. 1–16.
- [117] P. Bourdin, A. Gatto, and M. I. Friswell, “Performing co-ordinated turns with articulated wing-tips as multi-axis control effectors,” *Aeronaut. J.*, vol. 114, no. 1151, pp. 35–47, 2010.
- [118] N. Ameri, “Modelling Continuously Morphing Aircraft for Flight Control,” no. August, pp. 1–23, 2008.
- [119] N. Ameri, M. Lowenberg, and M. Friswell, “Modelling the dynamic response of a morphing wing with active winglets,” *AIAA Atmos. Flight ...*, no. August, 2007.
- [120] N. M. Ursache, T. Melin, A. T. Isikveren, and M. I. Friswell, “Morphing Winglets for Aircraft Multi-phase Improvement,” *7th AIAA Aviat. Technol. Integr. Oper. Conf.ATIO May*, no. September, pp. 18 – 20, 2007.
- [121] N. M. Ursache, T. Melin, a T. Isikveren, and M. I. Friswell, “Technology integration for active poly-morphing winglets development,” *Proc. ASME Conf. Smart Mater. Adapt. Struct. Intell. Syst. SMASIS2008*, vol. 1, pp. 775–782, 2008.

- [122] A. Gatto, F. Mattioni, and M. I. Friswell, "Experimental Investigation of Bistable Winglets to Enhance Aircraft Wing Lift Takeoff Capability," *J. Aircr.*, vol. 46, no. 2, pp. 647–655, Mar. 2009.
- [123] L. Falcão, A. Gomes, and A. Suleman, "Multidisciplinary Design Optimisation of a Morphing Wingtip," *2nd Int. Conf. Eng. Optim.*, pp. 1–7, 2010.
- [124] L. Falcao, A. a Gomes, and A. Suleman, "Design and Analysis of an Adaptive Wingtip," in *52nd AIAA/ASME/ASCE/AHS/ASC Structures, Structural Dynamics and Materials Conference*, 2011.
- [125] L. Falcao, a. a. Gomes, and a. Suleman, "Aero-structural Design Optimization of a Morphing Wingtip," *J. Intell. Mater. Syst. Struct.*, vol. 22, no. 10, pp. 1113–1124, 2011.
- [126] D. D. Smith and R. M. Ajaj, "Multiobjective Optimization for the Multi-Phase Design of Active Polymorphing Wings," in *52nd AIAA/ASME/ASCE/AHS/ASC Structures, Structural Dynamics and Materials Conference*, 2011, no. 4–7 April.
- [127] D. D. Smith, R. M. Ajaj, and S. Park, "Multi-disciplinary Design Optimization Of An Active Morphing Wing," in *27th International congress of the Aeronautical Sciences*, 2010, pp. 1–11.
- [128] A. Shelton, A. Tomar, J. Prasad, M. Smith, and N. Komerath, "Active Multiple Winglets for Improved Unmanned-Aerial-Vehicle Performance," *J. Aircr.*, vol. 43, no. 1, pp. 110–116, 2006.
- [129] C. R., C. F.M., C. L.G.N., and E. R.M.U., "Aerodynamic Analysis of Multi-Winglets for Low," in *27th International congress of the Aeronautical Sciences*, 2010, pp. 1–10.
- [130] F. M. Catalano, "Experimental Analysis Of Aerodynamics Characteristics Of Adaptive Multi--Winglets," in *24th International congress of the Aeronautical Sciences*, 2004, pp. 1–9.
- [131] A. Gatto, P. Bourdin, and M. I. Friswell, "Experimental investigation into the control and load alleviation capabilities of articulated winglets," *Int. J. Aerosp. Eng.*, vol. 2012, 2012.
- [132] A. Gatto, P. Bourdin, and M. I. Friswell, "Experimental Investigation into Articulated Winglet Effects on Flying Wing Surface Pressure Aerodynamics," *J. Aircr.*, vol. 47, no. 5, pp. 1811–1815, 2010.
- [133] D. D. Smith, M. H. Lowenberg, D. P. Jones, and M. I. Friswell, "Computational and Experimental Validation of the Active Morphing Wing," *J. Aircr.*, vol. 51, no. 3, pp. 925–937, May 2014.
- [134] D. D. Smith, M. H. Lowenberg, D. P. Jones, M. I. Friswell, and S. Park, "Computational and Experimental Analysis Of The Active Morphing Wing Concept," 2012, pp. 1–9.

- [135] M. M. Keihl, R. S. Bortolin, B. Sanders, S. Joshi, and Z. Tidwell, "Mechanical properties of shape memory polymers for morphing aircraft applications," in *Smart Structures and Materials 2005: Industrial and Commercial Applications of Smart Structures Technologies*, 2005.
- [136] T. Yokozeki, S. I. Takeda, T. Ogasawara, and T. Ishikawa, "Mechanical properties of corrugated composites for candidate materials of flexible wing structures," *Compos. Part A Appl. Sci. Manuf.*, vol. 37, no. 10, pp. 1578–1586, 2006.
- [137] M. T. Kikuta, "Mechanical Properties of Candidate Materials for Morphing Wings," Virginia Polytechnic Institute and State University, 2003.
- [138] D. Bornengo, F. Scarpa, and C. Remillat, "Evaluation of hexagonal chiral structure for morphing airfoil concept," *Proc. Inst. Mech. Eng. Part G J. Aerosp. Eng.*, vol. 219, no. 3, pp. 185–192, 2005.
- [139] K. R. Olympio and F. Gandhi, "Flexible Skins for Morphing Aircraft Using Cellular Honeycomb Cores," *J. Intell. Mater. Syst. Struct.*, vol. 21, no. 17, pp. 1719–1735, 2010.
- [140] K. R. Olympio and F. Gandhi, "Zero Poisson's Ratio Cellular Honeycombs for Flex Skins Undergoing One-Dimensional Morphing," *J. Intell. Mater. Syst. Struct.*, vol. 21, no. 17, pp. 1737–1753, 2010.
- [141] K. R. Olympio, "Design of a passive flexible skin for morphing aircraft structure," The Pennsylvania State University, 2006.
- [142] K. Olympio and F. Gandhi, "Zero- ν Cellular Honeycomb Flexible Skins for One-Dimensional Wing Morphing," in *48th AIAA/ASME/ASCE/AHS/ASC Structures, Structural Dynamics, and Materials Conference*.
- [143] E. a. Bubert, B. K. S. Woods, K. Lee, C. S. Kothera, and N. M. Wereley, "Design and Fabrication of a Passive 1D Morphing Aircraft Skin," *J. Intell. Mater. Syst. Struct.*, vol. 21, no. 17, pp. 1699–1717, Sep. 2010.
- [144] C. Thill, J. a Etches, I. P. Bond, K. D. Potter, and P. M. Weaver, "Composite corrugated structures for morphing wing skin applications," *Smart Mater. Struct.*, vol. 19, no. 12, p. 124009, 2010.
- [145] Y. Xia and M. I. Friswell, "Equivalent models of corrugated laminates for morphing skins," vol. 7977, p. 79771I–79771I–10, 2011.
- [146] Y. Xia, O. Bilgen, and M. I. Friswell, "The effect of corrugated skins on aerodynamic performance," *J. Intell. Mater. Syst. Struct.*, vol. 25, no. 7, pp. 786–794, 2014.
- [147] M. Tamai, Z. Wang, G. Rajagopalan, and H. Hu, "Aerodynamic Performance of a Corrugated Dragonfly Airfoil Compared with Smooth Airfoils at Low Reynolds Numbers," *45th AIAA Aerosp. Sci. Meet. Exhib.*, pp. 1–12, 2007.
- [148] C. Thill, J. a Etches, I. P. Bond, P. M. Weaver, and K. D. Potter, "Experimental and parametric analysis of corrugated composite structures for

- morphing skin applications,” *19Th Int. Conf. Adapt. Struct. Technol.*, 2008.
- [149] C. Thill, J. a. Etches, I. P. Bond, K. D. Potter, P. M. Weaver, and M. R. Wisnom, “Investigation of trapezoidal corrugated aramid/epoxy laminates under large tensile displacements transverse to the corrugation direction,” *Compos. Part A Appl. Sci. Manuf.*, vol. 41, no. 1, pp. 168–176, 2010.
- [150] C. Thill, J. D. Downsborough, S. J. Lai, I. P. Bond, and D. P. Jones, “Aerodynamic study of corrugated skins for morphing wing applications,” *Aeronaut. J.*, vol. 114, no. 1154, pp. 237–244, 2010.
- [151] H. Y. Mark Drela, “AVL 3.30 User Primer.”
- [152] C. E. Lan, “A quasi-vortex-lattice method in thin wing theory,” vol. 11, no. 9, 1974.
- [153] Krishnamoorthy Karamcheti, “Principles of ideal fluid aerodynamics.” John Wiley & Sons, New York, p. 518, 1967.
- [154] R. L. Pereira, “Validation of software for the calculation of aerodynamic coefficients with a focus on the software package Tornado,” p. 55, 2010.
- [155] F. Hitchens, “Reflex Camber Airfoil,” *The Encyclopedia of Aerodynamics*. Andrews UK Limited, 2015.
- [156] P. J. Roache, “Quantification of Uncertainty in Computational Fluid Dynamics,” *Annu. Rev. Fluid Mech.*, vol. 29, no. 1, pp. 123–160, 1997.
- [157] C. Marchi and A. Silva, “Multi-dimensional discretization error estimation for convergent apparent order,” *J. Brazilian Soc. Mech. ...*, vol. XXVII, no. 4, 2005.
- [158] “ANSYS Mechanical APDL Theory Reference,” vol. 15317, no. November, pp. 724–746, 2013.
- [159] TheConnector, “Easy Meshing with Structured Accuracy.” [Online]. Available: <http://www.pointwise.com/theconnector/May-2012/Overset-Grids-in-Pointwise.shtml>. [Accessed: 24-Aug-2015].
- [160] J. T. M. and C. T. Shaw, *Finite Elements in Mechanical Design*. McGraw Hill International, 1996.
- [161] A. Inc., “ANSYS 10.0 Documentation : Selecting a Solver,” 2005.
- [162] A. Barlow, J. B., Rae, W. H., Jr., and Pope, *Low-Speed Wind Tunnel Testing*, 3rd ed. New York: Wiley-Interscience, 1999.
- [163] C. J. Wenzinger, “Wind Tunnel Investigations of a ordinary and split flaps on airfoils of different profile,” Langley Field, VA, 1935.
- [164] R. C. P. and J. A. Shortal, “Wind Tunnel Investigations of wings with ordinary ailerons and full span external airfoil flaps,” Langley Field, VA., 1937.
- [165] M. Sadraey, *Aircraft Design: A Systems Engineering Approach, Chapter 12*

Design of Control Surfaces. Wiley Publications, 2012.

- [166] P. F. Ailerons and F. Ailerons, “ProAdvice 3 : AILERON SIZING,” pp. 1–12, 2011.
- [167] S. Esdu, “Rolling moment derivative , $L \xi$ for plain ailerons at subsonic speeds,” no. August 1988, 1992.
- [168] I. H. Abbott and A. E. Von Doenhoff, “Theory of Wing Sections: Including a Summary of Airfoil data,” *Press*, vol. 11, p. 693, 1959.
- [169] I. Lekakis, “Calibration and signal interpretation for single and multiple hot-wire/hot-film probes,” *Meas. Sci. Technol.*, vol. 7, no. 10, pp. 1313–1333, 1999.
- [170] F. E. Jørgensen, “How to measure turbulence with hot-wire anemometers a practical guide,” *Dantec Dyn.*, p. 3244, 2002.
- [171] A. INC., “MC3A manual(Dynamometer Instructions).” p. 2000.
- [172] AMTI, “DigiAmp Technical Reference Manual,” 2003.
- [173] A. M. T. Inc., “Dynamometer Instructions (MC3A manual).” Watertown, Massachusetts.
- [174] P. W. C. E. L Houghton, *Aerodynamics for Engineering Students*, 5th ed. Oxford: Butterworth Heinemann, 2003.
- [175] F. M. T. J. and B. T., “Experimental studies of the Eppler 61 airfoil at low Reynolds numbers,” *AIAA Pap.*, vol. 82, no. 0345.
- [176] P. R. B. and D. K. Robinson, *Data Reduction and Error Analysis for the Physical Science*, 3rd ed. New York: McGraw Hill Higher Education, 2003.
- [177] W. G. S. Hugh W. Coleman, *Experimentation and Uncertainty Analysis for Engineers*. John Wiley & Sons, 1999.
- [178] J. R. Taylor, *An Introduction to Error Analysis: The Study of Uncertainties in Physical Measurements*, vol. 51, no. 2. California: University Science Books, 1983.
- [179] W. Horten, Reimar and Horten, “Toward the theory of Flying Wings,” 1984. [Online]. Available: http://www.nurflugel.com/Nurflugel/Horten_Nurflugels/horten_nurflugels.html. [Accessed: 08-Feb-2016].
- [180] M. Simons, “Model Aircraft Aerodynamics.” pp. 1–331, 1994.
- [181] T. Cebeci, *Numerical and Physical Aspects of Aerodynamic Flows IV*. New York: Springer-Verlag- Berlin Heidelberg GmbH, 1990.
- [182] N. S. Khot, J. V. Zweber, D. E. Veley, H. -Oslash, and F. E. Eastep, “Flexible Composite Wing with Internal Actuation for Roll Maneuver,” *J. Aircr.*, vol. 39, no. 4, pp. 521–527, Jul. 2002.
- [183] N. S. Khot, F. E. Eastep, and R. M. Kolonay, “Method for Enhancement of

the Rolling Maneuver of a Flexible Wing,” *J. Aircr.*, vol. 34, no. 5, pp. 673–678, 1997.

APPENDIX-A

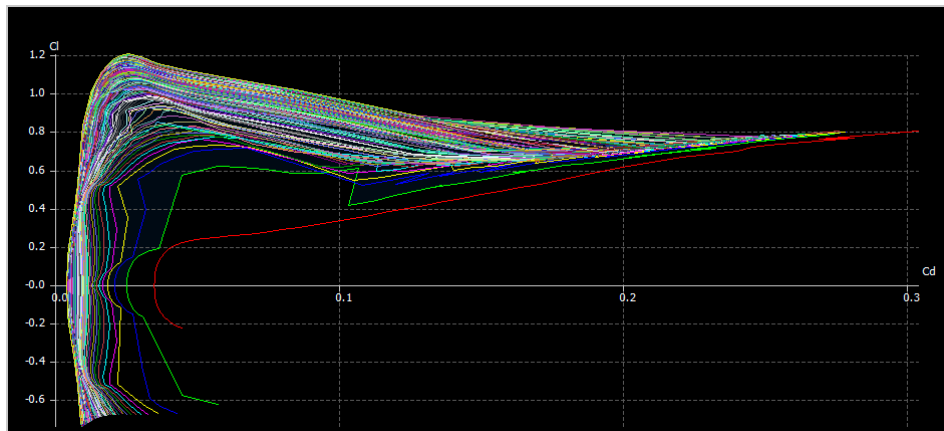


Figure A- 1 Airfoil data analysis C_L/C_D

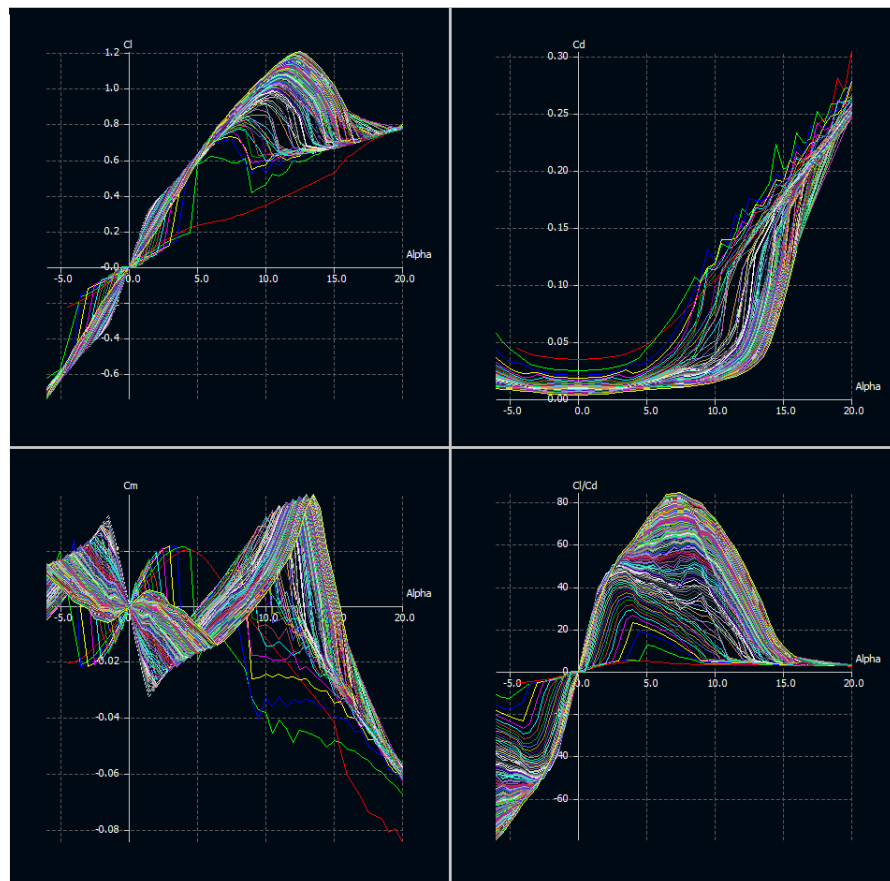


Figure A- 2 Airfoil data analysis: C_L versus alpha (Up-Left), C_D versus alpha (Up-Right), C_m versus alpha (Down-Left), and C_L/C_D versus alpha (Down-Right).



Figure A- 3 Sanded Wing and Morphing Structure.



Figure A- 4 Enamel Spray paint & Clear Lacquer for Wing.

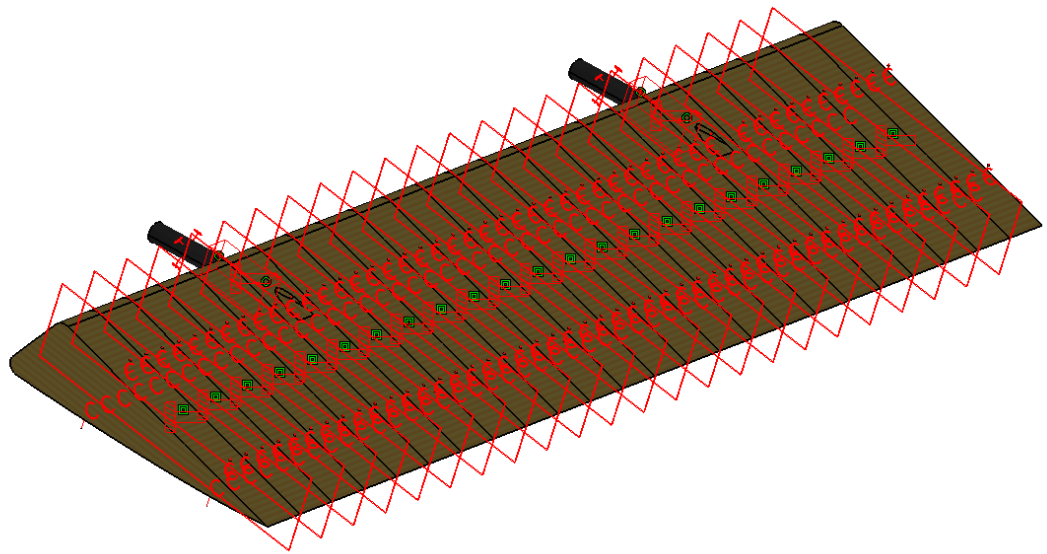


Figure A- 5 CATIA Structural Analysis Setup for Aileron

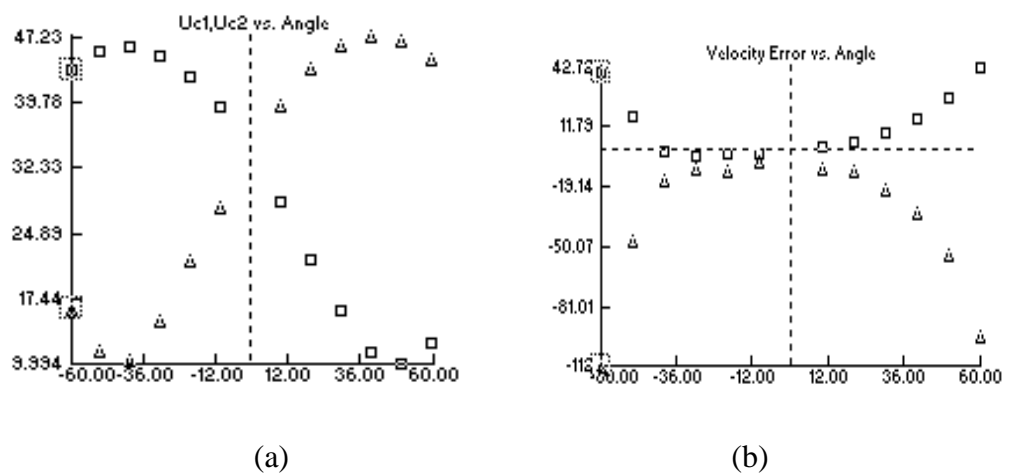


Figure A- 6 Directional Calibration Graphs: (a) Probe Velocity versus Angle and (b) Velocity error versus angle.

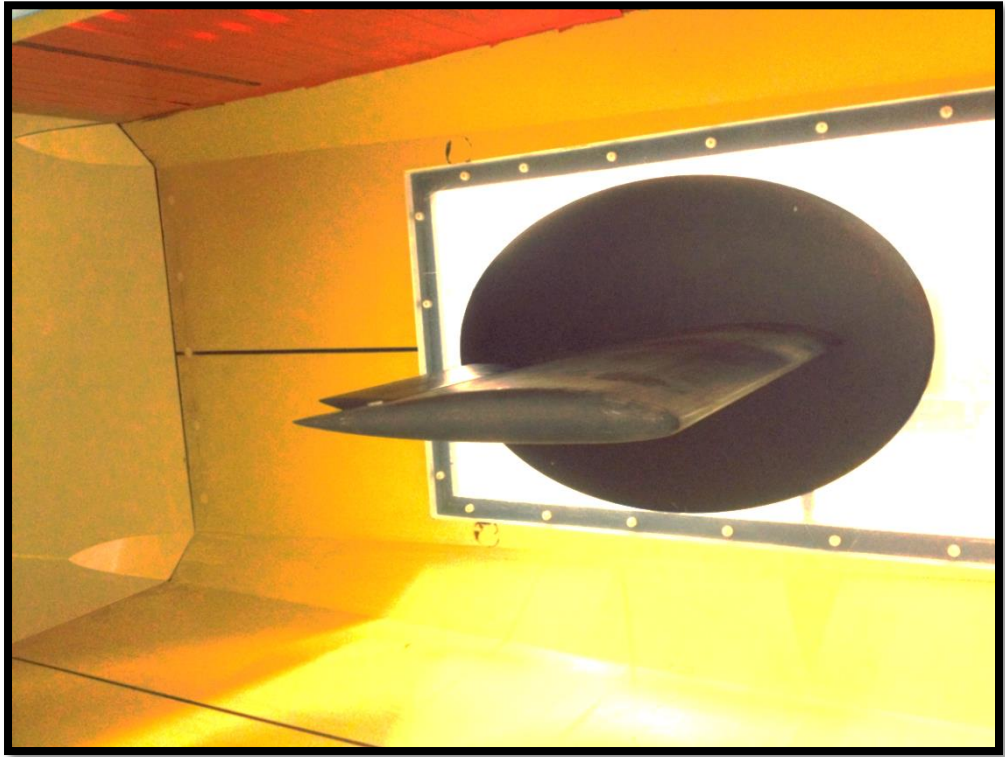


Figure A- 7 Wind Tunnel Setup for Aileron (-10°).

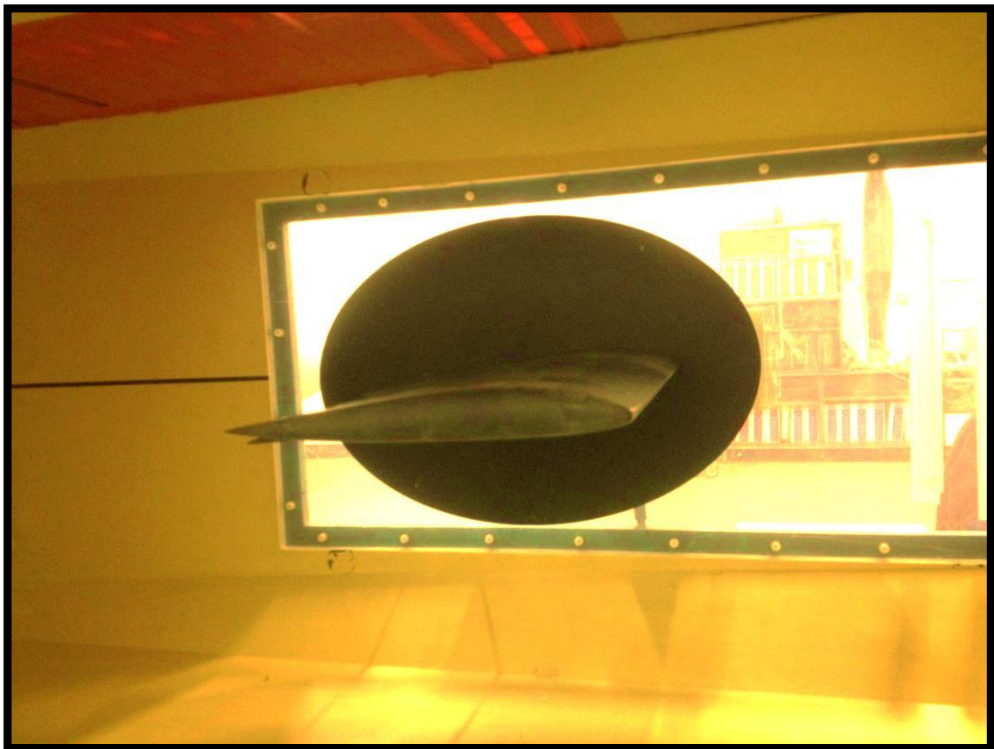


Figure A- 8 Wind Tunnel Setup for Aileron (+10°).

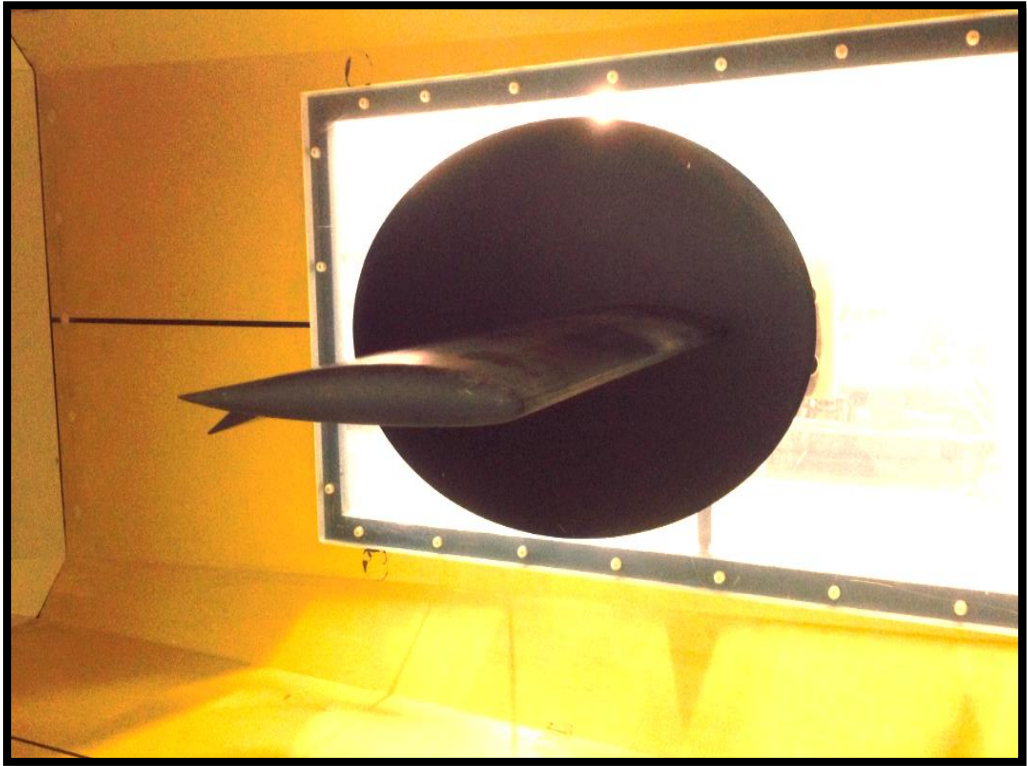


Figure A- 9 Wind Tunnel Setup for Aileron (+20°).

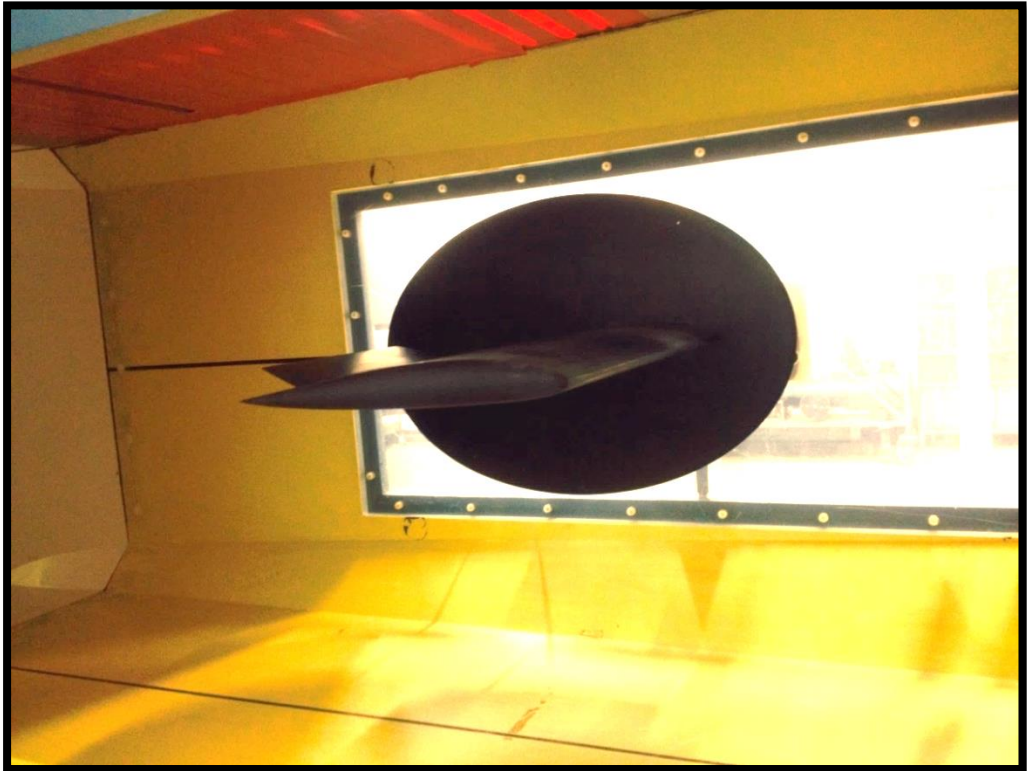


Figure A- 10 Wind Tunnel Setup for Aileron (-20°).

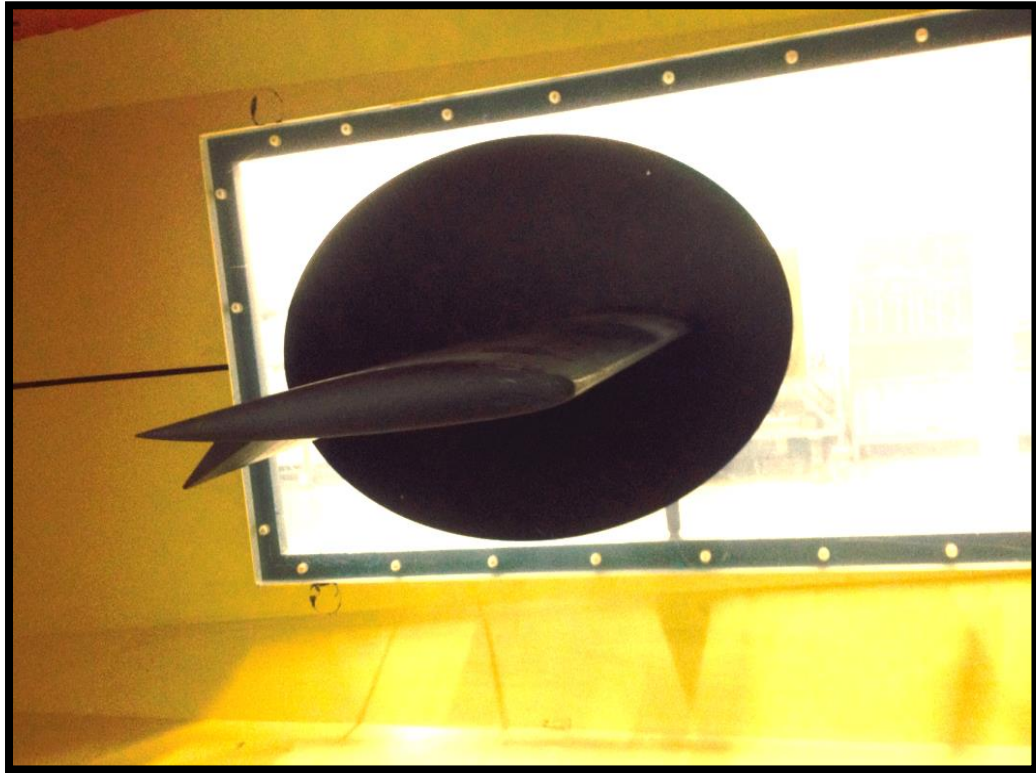


Figure A- 11 Wind Tunnel Setup for Aileron (+30°).

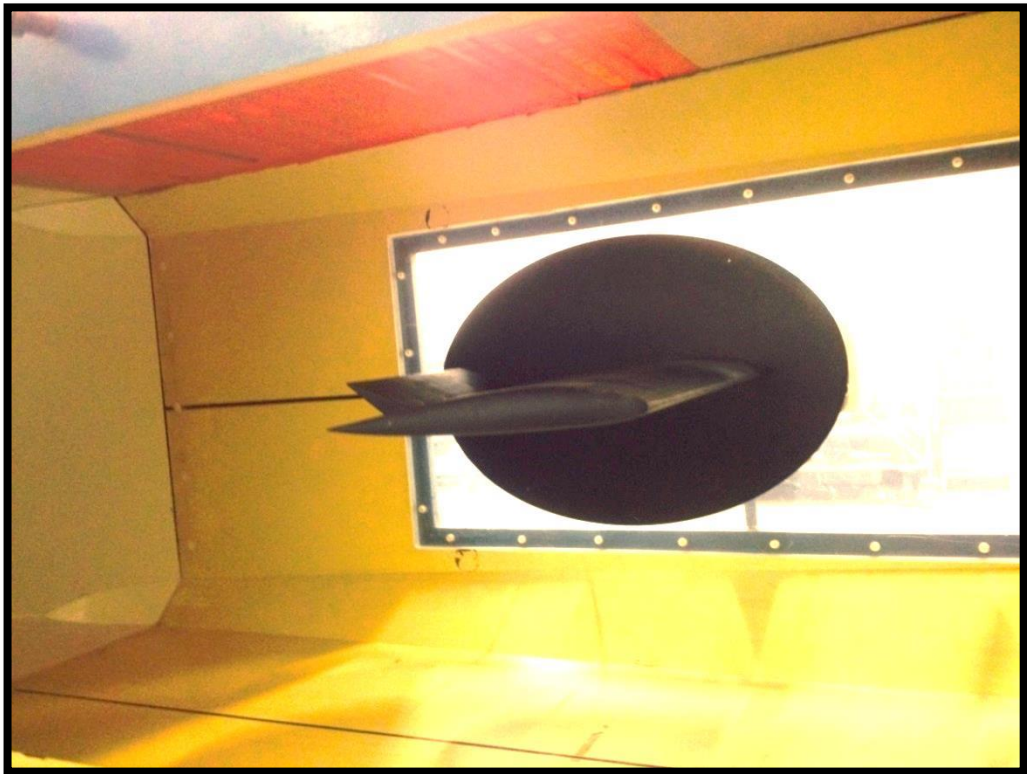


Figure A- 12 Wind Tunnel Setup for Aileron (-30°).

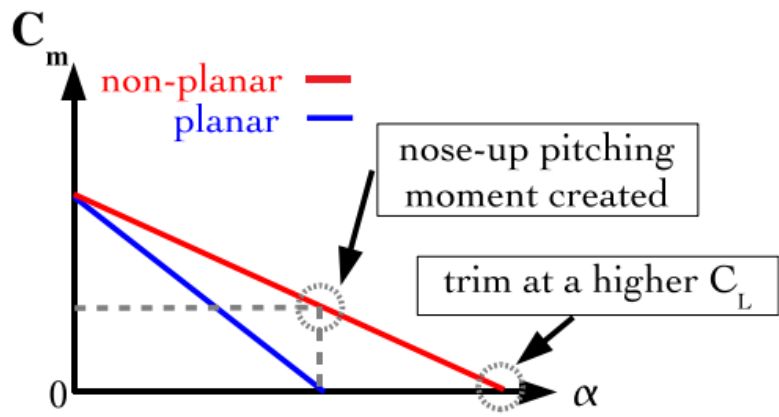


Figure A- 13 Effect of deflected tips on pitch: when one or both tips of the trimmed, longitudinally stable, planar configuration are folded up or down at fixed angle of attack, a nose-up pitching moment is created (aerodynamic center jumps forward while CG is fixed) reduced static margin, C_m is less negative). If the angle of attack is allowed to be adjusted, one can then trim at a larger C_L [114].

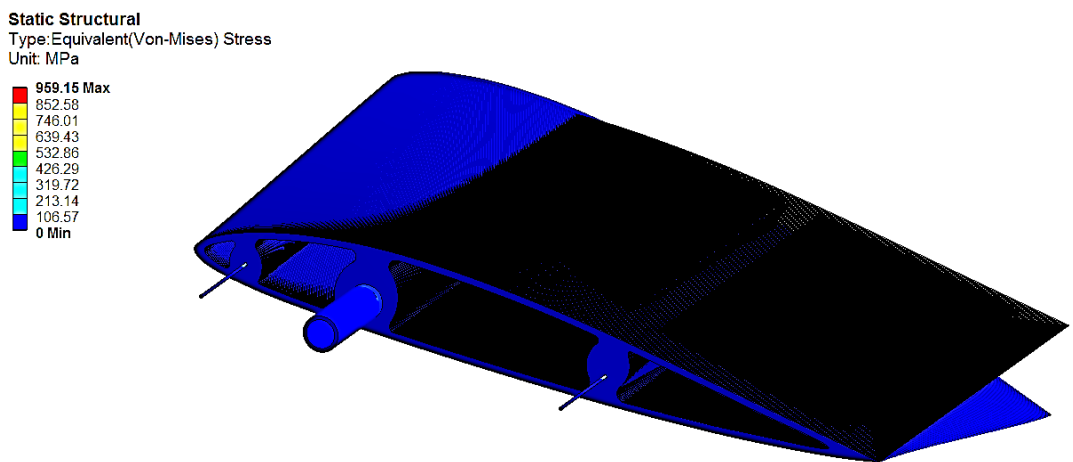


Figure A- 14 Equivalent stress results for $r = 1$ mm (Wash-in) .

Static Structural
 Type: Equivalent(Von-Mises) Stress
 Unit: MPa

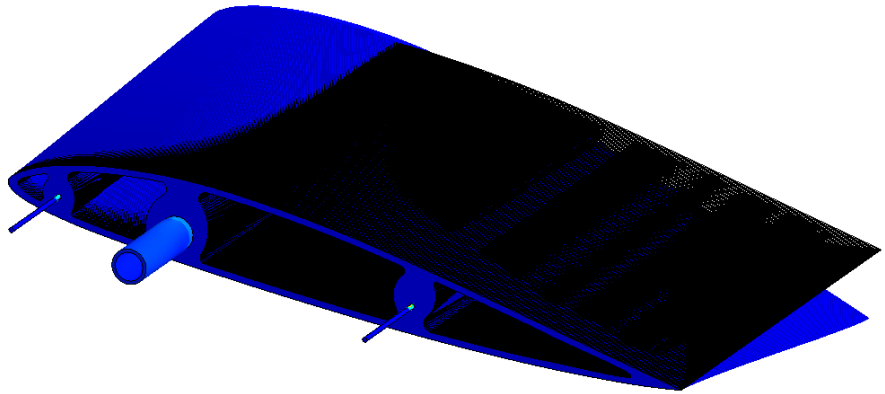
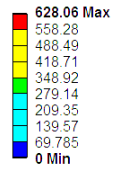


Figure A- 15 Equivalent stress results for $r = 1.5$ mm (Wash-in).

Static Structural
 Type: Equivalent(Von-Mises) Stress
 Unit: MPa

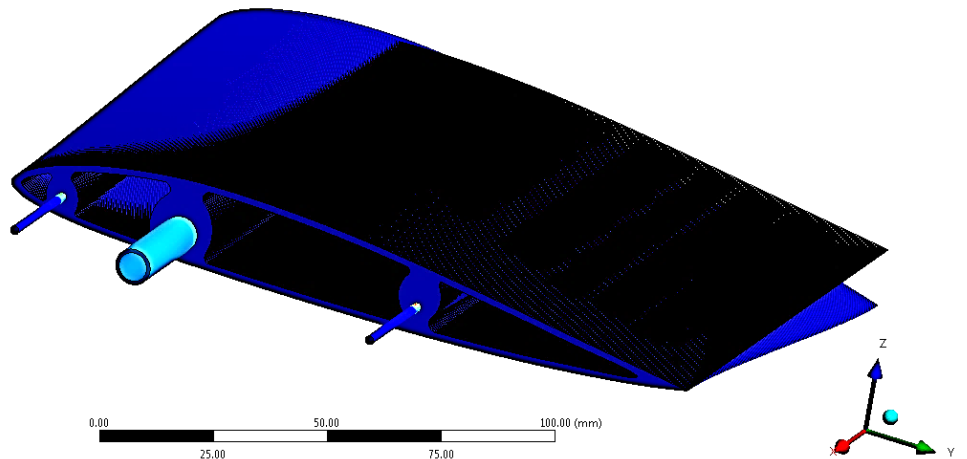
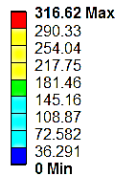


Figure A- 16 Equivalent stress results for $r = 2.5$ mm (Wash-in).

Static Structural
 Type: Equivalent(Von-Mises) Stress
 Unit: MPa

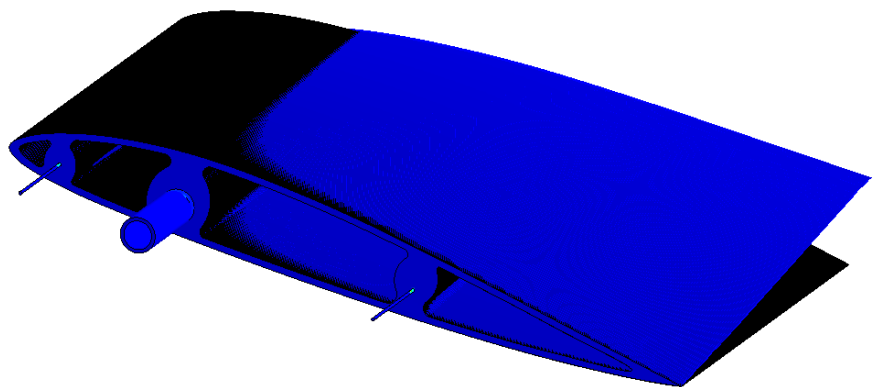
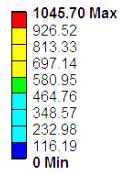


Figure A- 17 Equivalent stress results for $r = 1$ mm (Wash-out).

Static Structural
Type: Equivalent(Von-Mises) Stress
Unit: MPa

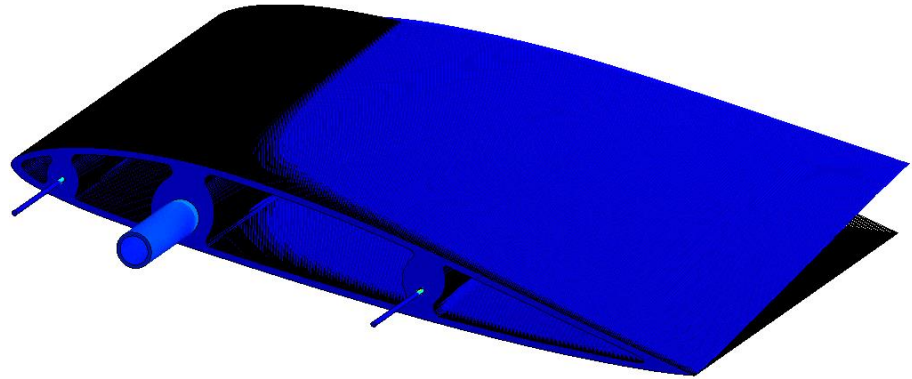
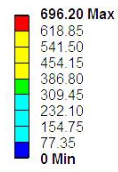


Figure A- 18 Equivalent stress results for $r = 1.5$ mm (Wash-out).

Static Structural
Type: Equivalent(Von-Mises) Stress
Unit: MPa

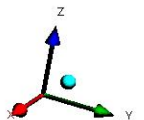
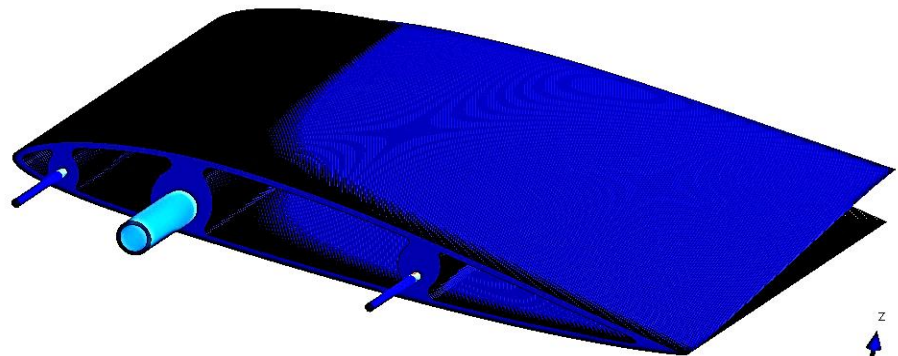
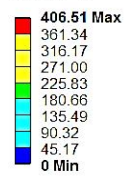


Figure A- 19 Equivalent stress results for $r = 2.5$ mm (Wash-out).

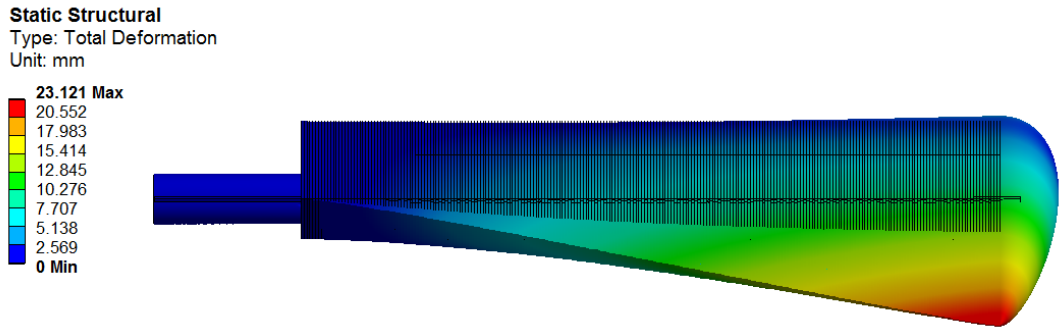


Figure A- 20 Deformation Results for $r = 1$ mm (Wash-in).

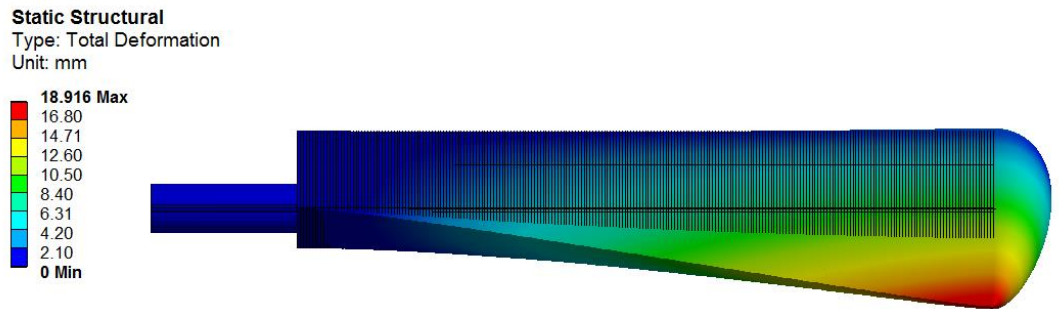


Figure A- 21 Deformation Results for $r = 1.5$ mm (Wash-in).

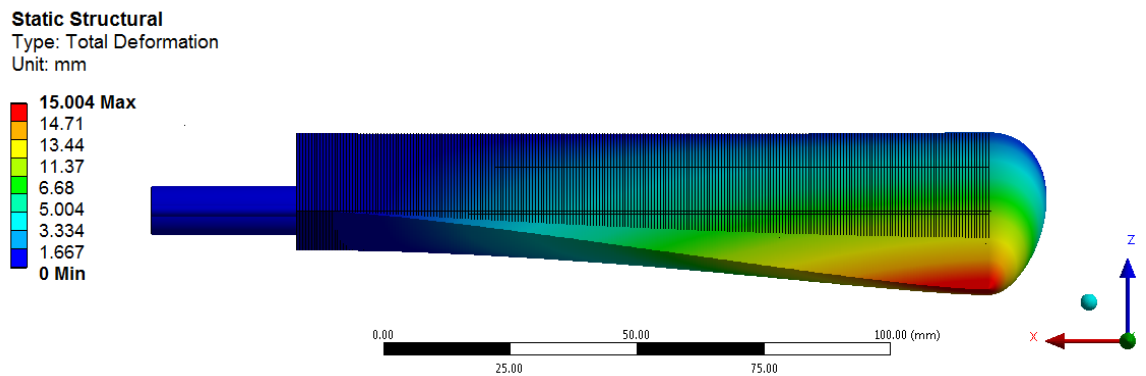


Figure A- 22 Deformation Results for $r = 2.5$ mm (Wash-in).

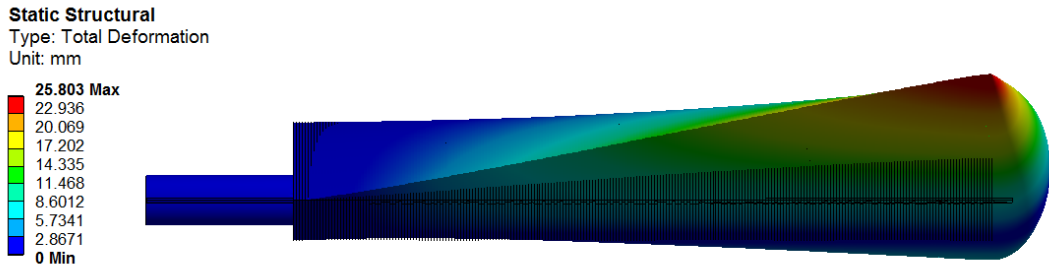


Figure A- 23 Deformation Results for $r = 1$ mm (Wash-out).

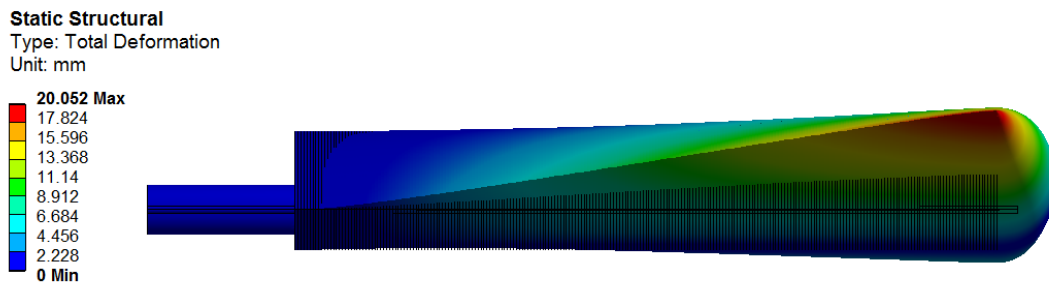


Figure A- 24 Deformation Results for $r = 1.5$ mm (Wash-out).

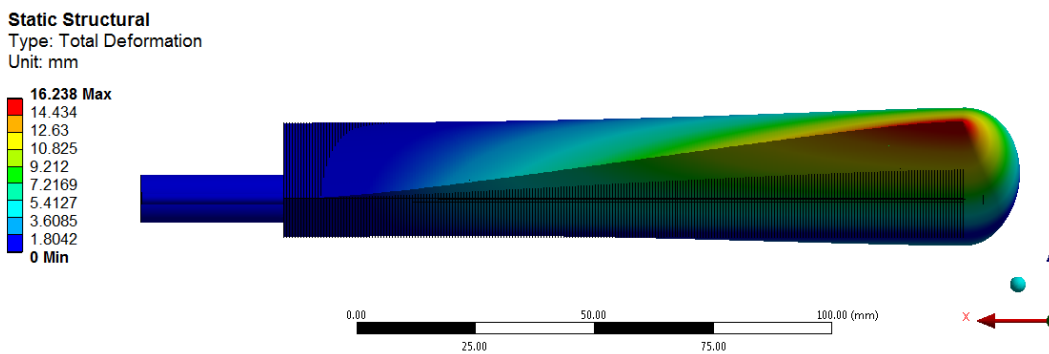


Figure A- 25 Deformation Results for $r = 2.5$ mm (Wash-out) .

Static Structural
Type: Equivalent(Von-Mises) Stress
Unit: MPa

463.14 Max
411.68
360.22
308.76
257.3
205.84
154.38
102.92
51.46
1.7463e-18 Min

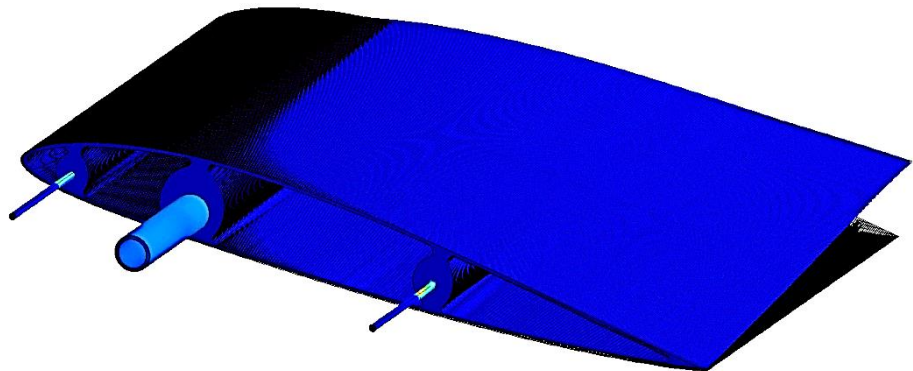


Figure A- 26 Equivalent stress results for $t=1$ mm (Wash-out).

Static Structural
Type: Equivalent(Von-Mises) Stress
Unit: MPa

350.47 Max
311.53
272.59
233.65
197.7
155.76
116.82
77.882
38.941
1.6117e-18 Min

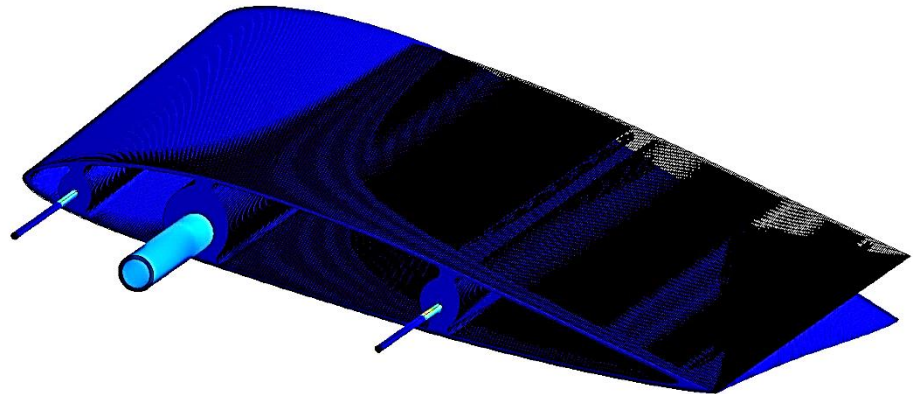


Figure A- 27 Equivalent stress results for $t=1$ mm (Wash-in).

Static Structural
Type: Equivalent(Von-Mises) Stress
Unit: MPa

454.19 Max
403.72
353.26
302.79
252.33
201.86
151.4
100.93
50.465
1.6846e-18 Min

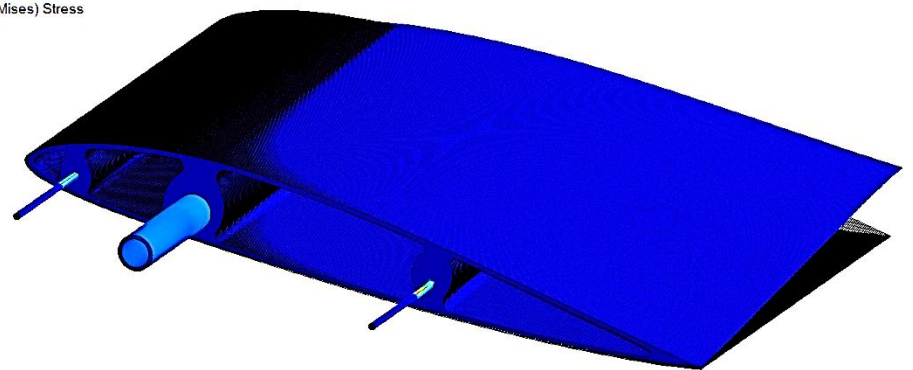


Figure A- 28 Equivalent stress results for $t=1.5$ mm (Wash-out).

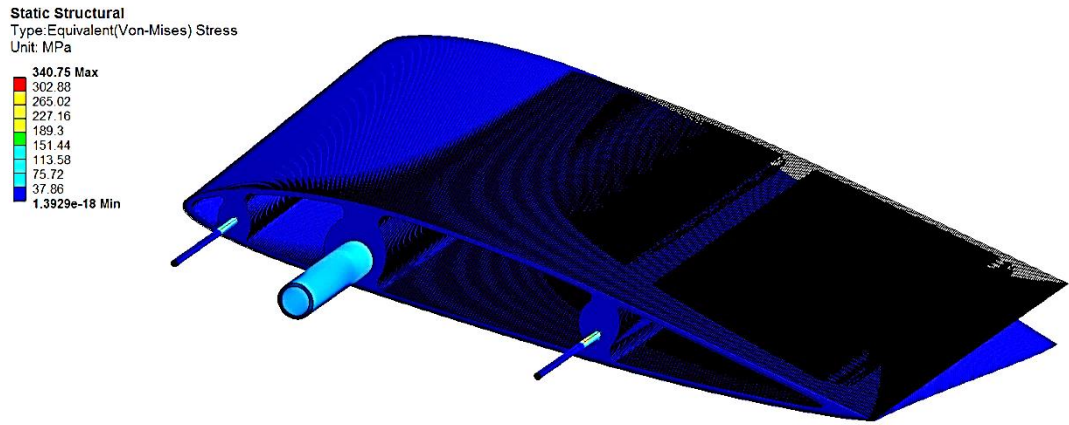


Figure A- 29 Equivalent stress results for $t= 1.5\text{mm}$ (Wash-in).

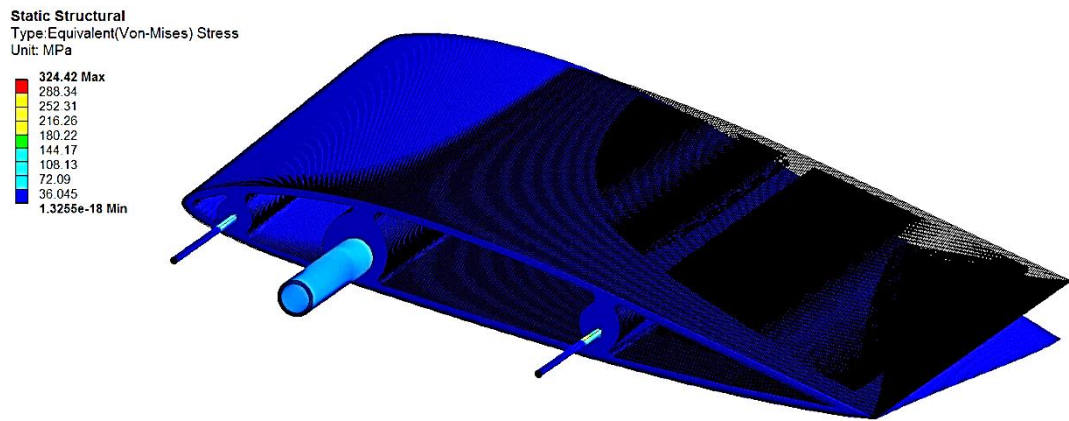


Figure A- 30 Equivalent stress results for $t= 2\text{mm}$ (Wash-in).

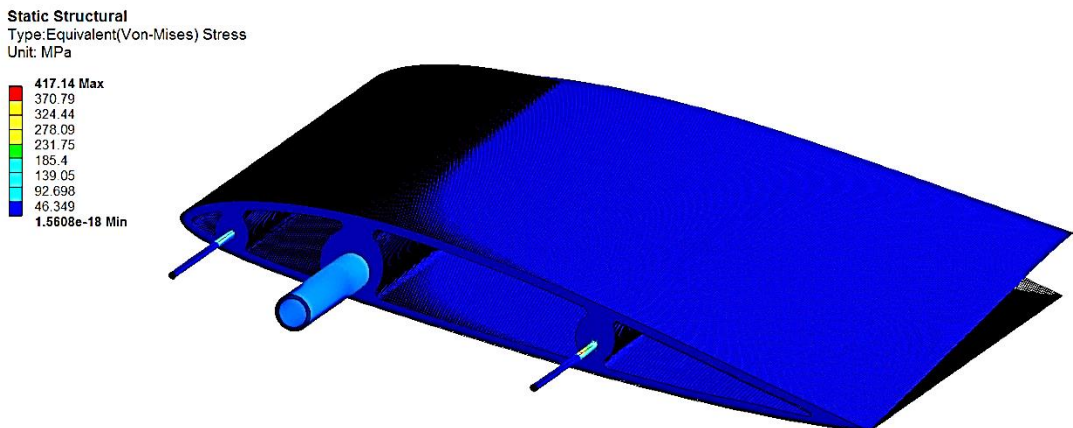


Figure A- 31 Equivalent stress results for $t= 2.5\text{mm}$ (Wash-out).

Static Structural
Type: Equivalent(Von-Mises) Stress
Unit: MPa

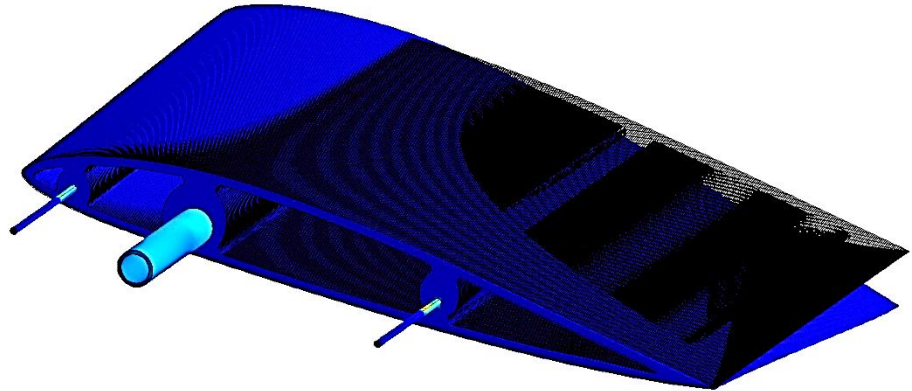
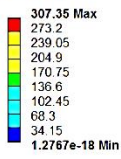


Figure A- 32 Equivalent stress results for $t= 2.5\text{mm}$ (Wash-in).

Static Structural
Type: Equivalent(Von-Mises) Stress
Unit: MPa

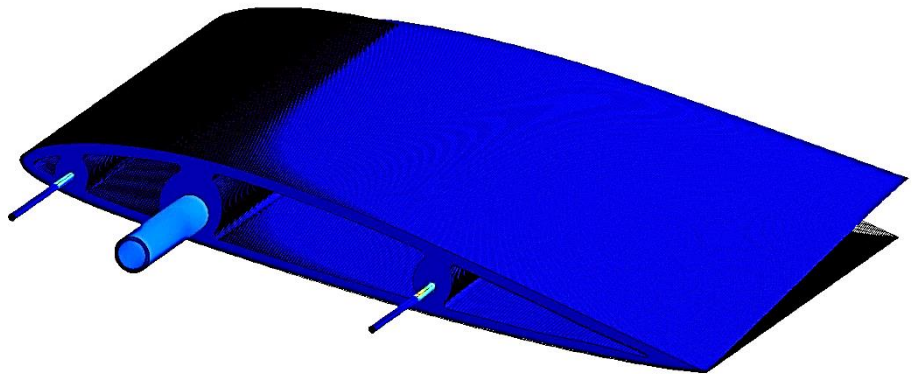
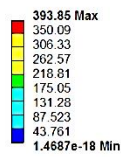


Figure A- 33 Equivalent stress results for $t= 3\text{mm}$ (Wash-out).

Static Structural
Type: Equivalent(Von-Mises) Stress
Unit: MPa

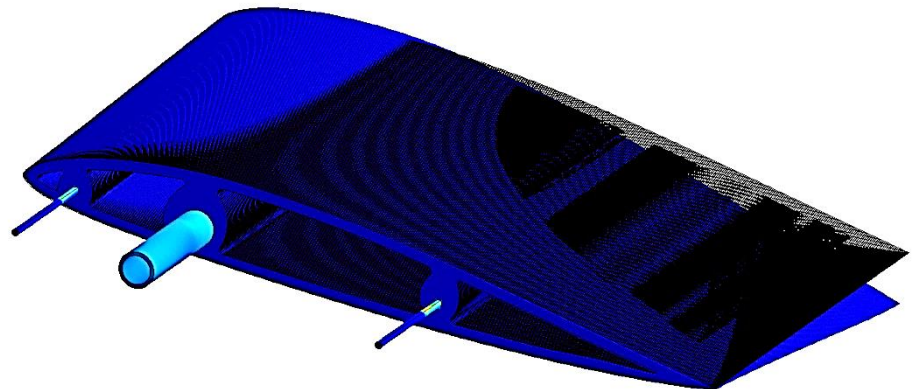
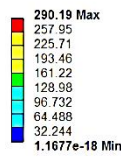


Figure A- 34 Equivalent stress results for $t= 3\text{mm}$ (Wash-in).

Static Structural
Type: Equivalent (Von-Mises) Stress
Unit: MPa

213.06 Max
189.39
165.72
142.04
118.37
94.695
71.022
47.348
23.674
7.5009e-8 Min

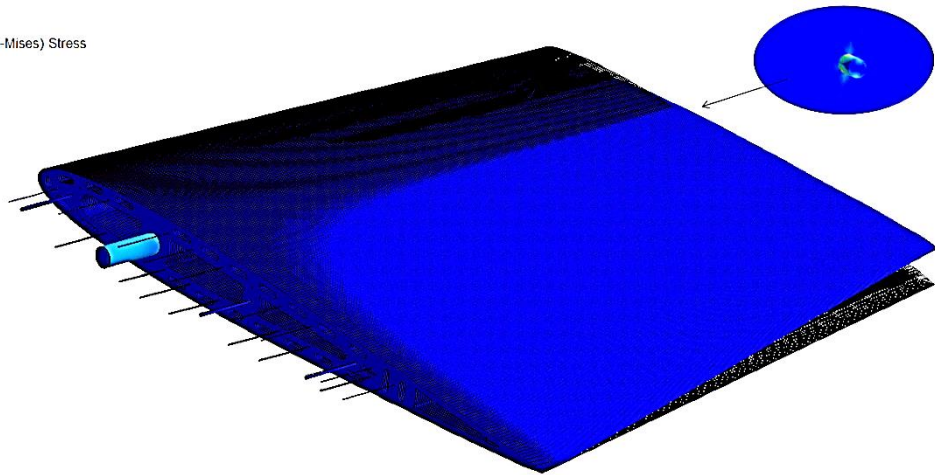


Figure A- 35 Von-Mises stress for 20 rods twist system.

Static Structural
Type: Equivalent (Von-Mises) Stress
Unit: MPa

225.35 Max
200.31
175.27
150.24
125.2
100.16
75.118
50.078
25.039
2.25e-7 Min

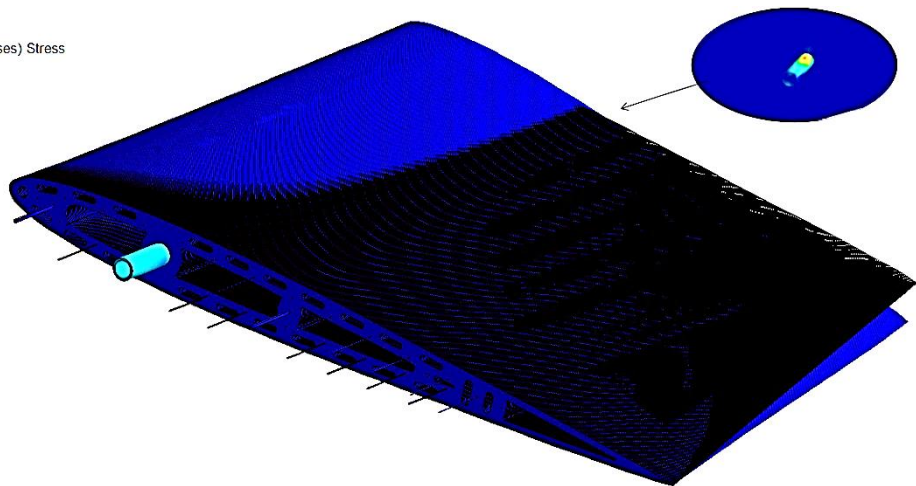


Figure A- 36 Von-Mises stress for 17 rods twist system.

Static Structural
Type: Equivalent (Von-Mises) Stress
Unit: MPa

458.91 Max
407.92
356.93
305.94
254.95
203.96
152.97
101.98
50.99
0 Min

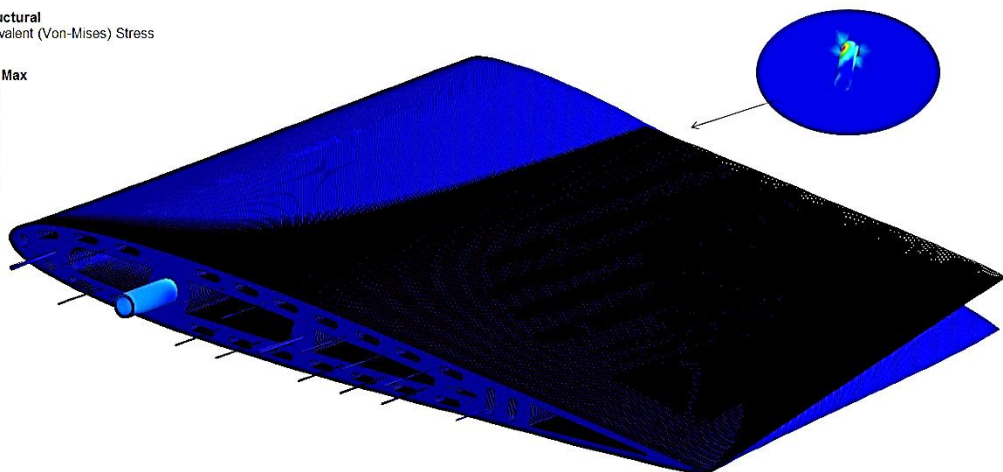


Figure A- 37 Von-Mises stress for 16 rods twist system.

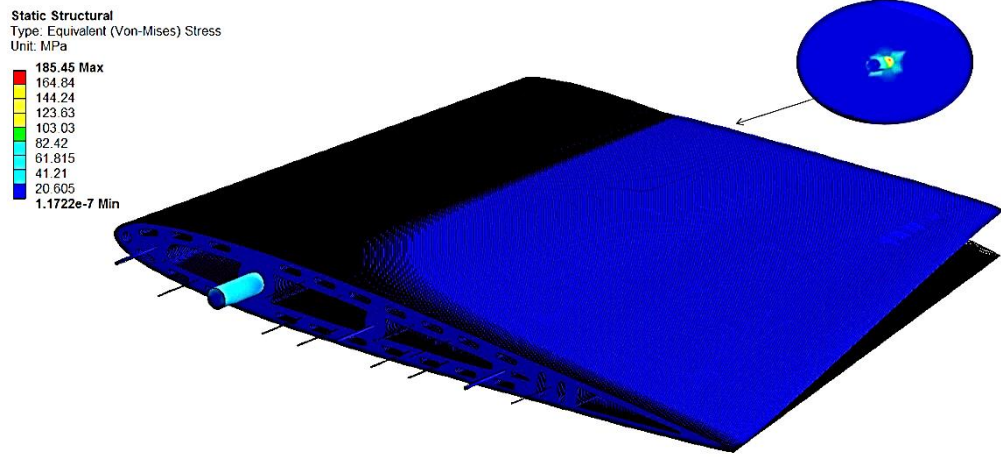


Figure A- 38 Von-Mises stress for 15 rods twist system.

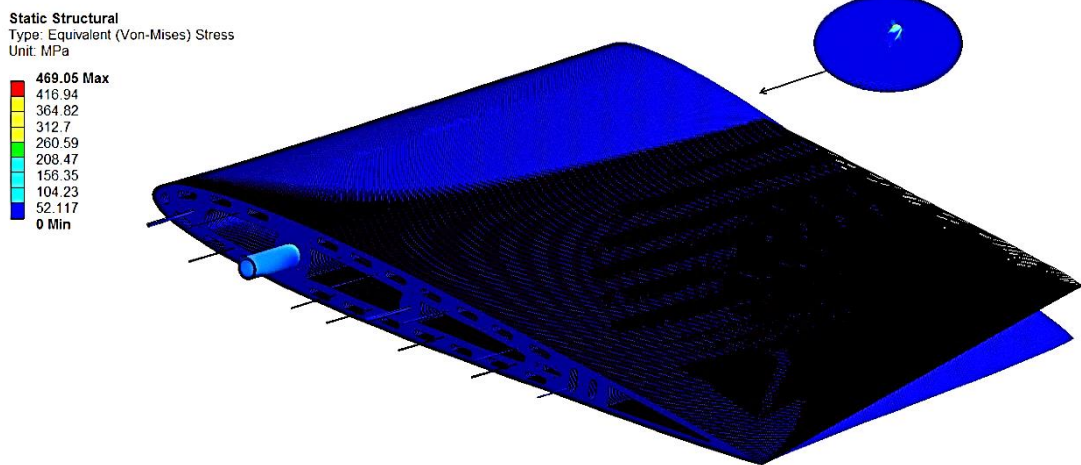


Figure A- 39 Von-Mises stress for 14 rods twist system.

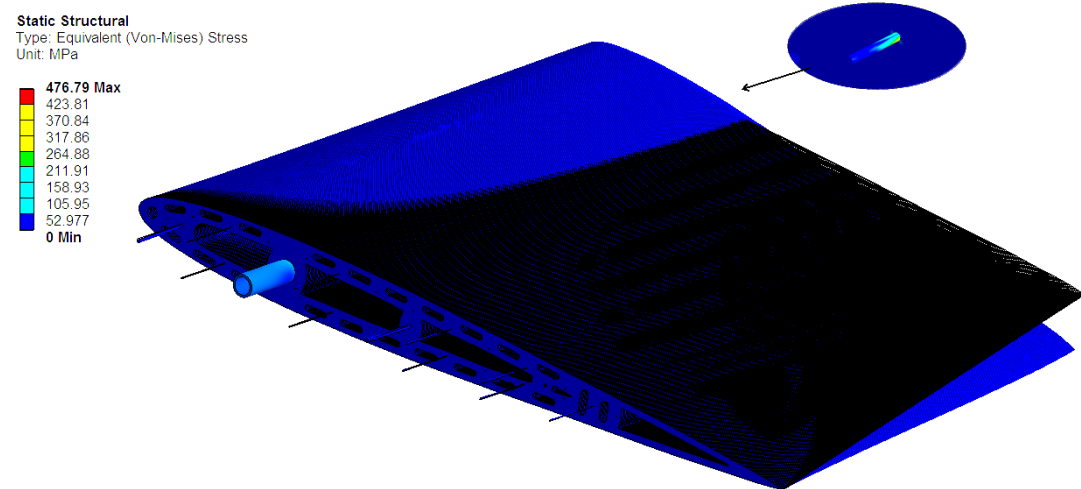


Figure A- 40 Von-Mises stress for 12 rods twist system.

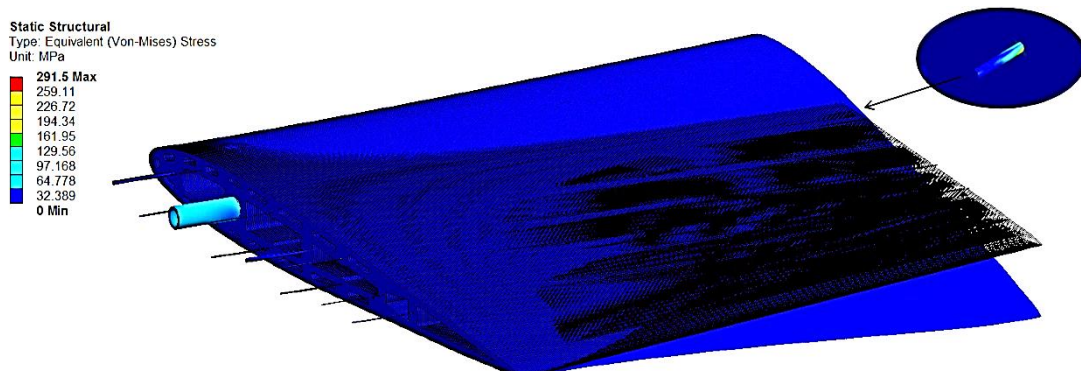


Figure A- 41 Von-Mises stress for 11 rods twist system (washin).

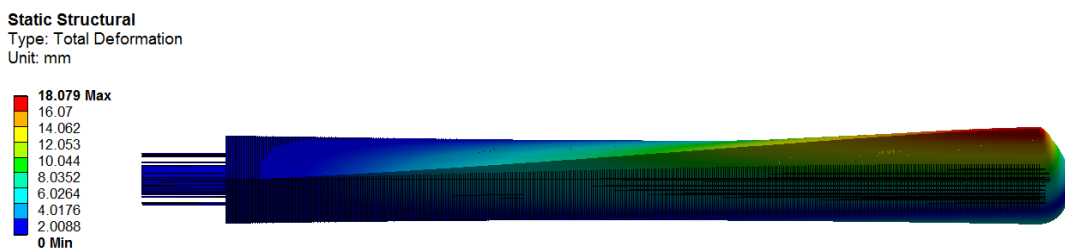


Figure A- 42 Total Deformation for 20 rods twists system.

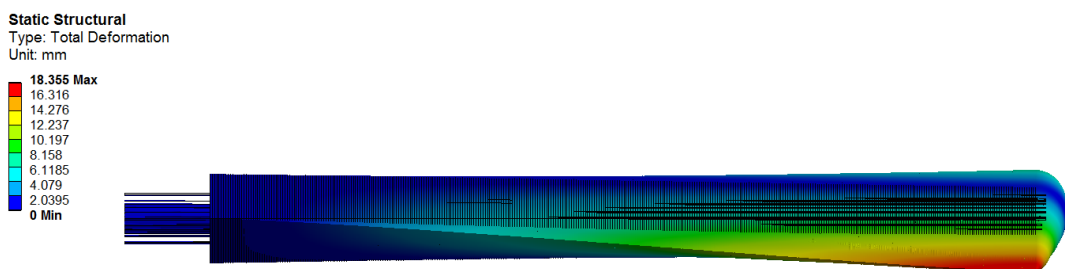


Figure A- 43 Total Deformation for 17 rods twists system.

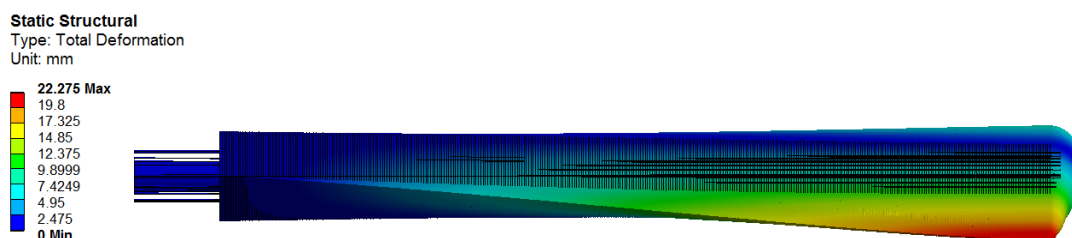


Figure A- 44 Total Deformation for 16 rods twists system.

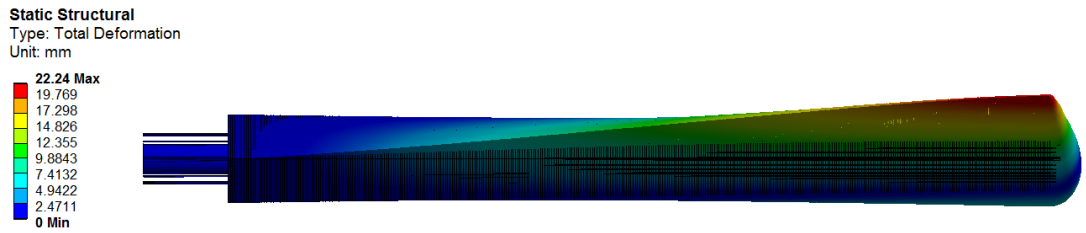


Figure A- 45 Total Deformation for 15 rods twists system.

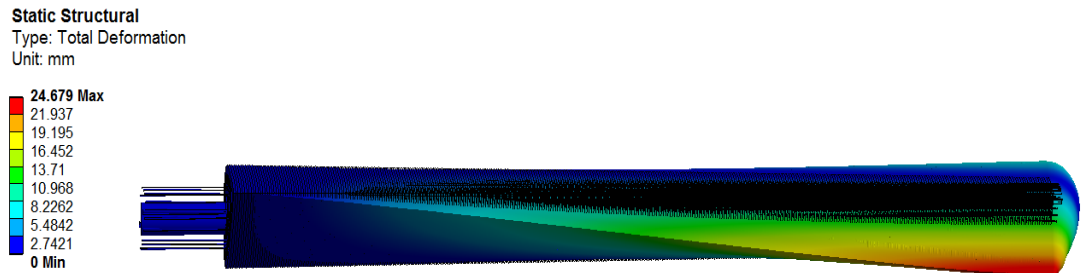


Figure A- 46 Total Deformation for 14 rods twist system.

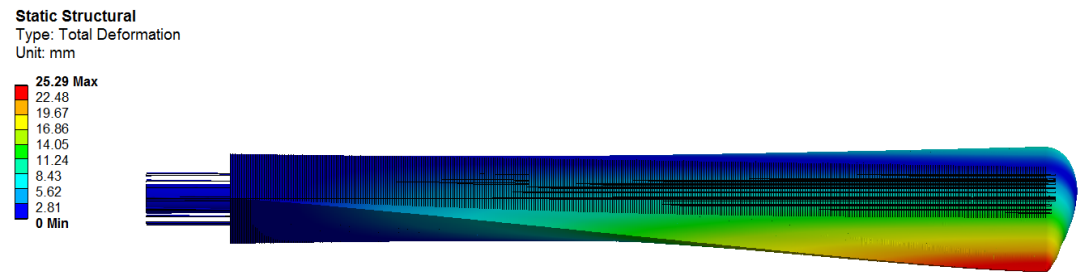


Figure A- 47 Total Deformation for 12 rods twists system.

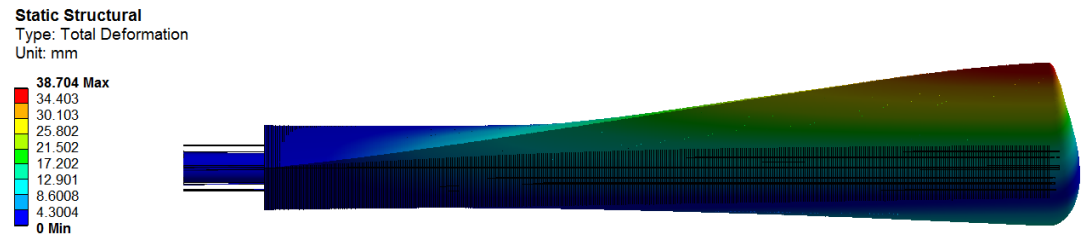


Figure A- 48 Total Deformation for 11 rods twists system (washout).

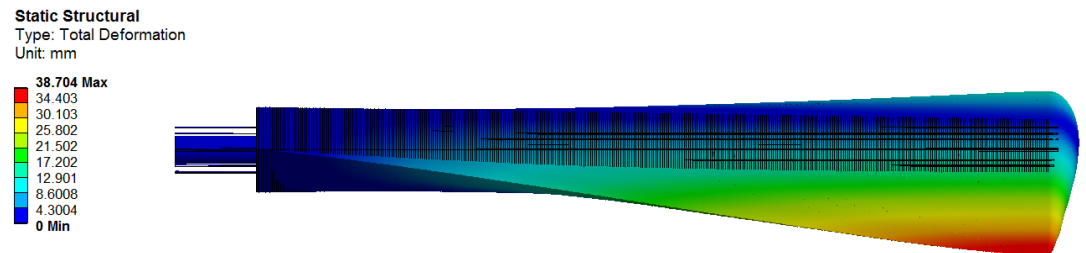


Figure A- 49 Total Deformation for 11 rods twists system (washin).